Experimental Assessment of the Mechanical Behavior of Immersion Joints and a Seismic Mitigation Method in Immersed Tunnels

Experimentele evaluatie van het mechanisch gedrag van de zinkvoegen en van een methode voor de vermindering van het risico bij aardbevingen bij afgezonken tunnels

Wenhao Xiao

Promotoren: prof. dr. ir. L. Taerwe, prof. dr. Y. Yuan
Proefschrift ingediend tot het behalen van de graad van
Doctor in de ingenieurswetenschappen: bouwkunde

UNIVERSITEIT
GENT

Vakgroep Bouwkundige Constructies
Voorzitter: prof. dr. ir. L. Taerwe
Faculteit Ingenieurswetenschappen en Architectuur
Academiejaar 2017 - 2018

ISBN 978-94-6355-094-9
NUR 956
Wettelijk depot: D/2018/10.500/12

Supervisor

Prof. dr. ir. Luc Taerwe

Department of Structural Engineering, Ghent University, Belgium

Prof. dr. ir. Yong Yuan

Tongji University, Shanghai, China

Examination Committee

em. Prof. dr. ir. Hendrik Van Landeghem

Department of Industrial Systems Engineering and Product Design, Ghent University, Belgium (Chairman)

Prof. dr. ir. Wouter De Corte

Department of Structural Engineering, Ghent University, Belgium (Secretary)

Prof. dr. ir. Luc Taerwe

Department of Structural Engineering, Ghent University, Belgium (Supervisor)

Prof. dr. ir. Yong Yuan

Tongji University, Shanghai, China (Supervisor)

Prof. dr. ir. Bart De Pauw

Department of Civil Engineering, Ghent University, Belgium

Prof. dr. ir. Hervé Degée

Department of Structural Engineering, Ghent University, Belgium

em. Prof. dr. ir. Joost Walraven

TU Delft, the Netherlands

Prof. dr. ir. Haitao Yu

Tongji University, Shanghai, China

Prof. dr. ir. Robby Caspeele

Department of Structural Engineering, Ghent University, Belgium

Research Institute

Magnel Laboratory for Concrete Research,
Department of Structural Engineering, Ghent University,
Technologiepark-Zwijnaarde 904, B-9052, Ghent, Belgium

This research was supported by China Scholarship Council (CSC)

UNIVERSITEIT GENT

FACULTEIT INGENIEURSWETENSCHAPPEN EN ARCHITECTUUR

CHINA SCHOLARSHIP COUNCIL

CONTENTS

ACKNOWLEDGEMENTS

After about three years of work, my dissertation is now finally in front of me. This work would not have been possible without the support and contribution of several people.

First of all, I would like to show my deepest gratitude to my two supervisors Prof. Luc Taerwe and Prof. Yong Yuan who gave me the chance of becoming a member of the 'Magnel Lab'. I am grateful for your support, trust and guidance throughout my PhD research. Your wisdom, patience, and passion for being a researcher inspired me at the same time. As such, I really appreciate all your support to my research and dissertation we were working on in the past few years. It is my great honor to have worked in your team and it was pleasant as well I will gladly reminisce about the time at Ghent University. Also Prof. Yu Haitao in Tongji University helped me a lot during my PhD study and I would like to give my appreciation to him as well.

I would like to express my thanks to the Chinese Scholarship Council for providing me a scholarship for my PhD study (No. 201406260199). I would never have had the chance to study abroad without such financial support.

During my doctoral studies I have performed extensive experimental investigations. As a joint research between Ghent University and Tongji University, the experiments were conducted in the State Key Laboratory for Disaster Reduction in Civil Engineering, Tongji University. This PhD research can be seen as a first main activity in the framework of the recently established Belgium-China Joint Laboratory for Industrialized Construction. The conducted large-scale tests on immersion joints form a large part of my thesis, which would not have been possible without the unconditional help and support of the technical staff. I am very grateful for your advice and the suggestions regarding the execution of my experiments. Furthermore, a lot of

Chinese colleagues in Tongji University supported me while conducting the experiments. Your support during the time-consuming measurements was outstanding and very helpful. I want to thank the Hong Kong-Zhuhai-Macao Bridge Authority for providing all the technical data and support for my experiments and research related to this spectacular project and I am proud of having been working on that. Thank you all!

I also would like to express a special acknowledgement to the staff of the Magnel Laboratory for Concrete Research. I appreciate the mutual support we gave each other and I consider our collaboration as a great personal gain. Moreover, I would like to thank Marijke, Christel and my officemates for their friendly help. I want to thank you all again for making my stay at the Magnel Lab so unique.

Sincere thanks go to my family. I particularly wish to thank my parents and my girlfriend, Xi, for their endless support and encouragement throughout my life and especially during my doctoral studies in Ghent, a city which is far away from you.

Wenhao Xiao, November. 2017

LIST OF SYMBOLS

Roman symbols

A_m	cross-sectional area of the model (chapter IV)
A_p	cross-sectional area of the prototype (chapter IV)
A_s	-total area of the longitudinal reinforcement (chapter IV) -estimated cross-sectional area of the rubber (chapter VII)
A	cross-sectional area of the connecting region of the BEDD (chapter IX)
a_0	fitting coefficient of $f(t)$ (chapter VI)
a_1	fitting coefficient of $f(t)$ (chapter VI)
a	rotation angle at the yielding point A (chapter VIII)
b	width of a tenon (chapter IV) bending moment at the first yielding point A (chapter VIII)
b_1	fitting coefficient of $f(t)$ (chapter VI)
C	damping of the structure (chapter III)
C_l	dimensional ratio (chapter IV)
C_1 and C_2	empirically determined material constants (chapter V)

D_m	diameter of the reinforcement in the model (chapter IV)
D_p	diameter of the reinforcement in the prototype (chapter IV)
d_j	-difference between the maximum (40kN) and minimum (-40kN) shear -displacement (chapter VI)
d_{dyn}	dynamic dislocation (chapter VI)
d_{la1} to d_{la4}	recorded displacement from laser transducer La1 to La4 (chapter VI)
d_{max} and d_{min}	maximum and minimum dynamic shear displacement (chapter VI)
d_i	the shear displacement of the joint at step *i* of the test (chapter VII)
d	original height of the rubber seal (chapter VII)
d_s	shear displacement of the rubber seal (chapter VII)
d_a	axial displacement of the rubber seal (chapter VII)
d_r	relative deformation (chapter VII)
d_j	deformation of the joint (chapter VIII)
d_{BEDD}	deformation of the BEDD (chapter VIII)
d_{ru}	deformation of the rubber (chapter VIII)
d_A	deformation of the BEDD at point A (chapter VIII)
d_{a1}	average displacement of the transducers at the same side (chapter IX)
d_{a2}	average displacement of the transducers at the same side (chapter IX)
d_1 to d_4	recorded displacement of #1 to #4 shear transducers (chapter IX)
E_{in}	input earthquake energy (chapter III)
E_A	energy consumed by the seismic mitigation devices (chapter III)
E_D	energy consumed by damping (chapter III)
E_R	kinetic and potential energy of the structural vibration (chapter III)
E_S	consumed energy due to the non-elastic deformation or damage of the main structure (chapter III)

E_m	elastic modulus of the model (chapter IV)
E_p	elastic modulus of the prototype (chapter IV)
E	Young's Modulus of the steel (chapter IX)
$F(t)$	arbitrary external loading (chapter III)
F_m	force of the model (chapter IV)
F_p	force of the prototype (chapter IV)
f_{tk}	characteristic value of the tensile strength of concrete (chapter IV)
F_v	shear force acting on a tenon (chapter IV)
F_{vk}	cracking load of a tenon (chapter IV)
f_y	design value of the tensile stress of the reinforcement (chapter IV)
F_y	yielding force of the BEDD (chapter VII)
F1 to F4	fitting curves 1 to 4 (chapter V)
F	axial force (chapter V)
F_a	axial force applied to the rubber seal (chapter VII)
F_1	positive peak force of the force-displacement curve of the BEDD (chapter VIII)
F_2	negative peak force of the force-displacement curve of the BEDD (chapter VIII)
$\boldsymbol{F}$	optimization objective function (chapter VIII)
F_A	force of the BEDD at point A (chapter VIII)
F_B	internal force of the BEDD (chapter IX)
F_{B1} and F_{B2}	internal forces of the two BEDD's respectively (chapter IX)
$f(t)$	the first order Fourier equation (chapter VI)
G_m	shear modulus of the model (chapter IV)
G_p	shear modulus of the prototype (chapter IV)

h_0	the lever arm of the reinforcement (chapter IV)
H_r	hardness of the rubber (chapter V)
I_1 and I_2	the first and the second invariant of the unimodular component of the left Cauchy-Green deformation tensor (chapter V)
i	loading step (chapter VII)
k	stiffness of the shear keys (chapter II)
K	stiffness of the structure (chapter III)
k_0	axial spring stiffness (chapter V)
k_1 to k_4	slope of the portions $\overline{OA}$ to $\overline{CD}$ (chapter V)
k_1 and k_2	slopes of the mechanical model of the joint (chapter VIII)
k_s	flexural loading stiffness of the immersion joint (chapter V)
k_s^u	flexural unloading stiffness of the immersion joint (chapter V)
k_{axial}^j	axial stiffness of the immersion joint (chapter V)
k_{axial}^s	axial stiffness of the tunnel element (chapter V)
k_{bend}^j	flexural stiffness of the immersion joint (chapter V)
k_{bend}^s	flexural stiffness of the tunnel element (chapter V)
k_j^s	static shear stiffness of the joint (chapter VI)
k_s^s	shear stiffness of the tunnel element (per unit length) (chapter VI)
k_j^d	dynamic shear stiffness of the joint (chapter VI)
k^{sf}	shear stiffness (chapter VII)
k_i^{sf}	shear stiffness at step i of the test (chapter VII)
k_{rubber}	shear stiffness of the rubber (chapter VII)
k_a	axial stiffness of the rubber (chapter VII)
k_i^{cf}	shear stiffness of the joint with the concrete shear keys (chapter VII)

k_{b1}	slope of the initial loading portion of the force-displacement curve of the BEDD (chapter VII)
k_{BEDD}	elastic stiffness of the BEDD (chapter VIII)
k_f	diagonal flexural stiffness of the joint (chapter IX)
l_m	dimension of the model (chapter IV)
l_p	dimension of the prototype (chapter IV)
l	total length of the BEDD (chapter VIII)
L1 to L5	loading point 1 to 5
La1 to La4	laser transducers 1 to 4 (chapter VI)
L	distance between the two BEDD's (chapter VIII)
L_T	distance between the transducers on the two sides of the element (chapter IX)
M	mass of the structure (chapter III)
M_m	bending moment of the model (chapter IV)
M_p	bending moment of the prototype (chapter IV)
M_j	bending moment of the joint (chapter VIII)
M_{BEDD}	bending moment of the BEDD (chapter VIII)
M_{ru}	bending moment of the rubber (chapter VIII)
M_L	bending moment of the loading branch of the mechanical model of the joint (chapter VIII)
M_{LU}	bending moment of the unloading branch of the mechanical model of the joint (chapter VIII)
M_{max} and M_{min}	applied maximum and minimum bending moments (chapter IX)
M_{BEDD}	bending moment taken by the BEDD (chapter IX)
N1 to N4	shear damage in the negative direction (chapter VII)
N_j	axial force of the joint (chapter VIII)

N_{BEDD}	axial force of the BEDD (chapter VIII)
N_{ru}	axial force of the rubber (chapter VIII)
N_q	yielding force of the BEDD (chapter VIII)
P-1 to P-9	transducers 1 to 9 (chapter IV)
P1 to P4	shear damage in the positive direction (chapter VII)
Q	-difference between the maximum (40kN) and minimum (-40kN) shear force (chapter VI) -shear force applied to the rubber seal (chapter VII)
Q_{max} and Q_{min}	positive and negative amplitude of the dynamic shear displacement (chapter VI)
Q_i	shear force of the joint at step *i* of the test (chapter VII)
r_m	reinforcement ratio in the model (chapter IV)
r_p	reinforcement ratio in the prototype (chapter IV)
r_{axial}	index for the ratio of axial stiffness (chapter V)
r_{bend}	index for the ratio of flexural stiffness (chapter V)
r_s	shear stiffness ratio (chapter VI)
R_b	resistance of a bolt (chapter IV)
R_F	friction force between the shear box and the element (chapter IV)
R_{sk}	resistances of a shear key (chapter IV)
S	area of the hysteretic loop (chapter VIII)
T	natural period (chapter III)
T1 to T10	tenon 1 to tenon 10 (chapter VII)
$\boldsymbol{W}$	strain energy density function (chapter V)
$\ddot{x}_g$	acceleration of the ground motion (chapter III)
$\ddot{x}_s$	acceleration of the structure (chapter III)

$\dot{x}_s$	velocity of the structure (chapter III)
x_s	displacement of the structure (chapter III)

Greek symbols

α	torsion angle (Chapter II)
a_0	the lever arm of the shear force (chapter IV)
γ_m	shear strain of the model (chapter IV)
γ_p	shear strain of the prototype (chapter IV)
δ	compression (chapter V)
δ_A to δ_D	the compression at points A to D
δ_1	positive peak displacement of the force-displacement curve of the BEDD (chapter VIII)
δ_2	negative peak force of the force-displacement curve of the BEDD (chapter VIII)
δ_c	residual displacement of the force-displacement curve of the BEDD (chapter VIII)
δ_y	yielding deformation of the BEDD (chapter VIII)
Δl	axial deformation (chapter II)
Δq	shear deformation (chapter II)
Δw	differential deformation (chapter II)
ε_m	strain of the model (chapter IV)
ε_p	strain of the prototype (chapter IV)

ε	obtained strain of the BEDD (chapter IX)
λ	Poisson ratio (chapter VII)
θ	rotation (chapter II, chapter IX)
θ_r	racking angle (chapter VII)
θ_1	rotation at the turning point of the mechanical behavior of the joint (chapter VIII)
θ_2	maximum rotation of the joint (chapter VIII)
θ_{max} and θ_{min}	applied maximum and minimum rotations of the joint (chapter IX)
σ_m	stress of the model (chapter IV)
σ_p	stress of the prototype (chapter IV)
τ_m	shear stress of the model (chapter IV)
τ_p	shear stress of the prototype (chapter IV)
ω	fitting coefficient of $f(t)$ (chapter VI)

Abbreviations

BEDD	buckling energy-dissipation device
BRB	buckling restrained brace
CSS	compression-shear static loading cases
CSD	compression-shear dynamic loading cases
JSCE	Japan Society of Civil Engineering
HSK1	horizontal shear keys type 1

HSK2	horizontal shear key type 2
HZML	Hong Kong-Zhuhai-Macao Link
MaWD	maximum water depth
MiWD	minimum water depth
N	negative direction
P	positive direction
RC	reinforced concrete
SRB	styrene-butadiene rubber
TMD	Tuned mass damping
TLD	Tuned liquid damping

SUMMARY

With the rapid progress of urbanization, an increasing number of infrastructure works have been constructed by engineers around the world since the past two centuries, among which many tunnels. Due to the advantages compared to other tunnel types, immersed tunnel techniques are widely adopted and nowadays there are more than 200 immersed tunnels worldwide. The immersion joints, which are between the adjacent tunnel elements, are normally regarded as the weakest parts in the tunnel due to their smaller stiffness than that of the elements. Moreover, the immersion joint is the key component in the water proof system. When an immersed tunnel experiences various loadings, i.e. earthquakes, differential settlement, sinking ships or anchorage impact, deformations occur in the joint and excessive deformations could cause possible damage to the joint, resulting in water leakage which jeopardizes the safety of the immersed tunnel. As known, the configuration of an immersion joint is complicated, mainly involving the primary rubber seal, the secondary rubber seal, the shear keys, the steel shell and the pre-stressing cables. Such a complex configuration leads to difficulties to investigate the behavior of the joint. To have a comprehensive understanding of that, an experimental investigation on the joint subjected to combined loadings is reported in the present thesis. In particular, the behavior of the joint subjected to excessive shear deformation is investigated and subsequently, the failure behavior is also included. It is widely recognized that the shear keys have an important contribution to the shear behavior of the joint. However, the failure behavior of the joint with both the shear keys and the rubber seal is largely unknown due to the lack of experimental investigations. Moreover, it is proved that the flexible immersion joint has a contribution in the seismic response reduction but the application of seismic mitigation devices

in the joint has never been considered though such concept has been accepted for buildings for decades. Therefore, the main part of the thesis was divided into two parts, more specifically the mechanical behavior of the joint and the seismic mitigation for immersion joint respectively.

Based on an extensive literature review, an experimental program has been elaborated in order to investigate the mechanical behavior of the joint subjected to axial, bending and shear loadings. A geometric scale of 1:10 was selected for technical reasons, such as manufacturing, testing and measurements. Based on that, two tunnel elements, between which an immersion joint was positioned, were designed as well as the rubber seal and the shear keys. The dimensions of a single element are 3800mm x 1150mm x 1250mm with the walls and slabs having a thickness of 150mm. The cross-sectional dimensions of the rubber seal are 37.5mm x 70mm (flange including) with a total length of 9.67m. Two types of shear keys have been investigated, namely steel shear keys and concrete shear keys and each type of the shear keys was divided into two groups depending on their position in the joint and the loading situation. The steel shear keys were connected to the element by bolts while the concrete shear keys were casted together with the element to increase the shear strength.

For the model specimens, a unique test set-up has been developed allowing that one element is movable while the other one is fixed, resulting in an axial, bending and shear deformations in the joint respectively. Only horizontal loading was applied in this experiment. The axial load and the bending moment were provided by a set of four hydraulic jacks which are controlled independently while the shear force was applied by an additional jack. Further, a testing procedure was elaborated, consisting of three loading protocols, namely axial compression, compression-bending moment and compression-shear loading cases. For the axial loading case, the hydraulic jacks first provided the gradually increasing axial force then the jacks were unloaded. For the compression-bending case the axial force was applied to an specific value to simulate the initial water pressure in the joint and then a bending moment was imposed. The immersion joint was allowed to rotate, resulting in the occurrence of an opening of the joint. For the shear loading cases, an axial force was also applied at the beginning followed by a reciprocating shear force with increasing amplitude. The shear force was increased until all the

shear keys failed. During the experiments, measurements were executed after each successive increase of the load or displacement, comprising axial and shear deformations.

Regarding the axial and flexural performance of the joint, the compression-release curve and the bending moment-rotation curves with different levels of axial forces were obtained. Through the obtained load-deformation curves, both the axial stiffness and the flexural stiffness of the joint were derived for use in practice. During this testing cases, a hysteretic loop was observed in both axial and flexural behavior of the joint, indicating that the rubber seal is not perfectly hyper-elastic material as assumed and energy-dissipation did occur. Moreover, an asymmetric bending behavior was observed as the axial force increased.

The static and dynamic behavior of the joint were investigated by imposing static and dynamic shear loading respectively. The static and dynamic load-displacement curves of the joint with different loading scenarios were obtained. Accordingly, the static and dynamic shear stiffness of the joint were derived as well. A comparison was made between the static and dynamic shear performance of the joint. The failure behavior of the joint with the steel shear keys and concrete shear keys were investigated by applying reciprocating shear loads with increasing amplitude under a constant axial force. The failure mode of the joint with these two types of shear keys as well as the shear capacity of the joint were obtained. Both series of test results show that the shear keys were not activated at the same time, resulting in a difference between the design shear capacity and experimental one. Finally, a significant contribution of the rubber seal in the shear direction was found, indicating that the shear behavior of the rubber seal should be taken into account in the design procedure.

A general literature study with respect to seismic mitigation methods was performed serving as a starting point for the application to immersion joints. To achieve this, a buckling energy-dissipation device (BEDD) on the basis of the Buckling Restrained Brace (BRB) was introduced and a detailed design procedure for the seismic mitigation device in the joint was provided supposing that the device can work in coordination with the joint in such a way that the maximum energy dissipation is reached. In order to validate the design procedure, a large-scale experiment was conducted on an immersion joint subjected to compression-bending moment cases. The bending moment-rotation curves of the joint with seismic mitigation

devices as well as the hysteretic performance of the device itself were obtained through axial transducers and strain gauges on the device. It was experimentally proved that the hysteretic performance of the joint was enhanced by using the seismic mitigation device though the performance of the device itself did not meet the expectation. However, it indicated that such application of the seismic mitigation method has a high potential in energy dissipation in immersion joints.

In the presented PhD thesis, the mechanical behavior of the joint subjected to axial, flexural and shear loadings and the seismic mitigation method for immersion joints have been studied comprehensively in an experimental way. As the first attempt ever on such issue, the results gained from these investigation give clear insights on the behavior of joint under different loading scenarios. The obtained stiffnesses can be used in further numerical analyses. The proposed seismic mitigation method for immersion joints is shown to be feasible not only to enhance the seismic performance of the joint but also to provide an additional way for energy dissipation of immersed tunnels. The material characteristics of the rubber seal are found to play a much more important role than what is expected from conventional design.

SAMENVATTING

Door het snelle verstedelijkingsproces zijn de afgelopen twee eeuwen een toenemend aantal infrastructuurwerken wereldwijd gebouwd door ingenieurs, waaronder vele tunnels. Door de voordelen ten opzichte van andere types van tunnels, worden afgezonken tunnels op ruime schaal toegepast en tegenwoordig zijn er wereldwijd meer dan 200 afgezonken tunnels in gebruik. De zinkvoegen, die zich tussen aangrenzende tunnelelementen bevinden, worden normaal als de zwakste onderdelen van deze tunnels gezien, wegens hun kleinere stijfheid ten opzichte van de tunnelelementen. Bovendien is de zinkvoeg het belangrijkste onderdeel in het verzekeren van de waterdichtheid. Wanneer een afgezonken tunnel onderworpen wordt aan belastingen, zoals aardbevingen, differentiële zettingen, zinkende schepen of ankerimpact, treden vervormingen in de voeg op. Overmatige vervormingen kunnen mogelijk schade aan de voeg veroorzaken. Dit kan op zijn beurt resulteren in waterlekken die de veiligheid van de tunnel in gevaar kunnen brengen. Zoals bekend is de configuratie van een zinkvoeg vrij ingewikkeld. De hoofdcomponenten zijn het primaire rubberprofiel, het secundaire rubberprofiel, de tandverbindingen, de staalplaat en de voorspankabels. Deze complexe configuratie maakt het moeilijk om het gedrag van een zinkvoeg te onderzoeken. Om een goed begrip te bekomen over het mechanisch gedrag van de zinkvoeg wordt in dit proefschrift experimenteel onderzoek verricht naar zinkvoegen onderworpen aan gecombineerde belastingsconfiguraties. In het bijzonder wordt onderzoek verricht naar het gedrag van de voeg onder grote dwarskrachtvervormingen. Vervolgens wordt ook het faalgedrag van de verbinding bestudeerd. Het is algemeen aanvaard dat de tandverbindingen een grote invloed hebben op het afschuifgedrag van de verbinding. Het faalgedrag van een zinkvoeg met zowel

tandverbindingen als rubberprofielen is echter nog grotendeels onbekend door het gebrek aan experimentele resultaten. Bovendien is het bewezen dat een flexibele zinkvoeg een bijdrage levert tot het verminderen van de respons onder seismische acties, maar de toepassing van speciale voorzieningen voor het verminderen van het risico bij aardbevingen ter plaatse van de zinkvoegen werd nog nooit eerder overwogen terwijl dit concept al decennia lang gebruikt wordt in gebouwen. Bijgevolg werd dit proefschrift grotendeels opgesplitst in twee delen: het mechanisch gedrag van de zinkvoeg en de vermindering van het risico bij aardbevingen.

Op basis van een uitgebreide literatuurstudie is een experimenteel programma uitgewerkt om het mechanische gedrag van de voeg onderworpen aan axiale belasting, buigende momenten en afschuiving te onderzoeken. Voor het proefmodel werd een geometrische schaal van 1:10 geselecteerd op basis van technische aspecten zoals vervaardiging, beproeving en uitvoerbaarheid van de metingen. Op basis daarvan werden twee tunnelelementen, met tussenin een zinkvoeg, ontworpen evenals het rubberprofiel en de tandverbindingen. De buitenafmetingen van een element bedragen 3800 mm x 1150 mm x 1250 mm en de wanden en platen hebben een dikte van 150 mm. De afmetingen van de dwarsdoorsnede van het rubberprofiel zijn 37,5 mm x 70 mm (inclusief flens) met een totale lengte van 9,67 m. Er werden twee types tandverbindingen onderzocht , namelijk stalen tandverbindingen en tandverbindingen in gewapend beton. Elk type tandverbinding werd verdeeld in twee groepen naargelang hun positie in de voeg en de belastingssituatie. De stalen tandverbindingen waren verbonden met het element door middel van bouten, terwijl de betonnen tandverbindingen samen met het element werden gebetonneerd om de afschuifsterkte te verhogen.

Voor het belasten van de proefmodellen werd een unieke testopstelling ontwikkeld waarbij het ene element beweegbaar is terwijl het andere element vastgeklemd is. Deze opstelling laat toe om de voeg te onderwerpen aan verschillende types vervormingen namelijk axiale vervormingen, buigvervormingen en afschuiving. Er werden enkel horizontale belastingen uitgevoerd in dit experiment. De axiale belasting en het buigend moment werden uitgeoefend door een set van vier hydraulische vijzels die onafhankelijk werden aangestuurd terwijl de afschuifkracht werd uitgeoefend door een bijkomende vijzel. Verder werd een testprocedure uitgewerkt bestaande uit drie belastingsprotocols, namelijk axiale druk, druk en buiging en druk

en afschuiving. In het geval van de axiale drukbelasting zorgen de hydraulische vijzels eerst voor een geleidelijk toenemende axiale kracht, waarna ontlasting optreedt. In het geval van druk en buiging werd de axiale kracht uitgeoefend tot aan een bepaalde waarde om de initiële waterdruk in de verbinding te simuleren. Vervolgens werd een buigend moment uitgeoefend. waarbij een rotatie van de zinkvoeg optrad, met opening van de voeg tot gevolg. In het geval van afschuiving werd ook eerst een axiale kracht uitgeoefend, gevolgd door een cyclisch variërende afschuifkracht met toenemende amplitude. De afschuifkracht werd verhoogd tot wanneer alle tandverbindingen faalden. Tijdens de experimenten werden metingen van de axiale vervorming en de relatieve afschuiving uitgevoerd na elke toename van de belasting of vervorming.

Voor de evaluatie van het gedrag van de voeg onder axiale druk en buiging werden de druk-ontlastingscurve en de buigend moment-rotatiecurve onder verschillende niveaus van axiale druk bepaald. Op basis van de verkregen belasting-vervormingsdiagrammen werden zowel de axiale stijfheid als de buigstijfheid van de voeg afgeleid met het oog op praktische toepassingen. Tijdens de proeven werd een hysteresislus waargenomen in zowel bij het axiale als het buiggedrag van de voeg. Dit geeft aan dat de rubberen afdichting geen perfect hyper-elastisch materiaal is en dat er energiedissipatie optrad. Bovendien werd een asymmetrisch buiggedrag waargenomen bij een toenemende axiale kracht.

Het statisch en dynamisch gedrag van de verbinding werd onderzocht door respectievelijk een statische en dynamische afschuifbelasting op te leggen. De statische en dynamische belasting-verplaatsing diagrammen van de voeg werden op die manier verkregen voor verschillende belastingssituaties. Daaruit werden ook de statische en dynamische afschuifstijfheid van de verbinding afgeleid en er werd een vergelijking gemaakt tussen het statisch en dynamisch afschuifgedrag van de voeg. Het faalgedrag van de voeg met stalen tandverbindingen en betonnen tandverbindingen werd onderzocht door het uitoefenen van een cyclische afschuifkracht met toenemende amplitude onder een constante axiale kracht. Zo werden het faalgedrag van de voeg voor deze twee types tandverbindingen evenals de afschuifcapaciteit van de voeg verkregen. De beide reeksen proefresultaten laten zien dat de tandverbindingen niet tegelijkertijd geactiveerd worden, hetgeen resulteerde in een verschil tussen de

ontwerpcapaciteit en de experimenteel bekomen waarde. Tenslotte werd een significante bijdrage van het rubberprofiel in de afschuifrichting vastgesteld. Dit geeft aan dat er rekening moet gehouden worden met het afschuifgedrag van de rubberen afdichting in de ontwerpprocedure.

Een algemene literatuurstudie met betrekking tot methodes voor de vermindering van het risico bij aardbevingen werd uitgevoerd als startpunt voor de toepassing in zinkvoegen. Om dit te bereiken, werd een 'knikenergiedissipatietoestel' (BEDD – buckling energy dissipation device) op basis van de 'Buckling Restrained Brace' (BRB) geïntroduceerd. Een gedetailleerde ontwerpprocedure voor dit toestel, dat over de voeg aangebracht wordt, werd uitgewerkt, waarbij ervan uitgegaan wordt dat het toestel samen met de voeg op een zodanige manier werkt dat maximale energiedissipatie bereikt wordt. Om de ontwerpprocedure te valideren werd een grootschalig experiment uitgevoerd op een zinkvoeg onderworpen aan een combinatie van een drukkracht en een buigend moment. De buigmoment-rotatie krommen van de voeg met BEDD's en het hysterisgedrag van het toestel zelf, werden verkregen aan de hand van metingen met verplaatsingsopnemers en rekstrookjes. Experimenteel werd aangetoond dat het hysteresisgedrag van de voeg werd verbeterd door gebruik te maken van het BEDD-toestel, alhoewel de prestaties van het toestel zelf niet aan de verwachting voldeden. Dit wijst erop dat een dergelijke toepassing een groot potentieel in zich heeft voor energiedissipatie in zinkvoegen.

In dit proefschrift werd het mechanische gedrag van een zinkvoeg onderworpen aan axiale, buig- en afschuifbelastingen en een methode voor de vermindering van het risico bij aardbevingen voor zinkvoegen uitgebreid bestudeerd langs experimentele weg. Als eerste poging ooit op dit vlak, leveren de resultaten die uit dit onderzoek zijn verkregen een duidelijk inzicht in het gedrag van de voeg onder verschillende belastingssituaties. De verkregen waarden van de stijfheden kunnen worden gebruikt in verdere numerieke analyses. De voorgestelde methode voor de vermindering van het risico bij aardbevingen voor zinkvoegen blijkt niet alleen uitvoerbaar te zijn om de seismische prestaties van de voeg te verbeteren maar biedt ook een extra mogelijkheid voor energiedissipatie in afgezonken tunnels. Tenslotte merken we op dat de materiaalkarakteristieken van de rubberprofielen een veel belangrijker rol blijken te spelen dan aangenomen in de gebruikelijke ontwerpmethodes.

CHAPTER I

GENERAL INTRODUCTION

Hong Kong-Zhuhai-Macao Bridge Immersed Tunnel, China

(CCCCHZMB)

I. General Introduction

I.1. General aspects

With the rapid process of urbanization, increasing numbers of infrastructure works have turned into engineers' view around the world since the past two centuries. Faced with the crossing of a waterway, i.e. river, channel or estuary, either a bridge above it or a tunnel underneath it needs to be selected. Under some circumstances, a bridge is not an advisable option due to the reasons like air traffic, ship navigation, visual intrusion and a tunnel is required. Before making a decision, one of the most important parameters to be taken into account is the cost of this construction, which is confined basically by the length and by the depth of the tunnel. The most common alternatives of a tunnel construction are listed in ascending order: (1) Conventional tunnel, (2) Bored tunnel, (3) Cut-and-cover tunnel, (4) immersed tunnel and (5) submerged floating tunnel.

Conventional tunnels and bored tunnels are mostly deep buried with at least an overhead cover of a full diameter of the tunnel. The conventional tunneling is mainly adopted in a hard rock situation rather than in soft soil occurring as mostly occurs under waterways. A bored tunnel may be applicable but it requires a longer approach as it has to go deeper. The application of the shallow buried cut-and-cover tunneling is not suitable for a waterway especially a deep and wide one as an enormous cost may occur due to the required cofferdam and because the existing ship navigation has to be interrupted during construction. However, the cut-and-cover tunneling is widely accepted as an approach part connecting the tunnel and the banks. The immersed tunnel is also a shallow buried structure with only 2 or 3-meters gravel or sand backfill cover on top. The submerged floating tunnel requires the least water depth, which is only several meters beneath the water level. However, an interruption or a threat for the navigation ship traffic may also occur. So far, no practical application is known for this new type of tunnel.

Figure I.1 shows a general layout of an immersed tunnel. Normally it consists of a main immersed part with several tunnel elements under the waterway. The cut-and-cover tunnel may

be used as a transition part as the tunnel starts to go up to the banks. In some cases, the bored tunnel is also adopted as replacement depending on the actual situation. Then the tunnel continues to reach the bank or the ground level through the open approach ramp.

The typical construction for an immersed tunnel is that the tunnel elements are firstly fabricated and casted in a dry dock. Then the finished tunnel element is floated in the water and transported to the location by a tow barge. Afterwards, the element is sunk into a trench by using a proper ballast which has been excavated in the bed of the waterway. To connect the new element to the previous one under water, the tunnel elements are pulled together, forming a sealing joint between them. Finally, the trench is backfilled with gravel or sand to form a protection against anchors and sinking vessels.

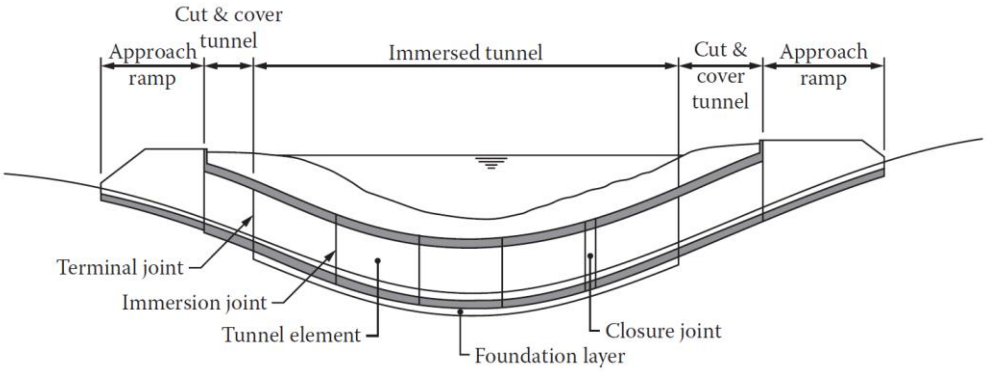

Figure I.1 General layout of an immersed tunnel (Lunniss & Baber, 2013)

Compared to other types of tunnels, immersed tunnels provide a wide range of advantages:

-The immersed tunnel can offer a great flexibility to its cross-section and it remarkably increases the cross-sectional utilization rate;

-The factory-style manufacturing process ensures the quality of the reinforced concrete elements as well as the waterproof system;

-The total length of the tunnel is shortened as it is a shallow-buried underground structure, in such a way that the overall cost for the main tunnel part is, to some extent, reduced. Different lengths of a bridge, an immersed tunnel and a bored tunnel are directly compared as an example

in Figure I.2. It can be seen that the immersed tunnel has the shortest length, followed by the bored tunnel and bridge.

All this results in the fact the immersed tunneling method becomes more and more widely used as it could be the most efficient way to cross a waterway.

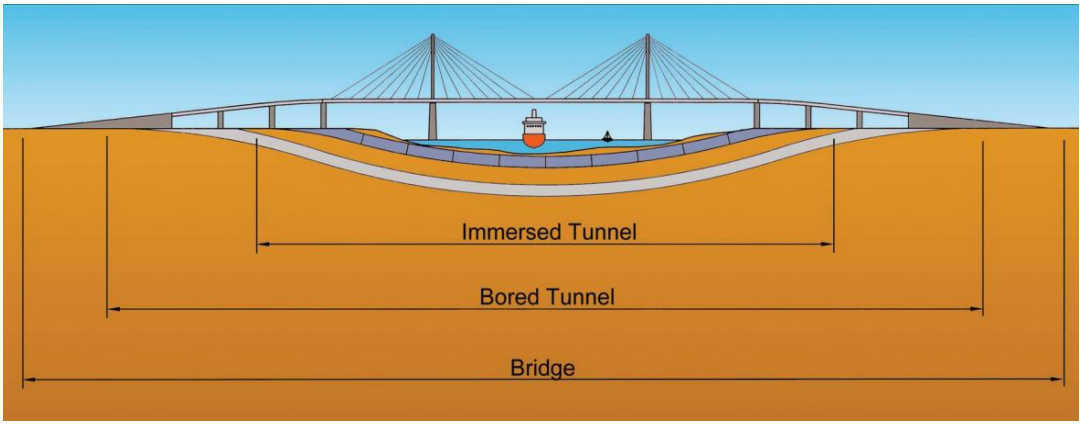

Figure I.2 Length comparison between different water-crossing ways (ITA, 2016)

I.2. History and development of immersed tunnels

The first concept of an immersed tunnel originally dates back to the early 1800's in England (Lunnuss & Baber, 2013). At that moment, Brunel had an idea to build an immersed tunnel across the river Thames in London. In 1803, a British engineer, Henry Tessier de Mottray, proposed to build an iron immersed tunnel between England and France. In 1808, Richard Trevithick proposed a construction method to build a tunnel element in a dewatered cofferdam in the river Thames. Two years later, Charles Wyatt also came up with a detailed design proposal for crossing the river Thames. This proposal adopted 50ft long brick cylindrical immersed elements, considering the water-tightness and the possible impact from the anchors, which is regarded as the first true immersed tunnel concept. Before achieving it, a full scale trial was conducted by John Isaac Hawkins and, unfortunately, the trial was terminated halfway due to its high cost, leading to abandoning this project. Afterwards, in the following decades, a number of concepts or proposals emerged not only in England but also in various western

European countries and the United States. However, none of these plans were implemented and the immersed tunneling construction remained in a theoretical stage due to objective reasons like national security concerns and banking crisis.

Eventually, the first immersed tunnel was built in 1893 as a sewage from Boston to Deer Island station in the United States. Along with the late birth of the immersed tunnel, immersed tunnel construction techniques were soon followed by other European countries. Another great milestone for immersed tunnels occurred again in the United States in 1910 as the first immersed tunnel for transportation, specifically railways, was constructed in the Detroit river. This tunnel consisted of 10 twin steel tube elements with a typical length of 80 meters. Since then, the steel immersed tunnel was developed and soon become a popular tunneling technique for crossing a waterway first in the United States and then in other part of the world until the 1980's.

On the other side of the Atlantic Ocean, another important form of immersed tunnel, i.e. the concrete immersed tunnel, came into play in Europe due to a much higher steel price and less-developed steel industry than in the United States. The Friedrichshagen Tunnel in Germany in 1927 is regarded as the first concrete immersed tunnel. After a decade, a groundbreaking project was made by the Danish contractor Christiani & Nielsen who constructed a rectangular reinforced concrete immersed tunnel in Rotterdam, along with the birth of the GINA rubber, which is the most important part in modern immersed tunnel techniques. Since then, concrete immersed tunnels entered into a rapid developing stage and this technique was adopted for many European roads and railways in the next thirty years. As more concrete immersed tunnels were built, some issues like thermal shrinkage cracking were paid much attention. To solve it, segmental concrete immersed tunnels were introduced by the Dutch along with its first application in Netherlands in the 1960's.

Apart from Europe and the United States, at the same period, such technique spread to Japan and the first immersed tunnel was constructed there. Unlike those regions which have a preference for one type of immersed tunnel, it seems that both steel and concrete tunnels are accepted in Japan. Moreover, another form called composite sandwich immersed tunnel was only used there though it was proposed by a British company. Due to the earthquake-sensitive

location of Japan, the Japanese were innovative and various earthquake-resistant joints in tunnels were developed, i.e. the Bellows joint and the Crown Seal joint (Akimoto, 2002).

It can be concluded that the immersed tunnel was proposed in England, implemented in the United States and developed in The Netherlands and Japan. Recently, a new boost of immersed tunnels was launched in China as there have been 8 new immersed tunnels since 2010. Figure I.3 presents the cumulative number of immersed tunnels by year. After the 1970's, more and more immersed tunnels were built around the world and until now, more than 180 immersed tunnels have been constructed in the past century.

It can be seen from the aforementioned history of the immersed tunnel that there are three major types of immersed tunnels based on their structural form, which are steel shell, concrete, and sandwich immersed tunnel respectively. There are more forms of each type of immersed tunnel which are elaborated as follows.

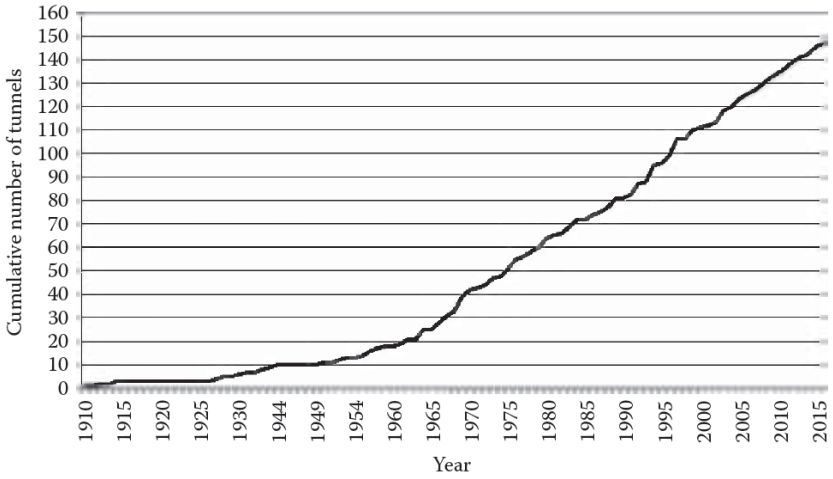

Figure I.3 Cumulative number of immersed tunnels by year (Lunniss & Baber, 2013)

The steel shell immersed tunnel mainly involves the single steel shell and the double steel shell immersed tunnel, in which the circular cross-section was mostly used. In the single steel shell, a steel membrane was used as a waterproof while the reinforced concrete lining was placed in the inner side in a way that they provide resistance against the external force together. Compared to the single steel shell, the double steel shell uses two layers of steel and there is concrete between the steel shells to strengthen the structure. In most cases, the joints between

steel elements were welded up to form a continuous tunnel structure. The corrosion of the steel is the main concern for the designer. With the development of concrete elements, this type of immersed tunnel was gradually out of sight and only a few tunnels adopted this method after the 1980's.

Most of the immersed tunnels constructed recently are rectangular reinforced concrete immersed tunnels. Its great advantages, such as flexibility in cross-section and efficiency of water-tightness, lead themselves to a popularity worldwide. There are two main types referring to monolithic and segmental immersed tunnels but the main structure is made by reinforced concrete. In the early age, the concrete tunnel element was a continuous structure and they were cast as a whole as the element was not too long at that moment. In this way, the thermal shrinkage cracking could not be avoided and it was the greatest threat for the tunnel as the water may penetrate through the cracks. Basically, an external membrane was required to ensure the water tightness. To improve it, the segmental tunnel element was introduced. The length of a tunnel section was limited to 22-25m so that the shrinkage cracks were completely eliminated. Moreover, the absence of an external membrane also lowered the cost. Despite of their element forms, the joint between the concrete elements are mainly flexible or semi-flexible joints, basically consisting of the GINA rubber, the Omega rubber, steel shell, shear keys and pre-stress cables. The concrete immersed tunneling technique now becomes the most common construction method if the immersed tunneling is adopted by the project owners.

Apart from the above immersed tunneling techniques, the steel-concrete-concrete composite structure tunnel element, which is also referred as "Sandwich composite", was developed due to the troublesome concrete work for steel shell tunnels and a shortage of dry docks for concrete tunnel elements in Japan (Kimura et al. 2002). This construction technique has a main structural member for which the concrete is sandwiched integrally in a closed section formed by two thin steel plates. The composite action is achieved through the shear connectors, shear reinforcing steel plates, or other members, which can be seen in Figure I.4. This type of immersed tunnel is suitable for Japan because the destructive energy can be absorbed by the steel plates. However, no practical application is found outside Japan until 2017 it is adopted for a closure joint in the Hong Kong-Zhuhai-Macao Link immersed tunnel.

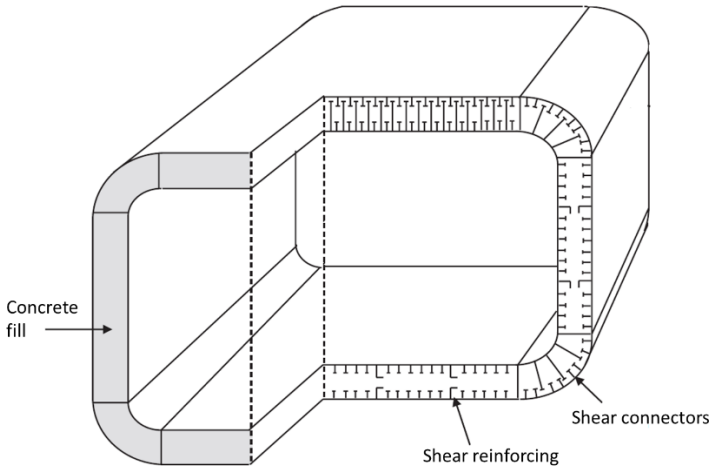

Figure I.4 Sandwich composite immersed tunnel element (Lunniss & Baber, 2013)

From the historical development, the technical trend for immersed tunnels can be concluded as follows:

(1) Longer total length and longer elements are adopted:

For the first immersed tunnel in the United States, the total length of the tunnel was only 782m, including 10 78.2-meter-long tunnel elements. In 1966, the total length reached 2855m in Rotterdam and each element was 90m long. Until 2000, the numbers for total length and the element length are 3510m and 175m for the Oresund Link. The number keeps increasing in the Hong Kong-Zhuhai-Macao Link (5664m) and even it will reach 18000m with 217-meter-long elements in the Fehmarnbelt Link, which is expected to be finished in 2025.

(2) From single function to multifunction (Chen, 2002):

At the early age, the tunnel was applied for only road traffic, railways or utility. As the development of the concrete immersed tunnel, the cross-sectional dimension of the tunnel became much larger and various cross-sectional configurations have been applied as well as different combinations of traffic and utilities occur in the same tunnel.

(3) The reinforced concrete element becomes popular:

As the reinforced concrete immersed tunnel can provide various advantages over the other forms, there is no doubt that it has come to the first option for immersed tunnels. Almost all the

immersed tunnels constructed during the past two decades adopt the reinforced concrete tunnel element. Other promoting factors like foundation treatment, advanced concrete techniques and advanced manufacturing management also contribute a lot.

I.3. Immersion joint

I.3.1. Introduction

There are several types of joints in an immersed tunnel project, which are the immersion joints, the terminal joint and the closure joint. Referring to Figure I.1, the immersion joint is basically the most common as it is the joint between the adjacent elements. The terminal joint is the joint at the end of the tunnel and the closure joint is the joint which is constructed as the last. In some instances, segmental joints are also introduced between the segments in segmental immersed tunnel. No matter which joint it is, the objective of the joint is the same, creating a watertight structure and avoiding leakage.

Initially, under water concrete was used for the immersion joint but such joints are always rigid and cannot allow movement (Ingerslev, 2015). Later on, this type of immersion joint was replaced by the joint with primary rubber seals and most of them have become GINA profiles since 1966. This type of joint provides enough flexibility to accommodate the movement caused by earthquake or differential settlement as it has a smaller stiffness compared to the tunnel element. It was named a ‘flexible’ joint to represent its flexible characteristics against the rigid joint. Figure I.5 demonstrates the immersion process of this immersion joint with the primary rubber seal. When the element is positioned in the trench, it is pulled towards the previous element by hydraulic jack or cables, resulting in an initial compression in the primary rubber seal providing the initial water-tightness. Afterwards the water between the bulkhead of the element is pumped out and a further compression occurs on the rubber due to the out-of-balance hydrostatic pressure. Then the bulkheads are removed and the internal finishing work continues, including the installation of the secondary rubber seal (Omega seal), which is commonly paired with the primary seals.

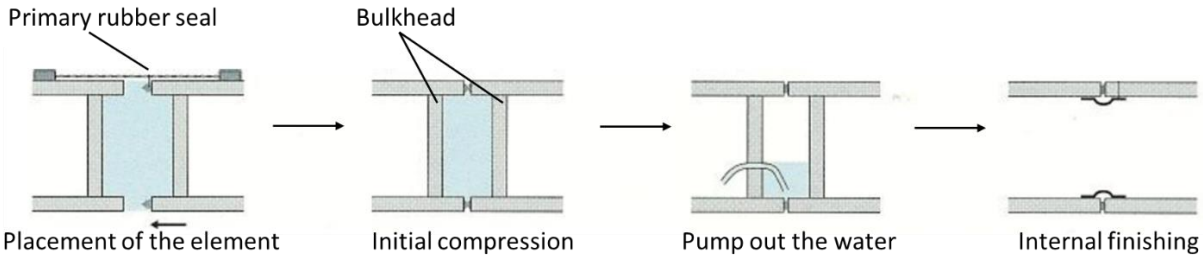

Figure I.5 Immersion process (Van Oorsouw, 2010)

It can be seen that the immersion joints are the most important part in immersed tunnels and the tunnels cannot be constructed nor work without them. As the flexible joint became the most commonly used joint type in immersed tunnels, this type of joint is focused on in this thesis. Generally, a conventional flexible immersion joint mainly consists of the primary rubber seals, secondary rubber seals, steel shell, shear keys and steel cables. The rubber seals and the shear keys are discussed separately in the following section.

I.3.2. Rubber seals

Figure I.6 shows the details of the 'flexible' joint with the rubber seals. As mentioned, the primary rubber seal and the secondary rubber seal are the main waterproof components in the joint, forming a double-waterproof system and they are indispensable for this type of immersion joints.

(1) The primary rubber seal

The primary rubber seal is generally made from natural rubber or styrene-butadiene (SBR) rubber, which is regarded as a hyper-elastic material. There are various forms of the primary rubber seals which have been applied in existing projects. Figure I.7 shows different types of the cross-section of the primary seals. The mechanical characteristics of the rubber seal depend on its cross-sectional shape. For example, there is a hole in type I and II in Figure I.7, resulting a larger compression compared to type III and IV. Type V and VI, created by the Japanese, have a higher capacity for water pressure and shear resistance, which is suitable for joints subjected to large external forces and deformations. The choice of the primary rubber seal depends on the requirements of the project.

Generally, the GINA rubber seal is clamped on the steel shell through the bolts and the steel strips (Figure I.9 (a)), adhering to the external perimeter of the joint which can be seen in Figure I.8. After immersion of the joint, the GINA rubber is always highly compressed and becomes stiff, ensuring the safety of the tunnel from leakage. Hence, the long-term relaxation and creep deformation are the main concerns for the designer. However, the mechanical behavior of the rubber still needs to be paid enough attention as the stiffness of the rubber may affect, for instance, the seismic behavior of the whole immersed tunnel.

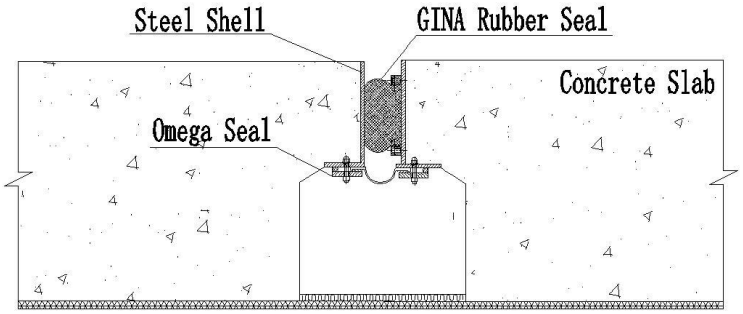

Figure I.6 Details of an immersion joint

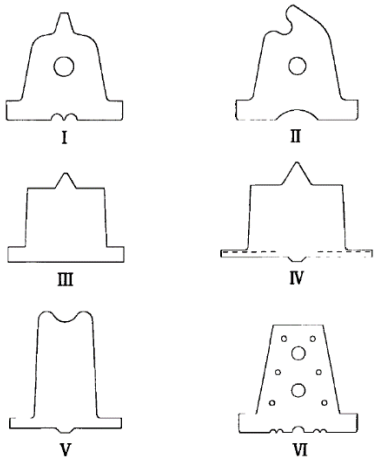

Figure I.7 Common cross-sections of the primary seals (Liu, 2009)

(2) The secondary rubber seal

Once the primary rubber seal fails, the secondary rubber seal start to work as a water proof component. This type of rubber seal is designed to have a capability to accommodate a large

range of joint deformations. The Omega profile is most commonly used as secondary rubber seal. The same clamping way is also applied to the Omega seal, the flange of it is fixed on the steel shell (Figure I.9 (b)), of which the clamping part is the main concern for waterproof. Differing from the GINA rubber seal, there is no initial compression or tension in the Omega seal after its installation. No further discussion is being made in this thesis as it has little contribution on the mechanical behavior of the joint.

Figure I.8 The GINA rubber in an actual project (www.yantu.com)

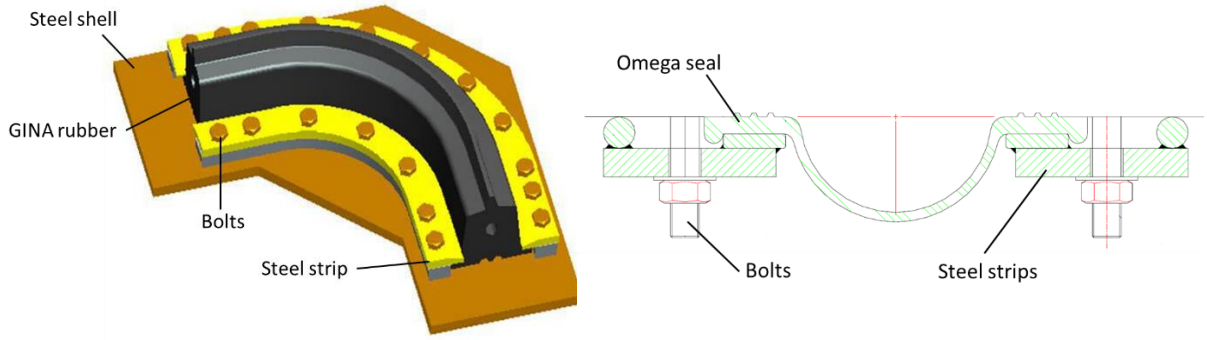

(a) The GINA rubber (b)The Omega rubber (Trelleborg, 2017)

Figure I.9 Details of the GINA rubber and the Omega rubber

I.3.3. Shear keys

Another important component in the joint are the shear keys. The shear keys are a structural component in the joint that provide the resistance against the shear force transferred from one element to another. During the operation of the immersed tunnel, earthquake or differential settlement may occur, resulting in a deformation in the immersion join as it can accommodate a certain level of deformation. If such deformation exceeds the allowed value, damage could occur in the watertight components and may induce leakage, thus jeopardizing the safety of the joint. To prevent putting the tunnel into risk, the shear keys are introduced and they are indispensable to resist transversal and vertical deformations.

Based on the materials, there are two main different types, steel shear keys and concrete shear keys respectively. Both the steel and concrete shear keys can be located both on the walls or the slabs. According to their location, they are categorized as vertical and horizontal shear keys. Figure I.10 displays the horizontal concrete shear keys and vertical steel shear keys in immersion joints. All the shear keys are normally installed after the immersion of the joint but not immediately. This is because, taking the vertical direction as an example, there is a certain amount of settlement occurring soon after immersion, especially when the tunnel is located on a soft soil foundation. This can lower the possible loading acting on the shear keys. The details of both these shear keys are given in the next section.

(a) The horizontal concrete shear keys (CCCCHZMB)

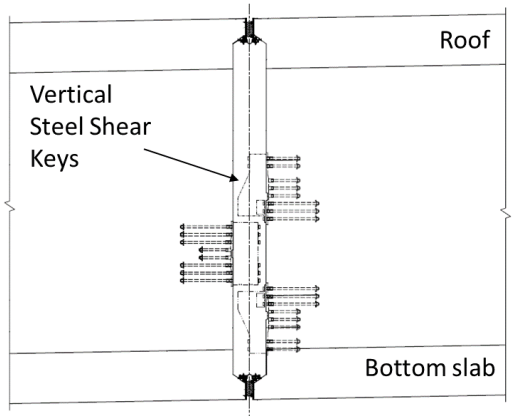

(b) The vertical steel shear keys

Figure I.10 Two types of shear keys in immersion joints

I.4. Project background

I.4.1. Basic information

The thesis is supported by the Chinese National Key Technology R&D Program 'Key Technology of Design and Construction for the Open Sea Ultra-long Immersed Tunnel in the Condition of Soft Subsoil and Weak Sediment', which is based on an actual project: the Hong Kong-Zhuhai-Macao link (HZM link).

The Hong Kong-Zhuhai-Macao link is located on the estuary of the Pearl River Delta, in the southern part of China, linking Hong Kong in the east and Zhuhai & Macao in the west. The main part of this link is a combination of bridges and an tunnel with a total length of 29.6 km, including two artificial islands as a transition part between the bridges and the tunnel. The structural part has been finished already in 2017. This link is expected to be finished at the end of 2017. The completion of this project will reduce the journey time to cross the estuary and provide a strategic link for the development of the Pearl River Delta region as a whole (Hussain et al., 2011). Figure I.11 displays the location of this project.

The bridge and tunnel parts have a dual 3-lane with a design speed of 100km/h as well as a design service life of 120 years. The geotechnical and marine conditions are quite complicated. The maximum water depth of a tunnel element is 44.5m. As the location is at the estuary, the sea bed is covered by thick layers of muck, muck soil, silt clay etc. and the thickness over the bedrock ranges from 50m to 110m (Chen et al., 2015). The highest and lowest water level are +3.51m and -1.52m with an average water level of 0.54m. Also, the changeable weather and frequent typhoons in that region may challenge the construction of the project. Moreover, there is a tectonic fault zone in the bedrock crossing the tunnel alignment (Hu et al., 3015). Although a strong earthquake has never happened in this region, the magnitude of the seismic precautionary intensity is VIII. The navigation requirements as well as the environmental issues are also a key concern for construction. All the mentioned factors added to a great complexity in constructing this project.

Figure I.11 The Hong Kong-Zhuhai-Macao link (Yan et al., 2016)

I.4.2. Tunnel element

Figure I.12 shows the sketch of the immersed tunnel in the HZM link. The total length of the tunnel is 5990m, including a 5664-meter-long immersed tunnel, which consists of 33 segmental tunnel elements. Each typical tunnel element has a length of 180m and it is assembled through 8 segments with 22.5m in length. C45 waterproof concrete and reinforcement covered by a protective layer are applied to avoid leakage through the structure. The cross-sectional form of the tunnel element is two-bore for traffic and one middle gallery for pipelines and escape purpose with a dimension of 37.95m in width and 11.4m in height. The thickness of the wall and the slab is 1.6m. The precast steel-concrete-steel 'sandwich' closure joint locates between Element 29 and 30, and it is installed as a complete structure by using a new construction technique that requires no under water concrete while a semi-flexible joint is adopted between the adjacent elements.

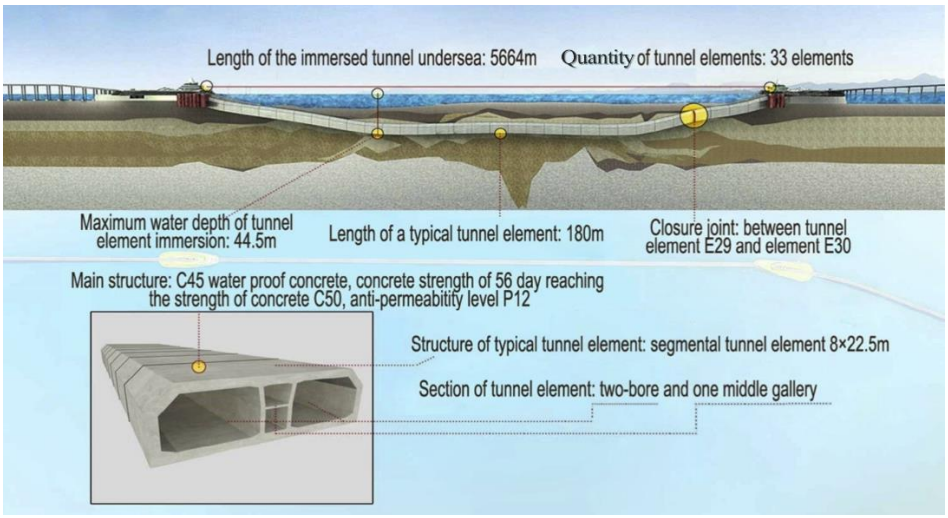

Figure I.12 Sketch of the immersed tunnel in the HZM link (CCCCHZMB)

I.4.3. The semi-flexible immersion joint

A semi-flexible immersion joint is adopted in this project as it consists of the GINA rubber seal, the Omega rubber seal, the steel shell and the shear keys. The cross section of the immersion joint in the HZM link is shown in Figure I.13(a). The GINA-profile rubber seal is used and produced by a Dutch company. It is fixed to the external perimeter of the joint and the clamping way is the same as shown in Figure I.9. There are 4 different GINA rubber seals with different hardness in order to accommodate different compressions caused by the water pressure in joints at different depths. There are 2 groups of horizontal shear keys on the bottom slab and 4 groups of vertical shear keys on the walls. Among them, the horizontal shear keys and the vertical shear keys on the middle walls are made of reinforced concrete while the vertical shear keys on the side walls are steel shear keys. Between the shear keys, the rubber bearing is used as a buffer unit.

Figure I.13 (b) shows the original design of the immersion joint in the HZM link. The difference from the actual joint is that the horizontal steel shear keys were used on the roof and bottom slab instead of the concrete shear keys on the bottom slab. The other parts of the joint are basically the same. The reason that the design was modified is that the installation of the steel

shear keys on slabs is difficult to achieve and casting the concrete shear keys on site is easier for construction.

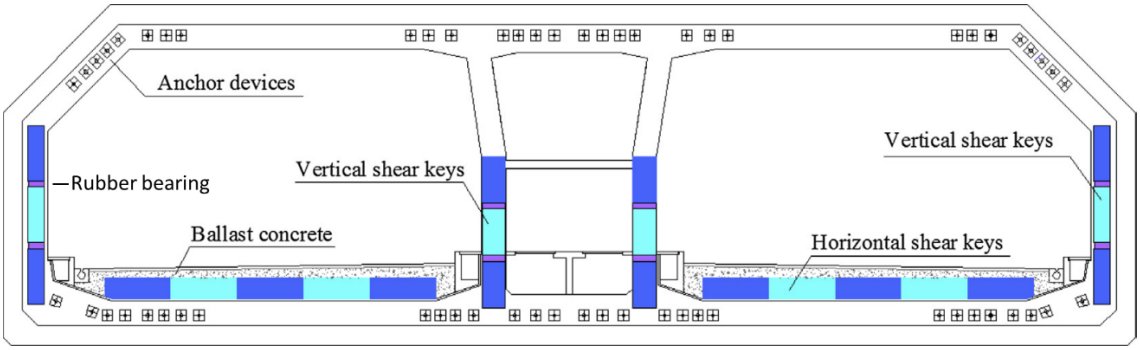

(a) Cross-section of the immersion joint (Hu et al., 2015)

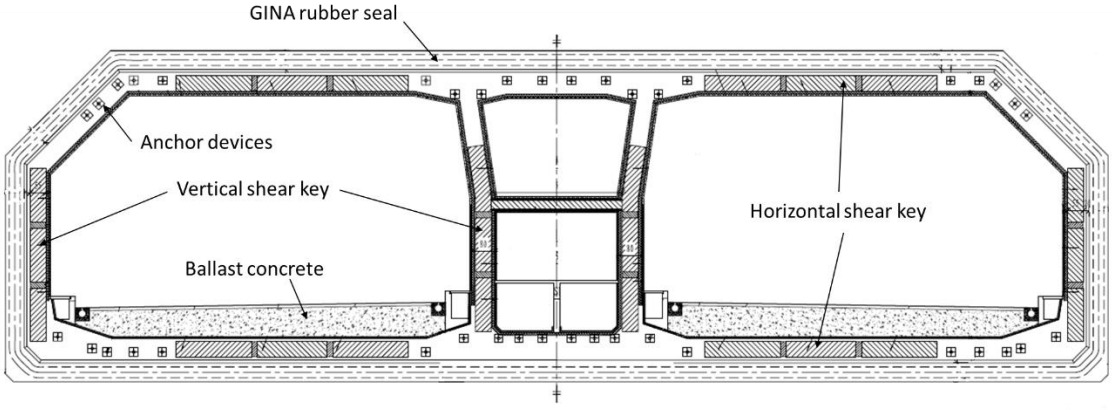

(b) Original design of the immersion joint

Figure I.13 Immersion joint in the HZM link

I.5. Research scope and methodology

I.5.1. Lacunae of current knowledge

It is widely acknowledged that the deformation of tunnels subjected to various types of loading are mainly taken by the immersion joint due to its smaller stiffness compared to the concrete

elements. The joint is also designed as a water proof structure to prevent leakage under any circumstances. However, the water-tightness of the joint will be challenged if the deformation exceeds the allowable value or some components in the joint, e.g. the shear keys, will fail and this may threaten the safety of the immersed tunnel.

Generally, there are two main research topics related to immersed tunnels, the waterproof issue and the durability of the tunnel. Water leakage has to be avoided absolutely as the tunnel is shallow buried under the waterway. The water proof of the joint and the tunnel element, as well as their behavior under seismic excitation, have been investigated profoundly during the past decades. Moreover, it is known that once the joint has been installed, the retrofit or repair of the joint is going to be difficult and sometimes impossible. Hence the durability of the tunnel, in other words the long term waterproof issue of the tunnel, has also become a main concern for designers. However, the mechanical behavior of the immersion joint is essential for both these two issues as the water proof issue could not be investigated without a comprehensive understanding of how the joint behaves under different situations.

Hence, the mechanical behavior of the immersion joint has been profoundly investigated during the past decades but mostly limited to numerical methods as it is the most economical way of studying it. This may rise a problem of selection of the parameters, in the model, like the stiffness which are unreliable by lack of verifications by experiments. The experimental work for immersion joints decreased remarkably since the pioneering work done in 1990’s in Japan although there are numbers of immersed tunnels that have been built since that period. Until now, only an extremely limited number of large-scale tests have been conducted to investigate the mechanical behavior of immersion joints. Particularly, the shear behavior of the joint and the cooperation of the rubber and the shear keys are of crucial importance as well as the axial behavior which has been studied previously by some researchers. As of today, a profound insight into the shear behavior of immersion joints, particularly the shear behavior of the shear keys, the primary rubber seal and their combination, is, to the knowledge of the author, lacking and it requires more attention and profound research.

In addition, the lack of knowledge also applies to the seismic mitigation of the immersion joint though the 1995 Great Hanshin earthquake has initiated a sharp increase in research activities for seismic response of immersed tunnels and immersion joints. As the concept of seismic mitigation is mostly applied to the field of surface structures and bridges, the seismic mitigation research in underground structures, especially in immersed tunnels, is scarce.

I.5.2. Research scope

The scope of this thesis is to perform a comprehensive analysis of the semi-flexible immersion joint, considering both steel shear keys and concrete shear keys, in the framework of the mechanical behavior of the immersion joint subjected to axial, shear and combined forces. The GINA-profile rubber seal is also taken into account.

A new concept of seismic mitigation method for immersion joints is also proposed, which allows the energy dissipation to occur in the joint through external mitigating devices. However, it is limited to the axial direction due to the fact that the joint has more potential in axial direction than the other direction in seismic mitigation.

A comprehensive study is performed by a series of structural experiments and the mechanical behavior, and the seismic mitigation concept of the semi-flexible immersion joint is elaborated as far as possible. However, it has to be recognized that it is impossible to cover all the aspects of the structural behavior of immersion joints within the scope of a single PhD thesis.

I.5.3. Methodology

First, a substantial literature review is given covering the general mechanical behavior of the immersion joint, the separate behavior of the rubber seals and the shear keys as well as the water-tightness of the joint. The seismic analysis for the immersion joint and the seismic mitigation method for underground structures is also explored.

Secondly, the needs for studying the mechanical behavior of the immersion joint subjected to axial, shear and combined loading and the seismic mitigation for the joint are made clear based on the literature review. A unique large-scale experimental program was developed allowing quasi-static loading tests on an modeled immersion joint between two tunnel elements under

the axial, shear, and combined loading. Then the loading and measurement protocol are elaborated based on the design purpose and accordingly a complicated steel loading frames were designed and built, which is followed by the execution of the experiments.

Simultaneously to the experiments for the mechanical behavior of the immersion joint, a seismic mitigation method for immersion joints was proposed by means of a conventional mitigation device. The design procedure of this method was derived according to the model immersion joint. Subsequently, the application of the mitigated devices in the joint was implemented and the test for this was conducted.

In total, all the experiments were conducted successfully in the State Key Laboratory for Disaster Reduction in Civil Engineering, Tongji University, China. This newly built lab provided a safe and rigorous testing environment, ensuring the success of the experiment. Further, the obtained data for both mechanical behavior and seismic mitigation for immersion joints were analyzed and discussed in detail.

I.6. Outline of this thesis

This PhD thesis includes ten chapters, which can be grouped into five main parts shown as below:

(1) A general introduction about the basic information of the immersion joint and project background as well as the content of this PhD research;

(2) **PART A**: A comprehensive introduction with respect to the mechanical behavior and seismic mitigation of the immersion joint are provided respectively;

(3) **PART B**: The experimental program and the results of the mechanical behavior of the joint are described and discussed;

(4) **PART C**: The design procedure and the experimental results related to the seismic mitigation method for the immersion joint are given.

(5) The conclusions and the suggestions for further development are enclosed as the final part;

Figure I.14 displays the structure of this thesis and the basic content of each chapter. After a general introduction on this research topic in the current **Chapter I**, **Part A**: State-of-the-Art on two separate topics is given. The mechanical behavior of the immersion joint, i.e. how the joint behaves under different loadings and what is the failure mode of the joint etc, is explained in **Chapter II**, which is followed by **Chapter III**. A comprehensive seismic mitigation method is illustrated and different types of seismic mitigation devices are distinguished. The current common seismic mitigation method for underground structures is also explored.

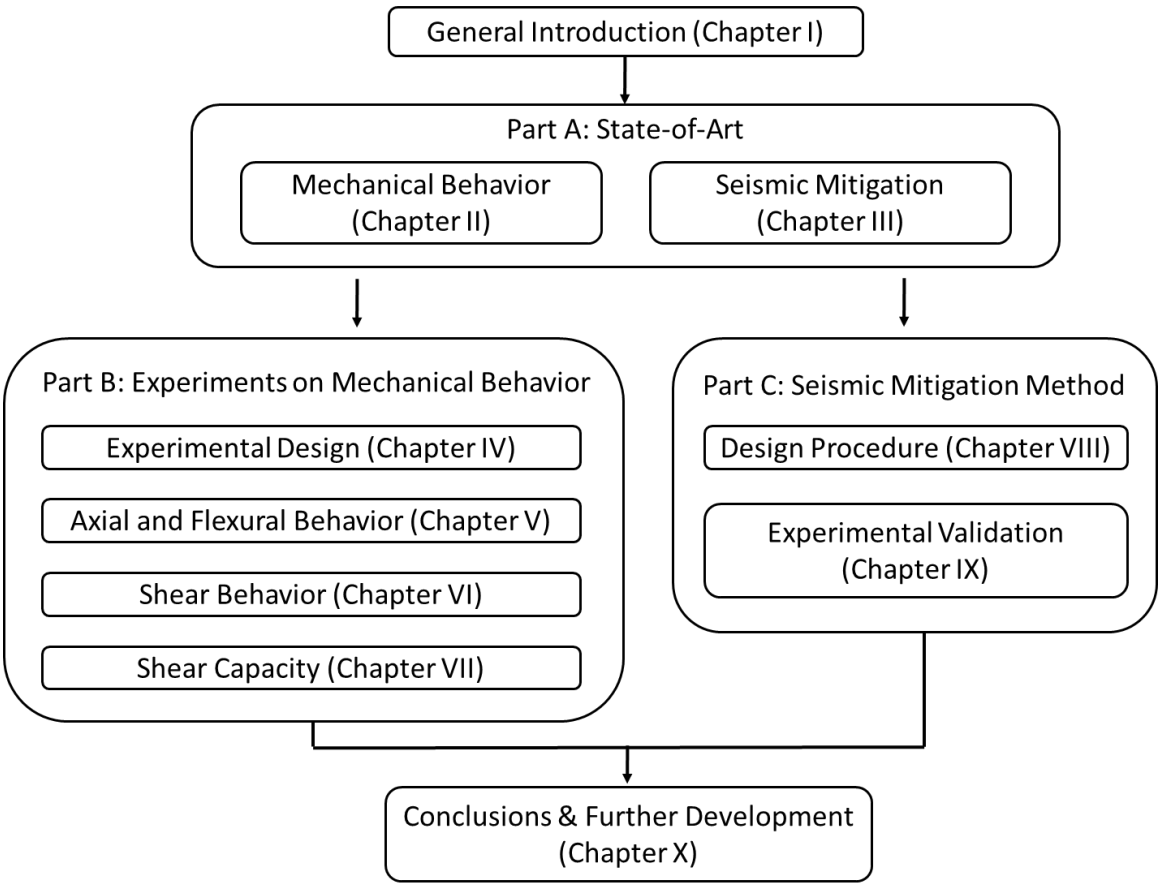

Figure I.14 Outline of this thesis

Four chapters related to the experimental analysis of the mechanical behavior compose Part B, in which the a large-scale experimental investigation is performed. The detailed experimental design including the test set-up and quasi-static loading protocols is provided in **Chapter IV**. The results and corresponding discussions of axial and flexural behavior, shear behavior and

shear capacity of the joint are given in **Chapter V**, **VI** and **VII** respectively. The shear behavior of the joint with both two types of shear keys, reinforced concrete and steel shear keys respectively, is analyzed.

Parallel to **Part B**, a seismic mitigation method for immersion joints is demonstrated in **Part C**, consisting of two chapters. In **Chapter VIII**, the design concept of this method is proposed and the detailed design procedure is given. Based on the model immersion joint, the experimental analysis is performed and validation of the seismic mitigation method is provided in **Chapter IX**.

Finally, a summary of this thesis and general conclusions are given in the last chapter, **Chapter X**, together with some ideas and suggestions for the further development of the presented topic.

I.7. References

Akimoto, K., Hashidate, Y., Kitayama, H., & Kumagai, K., 2002. Immersed tunnels in Japan: recent technological trends. Paper presented at the International Symposium on Underwater Technology, Tokyo, Japan.

CCCCHZMB, 2011. Tunnel Design Solution [Format: Image]. <http://www.cccchzmb.com/P53- 119.biz>.

Chen, S., 2002. Design and Construction of Immersed Tunnels, fifth ed. China Science Publishing & Media Ltd, Beijing. (in Chinese)

Chen, S., Su, Z., Chen, Y., 2015. New Technologies Used for Immersed Tunnel of Hongkong-Zhuhai-Macao Bridge Project. Tunnel Construction. 35, 396-403. (in Chinese)

Ingerslev, C., Quinn, S., Carter, E., 2015. Immersed tunnels – Immersion Joints. Proceedings of the ITA WTC 2015 Congress and 41st General Assembly, Dubrovnik, Croatia.

Hu, Z., Xie, Y., Wang, J., 2015. Challenges and strategies involved in designing and constructing a 6 km immersed tunnel: A case study of the Hong Kong-Zhuhai-Macao Bridge. Tunnelling and Underground Space Technology. 50, 171-177.

Hussain, N., Wong, C., Carter, M., 2011. Hong Kong Zhuhai Macao Link. Proceeding of the Twelfth Asia-Pacific Conference on Structural Engineering and Construction. 14, 1485-1492.

ITA Working Group 11 for Immersed and Floating Tunnels, 2016. An Owners Guide to Immersed Tunnels, ITA report N7.

Kimura, H., Kojima, I., Moritaka, H., 2002. Development of Sandwich-Structure Submerged Tunnel Tube Production Method, Nippon Steel Technical Report No:86 JULY 2002.

Liu, Z. G., 2009. Behavior and safety assessment of immersion joints in immersed tunnels. Master thesis, Tongji University, Shanghai. (in Chinese)

Lunniss R., Baber, J., 2013. Immersed Tunnels, first ed. CRC Press, Boca Raton.

Trelleborg Ridderkerk BV, 2017. Product brochure: Omega seals [PDF]. <http://www.trelleborg.com/en/engineered-products/products--and--solutions/tunnel--seals>.

Van Oorsouw, R. S. 2010. Behavior of segment joints in immersed tunnels under seismic loading. Master thesis, Delft University of Technology, Delft.

Yan, X., Yuan, J., Yu, H. et al., 2016. Multi-point shaking table test design for long tunnels under non-uniform seismic loading. Tunnelling and Underground Space Technology. 59, 114-126.

CHAPTER II

MECHANICAL BEHAVIOR OF IMMERSION JOINTS

Detroit River immersed tunnel, USA

(Baber, 2013)

II. Mechanical Behavior of Immersion Joints

II.1. General introduction

From the previous chapter, it is known that there are various types of immersion joints and that they are the weakest unit in immersed tunnels as the stiffness of the joint is relative small resulting in the occurrence of deformations. Whatever the type of immersion joint is, the design of it has to consider various actions during its service life, i.e. water pressure, earthquake, settlement of foundation, shock from shipwrecks etc. Meanwhile, an immersion joint should include a water-proof part as an indispensable system. Therefore, knowledge of the deformation of a joint under various loading conditions is important for a safe, reliable, and water-proof design.

As a basic of requirement, the design of any immersed tunnel aims to ensure that the water proof of the immersion joint can be guaranteed. Therefore, design criteria in the serviceability conditions are based on a design value for the deformation, which should be smaller than the allowance to avoid leakage. As such, the design of the immersion joint is usually deformation-based and the behavior of the immersion joint can be reflected by its stiffness in different directions. One of the focuses of the mechanical behavior of the immersion joint should be investigations on its stiffness and how it deforms under various loading situations in order to prevent excessive deformation.

Additionally, the ultimate state, referring to the loading resistance of the joint, surely should be taken into account in design. In this regard, the behavior of the shear keys, as mentioned in the previous chapter, is essential in analyses of this issue. The shear capacity and the failure mode of the shear keys determine the shear resistance of the joint in transversal direction.

In this chapter, Section II.1 is dedicated to the detailed behavior of the immersion joint subjected to different loadings. For this purpose, three different types of the deformation mode are distinguished, forming a general base of this thesis. The possible failure and the water tightness of the joint, in relation to the deformation, is elaborated and explained.

Section II.2 presents the current researches related to the mechanical behavior of immersion joints. This section starts with the early research activities about immersion joints, followed by detailed research aspects, including global behavior of the joint, the shear behavior, the water tightness and the rubber seal and the seismic issue. Finally, a summary of this literature study is provided in Section II.3.

II.2. Overview of the behavior of an immersion joint

II.2.1. Deformation mode

It is known that an immersed tunnel is shallow-buried and surrounded by soft soil in most cases. Due to various loadings, such as differential settlement, earthquake, possible sunk ship, temperature variations etc., deformations of the tunnel may occur. In this situation, most of the imposed deformations are focused on the immersion joint as its stiffness is normally smaller than that of the tunnel element. Based on the directions of the deformation, the deformation mode can basically be categorized into five basic types, namely axial deformation, bending deformation, shear deformation, torsion and racking, which will be discussed in detail.

(1) Axial deformation

Generally, the axial deformation Δl (Figure II.1 (a)) leads to either extension or compression in the joint. It should be noted that, due to the unique construction of immersed tunnels, the immersion joint remains under compression to form a water sealing. Therefore, extension in the joint causes relaxation in the rubber, increasing the risk of leakage. Normally, the axial deformation is induced by earthquakes or temperature variations along the tunnel axis. It should be noted that an initial compression exists in the joint due to water pressure.

(2) Bending deformation

If non-symmetrical axial deformation occurs in the joint, which means that the deformations at two sides of the joint are different, a rotation θ (Figure II.1 (b)) is observed along with a bending moment resisted basically by the rubber. Similar to the extension, excessive rotation causes

extension at one side, resulting in an increasing possibility of leakage. Based on the bending direction, there are horizontal and vertical bending deformations, induced mainly by earthquakes and differential settlements respectively.

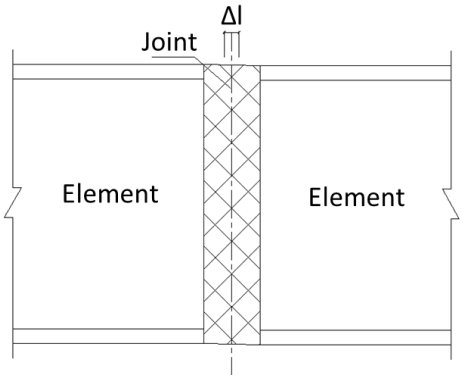

(a) Axial deformation

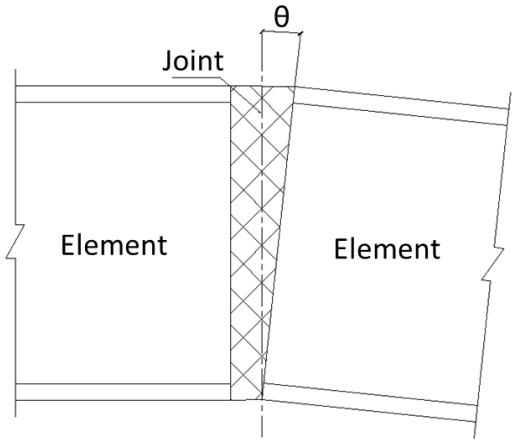

(b) Bending deformation

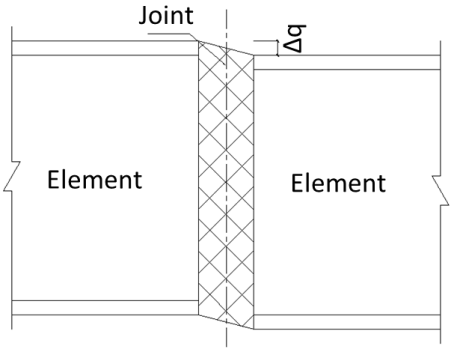

(c) Shear deformation

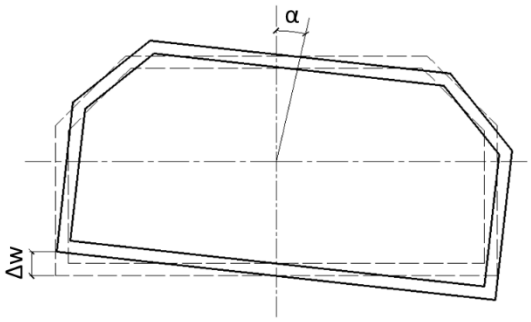

(d) Torsion

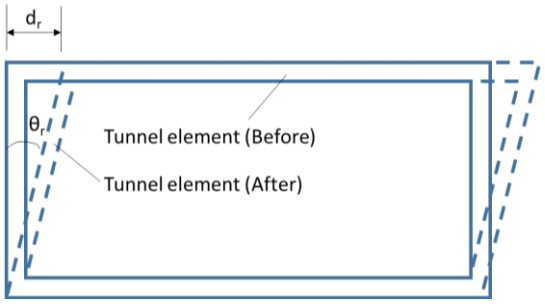

(e) Racking

Figure II.1 Basic deformation modes of an immersion joint

(c) Shear deformation (Figure II.1 (c))

Shear deformations normally arise together with the longitudinal bending due to the fact the pure shear situation rarely exists in reality. In design, small shear deformations are allowed to accommodate the surrounding movement as long as it does not exceed the shear allowance. Otherwise the same consequence, leakage, occurs, jeopardizing the safety of the tunnel. Similar to the bending deformation, the shear deformation can occur horizontally and vertically. Depending on the directions, the shear deformation normally is resisted by the installed steel or RC shear keys with a high shear capacity.

(d) Torsion

Torsion here represents the rotation in a vertical plane, resulting a rotation angle α and a differential deformation Δw between two sides as shown in Figure II.1 (d). Such torsion normally is caused by differential settlements and as a result, shear deformations arise, which are basically the same as the already mentioned shear deformations.

(e) Racking

Racking in immersed tunnels is not a common deformation mode and it is mostly induced by a non-uniform distribution of the internal forces in the tunnel. Normally, a racking behavior results in a relative deformation d_r and a racking angle θ_r as shown in Figure II.1 (e).

II.2.2. Failure modes

As known the stiffness of the joint is relatively smaller than that of the tunnel element, and hence, deformations induced by various loadings are mainly taken by the joint. As a consequence, the joint has more potential in damage than the tunnel element itself. As aforementioned, there are two main concerns regarding the serviceability and ultimate design state, which are the water proof capacity during construction and service life and the resistance against any external loading respectively. In accordance with these two concerns, there are two main possible failure modes in the joint, namely structural failure and water leakage respectively.

(1) Structural failure

The durability issue, such as the corrosion of the reinforcing steel and the deterioration of the rubber, and the resistance issue, such as stress concentrations, complex loading conditions or excessive loadings, have been paid much attention in the previous research and practical applications. The durability of the joint can be improved by applying more advanced materials and manufacturing techniques of the concrete, steel and rubber. The resistance-based failure is due to excessive loadings of the joint. However, during service life of an immersed tunnel, the loading normally comes from the movement of the tunnel element rather than being applied on the joint directly. Hence, the structural components, such as the shear keys, are always the focus of research.

(2) Water leakage

The water tightness of a joint is always the point of focus. Compared to the shield tunnel, there are less joints in immersed tunnels, lowering the chance of water leakage. As aforementioned, the primary rubber seal and the secondary rubber seal, which normally refer to the GINA rubber and Omega rubber respectively, are installed to constitute the water proof system of an immersion joint. If the primary seal fails, the secondary seal is activated to avoid the immediate leakage inside the tunnel. However, if the primary seal is damaged, which cannot be repaired with current techniques, the sustaining ingoing water penetrates the secondary seal and enters the tunnel. Although, so far, no severe water leakage has been reported in the current immersed tunnels, the behavior of the primary rubber seal was investigated by numerous researchers.

II.3. Previous research on the behavior of an immersion joint

II.3.1. Early research activities

The first recorded research attempt to rationalize the behavior of an immersed tunnel was performed by Hawkins in 1811 (Lunniss and Baber, 2013) who constructed two round 76m

long brick cylinders with an internal diameter of around 2.7m using the actual construction method and placing the specimen in the River Thames. Figure II.2 shows the schematic of the brick cylinders in this experiment. The joint between the cylinders was sealed by puddled clay and some leakage was found, which surely required more engineering efforts for the improvement of the water proof ability. Unfortunately, the experiments were terminated due to the high cost and abandoned finally. Therefore, no more information was obtained regarding the results of the test.

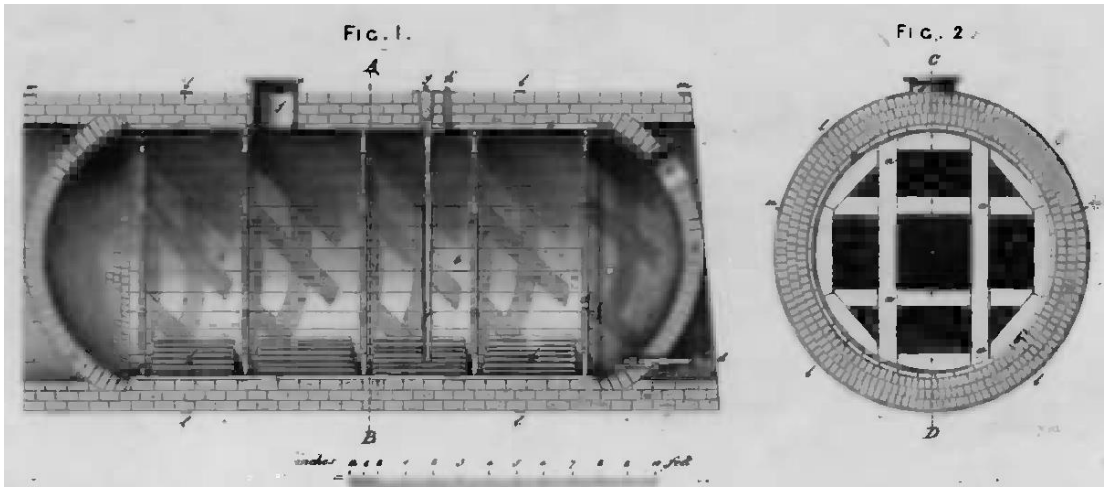

Figure II.2 Schematic of the first experiment on immersed tunnels (Lunniss and Baber, 2013)

In the following 150 years, though there were increasing numbers of immersed tunnels being constructed, the research activities seemed to be a bit legging behind. Before 1970, literature related to the behavior of immersed tunnels is hardly found and some papers were published but only reporting the design of the immersed tunneling projects. After 1970, research activities started to boom due to one of the possible reasons that the GINA rubber and the modern immersion techniques were invented by a Dutch engineer.

In the 1970's, the Port and Harbour Research Institute (Japan) published a series of reports related to research on the 'immersed tunnel'. For instance, Aoki et al. (1972) conducted an out-door dynamic model test to verify the earthquake resistive design method, involving two circular tunnel models in an artificial sand embankment. The earthquake resistant calculation was presented and verified by a dynamic model test with a geometric scale of 1/250 by Nakano

et al. (1973a). A computational analysis was performed but a large difference was found with the experimental results. The interaction between the tunnel and the soil was also examined (1973b) in consideration of various faults and settlements. Kiyomiya et al. (1975) obtained the dynamic responses of the Kinuura Submerged Tunnel under four actual earthquakes by installing several instruments. During the same period, Goto et al. (1975) also conducted an experiment to investigate the seismic response of submerged tunnels. Similar work as Kiyomiya (1975), Nasu et al. (1977) investigated the dynamic motion of the Ohgishima Tunnel by placing instruments. However, due to the seismic-sensitive location of Japan, the above researches mainly focused only on the global seismic behavior of the tunnel and the behavior of the joint was barely mentioned.

On the other side of the planet, Glerum et al. (1976) elaborated the design and the construction of some existing immersed tunnels in The Netherlands and detailed examples were given. Also, the experiments to investigate the hydrodynamic behavior of the tunnel during transportation and immersion as well as that of the tension piles was introduced.

During the 1980's, research attention regarding immersed tunnels was not only paid to seismic issues but also to other topics. Kuesel (1986) and Glerum et al. (1988) compared the immersed tunnels with the other forms of tunnels respectively and suggestions for the most appropriate application were given by both of them. The structural behavior of tunnel elements was studied by Van Tongeren and Tonnisen (1988), mainly focusing on two aspects: the ductility of concrete and the shear capacity of the tunnel structure. The calculation models for these two issues were presented and verified by their own experiments. In 1989, the seismic effect of the flexible immersion joint, involving the rubber seal and high strength tendons, was investigated by experimental and analytical methods by Ikeda et al. (1989) and it was the first published paper found by the author where the behavior of the joint was truly discussed. The experimental and analytical results show that the flexible joint can reduce by 30%-70% of the internal force of the tunnel during the earthquake. Figure II.3 shows the details of the dimensions of the used test specimen.

When it comes to the 1990's, with the development of computers and experimental techniques, the mainstream of the research on the behavior of immersion joints became diverse and it can

be categorized in several parts, namely mechanical models, shear behavior, water tightness and rubber joints, and seismic issues.

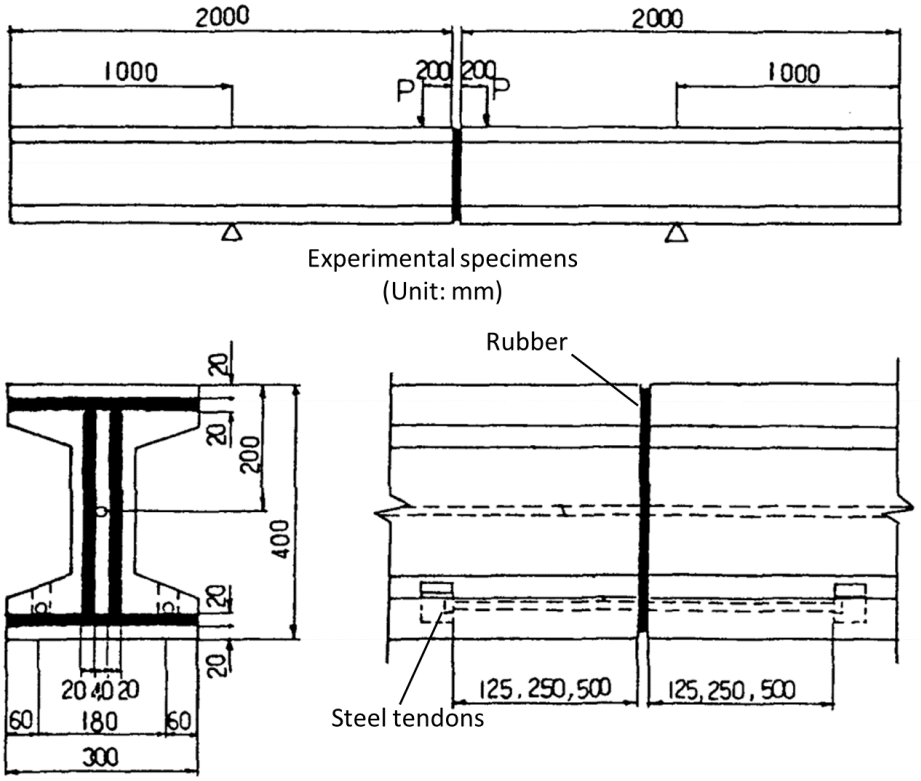

Figure II.3 Dimensions of the specimens with flexible joints (Ikeda et al., 1989)

II.3.2. Global mechanical models for immersion joints

The research related to the mechanical behavior of immersion joints started with the study of the global behavior. The first attempt was performed by Kiyomiya et al. (1992). A ¼ flexible immersion joint model with a rubber gasket and the cables was constructed and the axial and bending behavior of the joint were studied experimentally. Figure II.4 gives a view of the experiment. Different levels of initial compression were considered and a cyclic loading was applied. The experimental results show that the joint behaves unsymmetrically (Figure II.5) due to the non-linear behavior of the rubber gasket. The higher initial compression leads to a higher flexural stiffness. The internal force can be reduced remarkably by using a flexible immersion

joint rather than the rigid one. A non-linear behavior of the joint was found by this experiment. However, only the flexural behavior was focused on and neither the influence of the shear keys nor the shear behavior were mentioned.

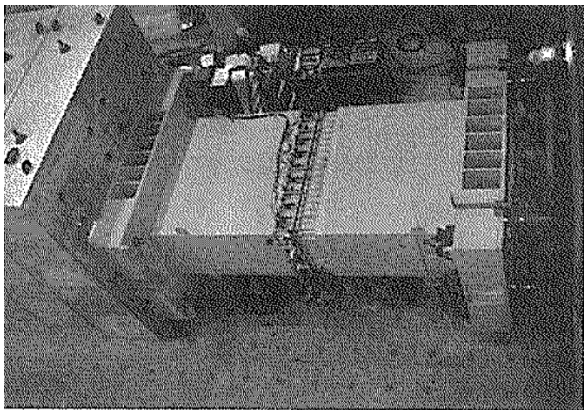

Figure II.4 Full view of the experiment (Kiyomiya et al., 1992)

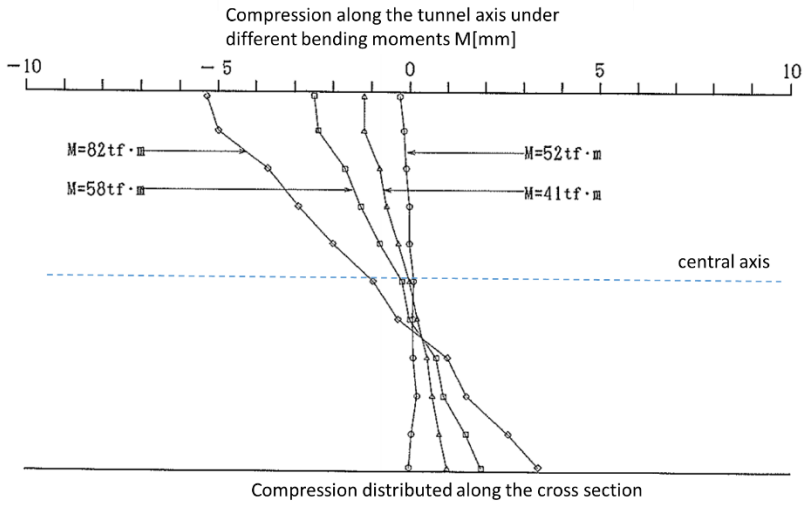

Figure II.5 Compression along the cross section of the joint under different bending moments (Kiyomiya et al, 1992)

Differing from the conventional immersion joint presented in Chapter I, a new type of the immersion joint, called Steel Spring Joint, was developed and examined by Hamazaki et al., (1999), with the axial static, axial cyclic and eccentric axial loading tests. The steel springs (Figure II.6) were installed in the joint, providing the tensile resistance against the joint opening.

A series of experiments confirmed that the steel spring joint behaves within elastic range and responds stably for cyclic loading and eccentric loading, proving the feasibility of such joint.

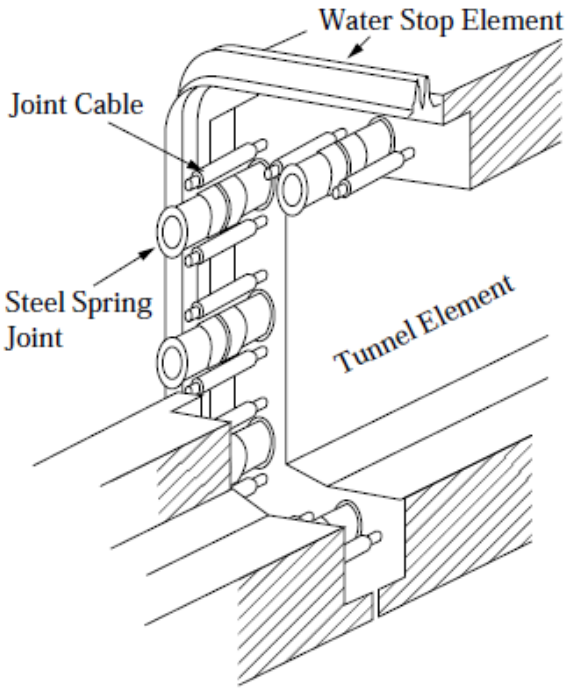

Figure II.6 Detail of the Steel Spring Joint (Hamazaki et al., 1999)

In order to quantify the behavior of the immersion joint, Xie et al. (2008) developed a mechanical model for circular immersion joints based on the static equilibrium equations. The axial, flexural and shear models were derived based on the basic mechanics. However, it was assumed that the joint behaves linearly in the axial direction which is over simplified and not in accordance with the actual situation. To improve it, Yu et al. (2012) used a bi-linear model to simulate the axial behavior of the joint and developed an analytical model to calculate the flexural behavior of the joint. Such a model was verified by a three-dimensional refined finite element analysis of the joint (Figure II.7). The joint was simulated by two 98-node frame, between which are non-linear springs. Also, a parametric study, considering the axial stiffness, positions of the rubber seal and the eccentricity of the imposed loadings, was performed by using the proposed analytical model. The obtained results show that the stiffness of the joint is sensitive to the stiffness of the rubber and the eccentricity of the loading.

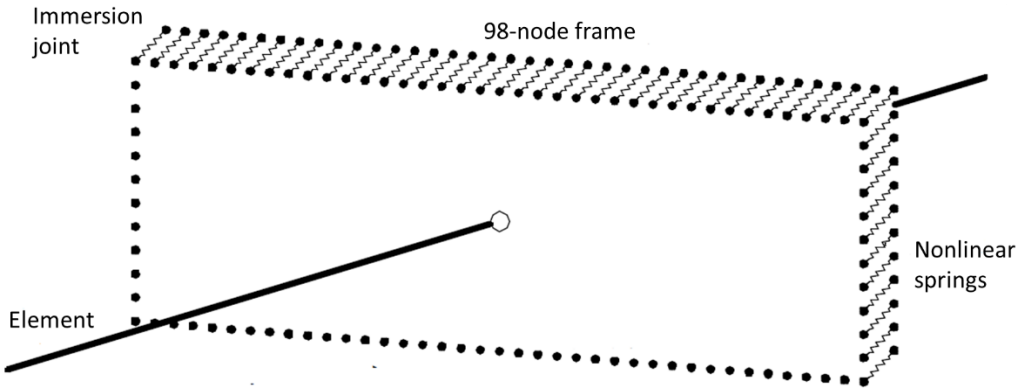

Figure II.7 Three-dimensional refined model of joint (Yu et al., 2012)

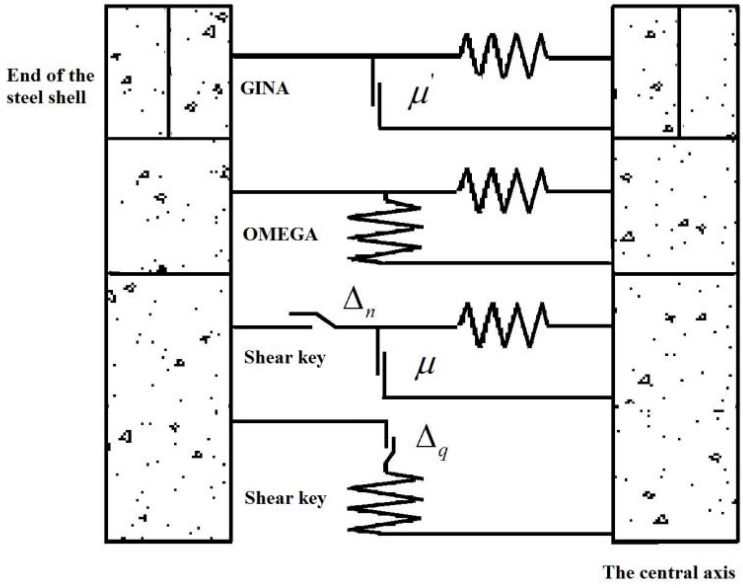

Figure II.8 Mechanical model of a joint with shear key (Ding and Liu, 2014)

A much more complicated model, called three-dimensional nonlinear stiffness mechanical model, for the immersion joint was proposed by Ding and Liu (2014), which is displayed in Figure II.8. The GINA rubber, Omega rubber and the shear keys were taken into account according to the structural characteristics and static equilibrium of the joints. Moreover, the contact analysis between the shear keys and different values of the initial compression of the joint were considered in detail. A case study based on an actual project was performed by using

this model as well as a parametric study, showing that a higher initial compression results in a higher resistance against the joint opening.

It can be found that the global mechanical behavior of the immersion joint was not comprehensively investigated by the aforementioned researches. Although recently several models have been proposed, the model itself relies on the input parameters. There is no experimental support for those models. Moreover, the failure of the joint was never taken into account.

II.3.3. Shear keys in immersion joints

In actual design, shear keys are always installed as main shear resistant part of an immersion joint. It is believed that the shear capacity of the shear keys determines the shear capacity of the joint. Based on the materials and the loading directions, there are several types of shear keys. However, all types of shear keys are used to provide strong capacity that no excessive shear deformation is allowed and as a result no leakage occurs.

There are no uniform configurations of the shear keys. They can be a concrete-steel composite structure, steel structure or reinforced concrete structure, which are used in various types of infrastructures. For example, Araujo et al. (2005) and Bozorgzadeh et al. (2006) conducted experiments on reinforced concrete and composite shear keys respectively. The detailed experimental results and the calculation model of these two types of shear keys were given.

In some researches, due to the fact that the shear keys normally have a relatively high strength and stiffness, it is assumed that the stiffness of the shear keys tends to be infinite in numerical analysis as a simplification. For example, Figure II.9 shows the force-displacement model of the shear keys proposed by Anastasopoulos et al. (2007) in seismic analysis for an immersed tunnel. The stiffness k of the shear keys is assumed to be infinitely high when the shear deformation exceeds the allowance. Surely, the failure or the plastic behavior of the shear keys was never taken into account in this model. Hence, such shear model was often adopted in seismic analysis and the shear behavior was not considered in those researches. A similar assumption of the shear key was also adopted by Lyngs (2008) in numerical analyses.

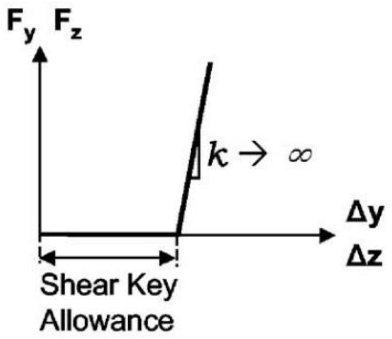

Figure II.9 Model of shear key (Anastasopoulos et al., 2007)

There are two main types of shear keys in an immersion joint, namely reinforced concrete and steel shear keys. Li (2000) carried out experiments on reinforced shear keys based on two different design methods from the relevant Chinese code. In total four shear keys were tested and the shear capacity of the keys was measured. Experimental results show that the obtained capacity was in accordance with the design value when the shear key was assumed as the end part of a simply support beam with non-uniform cross section. Suggestion for adding extra reinforcements were given and shown in Figure II.10.

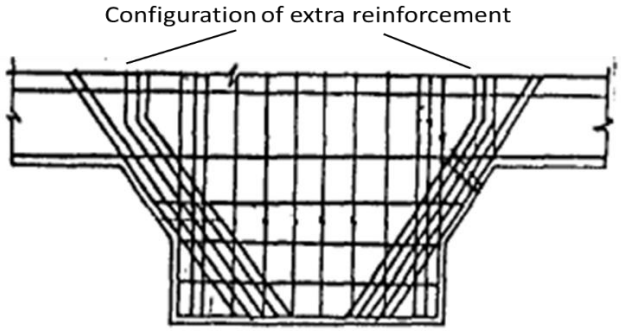

Figure II.10 Suggestion for reinforcement configuration (Li, 2000)

Full-scale experiments on two steel shear keys were conducted by Jiang (2001), mainly focusing on the strength of the shear keys. It was assumed that the embedded plate connecting the shear key and the concrete was subjected to combined loading, namely bending and shear loading. The vertical displacement-loading curve was obtained as shown in Figure II.11. The experimental results show that the obtained shear resistance was higher than the design value and the failure occurred in the welding line on the embedded plate. Some suggestions for design

to avoid jumping (See Figure II.11), such as increasing the thickness of the embedded plate or increasing the strength of the concrete, were given as well.

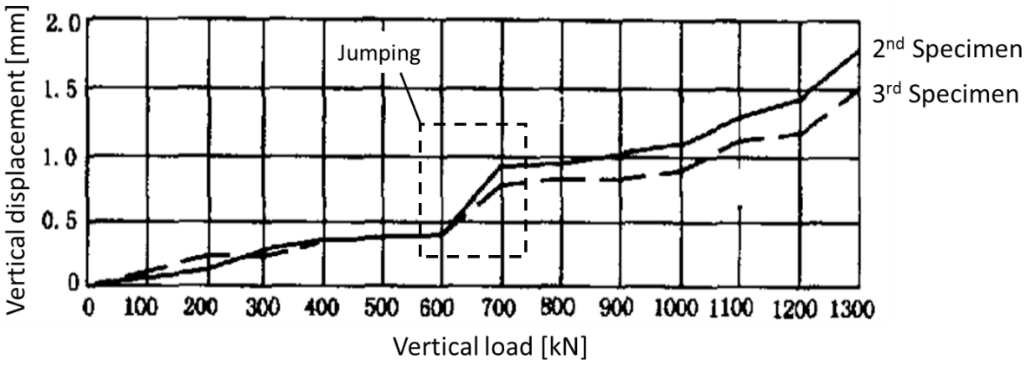

Figure II.11 Vertical movement vs load curve at the root of a shear key (Jiang, 2001)

In a modern immersed tunnel, shear keys are not only installed in immersion joints but also in segmental joints. Although there are some differences between these two types of shear keys, the mechanical behavior of them is quite similar. Both experimental and numerical studies on the behavior of shear keys in segmental joints have been performed by Hu (2013) in consideration of the differential settlement. In the experiment, three segments with two joints were constructed with a geometric scale of 1:4.69. The schematic of the experiment is shown in Figure II.12. The tunnel segments were buried inside sand to simulate the actual service condition and 138 hydraulic jacks were placed beneath the tunnel segment to provide vertical settlements. The bending, shear and torsion loading cases were considered as well as the ultimate loading condition. Based on the experimental results, the mechanical behavior of the shear keys under different loadings was obtained as well as the failure mode. The failure of the shear keys was caused by the compression and shear loadings. The numerical model was verified by the experimental results. Different shapes of the shear keys were compared and a modification for the current shear key design was suggested. However, there is only one tenon in each shear key of the segmental joints, which means that it is easier to obtain the behavior of it. Also, the primary rubber seal may be involved in the shear behavior of the immersion joint while in this experiment the full shear loading was taken by the shear keys.

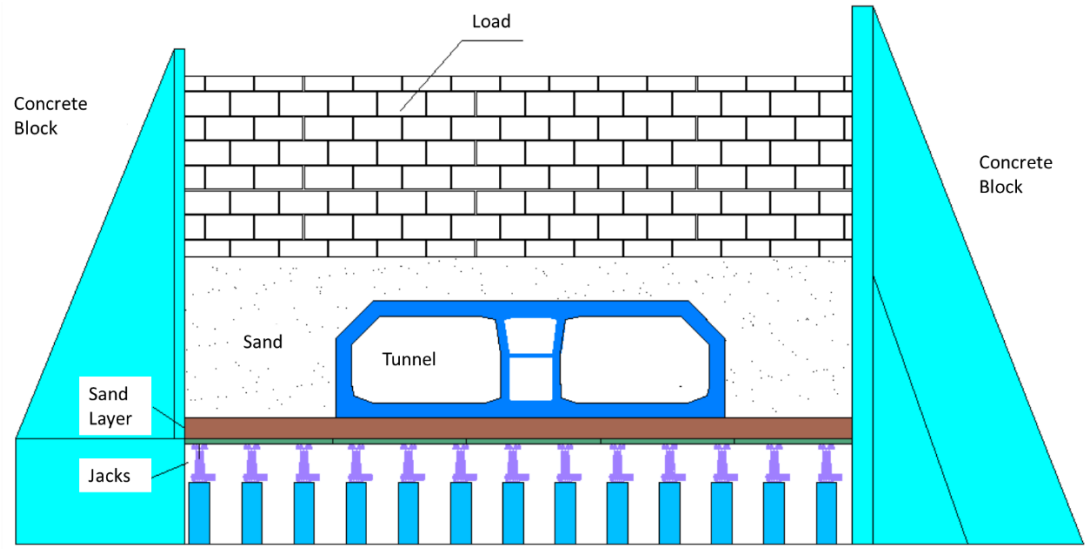

Figure II.12 Schematic of the experiment on segmental joints (Hu, 2015)

It can be concluded that the shear behavior of the immersion joint lacks of sufficient attention due to the fact that the shear keys normally have enough capacity and a relatively high stiffness. As a result, a simple linear or bi-linear model was always used to simulate the behavior of the shear keys in immersion joints and the failure of the keys and the contribution of the rubber was never considered.

II.3.4. The primary rubber seal and water tightness

The water tightness of the immersion joint is one of the most important concerns in design. Before, the water tightness of the tunnel elements was also a great concern. However, due to the rapid development of the crack-control techniques for casting the elements, the water tightness of the joint became the only issue regarding the water leakage. In immersion joints, the primary seal is dedicated to water proof as the seal is highly compressed after immersion. Therefore, the rubber seal and the water tightness cannot be separated in the research.

Regarding this issue, Guan at al. (1994) proposed the basic design procedure of the rubber seal subjected to water pressure, considering the temperature, construction error, earthquakes, rubber restraint component etc. Based on the first immersed tunnel project in China, a case study was given to verify the proposed design procedure.

Later on, Kiyomiya and Yajima (1997) performed a comprehensive study on the properties of the rubber gaskets in immersed tunnels, namely bearing capacity, water tightness, lateral bucking, endurance and anti-fire. In their study, four types of rubber seal with different hardness were tested in axial behavior under monotonic and cyclic loading. One rubber type was selected to be submitted to the water tightness test, which is shown in Figure II.13. As the compression increased, the higher water pressure resistance against leakage was found in the rubber. Moreover, the shear loading was considered and the results show that under the same compression, the higher water pressure causes large shear displacements. Additionally, L-shaped rubber models were tested to investigate the contact behavior between the rubber and the concrete under extreme loadings. The test results of four specimens showed that the contact pressure between the rubber and concrete decreases when the compression increases. Last but not least, the durability of the rubber, such as corrosion and fire resistance, was also tested and some suggestions were given.

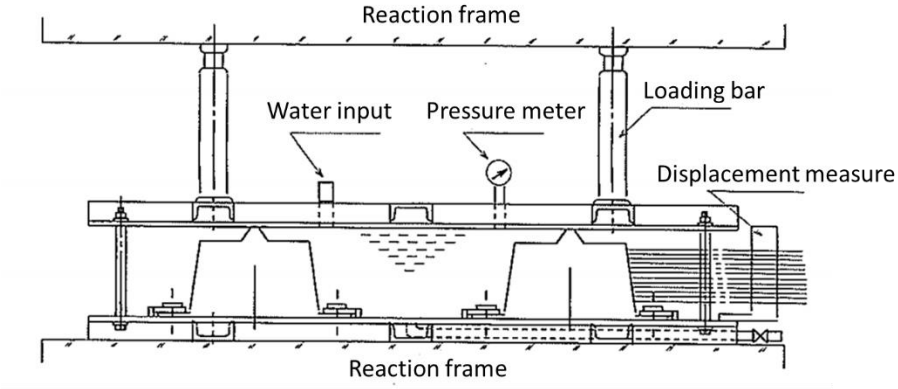

Figure II.13 Water tightness test (Kiyomiya and Yajima, 1997)

A series of experiments on the properties of the GINA rubber, also known as primary seal, were carried out by Lu (2004), including the compression test, water tightness test, compression-shear test, eccentric compression test (Figure II.14) and creep test. In the water tightness test, a similar test setup as the one from Kiyomiya was applied but the situations with and without attachment on the rubber were taken into account. The leakage firstly occurs in the bottom of the rubber in all cases. The shear test results show that the larger shear displacement, the larger sliding occurs. A smaller compression was observed in eccentric compression test compared to

the normal compression test. Moreover, a two-dimensional numerical analysis was conducted to investigate water tightness and to optimize the cross-sectional shape of the rubber. Based on the experimental and numerical results, suggestions on the rubber design and construction were given.

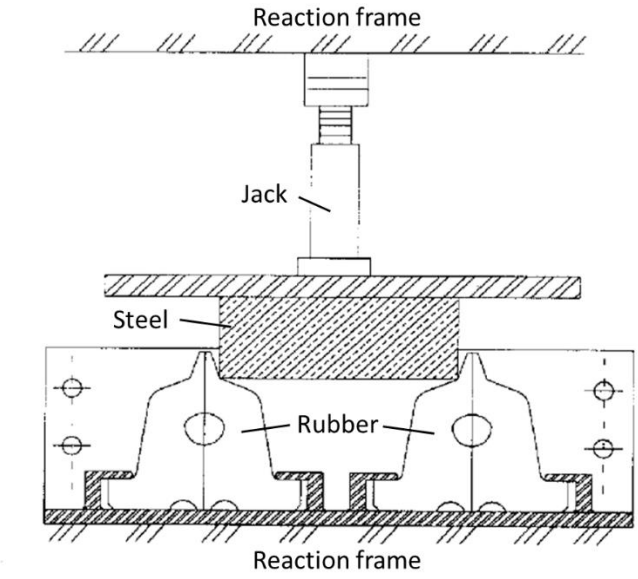

Figure II.14 Eccentric compression test (Lu, 2004)

Besides the aforementioned experiment on the rubber seal, a comprehensive behavior of the rubber seal subjected to various loadings was investigated by Liu (2009) through a three dimensional numerical analysis. The water tightness of the rubber was studied by analyzing the contact pressure, which is mainly influenced by the axial and bending loading on the joint. Figure II.15 displays the distribution of the contact pressure of the rubber along a quarter perimeter. It can be found that the maximum upper contact pressure around the corner part is relatively small and even in some points smaller than the maximum bottom contact pressure. Also, a minimum compression of 6mm of the rubber seal is sufficient to resist the water pressure against leakage. Based on the long-term behavior, the calculation model for the minimum compression of the rubber was provided.

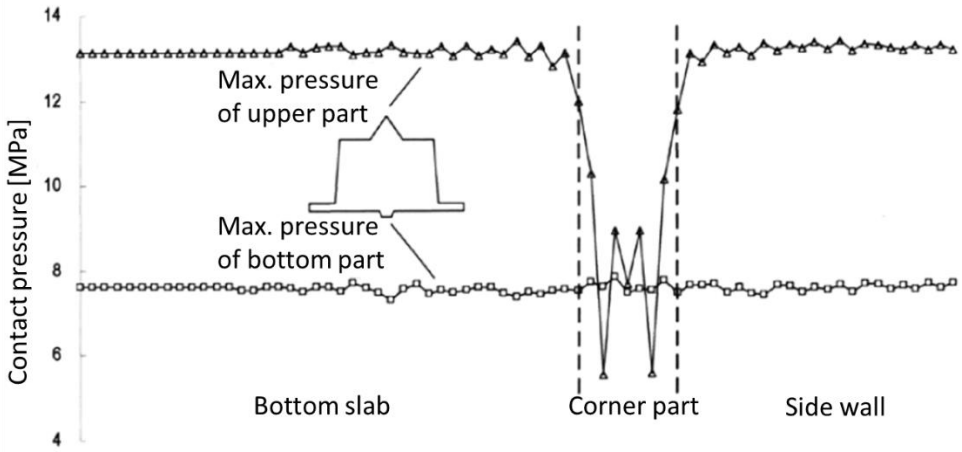

Figure II.15 Distribution of the contact pressure (Liu, 2009)

The researches on the rubber seal above were mainly based on the GINA type rubber seal. Apart from that, a new type of rubber seal (Figure II.16), which is reinforced by plastic fibers, was studied in a full-scale experimental and numerical way (Yokota et al., 2002). Both experimental and numerical results show that this new type of rubber seal can handle a shear displacement of up to 150mm and a water pressure of up to 300kPa. No harmful deformations and local distortion were observed on the surface of the rubber during the experiment. Additionally, no local strain beyond the allowable level was detected in any specimen in the numerical analysis. Such rubber seal has been applied to an actual project in Japan.

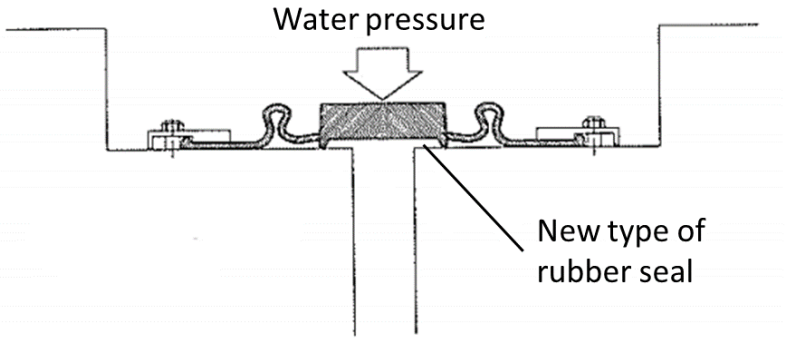

Figure II.16 Schematic of the new rubber seal (Yokota et al., 2002)

II.3.5. Seismic issues regarding immersion joints

Seismic issues regarding immersed tunnels are one of the most serious concerns in design practice, especially in seismic sensitive regions such as Japan and the Western part of the USA. The details of this topic are provided in the next chapter, which mainly discusses the seismic mitigation of an immersion joint.

II.4. Summary

Over the last century, research on the mechanical behavior of immersion joins became more and more significant and has been frequently discussed due to the fact that immersed tunnels became widely accepted around the world. The first attempt on this issue was made by Hawkins in 1811. However, this research was terminated and then during the next 150 years no research on this aspect was found. Until the 1970's, after the invention of the GINA rubber seal, attention was again paid to the immersion joints. Some model experiments on the behavior of the immersed tunnel were performed by the Port and Harbour Research Institute (Japan). However, most of these experiments focused on the dynamic response of the tunnel and soil-structure behavior rather than the structural behavior of the joint. Another dynamic experiment regarding the transportation and immersion was performed by Glerum (1976). Later on, the behavior of an immersion joint was first discussed by Ikeda (1989), showing that the flexible joint can reduce 30%-70% of the internal force in immersed tunnels. When it comes to the 1990's, with the development of computers and experimental techniques, the mainstream of the research on the behavior of immersion joints became diverse and it can be categorized in several parts, namely the mechanical model, shear behavior, water tightness and rubber, and seismic issues.

Regarding the global behavior of the joint, experiments were performed by Kiyomiya (1992, 2004), Hamazaki (1999) to investigate the axial and bending behavior of the joint. During the same period, some models were proposed by Xie (2008), Yu (2012) and Ding (2014), trying to describe the behavior of the joint by using a linear or bi-linear spring to simulate the joint.

However, such models lack experimental support and the failure of the joint was never considered.

When it comes to the shear behavior, shear keys are of importance having a high shear capacity to resist the shear force in the joint. Therefore, it is normally assumed in the numerical analysis by Anastasopoulos (2007) and Lyngs (2008), that the stiffness of the shear keys tends to be infinite and their behavior was simplified or even ignored. To detail the specific behavior of the component in the joint, experiments regarding the shear keys were performed by Li (2000) and Jiang (2001). Hu (2013) also carried out an experiment of the shear keys but in segmental joint, giving the detailed mechanical behavior of segmental reinforced concrete shear keys.

Researches also focused on the primary rubber seal and its water tightness performance through experimental and numerical studies. Numerical analyses were performed by Guan (1994), Kiyomiya (1997), Lu (2004) and Yokota (2002), and the results were verified by experiments under various loading protocols, showing that the primary rubber seal, mostly referred to as GINA rubber seal, has an excellent performance in water tightness. The detailed behavior of the GINA rubber was studied by Liu (2009), showing that the contact pressure of the rubber depends on its location and a minimum compression of 6mm of the rubber seal is sufficient to resist the water pressure against leakage. Moreover, a calculation model for the long-term compression of the rubber seal was proposed to assess the water resistance performance of the current rubber seal.

II.5. References

Anastasopoulos, I., Gerolymos, N., Drosos, V., 2007. Nonlinear Response of Deep Immersed Tunnel to Strong Seismic Shaking. Journal of Geotechnical and Geoenvironmental Engineering. 133, 1067-1090.

Aoki, Y., Tsuchida, H., Hayashi, S., 1972. Our-Door Dynamic Model Test of Trench Type Tunnel. Report of the Port and Harbour Research Institute. 11(2), 261-308. (in Japanese)

Araujo, D., Debs, M., 2005. Strength of shear connection in composite bridges with precast decks using high performance concrete and shear-keys. Materials and Structures. 38, 173-181.

Bozorgzadeh, A., Megally, S., Restrepo, J., et al., 2006. Capacity Evaluation of Exterior Sacrificial Shear Keys of Bridge Abutments. Journal of Bridge Engineering. 11(5), 555-565.

Ding, W., Liu, P., 2014. Research on the Three-Dimensional Nonlinear Stiffness Mechanical Model of Immersed Tube Tunnel Joints. In Proceedings of Geo-Shanghai 2014 International Conference, Shanghai, China. GSP 242, 1-14.

Glerum, A., Rigter, B., Eysink, W., et al., 1976. Motorway Tunnels Built by the Immersed Tube Method. Report of the Rijkswaterstaat Communications. No.25.

Glerum, A., 1988. Immersed Tunnels: Why, When and Where. Tunnelling and Underground Space Technology. 3(4), 347-351.

Goto, Y., Ota, J., Sato, T., 1973. On the earthquake response of submerged tunnels. In Proceedings of the 5th World Conference on Earthquake Engineering, Rome, Italy. 2B, 579-582.

Guan, M., Ren, X., Chen, Y., 1994. Water proof and immersion of the immersion joint. In Proceedings of the 8th Annual Conference of Tunnel and Underground Works Branch of China Civil Engineering Society, Beijing, China. 115-123. (in Chinese)

Hamazaki, Y., Yamaguchi, K., Takehana, N., et al., 1999. Steel Spring Joint for Immersed Tunnel. Kobe Steel Engineering Reports. 49(2), 57-60. (in Japanese)

Hu, Z., 2015. Research on action mechanisms and structural properties of segmental joint shear keys on immersed tunnel. PhD thesis, Chang'an University, Xi'an, China.

Ikeda, S., Kato, K., Hagihara, M., 1989. Study on Seismic Behavior of Reinforced Concrete Immersed Tunnels Having Flexible Joints. Doboku Gakkai Ronbunshu. 1989(402), 71-80. (in Japanese)

Jiang, J., 2001. Test and Design of Steel Shear Key of Immersed Tunnel. Modern Tunnelling Technology. 38(4), 40-43. (in Chinese)

Kiyomiya, O., Nakayama, S., Tsuchida, H., 1975. Observation of Dynamic Response of Kinuura Submerged Tunnel during Earthquakes and Dynamic Response Analysis. Report of the Port and Harbour Research Institute. No.221. (in Japanese)

Kiyomiya, O., Fujisawa, T., Yamada, M., et al., 1992. Mechanical Properties of Flexible Joint between Submerged Tunnel Elements. Report of the Port and Harbour Research Institute. No.728. (in Japanese)

Kiyomiya, O., Yajima, T., 1997. Some Properties of Rubber Gasket of Immersed Tunnel. Report of the Port and Harbour Research Institute. No.871. (in Japanese)

Kiyomiya, O., 2005. Seismic design method of immersed tunnel and effects of flexible joints. In Proceedings of the 31st ITA-AITES World Tunnel Congress, Istanbul, Turkey. 1, 635-640.

Kuesel, T., 1986. Alternative Concepts for Undersea Tunnels. Tunnelling and Underground Space Technology. 1(3/4), 283-287.

Li, Z., 2000. Calculation theory and experimental study on reinforced concrete shear key. Engineering Mechanics. 1(A01), 862-866. (in Chinese)

Liu, Z., 2009. Behavior and safety assessment of the immersion joint. Master thesis, Tongji University, Shanghai, China. (in Chinese)

Lu, M., 2004. Research on waterproofing of element joint of large immersed tunnel. Master thesis, Tongji University, Shanghai, China. (in Chinese)

Lunniss R., Baber, J., 2013. Immersed Tunnels, first ed. CRC Press, Boca Raton.

Lyngs, J., 2008. Model accuracy in aseismic design of immersed tunnel. Master thesis, Aalborg University, Aalborg, Denmark.

Nakano, T., Mori, K., 1973a. Earhtquake-Resistant Calculation and Dynamic Model Test on Trench Type Tunnel. Report of the Port and Harbour Research Institute. No.172. (in Japanese)

Nakano, T., Tabuchi, T., Aoki, Y., 1973b. A experimental study on the interaction between trench-type tunnels and soils. Report of the Port and Harbour Research Institute. 12(2), 63-84. (in Japanese)

Nasu, N., Kazama, S., Morioka, T., et al., 1977. Seismometric Investigation of the Motion of a Submarine Tunnel in Earthquake and at Ordinary Time. In Proceedings of the 6th World Conference on Earthquake Engineering, New Delhi, India. 3, 2554-2559.

Van Tongeren, H., Tonnisen, J., 1988. Immersed Tunnels: Why, When and Where. Tunnelling and Underground Space Technology. 3(4), 375-383.

Xie, L., Zhou, X., Yang, Q., 2008. Analysis on Mechanical Behavior of Tube Joints of a Submerged Floating Tunnel. Modern Tunnelling Technology. 45(4), 32-38. (in Chinsese)

Yokota, H., Iwanami, M., Kitayama, H., et al., 2002. Development of New Flexible Joint Structure for Submerged Tunnels. Report of the Port and Harbour Research Institute. No.1031. (in Japanese)

Yu, H., Yuan, Y., Liu, H., et al., 2012. Mechanical Model and Analytical Solution for Stiffness in the Joints of an Immersed-Tube Tunnel. Engineering Mechanics. 31(6), 145-150. (in Chinses)

CHAPTER III

SEISMIC MITIGATION

Rotterdam metro immersed tunnel, Netherlands

(source unknown)

III. Seismic Mitigation

III.1. Introduction

Earthquakes are one of the most destructive natural disasters to human living and it has been studied by numerous researchers in the past as well as the earthquake resistance of a structure due to the tremendous economic lost caused by previous earthquakes.

Earthquake resistance or seismic performance is mostly associated with surface structures, i.e. buildings, bridges or natural slopes, due to the fact that in general underground structures are less severely affected than surface structures at the same geographic location (Owen and Scholl, 1981). In recent decades, the interest in earthquake resistance of underground structures has increased significantly. It is believed that such interest was initially triggered by the damage to the Daikai metro station (Samata et al., 1997) during the Great Hanshin earthquake in Japan in 1995. Since then significant efforts have been made to quantify and enhance the seismic performance of underground structures.

Seismic mitigation is a concept to reduce the structural effects caused by earthquakes through additional equipment, which plays an important role in surface structures. However, such a concept is rather new for underground structures and few literature related to this topic is found. This chapter starts with a review on seismic mitigation. Different types of seismic mitigation methods as well as the corresponding devices are discussed. Details current research on seismic mitigation methods for underground structures are also presented and the experimental methods are listed separately. Finally, this chapter outlines the potential application of seismic mitigation on immersed tunnels, followed by a brief summary.

III.2. Seismic mitigation review

III.2.1. The concept of seismic mitigation

As well known, the soil and stratum movement occur as the earthquake strikes, resulting in the seismic response of both the surface buildings and underground structures. Generally, for a surface building, its seismic response is amplified gradually from the bottom to the top and excessive response (acceleration, velocity or displacement) may occur. Due to such excessive response,

-severe damage may occur in the main structure (like columns, beams or slabs), possibly resulting in collapses;

-no severe damage occurs in the main structure but in the non-structural components, such as walls, decoration or windows;

-or economic loss and secondary disasters caused by damage of the equipment in the structure.

Potential irrecoverable damage shall be avoided by appropriate control of the seismic response of a structure.

Previously, the increase of the structural stiffness is taken into account and the structural response approaches the ground movement, which is, however, non-economic and difficult to achieve. Later on, the method of decreasing the structural stiffness was proposed. Although the acceleration of the structure can be reduced, the story drift may exceed the allowable value. Therefore, a proper structural stiffness is of vital importance and the ductility of a structural system is determined in such a way that parts of the structure enter the non-elastic stage to consume more energy and reduce the seismic response. This approach is adopted as the most popular conventional seismic design concept worldwide. However, this concept is not easy to achieve and in some cases it is not suitable.

Hence, the idea of a new additional structural systems (Yuan and Chen, 2014), called seismic mitigation systems, was triggered, taking consideration of safety (no severe damage nor collapse), feasibility (suitable for various structures) and economy (no cost increase) issues. In

this structural system, the structural response can be properly controlled by adding additional external components, external actions, or changing the dynamic characteristic of the structure. With the efficient benefit in energy consumption, seismic mitigation methods were widely used by applying specific mitigation devices or adjusting the dynamic characteristics of the structure, which are well developed in seismic design and analysis of surface structures.

The seismic mitigation mechanism can be basically described by the general structural dynamics equation as follows (Clough and Penzien, 2003).

$$M\ddot{x}_s + C\dot{x}_s + Kx_s = F(t) - M\ddot{x}_g \tag{III.1}$$

where M, C and K are the mass, damping and stiffness of the structure respectively; $\ddot{x}_s$, $\dot{x}_s$ and x_s are the acceleration, velocity and displacement of the structure respectively; $\ddot{x}_g$ is the acceleration of the ground motion; and $F(t)$ represents the arbitrary external loading.

Dynamic responses of a surface structure subjected to seismic loadings could be remarkably reduced by adjusting the natural frequency ω or natural period T (by changing M and K), and/or by increasing the damping C or applying a proper external force $F(t)$. As a result, $\ddot{x}_s$, $\dot{x}_s$ and x_s can be limited to allowed value to ensure the safety of the structure and the people and the equipment in it within the serviceability limit state.

From the perspective of energy conversion during an earthquake, the concept of seismic mitigation can be explained by the following equations. For a conventional earthquake-resistant structure, it is presented as:

$$E_{iu} = E_R + E_D + E_S \tag{III.2}$$

and for the structure installed with seismic mitigation devices as:

$$E_{iu} = E_R + E_D + E_S + E_A \tag{III.3}$$

where E_{iu} is the input earthquake energy; E_R represents the kinetic and potential energy of the structural vibration; E_D represents the energy consumed by damping; E_S is the consumed energy due to the non-elastic deformation or damage of the main structure; and E_A is the energy consumed by the seismic mitigation devices.

Compared to the conventional structure, the structure installed with seismic mitigation devices can absorb the energy induced by the earthquake through the installed devices instead of experiencing serious damage or significant non-elastic deformation of the structure. In this way, the structure remains safe and its reaction to the earthquake is expected to attenuate remarkably.

III.2.2. Categories of seismic mitigation method

Based on different techniques, seismic mitigation methods of surface structures can be categorized as follows: seismic isolation method, energy dissipation method, tuned mass (liquid) damping method, active or semi-control method and hybrid control method.

(1) Seismic isolation method

This method is a technique to shift the nature frequency of a building by placing a horizontally flexible isolation device at the base of the structure (Gordon, 2012). The dynamic forces in the protected building are reduced in two ways: a sliding mechanism due to a friction and a rubber-made layer with adequate damping properties (Barbat, 1997).

(2) Energy dissipation method

Differing from the seismic isolation method, the energy dissipation method consists in adding an extra component in the structure in the way that the global structural ductility is achieved by the local component, such as viscoelastic dampers (Tsai, 1992), buckling restrained braces (Sun, 2011) or metallic dampers (Basu, 2016) etc.

(3) Tuned mass (liquid) damping method (TMD/TLD)

The natural frequency of a building can also be shifted by placing a huge mass (metal or liquid) in the topside of the building (Zhang, 2017). The higher the building, the higher the inertia force that can be generated due to earthquake or wind actions. Theoretical and experimental research and practical applications all show that such method has been proved efficient in seismic response reduction for high-rise buildings.

(4) Active or semi-active control method

Except for the presented passive control TMD/TLD, an active or semi-active control method is also investigated. The principle of the active control is to provide external corrective forces in strategic points in the structure to constrain the response within predetermined performance limits by using a computer or smart materials (Cao, 1998 and Pinkaew, 2001).

(5) Hybrid control method

A hybrid control method combines the mentioned active and passive control which is the most common control employed in full-scale civil engineering applications (Spencer and Soong, 1999).

III.2.3. Seismic mitigation devices

In order to achieve the seismic mitigation in Eq. (III.3), a number of seismic mitigation devices are widely used in both structural and bridge engineering. Based on different energy dissipating principles, the seismic mitigation devices are commonly categorized by three different types, namely displacement-based type, velocity-based type and the other types.

(1) Displacement-based type

The displacement-based seismic mitigation device is a device by which the energy induced by the earthquake can be dissipated through a cyclic plastic (i.e. metallic damper) or friction (i.e. friction damper) behavior. The first concept of the seismic mitigation was proposed by Kelly et al. (1972) as well as the first attempt for the metallic damper with various shapes. Since then, huge progress has been made by a number of researchers and an increasing number of this seismic mitigation device came to the practical applications, i.e. buckling restrained braces (Sun et al., 2011), lead damper (Skinner et al., 1980), friction dampers (Bhaskararao and Jangid, 2006) etc.

(2) Velocity-based type

This type of seismic mitigation device, involves mainly two types, i,e. viscoelastic and viscous dampers respectively. The energy dissipation depends on the relative velocity between the two ends of the damper (Fu and Kasai, 1998; Lee and Taylor, 2001).

(3) Others

Besides the mentioned most commonly used seismic mitigation devices, there are still some other types, i.e. lead-rubber dampers (Robinson and Tucker, 1977) and shape memory alloy dampers (Baz et al., 1990).

III.3. Seismic performance and analysis of underground structures

III.3.1. Seismic performance and damage of underground structure

The seismic performance of underground structures is determined basically by the deformations imposed by the surrounding ground, which distinguishes them from surface structures. Therefore, the deformation behavior of the stratum and the deformation capacity of the underground structure play a key role in the seismic performance. The seismic performance of more than 200 underground structures has been studied and since 1974 numerous research project have been performed as e.g. Duke and Leeds (1959), Dowding and Rozan (1978), Owen and Scholl (1981), Power et al.(1998) etc. Various influencing factors on seismic performance, such as overburden depth, surrounding ground, peak ground acceleration and velocity, slope stability at tunnel portals etc., have been investigated through in-situ observations, and numerical and experimental analysis.

Generally, appreciably less damage is observed in underground structures than surface structures due to the fact that the static design often provides sufficient seismic resistance under low levels of ground shaking (Hashash et al, 2001). Various historical databases for different underground structures have been created by numerous researchers, showing that the underground structures suffer from small to severe damage but no collapse occurred until 1995. In 1995, the collapse of the Daikai subway station caused by the Great Hanshin earthquake is regarded as the first collapse of an urban underground structure, which raised huge concerns with respect to the seismic performance and has stimulated a sharp increase in research

activities for possible measures to mitigate damage to underground structures. Figure I.1 shows an example of the damage of a tunnel subjected to the 2008 Wenchuan earthquake in China. An example of a column collapse in the Daikai subway station is shown in Figure III.2.

Figure III.1 Cracking and spalling inside a mountain tunnel (Yu et al., 2016)

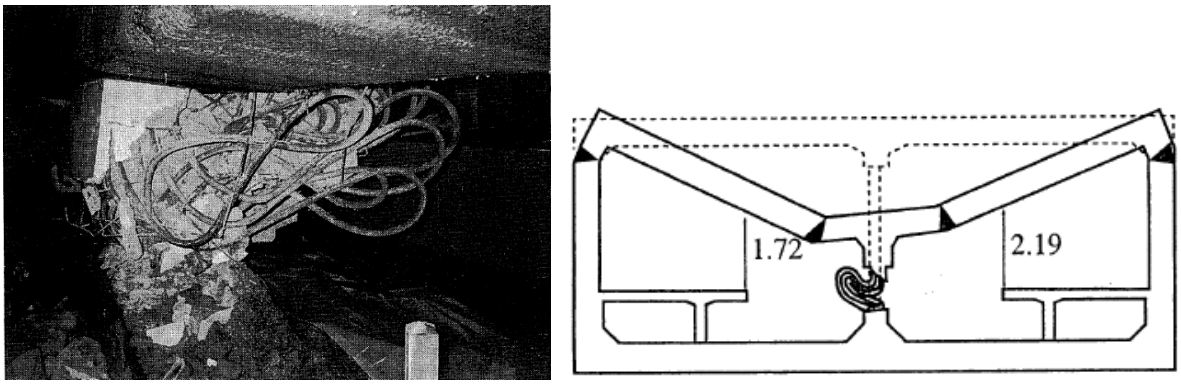

Figure III.2 Damage to the center column No. 10 (Iida et al., 1996)

III.3.2. Seismic analysis of underground structures

Ground shaking and ground failure like liquefaction are the two main concerns in the seismic analysis. As a result, the seismic response of underground structures is affected considerably by the kinematic loading induced by the surrounding ground, while the inertial loads of the structure itself are of secondary importance, which has been proved by Okamoto et al. (1973) through measurements of several immersed tunnels after earthquakes.

Owen and Scholl (1981) distinguished three major deformation modes of underground structures subjected to seismic actions, namely (1) axial compression and extension; (2) longitudinal bending; and (3) ovaling or racking, which are shown in Figure III.3. Axial and bending deformation in tunnels are caused by the components of seismic waves that produce motions parallel to and perpendicular to the longitudinal axis of the tunnel respectively. The ovaling and racking deformation are generated by the shear wave propagating normal to the axis of the tunnel. The axial and bending behavior is mainly taken into account in tunnels or pipelines as the tunnel/pipeline alignment dominates in the dimensions in most cases. The ovaling and racking behavior is analyzed both in tunnels and other underground structure such as subway stations.

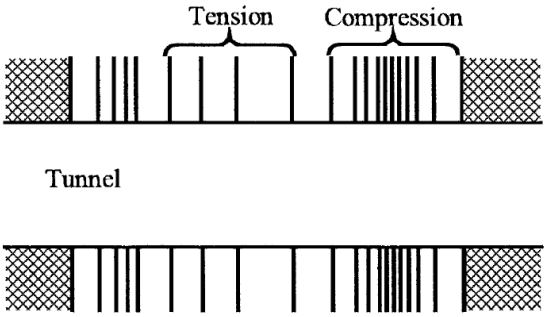

(a) Compression and extension

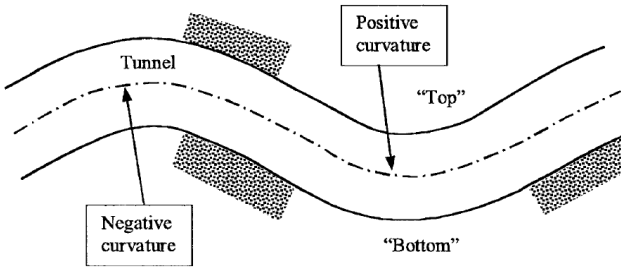

(b) Longitudinal bending (vertical cross section)

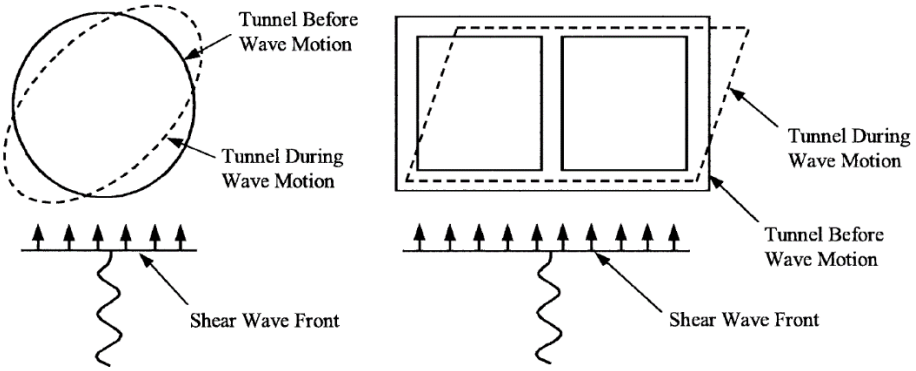

(c) Ovaling (left) and racking (right)

Figure III.3 Three major deformation modes of underground structures (Owen and Scholl, 1981)

(1) Axial and bending deformation

The axial behavior is also referred as the “worming effect” due to its similarity to the movement of a worm (Van Oorsouw, 2010). This effect is caused by the seismic waves in the longitudinal direction of the structure. If the surrounding ground of the tunnel is homogeneous and isotropic, the whole tunnel follows the same movement and behaves as a rigid body. Hence, there are no internal deformations and forces under this assumption. However, in reality, due to the complexity of the surrounding ground, relative deformations occur in the structure resulting in compression, extension and even bending.

The “snaking effect” is often used as the bending deformation in relation to the moving snake (Van Oorsouw, 2010). Unlike axial deformation, the bending deformation can cause the curvature of the tunnel, namely one side is compressed and the other side is extended. Another issue, the shear problem, also arises due to the snaking effect.

(2) Ovaling and racking

Ovaling and racking, corresponding to a circular and rectangular cross section respectively, refer to the cross-sectional behavior of underground structures, which is mainly influenced by the deformation of the surrounding ground. The analytical procedure of the seismic induced racking was proposed by Penzien (2000) and an analytical evaluation of the racking deformation of rectangular linings was presented.

Regarding immersed tunnels, the compression of the tunnel is mainly taken by the rubber seal in the joints and the tunnel elements. It is, to some extent, a positive load due to the fact that the compression can guarantee the water sealing in the joint and the concrete part of tunnel elements behaves better in compression than in tension. On the contrary, the extension is in any case harmful to immersed tunnels as neither the joint nor the element can resist extension. As a consequence, the sealing pressure decreases and leakage may occur, jeopardizing the water tightness of the tunnel. In some projects, which are located in seismic sensitive zones, there may be some couplers in the joints to limit the extension and to avoid severe consequences. The shear problem also draws a wide range of concerns. Due to the stiffness of the joint, the bending moment is transferred from one element to another element in the form of a bending

moment and a shear force. The bending moment is mainly taken by the rubber while the shear force is transferred by means of the shear keys.

As early as 1970's, some model tests for the seismic behavior of submerged tunnels and soil-structure interaction during earthquakes were conducted by several Japanese researchers, such as Aoki et al.(1972), Kiyomiya et al.(1975), Nakano et al. (1973), Tamura et al.(1975). In these experiments, the earthquake resistant design for immersed tunnels was examined and verified.

Based on this pioneering research, the rational earthquake-resistant design for immersed tunnels was elaborated and reported in "Specification for earthquake resistant design of submerged tunnels" by JSCE (1975), also clarifying that the seismic behavior of a submerged tunnel was related to its surrounding ground, as mentioned. The background of this design method was summarized and discussed by Okamoto (1978) with respect to soil stability, design concept and dynamic analysis. A model for dynamic analysis was proposed by using one-mass-spring system replacing the segment connected in axial direction by springs. Also, model vibration experiments were conducted and due to limitation at that moment only sinusoidal vibration in one direction was considered.

In 1984, a multi-mass-spring model basically considering only the axial direction was proposed by Hamada et al. where the tunnel was assumed as an infinite chain of elements as shown in Figure III.4. Two submerged tunnels were studied by using this model and the observed data and results showed that the axial and bending seismic responses depend on the ground velocity and acceleration. An effective reduction in seismic strain was found by using flexible joints between the elements.

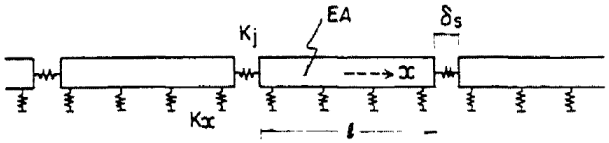

Figure III.4 Simple model for immersed tunnels (Hamada, 1984)

Based on years of practical experiences and researches in Japan, Kiyomiya (1995) summarized three dynamic response analysis for immersed tunnels, which were a multi-mass-spring system, a quasi-three-dimensional ground model and a finite element method respectively. Compared

to the multi-mass-spring method, the quasi-three-dimensional ground model was more suitable for complicated ground conditions. The application of a new flexible joint, referred to as Crown Seal, in Japan was also summarized (Kiyomiya, 2005) as such a joint has a potential to handle large deformations during earthquakes.

A seismic retrofit for an existing immersed tunnel was conducted by Taylor et al. (2002) due to the revealed significant vulnerabilities such as liquefaction triggering and liquefaction-induced ground movement. A 3D numerical model was established as shown in Figure III.5, considering the wave passage effect and post-liquefaction differential settlement loading. However, the proposed 3D numerical model was not a true 3D model because each tunnel element was simplified as a lumped mass, connected with the adjacent elements by springs. Finally both a structural and geotechnical solution for retrofit was proposed based on the results obtained from a 3D numerical analysis and a centrifuge test.

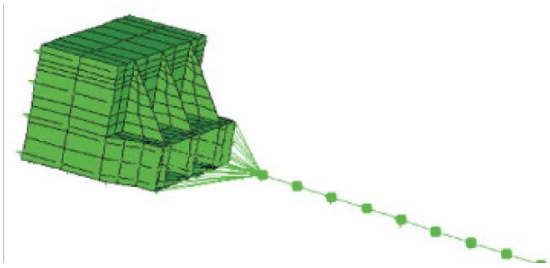

Figure III.5 Model of ventilation shaft and immersed tunnel (Taylor et al., 2002)

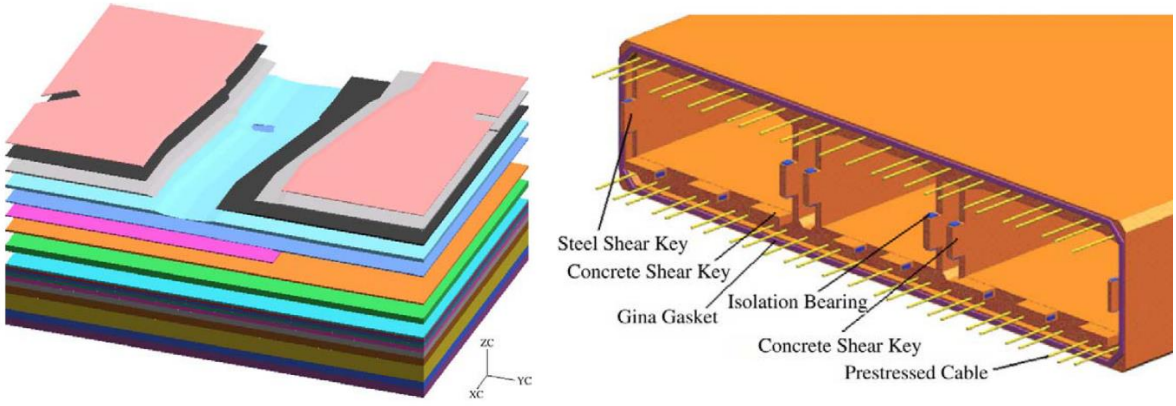

(a) Layout of the surrounding stratum (b) Details of the joint

Figure III.6 A three-dimensional model of an immersed tunnel (Ding et al., 2006)

Later on, a true three-dimensional numerical model with more than one million elements and nodes was built by Ding et al. (2006) based on a newly constructed immersed tunnel in Shanghai, which is the first attempt to use complex full scale model in numerical analysis. In this model, the detailed immersion joint, the tunnel element and the whole surrounding stratum were all taken into account, as displayed in Figure III.6. The relative deformation of the immersion joints is investigated under longitudinal and transversal seismic waves as well as the compression of the rubber seal and the tensile force of the cables in the joint. Such attempt proves that the finite element method is a feasible approach for a large analytical model for seismic analysis.

Anastassopoulos et al. (2007) proposed a non-linear finite element model to analyze the seismic performance of a deep immersed tunnel located on a seismic sensitive zone. The tunnel element was simulated as a beam considering shear rigidity while the joint was modeled with two 64-node frames, between which nonlinear springs were provided. The interaction between the elements and the soil was simulated by using springs and dashpots. The influence of the segment length, the shear allowance and the type of rubber seal were investigated. Numerical results show that the dynamic longitudinal deformation of the joints was affected by the segment length and the thickness of the rubber and that most of the imposed deformation was absorbed in the joints.

The racking, axial and curvature deformations of the immersed tunnel with different lengths of tunnel elements was taken into account in the seismic analysis by Vrettos et al. (2007) through a similar continuum beam model. Determination of the input motion on the tunnel and the derivation of the used spring values between soil and tunnel were given. Results indicated that a shorter length of the tunnel elements is more advantageous against seismic action.

Moreover, approximately during the same period, as there is a booming promotion of immersed tunnels in China since 1995, various papers related to seismic analysis based on actual project were published by Chinese researchers, such as Han and Zhou (1999), Yan et al. (2003), Fu et al. (2008), etc. They presented similar conclusions, showing that the lower stiffness of the joint can, to some extent, reduce the seismic response of a tunnel. However, the aforementioned models adopted by them were basically the same as that of Anastasopoulos.

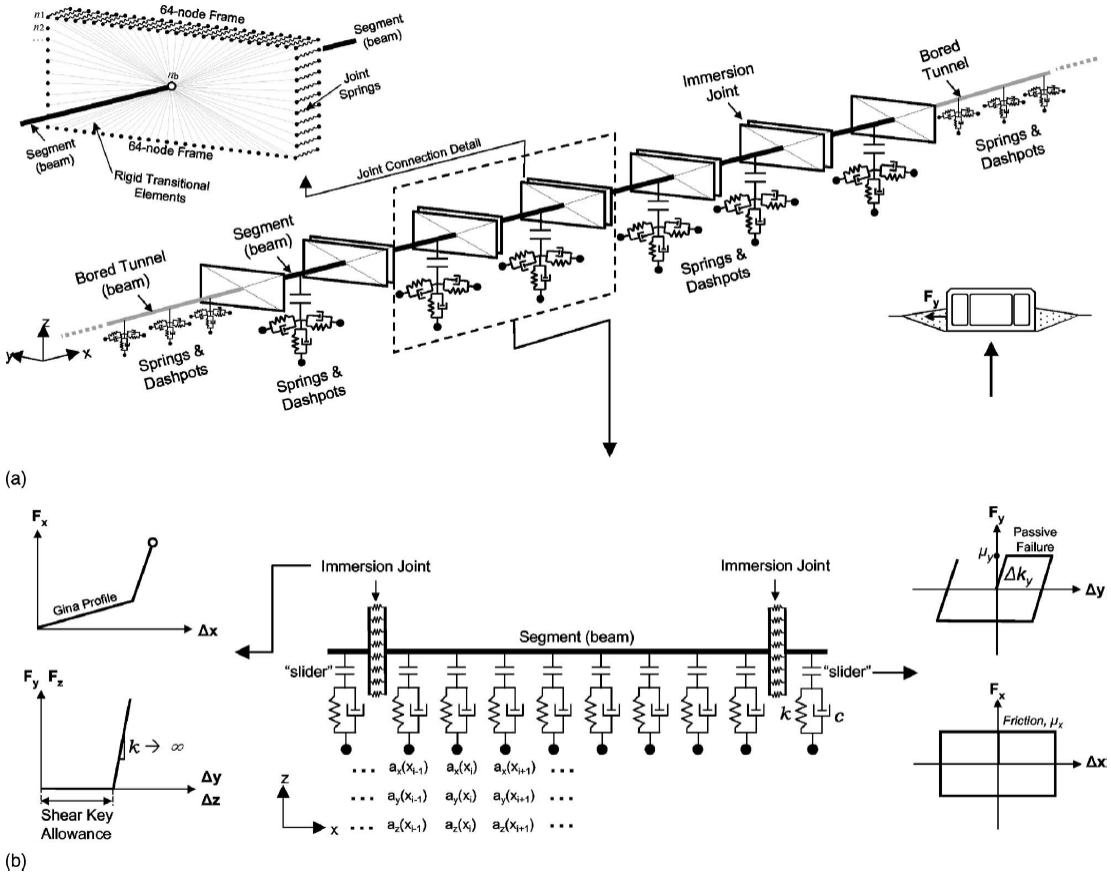

Figure III.7 Finite element model: (a) 3D view; (b) longitudinal section of the model (Anastasopoulos et al., 2002)

As the ultra-long immersed tunnel came into reality, another seismic problem, the consideration of non-uniform seismic excitation, was introduced to immersed tunnels by Yu et al. (2012) due to the possible significant variations in surrounding ground, which leads to a time lag of the seismic response in different locations of a tunnel. Later on, the non-uniform seismic analysis was conducted through a novel multi-point shaking table test (Yu et al., 2016 and Yuan et al., 2016). Moreover, a new multi-body dynamics method for longitudinal seismic response analysis for immersed tunnel was proposed by Yuan et al. (2015). Another shaking table test was conducted by Chen et al. (2017) mainly considering the soil-tunnel interaction. Experimental results show that soil liquefaction affects the propagation of seismic waves significantly as well as the dynamic responses of the tunnel..

Apart from the numerical and experimental researches, monitoring the existing immersed tunnels during earthquake to assess its seismic performance also became necessary. Dikmen (2016) presented the monitoring work for the Marmaray submerged tunnel in Istanbul during the 2014 Northern Aegean earthquake (Mw = 6.9). Obtained displacement time histories show that the tunnel was not affected by the long period waves from the earthquake.

III.4. Seismic mitigation and immersed tunnels

III.4.1. Seismic mitigation method for underground structures

As mentioned, the seismic performance of underground structures differs from that of surface structures due to the surrounding environment. Based on that, the solution for seismic mitigation for underground structures can be categorized as follows (Yuan and Chen, 2014):

(1) Ground treatment

The deformation of the surrounding ground can be reduced by improving the strength and stiffness through ground treatment methods and the response of the structure is decreased in this way. Grouting is one of the most common methods to reinforce the surrounding ground of the tunnel (Gao et al., 2005).

(2) Stiffness adjustment

The same as the surface structure, the stiffness of underground structures can be adjusted, increasing or decreasing, to accommodate the deformation of the surrounding ground. For example, the methods can be: changing the mass of the lining by choosing proper aggregates; adopting polymeric materials with higher damping; adopting assembling tunnel linings instead of casting it as a whole etc. The structural ductility is also considered with respect to more energy dissipation. However, an argument between increasing and decreasing stiffness of the structure has been existing in engineering applications due to the fact that a smaller stiffness can result in a better seismic performance but also in larger deformations, which is not necessarily compatible with the serviceability demand.

(3) Isolation layer method

This method is a technique where that an elastic isolation layer is placed between the tunnel structure and the surrounding ground in such a way that the deformation acting on the structure can be reduced. This is normally achieved by grouting in practice (Gao et al., 2005), Figure III.8 demonstrates the mechanism of the isolation layer for a mountain tunnel and the layer is simulated by several springs, through which the earthquake-induced deformation can be transferred from the ground to the tunnel. The numerical and experimental analyses have been conducted by Wang et al. (2010), showing that the installation of the isolation can reduce the maximum strain by 60% and a long-term seismic mitigation effect was found as well.

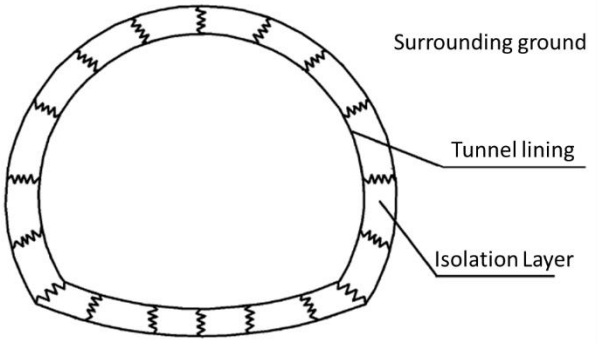

Figure III.8 Mechanism of the Isolation layer (Wang et al., 2010)

III.4.2. Seismic mitigation for immersed tunnels

Regarding immersed tunnels, as mentioned in Chapter I, the construction method and the structural features of the immersed tunnel are special and unique, determining that the current mitigation methods for underground structures are not suitable for immersed tunnels. For instance, as the immersed tunnel is shallow-buried and backfill is needed after immersion, the ground treatment may offer sufficient help to reduce the settlement but not the seismic mitigation. Applying a different stiffness to the tunnel elements located on different foundations seems to be beneficial. However, this solution adds a complexity in design and manufacturing of the elements because the elements are normally assembly-line produced. Also, the isolation layer is somehow extremely difficult to achieve due to the complicated underwater situation.

With respect to the joint between the elements, though the rubber seal is commonly regarded as a hyper-elastic material, experimental results show that a hysteretic performance was obtained (Xiao, 2015) and perhaps the rubber seal could be a component of energy mitigation. However, it is not wise to use the rubber seal as the seismic mitigation device due to the fact that the rubber is of vital importance in water sealing and additional requirements for the rubber may put the joint into a more risky situation during earthquake.

Therefore, no research has been reported on seismic mitigation for immersed tunnels as the conventional seismic mitigation methods are not suitable. Based on that, adding seismic mitigation devices in immersed tunnels can be an additional way to dissipate the energy caused by earthquakes. Generally, the immersion joint has a relative low stiffness, allowing a certain deformation in the joint, and hence, the seismic mitigation can be achieved by employing the seismic mitigation devices in such a way that the device can work in coordination with the joint.

III.4.3. Buckling restrained braces

As aforementioned, there are various seismic mitigation devices which have been widely examined and applied into practice for decades. Based on the structural characteristic and the external excitation, the proper type of seismic mitigation device can be determined. As mentioned, it is required that the installed seismic mitigation device crosses through the joint and is slender enough along the tunnel axis to make space for clearance. Based on that, the buckling restrained brace (BRB) is adopted in the current research stage to investigate the cooperation of the joint and the device. However, it should be noted that the seismic mitigation device is not limited to the BRB as the presented research is just the first attempt on this seismic issue.

The buckling restrained brace, which is made from an encased steel core into a steel tube, and confined with infill materials, has been widely adopted as seismic mitigation device worldwide. The schematic of the BRB is shown in Figure III.9. When the conventional steel brace is subjected to an excessive axial compressive force, the brace buckles and loses its load capacity. If a cyclic loading is applied to the brace, an asymmetric hysteretic behavior in compression and tension is found as well as a strength degradation in compression as shown in the left of

Figure III.9. If the buckling is restrained by an outer tube, approximately the same strength in compression and tension can be guaranteed. In this way the hysteretic performance is extensively enhanced and the energy dissipated by the brace is substantially increased. By such improvement to the brace, the BRB has successfully been transferred to the industry and implemented in a wide range of applications.

As shown in the right part of Figure III.9, a typical BRB generally consists of a steel core, a restrained casing and the unbonding layer or a gap between the core and the casing. The buckling of the steel core, which is normally made from low yielding steel, is restrained perpendicularly to the alignment of the steel core by a concrete or steel casing. In order to ensure that the steel core can slide freely inside the casing and the transversal deformation is allowed when the core yields, an unbonding material is required, or the unbonding material should be replaced by a gap.

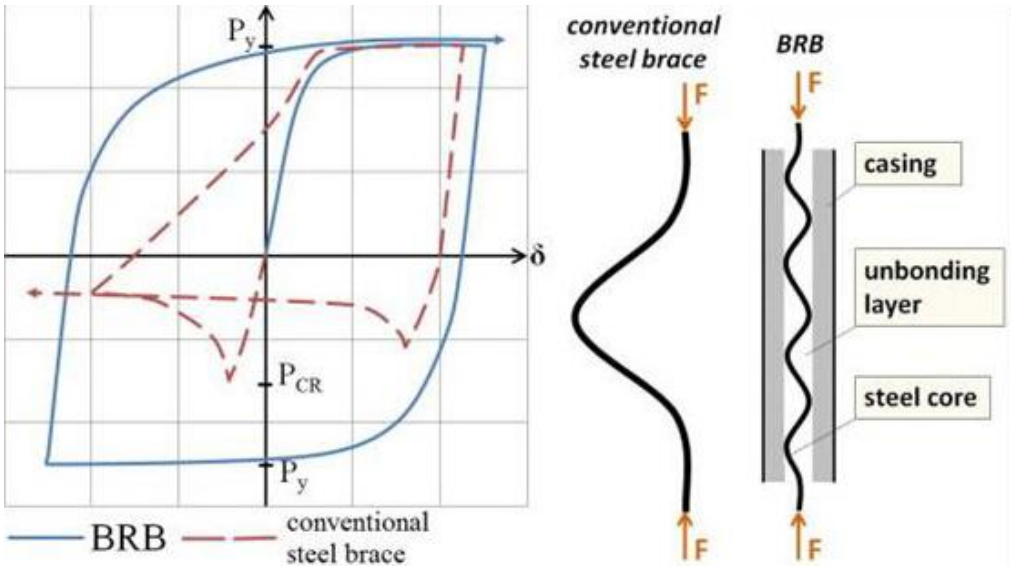

Figure III.9 The schematic of the BRB

(http://doktori.bme.hu/bme_palyazat/2013/honlap/Zsarnoczai_Adam_en.htm)

There is a consensus by the researchers that the first attempt to carry out experiments on a BRB was by Yoshino et al. (1971) but at that moment the BRB was called ‘Shear wall with braces’. Two specimens, one with a gap and another without, both including a steel core plate encased

by a reinforced concrete panel with some debonding material between the interface, were tested cyclically. The results show that a better energy dissipation was found in the brace with a gap.

A comprehensive pioneering work on BRBs was done and a BRB system was proposed by Wakabayashi et al. (1976) through a series of multi-level experiments from the property of the debonding material to a large-scale two-story frame with BRBs. The same type of BRB, with a steel plate and infilled reinforced concrete in the casing, as the one from Yoshino's work was applied. Besides, a panel BRB, which is also called stiffening brace system and the yielding part is embedded in a precast concrete panel, was also developed and tested.

Later on, more configurations of the BRB were developed, i.e. the mortar-infilled material replacing the reinforced concrete (Kimura et al., 1976), H or crisscross cross section of the steel core (Nagao et al., 1988) and square or circular cross section of the casing (Suzuki et al., 1994). Various configurations of the BRB with different cross sectional steel core and casing are illustrated in Figure III.10.

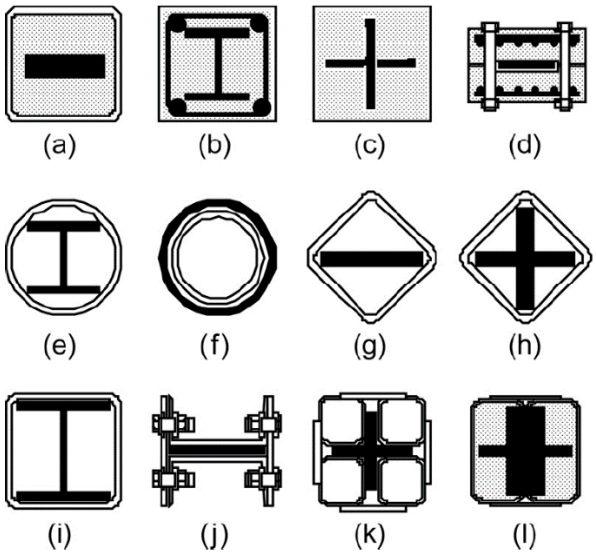

Figure III.10 Various cross-sections of the BRB (Xie, 2005)

Figure III.11 exhibits a typical axial force-displacement curve of the BRB recorded from an experiment. A stable hysteretic performance can be found in both compression and tension as the hysteretic loop grows in a stable way with increasing axial force. Similar results can also

be found in other experiments with different novel designs of the BRB (Sabelli et al., 2003; Iwata and Murai, 2006; Fahnestock et al., 2007; Bai and Ou, 2016) and during the past 50 years its effectiveness in energy absorption has been proved. The BRB has been used extensively in Japan (Black et al., 2004), China (SH Lanke Building Damping Tech. Co., Ltd.) and USA (Kersting et al., 2015). An example is shown in Figure III.12. Nowadays the BRB is still active subject of current research. Although the BRB has been accepted widely in buildings and bridges, there is still a gap in its application in underground structures, especially in immersed tunnels, which is going to be filled by the first attempt of this field presented in the following chapter.

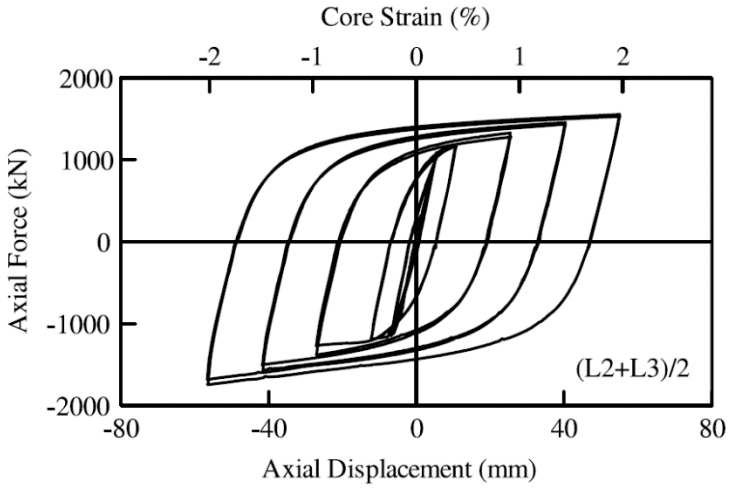

Figure III.11 A typical axial force-displacement curve of the BRB (Chou and Chen, 2010)

Figure III.12 A typical BRB in USA (Kersting et al., 2015)

III.5. Summary and conclusions

Earthquake resistance performance of surface building has gained great concern for more than a century. In this aspect, seismic mitigation is introduced as one of the possible and effective methods to reduce the seismic response of a building. The basic concept and the general mathematical expressions are presented to briefly give an overall idea of seismic mitigation methods. There are five different categories of seismic mitigation, namely seismic isolation method, energy dissipation method, tuned mass (liquid) damping method, active or semi-control method and hybrid control method, based on different techniques. To achieve the seismic mitigation in a structure, seismic mitigation devices are also introduced briefly. It can be concluded that the theory of seismic mitigation is well developed in the field of surface structures.

On the contrary, the seismic issue of underground structures has not gained much attention as it is generally assumed that the underground structures are less affected by earthquakes as they are 'protected' by the surrounding ground. In the early researches done by Duke (1959), Dowding (1978), Owen (1981) and Power (1998), more than 200 case studies have been conducted and no severe damage was found in tunnels. Approximately during the same period, the seismic performance of underground structures, mostly tunnels, was summarized and three possible deformation modes for underground structures were proposed by Owen (1981). Subsequently, an increasing numbers of researches have been performed regarding the seismic response during recent decades, triggered by the first observed collapse in a metro station after a severe earthquake in 1995.

With respect to immersed tunnels, the pioneering work of seismic analysis dates back to 1975. The seismic behavior of the submerged tunnel was investigated by a test and the site observations. In the same year, a rational earthquake resistance design for immersed tunnels was reported by JSCE. Later on, various numerical analyses on seismic performance of immersed tunnels were done by Okamoto (1978), Kiyomiya (1995a, 1995b), Taylor (2002), Ding (2006), Anastassopoulos (2007) etc. Since immersed tunnels were introduced in China, a number of Chinese papers were published during the same period i.e. Han (1999), Yan (2003),

Fu (2008), Yuan (2016) etc. Experimental research towards this issue is rare. Besides the pioneer test done by Tamura, the shaking table test for an ultra-long immersed tunnel was conducted by Yu (2016), taking the non-uniform seismic excitation into account and another shaking table test was done by Chen (2017) mainly involving the soil-tunnel interaction. It can be concluded that although a number of researches have been carried out, none of them are associated with the seismic mitigation method.

However, the concept of the seismic mitigation method for underground structures is not new. Previous researches done by Gao (2015), Wang (2010) and Yuan (2014) concludes that there are three main solutions achieving seismic mitigation, which is ground treatment, stiffness adjustment and isolation layer method. However, due to the special characteristics of the tunneling construction method, the structural features and the surrounding environment of immersed tunnels, the current seismic mitigation method for underground structures are not suitable. Therefore, a concept of combination of a seismic mitigation device and immersed tunnels was proposed, taking the advantage of the stunning hysteretic performance of the seismic mitigation device. To achieve it, the buckling restrained brace was introduced but not limited to this type of the seismic mitigation device.

As one of the main objectives of the present thesis is to explore the seismic mitigation for immersed joints in immersed tunnels, the current literature study focuses rather on the seismic performance of underground structure and immersed tunnels than the mechanical behavior of the buckling restrained brace (BRB). As such, only the major contributions and a brief introduction of the principle towards the BRB are reported. However, it is obvious that the effectiveness of seismic mitigation and hysteretic performance of the BRB is proved to be applicable in seismic design. The earliest attempt towards the BRB dates back to 1970s in Japan. So far, it is already a well-established design method around the world. Previous experimental and theoretical investigation have been performed by Yoshino (1971), Wakabayshi (1976), Kimura (1976), Nagao (1988), Suzuki (1994) with conventional configurations of the BRB. Subsequently, a more novel design for the BRB was published by Sabelli (2003), Iwata (2006), Fahnestock (2007), Bai (2016) etc. and similar excellent hysteretic performance was found.

With several years of development, the BRB has been widely adopted in Japan, China and USA. Now the BRB is still an active subject of current research.

Hence, a cooperation of the seismic mitigation device, like the BRB, and immersed tunnels, proposed in this thesis is the first attempt ever and it fills the gap related to the seismic mitigation method applied to immersed tunnels. Furthermore, details regarding the design procedure and its validation can be found in the following chapter.

III.6. References

Anastasopoulos, I., Gerolymos, N., Drosos, V., et al., 2007. Nonlinear Response of Deep Immersed Tunnel to Strong Seismic Shaking. Journal of Geotechnical and Geoenvironmental Engineering. 133, 1067-1090.

Aoki, Y., Tsuchida, H., Hayashi, S., 1972. Out-Door Dynamic Model Test of Trench Type Tunnel. Report of the Port and Harbour Research Institute (Ministry of Transport, Japan). 11(3), 261-308. (in Japanese)

Bai, J., Jinping, O., 2016. Earthquake-resistant design of buckling-restrained braced RC moment frames using performance-based plastic design method. Engineering Structures. 107, 66-79.

Barbat, A., Bozzo, L., 1997. Seismic Analysis of Base Isolated Buildings. Archives of Computational Methods in Engineering. 4, 153-192.

Basu, D., Reddy, P., 2016. A New Metallic Damper for Seismic Resilience: Analytical Feasibility Study. Structures. 7, 165-183.

Baz, A., Iman, K., McCoy, J., 1990. Active Vibration control of Flexible Beams Using Shape Memory Actuators. Journal of Sound and Vibration. 140, 437-456.

Bhaskararao, A., Jangid, R., 2006. Seismic analysis of structures connected with friction dampers. Engineering Structures. 28, 690-703.

Black, C., Makris, N., Aiken, I., 2004. Component Testing, Seismic Evaluation and Characterization of Buckling-Restrained Braces. Journal of Structural Engineering. 130, 880-894.

Cao, H., Reinhorn, A., Soong T., 1998. Design of an active mass damper for a tall TV tower in Nanjing, China. Engineering Structures. 20, 134-143.

Chen, X., Jing, L., Cui J., et al., 2017. Shaking-Table Tests for Immersed Tunnels at Different Sites. Shock and Vibration. 2017, 1-11.

Chou, C., Chen, S., 2010. Subassemblage tests and finite element analyses of sandwiched buckling-restrained braces. Engineering Structures. 32, 2108-2121.

Committee for Earthquake Resistant Design of Submerged Tunnel (Japan), 1975. Specifications for earthquake resistant design of submerged tunnels. Japan Society of Civil Engineering (JSCE), Tokyo.

Clough, R., Penzien, J., 2003. Dynamics of Structures. Computers & Structures, Inc., Berkeley.

Dikmen, S., 2016. Response of Marmaray Submerged Tunnel during 2014 Northern Aegean Earthquake (Mw=6.9). Soil Dynamics and Earthquake Engineering. 90, 15-31.

Ding, J., Jin, X., Guo, Y., et al., 2006. Numerical simulation for large-scale seismic response analysis of immersed tunnel. Engineering Structures. 28, 1367-1377.

Duke, C., Leeds, D., 1959. Effects of Earthquakes on Tunnels. USA.

Dowding, C., Rozen, A., 1978. Damage to rock tunnels from earthquake shaking. Journal of Geotechnical Engineering Division. 104, 175-191.

Gao, F., Shi, Y., Yan, S., et al., 2005. Study of Two Shock Absorption Measures in Tunnel. Chinses Journal of Rock Mechanics and Engineering. 24, 222-229. (in Chinses)

Gordon, P., Ryan, K., 2012. A Review of Seismic Isolation for Buildings: Historical Development and Research Needs. Buildings. 2, 300-325.

Fahnestock, L., Ricles, J., Sause, R., 2007. Experimental Evaluation of a Large-Scale Buckling-Restrained Braced Frame. Journal of Structu ral Engineering. 133, 1205-1214.

Fu, J., Wu, J., Xu, A., 2008. Seismic Response of Zhoutouzui Immersed Tunnel in Guangzhou. Journal of Hunan University (Natural Science). 35, 23-27. (in Chinses)

Fu, Y., Kasai, K., 1998. Comparative Study of Frames Using Viscoelastic and Viscous Dampers. Journal of Structural Engineering. 124, 513-522.

Hamada, M., 1984. Earthquake observation on two submerged tunnels and numerical analysis. In Proceedings of the 8th World Conference on Earthquake Engineering, California, USA. 3, 673-680.

Han, D., Zhou, A., 1999. A Study of the Equivalent Mass-System Models for the analysis of Earthquake Response of an Immersed Tunnel. Journal of South China University of Technology (Nature Science). 27, 108-114. (in Chinses)

Hashash, Y., Hook, J., Schmidt, B., et al., 2001. Seismic design and analysis of underground structures. Tunnelling and Underground Space Technology. 16, 247-293.

Iida, H., Hiroto, T., Yoshida, N., et al., 1996. Damage to Daikai Subway Station. Special Issue of Soils and Foundations. Jan, 283-300.

Iwata, M., Murai, M., 2006. Buckling-restrained brace using steel mortar planks; performance evaluation as a hysteretic damper. Earthquake Engineering and Structural Dynamics. 35, 1807-1826.

Kelly, J., Skinner, R., Heine, A., et al., 1972. Mechanisms of Energy Absorption in Special Devices for Use in Earthquake. Bulletin of the New Zealand National Society for Earthquake Engineering. 5, 63-88.

Kimura, K., Yoshioka, K., Takeda, T., et al., 1976. Tests on braces encased by mortar in-filled steel tubes. Summaries of Technical Papers of Annual Meeting of Architectural Institute of Japan. 51, 1041-1042. (in Japanese)

Kersting, R., Fahnestock, L., Lopez, W., 2015. Seismic Design of Steel Buckling-Restrained Braced Frames. NEHRP Seismic Design Technical Brief No.11 (NIST GCR 15-917-34). National Institute of Standards and Technology, Maryland.

Kiyomiya, O., Nakayama, S., Tsuchida, H., 1975. Observations of Dynamic Response of Kinuura Tunnel during Earthquakes and Dynamic Response Analysis. Technical Note of the Port and Harbour Research Institute (Ministry of Transport, Japan). No. 221. (in Japanese)

Kiyomiya, O., 1995. Earthquake-resistant Design Features of Immersed Tunnels in Japan. Tunnelling and Underground Space Technology. 10, 463-475.

Kiyomiya, O., 2005. Seismic design method of immersed tunnel and effects of flexible joints. In Proceedings of the 31st ITA-AITES World Tunnel Congress, Istanbul, Turkey. 1, 635-640.

Shanghai LANKE Building Damping Technology Co., Ltd. Historical Cases [Format: web pages]. < http://www.lankesoft.com/case >.

Lee, D., Taylor, D., 2001. Viscous Damper Development and Future Trends. The Structural Design of Tall Buildings. 10, 311-320.

Nagao, T., Mikuriya, K., Matsumoto, Y., et al., 1976. An experimental study on the elasto-plastic behavior of unbonded composite bracing (Part 1-4). Summaries of Technical Papers of Annual Meeting of Architectural Institute of Japan (Structural Engineering Section II). 1988, 1329-1336. (in Japanese)

Nakano, T., Tabuchi, T., Aoki, Y., 1973. An experimental study on the interaction between trench-type tunnels and soils. Report of the Port and Harbour Research Institute (Ministry of Transport, Japan). 12(2), 85-108. (in Japanese)

Okamoto, S., Tamura, C., Kato, K., 1973. Behavior of a submerged tunnel during earthquake. In Proceedings of the fifth World Conference on Earthquake Engineering, Rome, Italy. 1, 544-553.

Okamoto, S., Tamura, C., 1978. Earthquake-resistance design of submerged tunnels. IABSE Reports of the Working Commissions. 30, 71-93.

Owen, N., Scholl, R., 1981. Earthquake Engineering of Large Underground Structures. URS/John A. Blume & Associates, Engineers, San Francisco.

Penzien, J., 2000. Seismically induced racking of tunnel linings. Earthquake Engineering and Structural Dynamics. 29, 683-691.

Power, M., Rosidi, D., Kaneshiro, J., 1998. Seismic vulnerability of tunnels and underground structure revisited. Paper presented at the North American Tunneling 98, California, USA.

Pinkaew, T., Fujino, Y., 2001. Effectiveness of semi-active tuned mass damper under harmonic excitation. Engineering Structures. 23, 850-856.

Robinson, W., Tucker, A., 1977. A lead-Rubber Shear Damper. Bulletin of the New Zealand National Society for Earthquake Engineering. 10, 151-153.

Sabelli, R., Mahin, S., Chang, C., 2003. Seismic demands on steel braced frame building with buckling-restrained braces. Engineering Structures. 25, 655-666.

Samata, S., Ohuchi, H., Matsuda, T., 1997. A Study of the Damage of Subway Structures during the 1995 Hanshin-Awaji Earthquake. Cement and Concrete Composites. 19, 223-239.

Skinner, R., Tyler, R., Heine, A., et al., 1980. Hysteretic Dampers for the Protection of Structures from Earthquake. Bulletin of the New Zealand National Society for Earthquake Engineering. 13, 22-36.

Spencer, B., Soong, T., 1999. New Application and Development of Active, Semi-active and Hybrid Control Technology for Seismic and Non-seismic vibration in the USA. Paper presented at the International Post-SMiRT Conference Seminar on Seismic Isolation, Cheju, Korea.

Sun, F., Li, G., Guo, X., et al., 2011. Development of New-Type Buckling-Restrained Braces and Their Application in Aseismic Steel Frameworks. Advances in Structural Engineering. 14, 717-730.

Suzuki, N., Kono, R., Higasibata, Y., et al., 1994. Experimental study on H-section steel brace encased in RC or steel tube. Summaries of Technical Papers of Annual Meeting of Architectural Institute of Japan (Structural Engineering Section C-II). 1994, 1621-1622. (in Japanese)

Taylor, P., Ibrahim, H., Yang, D., 2005. Seismic retrofit of George Massey tunnel. Earthquake Engineering and Structural Dynamics. 34, 519-542.

Tsai, C., 1993. Innovative design of viscoelastic dampers for seismic mitigation. Nuclear Engineering and Design. 139, 165-182.

Van Oorsouw, R. S., 2010. Behavior of segment joints in immersed tunnels under seismic loading. Master thesis, Delft University of Technology, Delft, Netherlands.

Vrettos, C., Kolias, B., Panagiotakos, T., 2007. Seismic Response Analysis of an Immersed Tunnel Using Imposed Deformations. In Proceedings of the 4th International Conference on Earthquake Geotechnical Engineering, Thessaloniki, Greece. Paper No.: 1473.

Wakabayashi, M., Nakamura, T., Katagihara, A., et al., 1976. Experimental study on the elasto-plastic behavior of braces enclosed by precast concrete panels under horizontal cyclic loading Part I and II. Summaries of Technical Papers of Annual Meeting of Architectural Institute of Japan (Kinki Branch). 13, 121-128. (in Japanese)

Wang, M., Cui, G., 2010. Establishment of tunnel damping model and research on damping effect with model test in highly seismic area. Rock and Soil Mechanics. 31, 1884-1890.

Xiao, W., Yu, H., Yuan, Y., et al., 2015. Compression-bending behavior of a scaled immersion join. Tunnelling and Underground Space Technology. 49, 426-437.

Xie, Q., 2005. State of the art of buckling-restrained braces in Asia. Journal of Constructional Steel Research. 61, 727-748.

Yan, S., Pan, C., 2006. Seismic response analyses of an immersed tube tunnel. Modern Tunnelling Technology. 43, 15-21. (in Chinese)

Yoshino, T., Karino, Y., 1971. Experimental study on shear wall with braces: Part 2. Summaries of Technical Papers of Annual Meeting of Architectural Institute of Japan (Structural Engineering Section). 46, 403-404. (in Japanese)

Yu, H., Chen, J., Bobet, A., et al., 2016. Damage observation and assessment of the Longxi tunnel during the Wenchuan earthquake. Tunnelling and Underground Space Technology. 54, 102-116.

Yu, H., Yuan, Y., Xu, G., et al., 2012. Issues on the Seismic Design and Analysis of Ultra-long Immersed Tunnel. Journal of Shanghai Jiaotong University. 46, 94-98. (in Chinese)

Yu, H., Yuan, Y., Xu, G., et al., 2016. Multi-point shaking table test for long tunnels subjected to non-uniform seismic loadings-part II: Application to the HZM immersed tunnel. Soil Dynamics and Earthquake Engineering. In Press.

Yuan, Y., Chen, Z., 2014. Earthquake resistance and safety for urban underground space. Tongji Press, Shanghai. (in Chinese)

Yuan, Y., Yu, H., Li, C., et al., 2016. Multi-point shaking table test for long tunnels subjected to non-uniform seismic loadings-part I: Theory and validation. Soil Dynamics and Earthquake Engineering. In Press.

Zhang, H., Zhang, L., 2017. Tuned mass damper system of high-rise intake tower optimized by improved harmony search algorithm. Engineering Structures. 138, 270-282.

Zsarnoczai, A., 2013. Buckling Restrained Braced Frame Design Procedure Evaluation Through Experimental and Numerical Analyses [Format: web pages]. < http://doktori.bme.hu/bme_palyazat/2013/honlap/Zsarnoczai_Adam_en.htm >.

CHAPTER IV

EXPERIMENTAL DESIGN

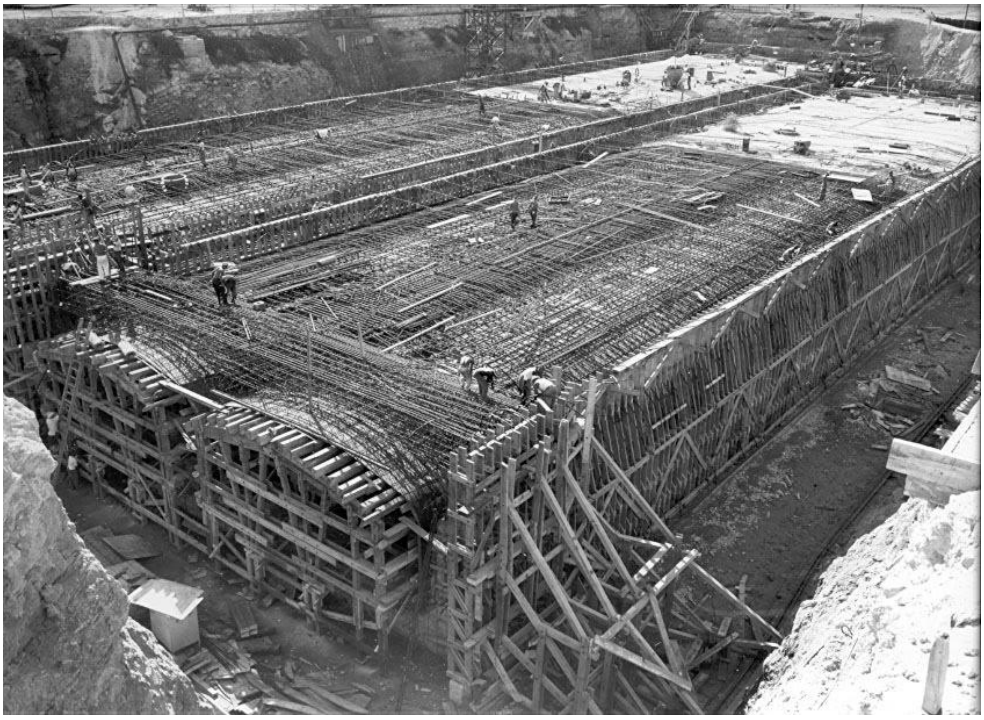

Havana immersed tunnel, Cuba

(source unknown)

IV. Experimental Design

IV.1. General introduction

In order to investigate the mechanical behavior of the whole immersion joint in more detail, a series of experiments involving three main loading tests on large-scale specimens are described in the present chapter. The experiments are conducted at a large scale on two immersion joints with steel shear keys and concrete shear keys respectively. The basic aim was to profoundly study and understand how the joint behaves under different loading situations. For all tested specimens, special attention was paid to the shear behavior of the joint and its influence on the shear resistance and failure mode of the two types of shear keys.

First of all, a justification of the experimental investigation is given in Section IV.2, explaining in detail why this particular test configuration was selected and what geometric scale of the experiment was chosen. In the next section, the detailed design of the model immersion joint is given by introducing the selected materials, the design of the tunnel element and the immersion joint. Accordingly, the test set-up in the laboratory is explained in Section IV.4, providing information about the designs based on different loading situations. Furthermore, the arrangement for measurement and the different loading protocols are presented in Section IV.5 and IV.6 respectively.

IV.2. Justification of the experimental investigation

When an immersed tunnel is subjected to various types of loading, such as earthquake, differential settlement or an accident event, the whole tunnel deforms to accommodate with the surrounding ground. Due to the smaller stiffness of the immersion joint, most of the deformations are taken by the joint rather than the tunnel element. The deformation can result in a high risk of water leakage through the joint, increasing the maintenance cost. As such, the behavior of the joint subjected to different loadings is of major importance for design.

Especially in case of extreme loading situations the risk of a structural failure increases and can result in permanent and irreparable damage to the joint, which will be demonstrated further on in the following chapters.

As mentioned in Chapter II, until now, a limited number of large-scale experiments have been performed to investigate the mechanical behavior of immersion joints. Particularly the axial and flexural performance of the joint requires more profound research. Specifically, the shear behavior of the joint was never examined before and it is a necessity to conduct such experiments. Furthermore, as these large-scale experiments are highly time-consuming and expensive, the design procedure for the geometric scale, the specimen and the test set-up is of crucial importance and requires a rigorous discussion.

As the objective of the experiment is to investigate the mechanical behavior of the joint subjected to different loading conditions, three main loading cases, namely axial, flexural and shear loading respectively, are considered. Based on that, an experimental program has been elaborated focusing on the behavior under these three loadings and the failure mode of the joint under shear loading is also considered.

A pure shear force is usually difficult to be imposed and may be associated with a bending moment acting on the joint at the same time. The existence of such bending moment could not be eliminated as the pure shear force is impossible to achieve in the experiment. In view of the real situation, such bending moment is confined within a relative small range.

Regarding the bending and shear loading cases, there are two types, i.e. a horizontal and a vertical one. However, only the horizontal bending and shear loadings are considered in this experiment. First, the execution of the vertical loading system would require a much more complicated test set-up. Moreover, the horizontal loading and vertical loading are essentially similar. Taking the bending moment as an example, Figure IV.1 shows the schematic of the horizontal and vertical bending in the joint. The difference between these two types of bending is only that the horizontal bending has a larger lever arm due to the rectangular cross section of the joint. Furthermore, the vertical bending and shear loadings involve the gravity forces,

adding complexity in data analysis afterwards. Therefore, only the horizontal behavior of the joint was considered.

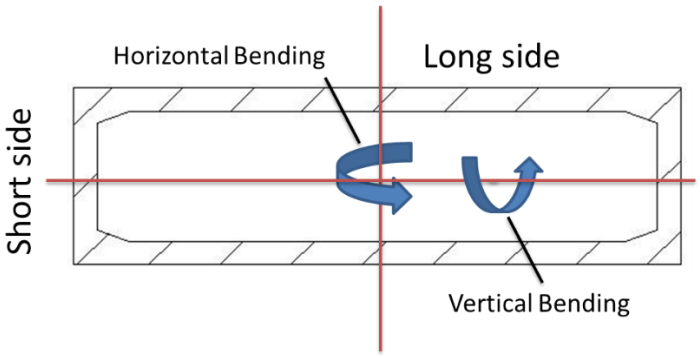

Figure IV.1 Horizontal and vertical bending

Another important concern of the experiments is the selection of the geometric scale due to the fact that the full scale test is impossible to perform. Too large scale may result in over capacity of the loading cell and the reaction wall while too small scale may lead to difficulty in manufacturing the shear keys and the primary rubber, hardly reflecting the actual structural characteristics. Hence, a profound discussion has been made and comparisons between different geometric scales in consideration of various factors are shown in Table IV.1. When the geometric scale is relatively large, for instant 1:1, the extremely high cost, which is approximately 464 million Euros, is unacceptable. Even when the geometric scale changes to 1:5, the cost is still high though the specimen can reflect the actual structural characteristics properly. On the contrary, if the geometric scale decreases to 1:20, it becomes more difficult to manufacture the shear keys due its small size though the cost is lower and the loading capacity is easier to achieve. As the geometric scale is as small as 1:25, the situation becomes even worse in manufacturing. Therefore, given the balance of different influencing factors, a geometric scale of 1:10 was chosen in this experiment. Then the dimension ratio C_l of the model (l_m) to the prototype (l_p) is 1:10. In consideration of the size of the specimen, the same material as the actual design is adopted to simulate the actual situation properly. The similarity ratio of strain, modulus and stress in this experiment can be determined by the following equations.

Table IV.1 Comparison between different geometric scales

Geometric Scale	Max. Axial Loading Required (Shear) [t]	Size of Tunnel Element (Height x Width) [m]	Size of Shear Key (Height x Width) / Rubber (Height)[cm]	Expected Compression of the Joint [mm]	Estimated Cost for Test [x 1,000 €]	Advantages	Disadvantage
1:1	23000 (3200)	11.4 x 38	110.8 x 75 / 37.5	150-200	464,000	Exactly the same with actual design	Extremely high cost; Oversize dimension; Impossible for loading;
1:5	920 (128)	2.3 x 7.6	22.2 x 15 / 7.5	30-40	150	Can reflect the structural characteristics; Easy measurement;	High cost; Requires high capacity of loading cell but possible;
1:10	230 (32)	1.14 x 3.8	11.1 x 7.5 / 3.75	15-20	44	Possibly achievable in loading; Basically reflects structural characteristics;	Simplification is required in some components;
1:20	60 (8)	0.57 x 1.9	5.5 x 3.8 / 1.88	7-10	21	Low cost; Easily achieved in loading; Small scale;	Too small for the shear keys and the rubber;
1:25	37 (5)	0.1 x 0.3	0.9 x 0.6 / 1.5	6-8	11	Very low cost; Low requirement for facility;	Impossible to manufacture the shear key and the rubber seal;

Strain:

$$\begin{cases} \frac{\varepsilon_m}{\varepsilon_p} = 1 \\ \frac{\gamma_m}{\gamma_p} = 1 \end{cases} \quad \text{(IV.1)}$$

Modulus:

$$\begin{cases} \frac{E_m}{E_p} = 1 \\ \frac{G_m}{G_p} = 1 \end{cases} \quad \text{(IV.2)}$$

Stress:

$$\begin{cases} \frac{\sigma_m}{\sigma_p} = 1 \\ \frac{\tau_m}{\tau_p} = 1 \end{cases} \quad \text{(IV.3)}$$

where ε_m, γ_m, E_m, G_m, σ_m, τ_m represent the strain, shear strain, elastic modulus, shear modulus, stress and shear stress of the model respectively; ε_p, γ_p, E_p, G_p, σ_p, τ_p represent the strain, shear strain, elastic modulus, shear modulus, stress and shear stress of the prototype respectively.

Based on that, the similarity ratio of other physical parameters can be determined as shown in Table IV.2. (Note: Subscript m and p stand for 'model' and 'prototype' respectively)

Table IV.2 Similarity ratio of other physical parameters

Physical Parameter	Similarities
Area	$\frac{A_m}{A_p} = \left(\frac{l_m}{l_p}\right)^2 = (C_l)^2 = 1/100$
Diameter of the reinforcement	$\frac{D_m}{D_p} = C_l = 1/10$
Reinforcement ratio	$\frac{r_m}{r_p} = 1$
Force	$\frac{F_m}{F_p} = \frac{\sigma_m A_m}{\sigma_p A_p} = 1/100$
Bending moment	$\frac{M_m}{M_p} = \frac{F_m l_m}{F_p l_p} = 1/1000$

IV.3. Model immersion joint

In total, there are two sets of tunnel elements and each set consists of two single elements. Moreover, there are 2 sets of GINA rubber seal and one set of steel and concrete shear keys respectively. All the experimental specimens are listed in Table IV.3. It should be noted that all the experiments are executed in the order as shown and some of the specimens were tested more than once.

Table IV.3 Specimens in the experiment

Order	Loading	Tunnel element	Shear keys	Rubber
1	Compression/Bending	Set-1	-	GINA-1
2	Compression-shear	Set-1	Steel shear keys	GINA-1
3	Seismic mitigation	Set-2	-	GINA-2
4	Compression-shear	Set-2	Concrete shear keys	GINA-2

IV.3.1. Material properties

The same materials as for the prototype are used in this experiment. The material properties based on the Chinese Code, Code for design of concrete structure (GB 50010-2010) and Code for design of steel structure (GB 50017-2003), are listed in Table IV.4.

Table IV.4 Material properties

Material	Design Value of Compressive Strength [MPa]	Design Value of Tensile Strength [MPa]	Design Value of Shear Strength [MPa]
C50 Concrete	23.1	1.89	-
HRB 400 Reinforcement	360	360	-
Q345 Steel	310	310	180
C4.8 Bolt	-	170	140

IV.3.2. Model tunnel element

To form an immersion joint, two model tunnel elements are required and the detailed design is based on an actual project. Figure IV.2 presents the prototype of the tunnel element in the actual project. The cross-section is 37.95m in width and 11.40m in height with chamfered upper corners and an average thickness of 1.55m. There are two middle walls inside the tunnel, forming two separate traffic bores and one middle gallery. The primary rubber seal is installed on the steel shell around the external perimeter of the joint, acting as the permanent water-tightness proof.

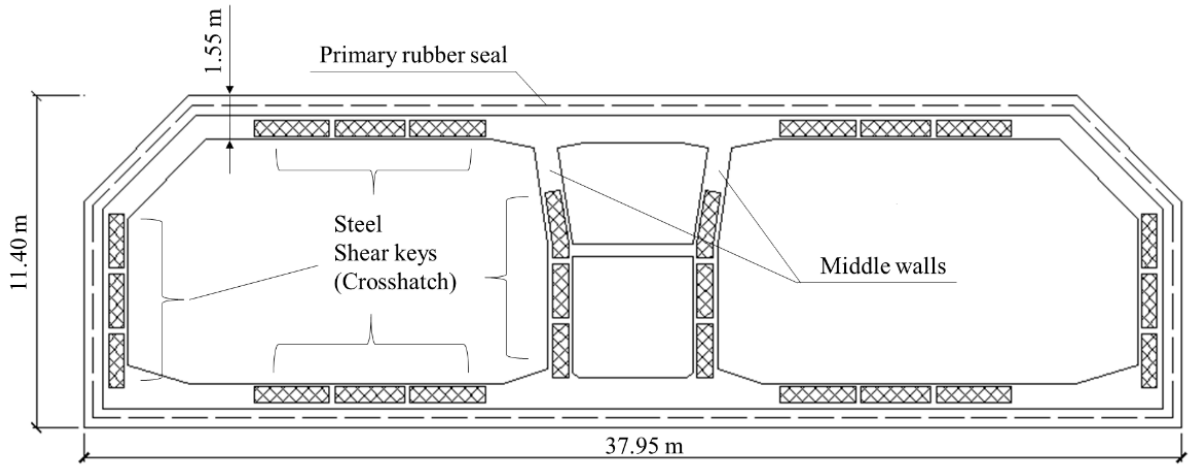

Figure IV.2 Prototype of the tunnel element

As mentioned, only the horizontal behavior of the immersion joint is taken into account. Therefore, some simplifications have been made with limited influence on the results: 1) as the shaped corners in passages and middle walls contribute insignificantly to compression or bending of the joint, the cross-sectional profile of the model element was simplified as rectangular; 2) the middle walls were not considered neither for the same reason; 3) only half the length of a tunnel element is selected as the attention is only paid to the joint; 4) the value of the dimension is a plural of 10mm for convenience of manufacturing. Based on these simplifications and the adopted geometric scale, the dimensions of a single model tunnel element with a width of 3800mm, a height of 1150mm, and a length of 1250mm, are provided in Figure IV.3. The thickness of the walls and the slabs is 150mm. There are two tunnel elements, Element A and Element B, as indicated. It should be noted that two types of shear keys are applied, resulting in two types of the immersion joint. However, the basic design of the tunnel element is the same. Figure IV.4 shows the photos of the model tunnel element.

The reinforcement arrangement follows the actual design and the dimensions are scaled down based on the geometric scale. The adopted volume reinforcement ratio is 2.073%. The strength of the element is verified based on the Chinese Code for design of concrete structure (GB 50010-2010) and further details are not provided here.

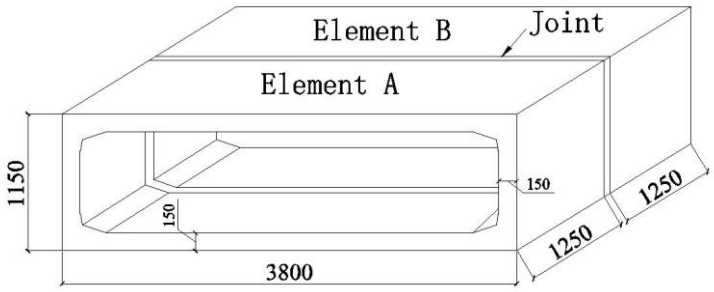

Figure IV.3 Model tunnel element

(a)Reinforcement of the element

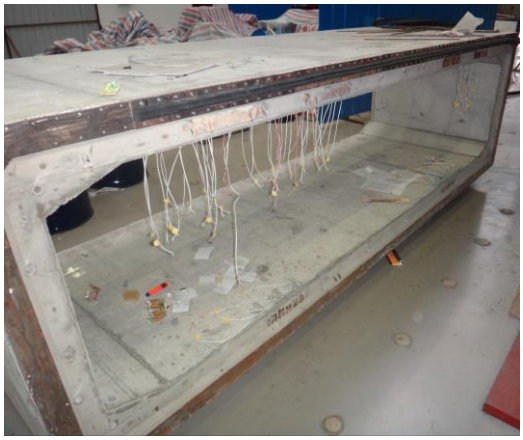

(b)Element after casting and installation

Figure IV.4 Photos of the model tunnel element

IV.3.3. Model immersion joint

The model immersion joint also follows the actual design (shown in Figure IV.5). Normally, a joint includes a primary rubber seal, a secondary rubber seal, shear keys and a steel shell. In this experiment, the secondary rubber seal and the steel shell are not adopted due to the negligible contribution to the mechanical behavior of the joint. The detailed design of the joint, namely the primary rubber seal, the steel shear keys and the concrete shear keys, are provided as follows.

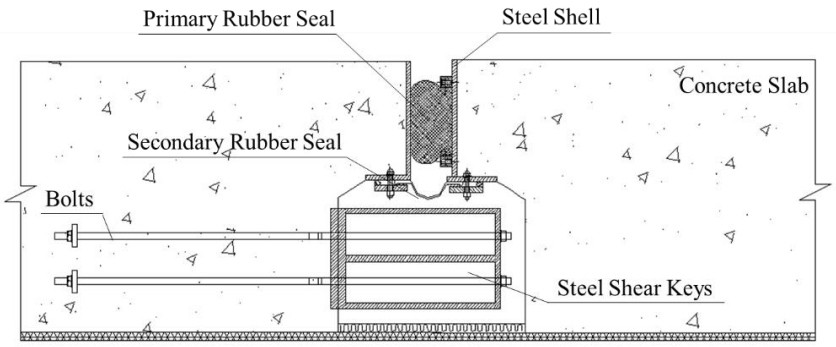

Figure IV.5 The prototype of the immersion joint

(1) Model primary rubber seal

In the prototype, there are four types of GINA rubber seal with different hardness and they are applied to different immersion joints, depending on the water depth. In this test, only one type of the GINA rubber with the hardness ranging from 55-60 shore A is used due to the limitation of the test. The model rubber seal is designed based on the geometric scale of 1:10, which means the shape of the model rubber is the same as that of the prototype and the model rubber is manufactured especially for this experiment. Although there are two types immersion joints, the same rubber seal is applied. As can be seen in Figure IV.6 (a), the GINA profile is used in this test, with a height of 37.5mm and a width of 70mm (including the flange). The total length of the GINA rubber in this experiment is 9.67m. Also the photo of the rubber seal is displayed in Figure IV.6 (b), and the physical parameters of the used rubber seal are listed in Table IV.5. Figure IV.6 (c) shows the comparison of the target load–compression curve and the curve from the model rubber seal, which are provided by the producer and own tests respectively. It should be noted that the model GINA rubber in the own tests is only 20cm long and without any restraint. The two curves basically follow the same trend. At 2500kN, the maximum compression for these two curves are 19.0 mm and 20.4 mm respectively and there is only 7% difference between them. Therefore, the model rubber seal can be considered to be representative for the actual rubber under compression.

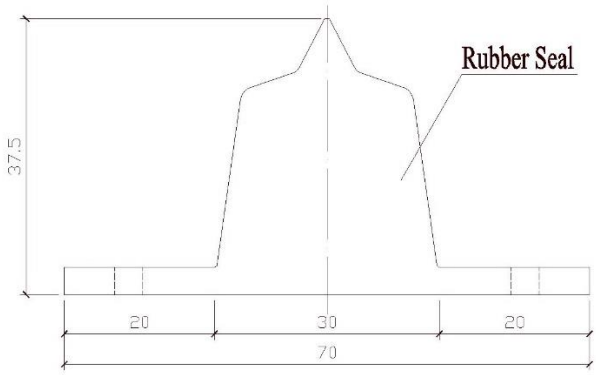

(a) Dimensions of the model rubber seal [mm]

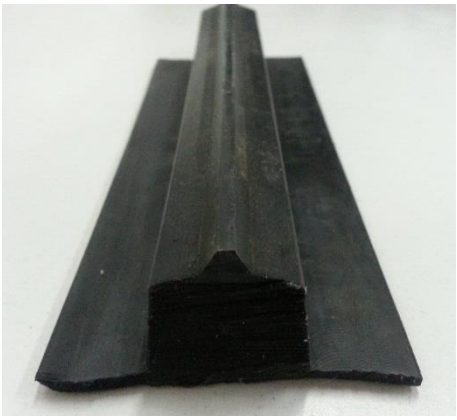

(b) Profile of model rubber seal

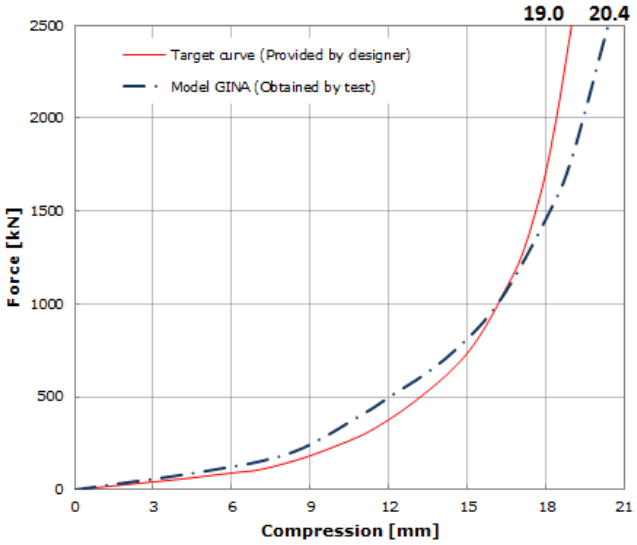

(c) Comparison of the target load–compression curve and the curve from model rubber seal

Figure IV.6 Model rubber seal in the immersion joint

In order to fix the rubber seal on the tunnel element, a special clamping equipment is required. The most common clamping system in engineering practice is shown in Figure IV.7. In this clamping system, the flange of the rubber is clamped by a steel strip, which is fixed to the steel shell through bolts or studs. In this way the rubber seal remains intact. However, due to the short flange, the rubber has a possibility of falling off when it is subjected to a concentrated force. In this experiment, as the geometric scale is 1:10, the flange of the rubber becomes too short to be clamped by this system. Hence, another clamping system as shown in Figure IV.8 (a) is needed. As shown, the flange of the rubber is extended, allowing the rubber to be clamped by the bolt in a way that the

bolt goes through the flange and is fixed on the steel shell. The GINA rubber after installation is shown in Figure IV.8 (b).

Table IV.5 Mechanical characteristics of the model rubber seal (provided by producer)

Characteristic	Value
Hardness	55-60 Shore A
Breaking Tenacity	14 MPa
Extensibility	>450%
Allowance Compressive Strength	10 MPa
Shear Modulus	0.97-1.47 MPa
Friction Coefficient	Steel:0.2; Concrete:0.3

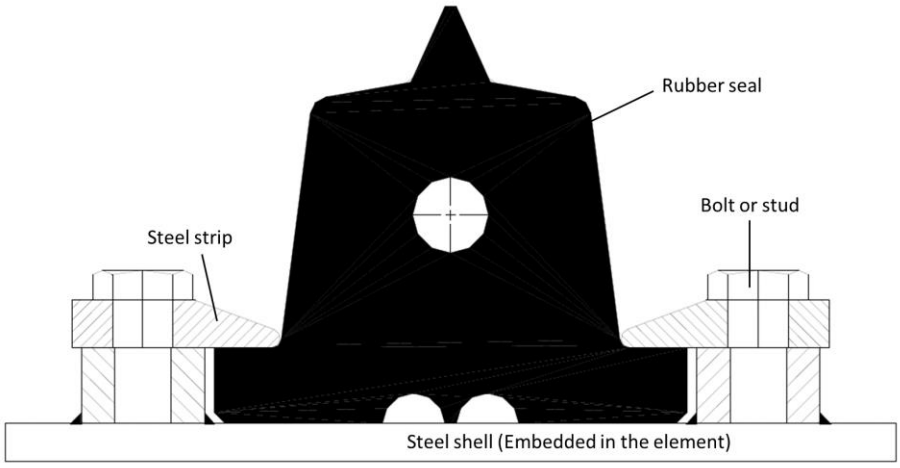

Figure IV.7 Normal clamping system in engineering practice (Trelleborg AB, 2017)

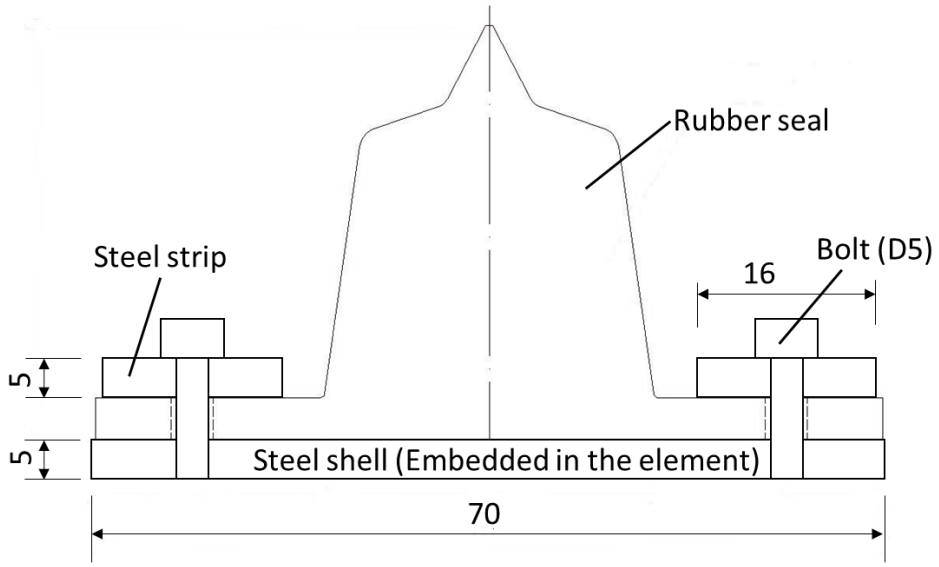

(a) The clamping system in this experiment [mm]

(b) Detailed view of model rubber seal after installation

Figure IV.8 The GINA rubber in this experiment

(2) Concrete shear keys

In actual design, the horizontal concrete shear keys are placed only on the bottom slab, being a part of the pavement, as shown in Figure IV.9. The concrete shear keys are fabricated and cast after the immersion of the joint. Therefore, the quality and the construction accuracy can be guaranteed. A detailed view of the joint with the concrete shear keys is given in Figure IV.10. The corbel behind the shear keys and the embedded steel bars are used to ensure the connection between the keys and the element.

In this experiment, the model concrete shear keys basically follow the actual design and some factors are eliminated as these parts make no contribution to the test, such as the pavement. Also the corbel is not considered and the embedded steel is replaced by the vertical reinforcement as the model shear keys are cast together with the tunnel element, providing a stronger connection between them. To provide the shear resistance in both directions, there are two types of shear keys in one group, namely HSK1 and HSK2, with three and two tenons respectively, and there are two groups of shear keys in the joint in total. Figure IV.11 presents the dimensions and position of the model concrete shear keys after scaling down. As can be seen, the dimensions of HSK1 are 1108mm x 148mm x 75mm while the ones of HSK2 are 1108mm x 180mm x 75mm. It should be noted that the original gap between the shear keys in the prototype is 20mm. Based on the geometric scale of 1:10, it should be 2mm. However, such value requires a too high construction accuracy and difficult to achieve. Hence, a gap of 5mm, 2.5 times as 2mm, is adopted.

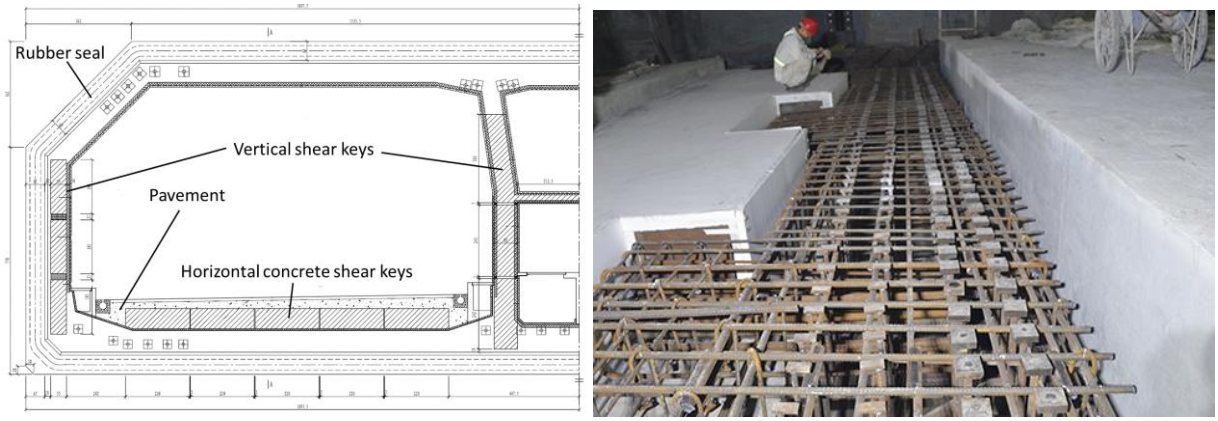

Figure IV.9 The prototype joint with concrete shear keys

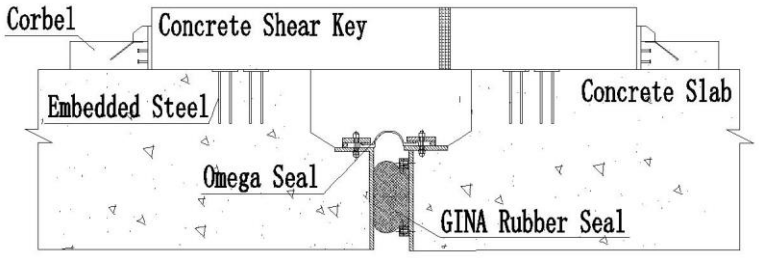

Figure IV.10 Detailed view of the prototype joint with concrete shear keys

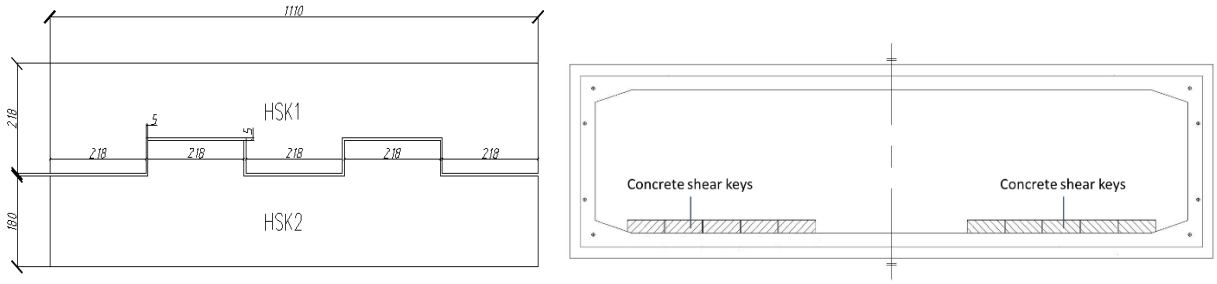

Figure IV.11 Dimensions and positions of the model concrete shear keys

Due to the geometric scale, the reinforcement in the model follows the same reinforcement ratio as the prototype. After scaling down, the configuration of the concrete shear keys were obtained and hence, the shear capacity can be calculated. According to the Chinese Code for design of concrete structure (GB 50010-2010), the longitudinal reinforcement in the tenon of the shear key determines the capacity of the shear key subjected to a shear force. Figure IV.12 shows a shear force F_v acting on a tenon. The longitudinal reinforcement on top of the tenon is assumed to resist the shear force and the tensile strength of the concrete around it is ignored. A static equilibrium equation around point 0 can be determined and then the maximum shear resistance can be calculated by the following equation.

$$F_v \leq \frac{0.85 A_s f_y h_0}{a_0} \tag{IV.4}$$

where A_s is the total area of the longitudinal reinforcement, which is determined according to the geometric scale; F_v represents the shear force acting on the tenon; a_0 and h_0 represents the lever arm of the shear force and the reinforcement respectively; f_y is the design value of the tensile strength of reinforcement.

Another concern for the concrete shear key is the cracking control. According to the Chinese Code, the cracking load F_{vk} for a tenon can be calculated by the following equation.

$$F_{vk} \leq 0.8 \frac{f_{tk} b h_0}{0.5 + \frac{a_0}{h_0}} \tag{IV.5}$$

where F_{vk} represents the cracking force acting on the tenon; a_0 and h_0 have the same meaning as above; f_{tk} is the characteristic value of the tensile strength of concrete; b is the width of a tenon.

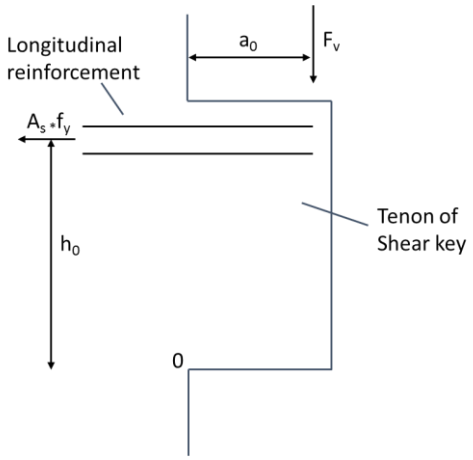

Figure IV.12 One tenon of the shear key

Based on the above equations, the cracking force and the shear capacity of a tenon are 42kN and 70kN respectively. As it is assumed that there are four tenons in two groups of shear keys working at the same time, the cracking force and the shear capacity of the complete joint are 168kN and 280kN respectively.

The detailed reinforcement arrangement of the shear keys is shown in Figure IV.13. Two reinforcement bars with a diameter of 8mm are used as longitudinal reinforcement to provide the resistance against the shear force. The ϕ8 reinforcement bars are used as vertical reinforcement and transversal reinforcement. The stirrups, which are not shown in the figure, have a bar diameter of 6 mm. In this way, the design of the concrete keys conforms to the Chinese design code.

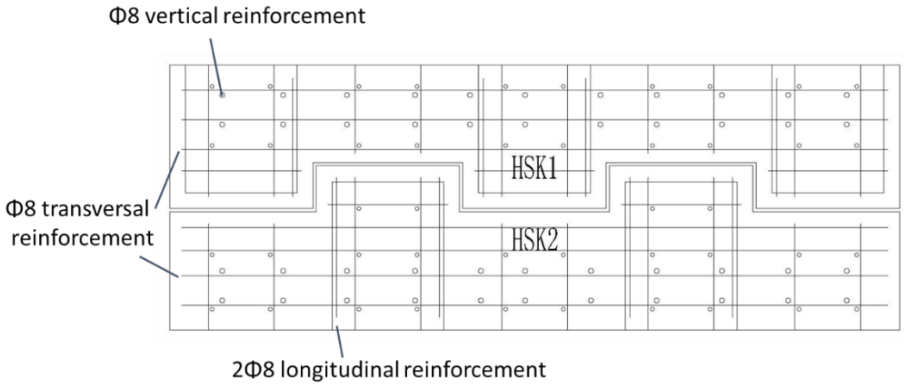

(a) Plan view of the reinforcement arrangement

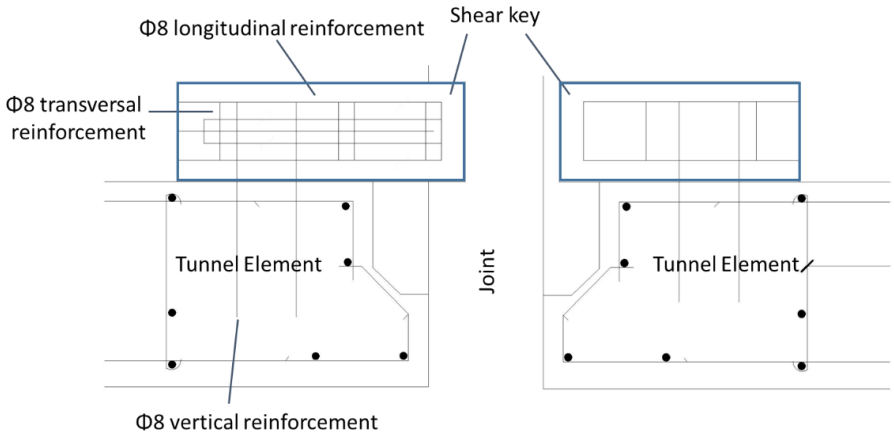

(b) Lateral view of the reinforcement arrangement

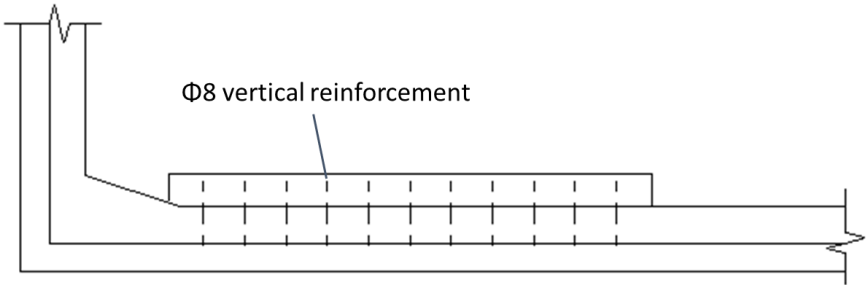

(c) Layout of the vertical reinforcement

Figure IV.13 Reinforcement arrangement of the model concrete shear keys

(3) Steel shear keys

In the actual design of the HZM immersed tunnel, the horizontal steel shear keys were adopted in preliminary design stage but finally replaced by concrete shear keys due to the complicated installation work for the steel shear keys. However, the experiments carried out regardless of this situation. As shown in Figure IV.14, the single prototype steel shear keys are box sections mounted on an embedded plate secured to the end the concrete tunnel element by studs ad steel bars. The steel box is a hollow box strengthened with stiffening ribs inside. The box-type steel shear keys are connected to the embedded plate by bolts going through the steel box. The dimensions of the steel box are 2400mm x 760mm x 550mm. The diameter of the bolts ranges between 56mm and 64mm, depending on the position.

To provide the shear resistance in horizontal direction, a three-part shear key is required in the joint. There are two types of shear keys, HSK1 and HSK2 respectively. One single shear key (HSK1) is fixed to one tunnel element and the other two shear keys (HSK2) to the other element. The two types of shear keys are staggered in the different elements, making that HSK1s are loaded in two directions while HSK2s are loaded in only one direction. By the prototype design shown in Figure IV.14, the possible failure modes for a single shear key could be 1) the failure of the shear box; 2) the failure of the bolts; and 3) the failure of the embedded plate or surrounding concrete. As for design, the shear box and the embedded plate are normally strong enough and the bolts are expected to fail.

In this experiment, the model steel shear keys basically follow the prototype design: 1) There are two types of model shear keys with staggered installation as shown in Figure IV.15 (a); 2) The dimensions of the shear box are scaled down by 1/10 and the shape of the shear box is the same as the actual one; 3) The number and diameter of the bolts in the model are also reduced due to the geometric scale; 4) The same clamping system of the steel box is applied by using the bolts.

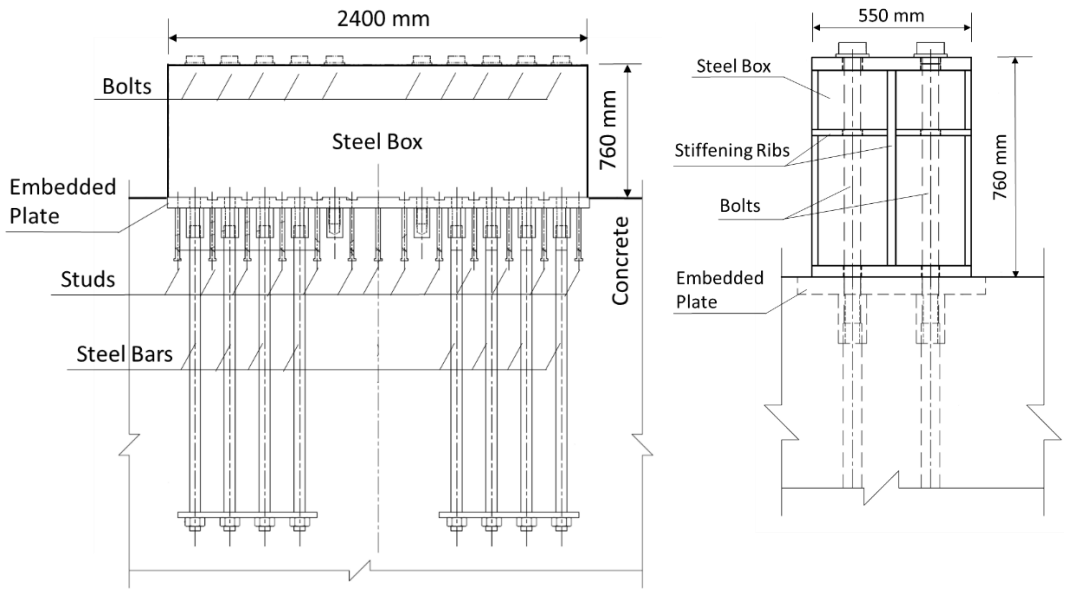

Figure IV.14 A single prototype steel shear key

For the model shear key, the bolts are also expected to fail during the experiment. Moreover, a bending moment may occur in the shear key when it is subjected to a shear force. However, the lever arm is very small (around 0.06m), only introducing a small tensile force in the bolt. Based on

that, it is assumed that the shear capacity of the shear key is provided by the shear capacity of the bolts and the friction force between the shear box and the tunnel element. Then the shear capacity of one shear key can be approximately calculated by the following equation:

$$R_{sk} = \sum R_b + R_F \tag{IV.6}$$

where R_{sk} and R_b represent the resistances of a shear key and a bolt respectively while R_F represents the friction force between the shear box and the element.

It should be noted that there is no normal force on the shear box nor an extra preload on the bolts, which means that the friction force is small. Moreover, due to the current techniques, the friction force in this test is difficult to measure. Therefore, it is assumed that the friction force can be ignored in the analysis of the test results.

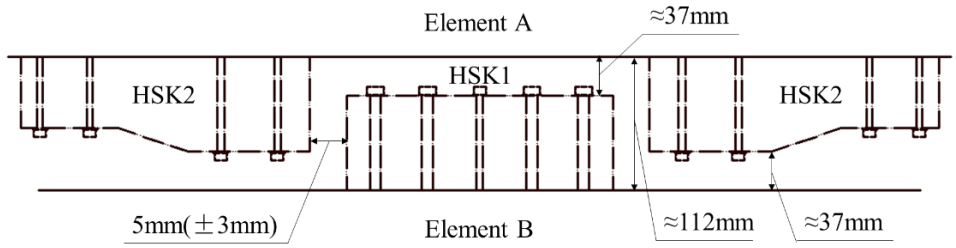

(a) Staggered installation of two types of shear keys

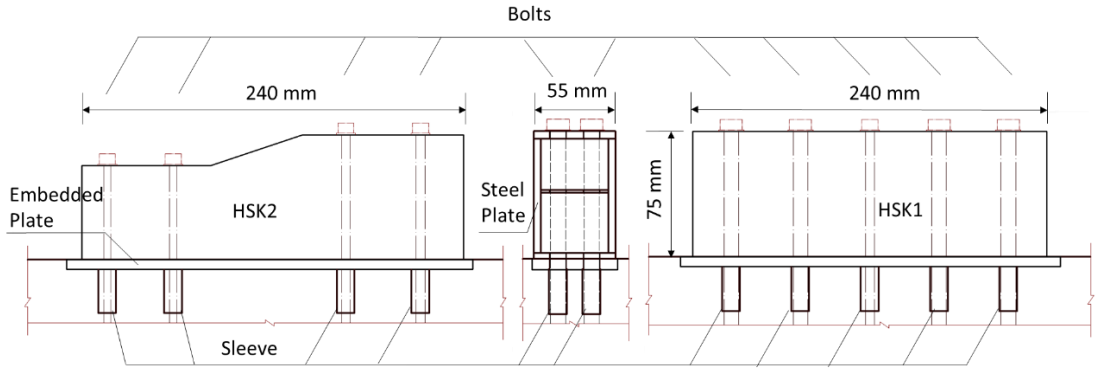

(b) Details of the model shear keys

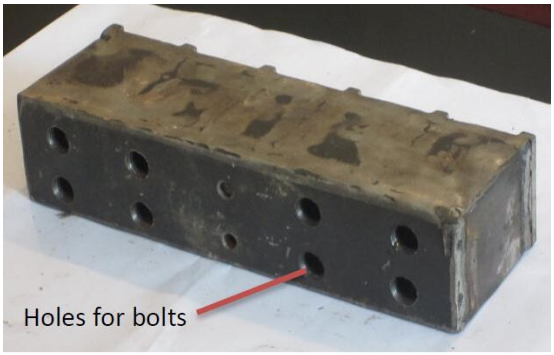

(c) HSK1

(d) HSK2

Figure IV.15 Model steel shear keys

According to the geometric scale, 8 bolts with a diameter of 12 mm and 2 bolts with a diameter of 8 mm are selected for each HSK1 while each HSK2 has 4 bolts with a diameter of 10 mm and 4 bolts with a diameter of 6 mm. The bolts are fixed with a sleeve welded to the embedded plate. The design capacity of one model shear key (HKS2) is calculated as approximately 180kN while the capacity of the complete immersion joint is assumed to be the sum of the shear capacities of the four shear keys, which is 720kN based on the Code for design of steel structure (GB 50017-2003). Moreover, it should be noted that in the test, a gap of around 5 mm (±3 mm) exists and the keys are not activated at the very beginning. Figure IV.15 (c) and (d) shows the photos of HSK1 and HKS2 respectively. It can be seen that the HSK1 has more bolts and a higher capacity than the HSK2. That is because the HSK1 has to resist the shear load from two directions as indicated in Figure IV.15 (a).

For the steel box, it is composed by small steel plates with a thickness of 5mm, connected to each other by welding and the stiffening ribs inside have a thickness of 4mm. The embedded plate, it is already placed on the correct position during the casting of the concrete element. The sleeve with the bolt into the concrete and the reinforcement, shown in Figure IV.16, provides a strong capacity against the shear and tensile force. Figure IV.17 shows the position of the steel shear keys at different places in the joint.

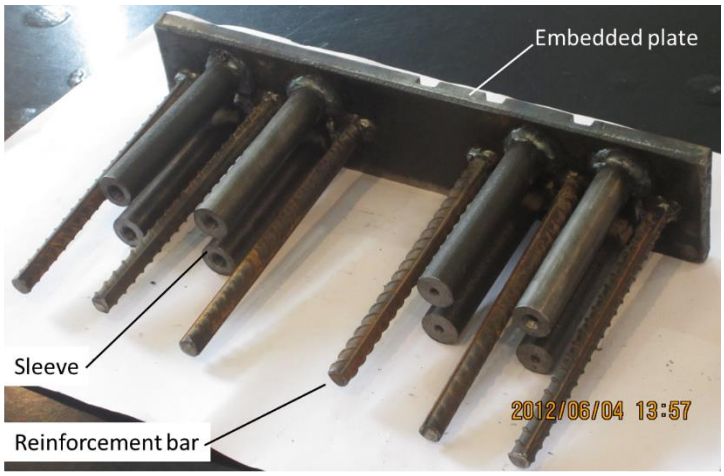

Figure IV.16 Embedded plate for the shear keys

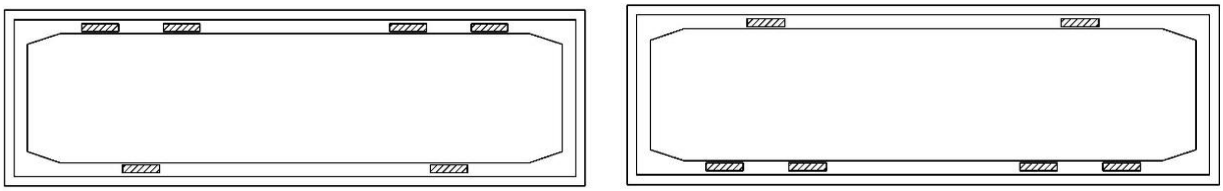

(a) Element A (b) Element B

Figure IV.17 Position of the shear keys in the joint

IV.4. Test set-up

As mentioned, the horizontal axial, bending and shear loading are all considered in this test. The applied test set-up is required to handle deformations from two directions and to provide the corresponding resistance. Therefore, a novel large-scale test set-up was developed allowing the experimental investigation of two tunnel elements exposed to both axial and transversal deformation. Figure IV.18 shows the loading application points (L1-L5) in this experiment. The axial force is applied by the four hydraulic jacks at the end of Element B. The four load application points (L1-L4) are loaded symmetrically in the vertical plane to make sure that the total axial force is exerted centrically. For imposing the cyclic bending moment to the joint, the bending moment can be produced by differentiating the forces of the hydraulic jacks. At each loading stage, keep

one couple of jacks (i.e. L1/L4) continue to load, while the other couple of jacks (correspondingly L2/L3) starts to unload, resulting in a bending moment in the joint. When the expected maximum value in the joint is reached, the two couples of jacks start to work inversely to produce a 'negative' moment in the joint till the maximum value is reached. Then, all the jacks are operated to their original equal forces, which makes the bending moment to return to zero. In this way a bending moment loading cycle is completed. The shear force is provided by one actuator along the area L5 in Figure IV.18, providing an approximate uniform linear shear load to the element. To achieve it, a round steel bar with a diameter of 50mm was placed in the loading connection, which can be seen in Figure IV.19 (d). Although the area L5 is as close as possible to the joint, an expected maximum bending moment of 180 kN·m in the joint is generated.

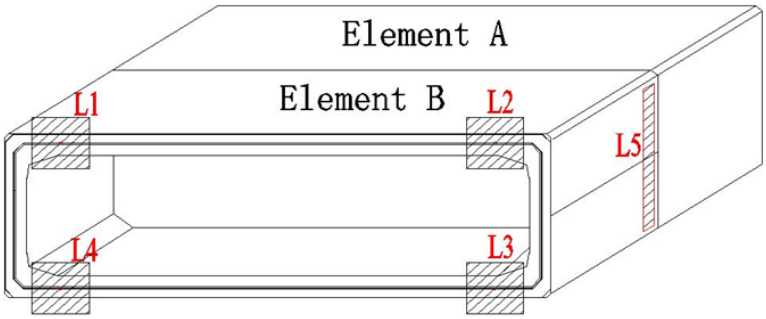

Figure IV.18 Loading application points in the tests

To achieve this, one tunnel element (Element A) is fixed horizontally while the other one (Element B) is movable in two horizontal directions, allowing compression and shear deformations of the immersion joint. As illustrated in Figure IV.19, the tunnel elements are placed on supports resting on a reaction floor, and are kept in position with the loading frames which are installed against an L-shaped reaction wall. Each part of the loading frame is marked in a different color depending on its function. Two horizontal frames (light-blue) provide the axial reaction when the model tunnel is subjected to a compressive force by the 4 hydraulic jacks (dark blue) installed on the reaction wall. There are two vertical frames placed next to the immersion joint. One frame (orange) is used to fix one element of the model tunnel, while the other one (green) provides a reciprocal shear force to the other element. Moreover, to avoid friction between the elements and the reaction floor, several column-supports with a spherical hinge bearing on top (red) are installed before the elements are positioned.

As mentioned, the axial forces are applied to Element B and then transferred to the joint. Figure IV.19(a) demonstrates the 4 loading points (dark blue) for the axial force. Four hydraulic jacks (dark blue) are situated between Element B and the reaction wall. The jacks are controlled synchronically to avoid rotation of Element B. The shear force is applied by an actuator (yellow), connecting to the element with a column and a round steel bar with diameter of 50 mm (Figure IV.19 (d)). There is also a steel plate between the steel bar and the concrete element to avoid stress concentration. The actuator can pull and push the element in this way and hence, the shear force can be reciprocal with varying amplitudes. Photos of the reaction frame during and after installation are shown in Figure IV.20.

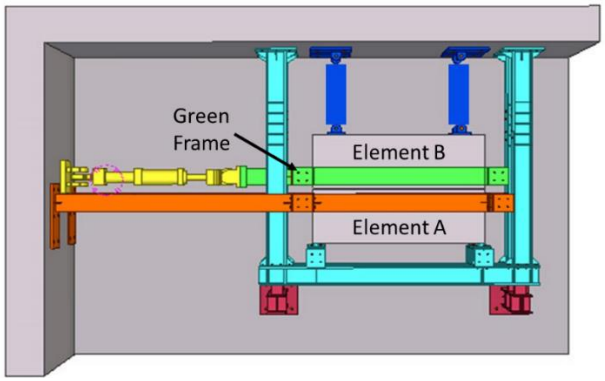

(a) Plan view

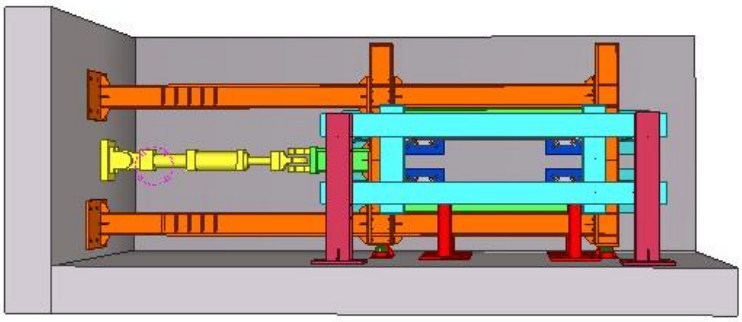

(b) Front view

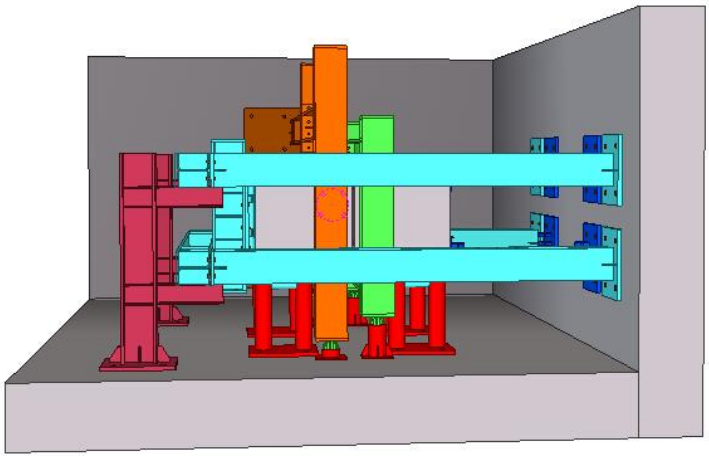

(c) Side view

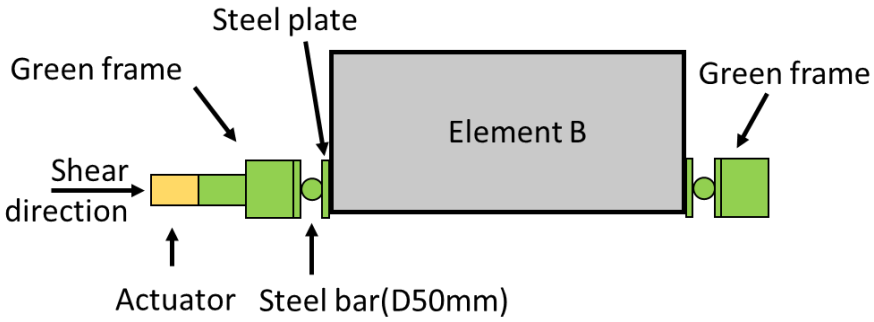

(d) Schematic of the shear loading connection

Figure IV.19 Set-up of testing system

(a) During installation

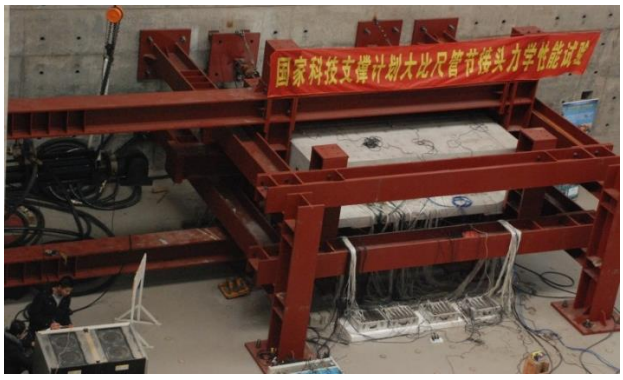

(b) Full view of the experiment after installation

Figure IV.20 Photos of the test set-up

IV.5. Measurements

In order to obtain the mechanical behavior of the joint, the axial and shear deformation are the main concern in this experiment. Therefore, the deformations in these two directions are measured by the installed transducers. For the axial direction, nine transducers (P-1 to P-9 as shown in Figure IV.21) are evenly distributed both along the joint on top of the specimens and inside the tunnel element. From the obtained displacement and the distance between the transducers on top, a simplified determination of the rotation angles could be calculated as well as the distribution of the displacement along the joint. Regarding the shear direction, as presented in Figure IV.22 (a), four transducers (Numbers 1 to 4) are placed near the corners of the cross-section of the joint. The transducers are positioned parallel to the shear force to obtain the relative displacement of the joint along this direction. Also, another 4 transducers (Numbers 5 to 8) are placed perpendicularly to the cross-sectional plane of the joint to measure the axial deformation. All these displacement values are collected by a digital data acquisition system. Furthermore, the input values of the loads are controlled and measured by the computers.

Moreover, in order to observe the shear keys in the joint during the test, video recording cameras are used as displayed in Figure IV.23. The real-time images captured by the cameras are shown on the monitor. The cameras are installed in the joint (Figure IV.23 (b)) and each camera focuses on one group of shear keys. If a shear key fails, it can be noticed on the monitor and then the failure can be recorded. Figure IV.23 (c) shows an example of shear keys captured by a camera.

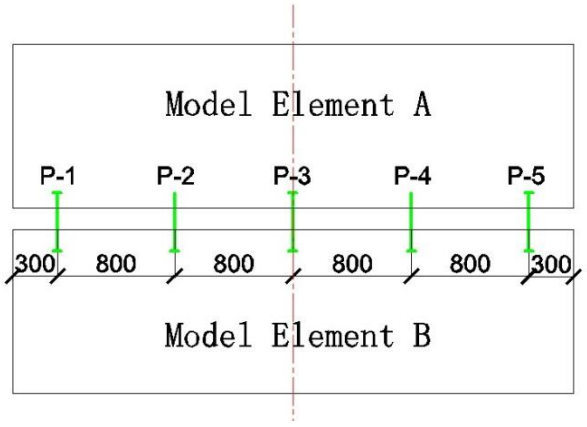

(a) Layout of the transducers

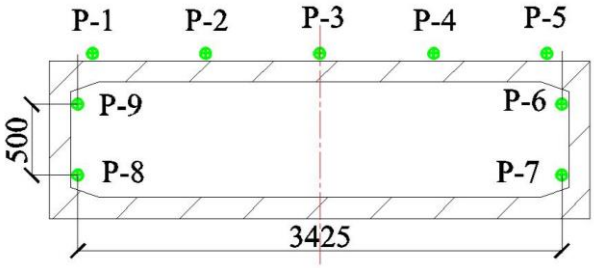

(b) Front view of transducers

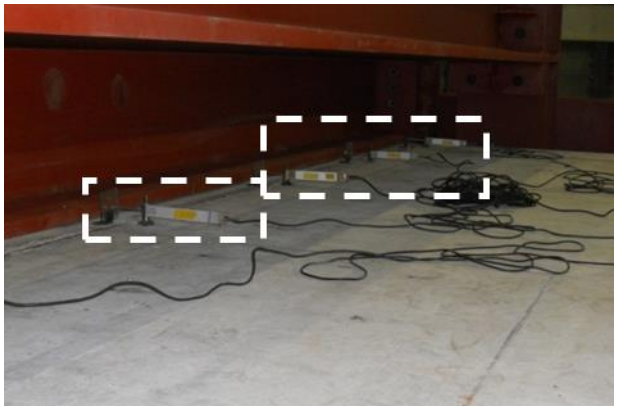

(c) Photos of transducers

Figure IV.21 Five transducers for axial deformation [mm]

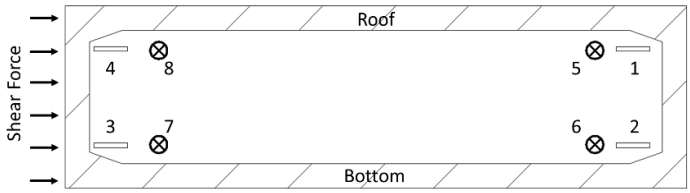

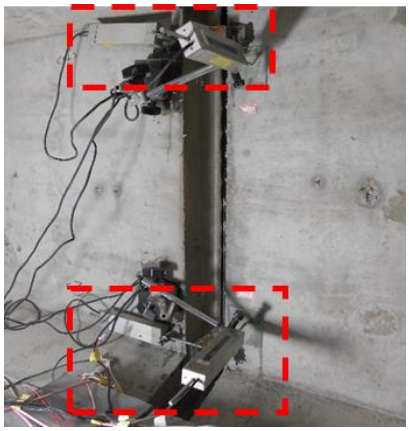

(a) Layout of the transducers

(b) Photos of transducers

Figure IV.22 Transducers for shear deformation

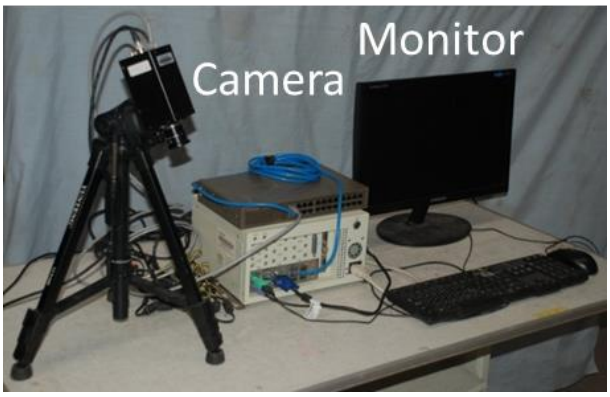

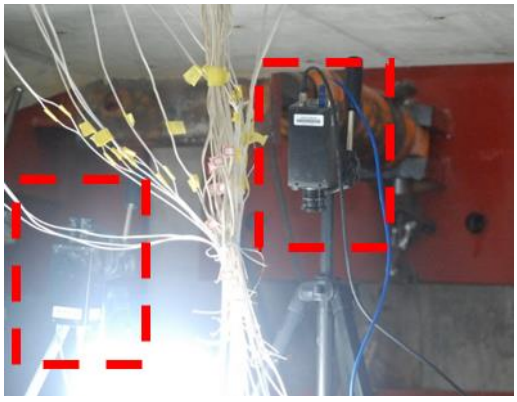

(a) Layout of the system

(b) Cameras in the joint

(c) An example of the photo for one shear key taken by a camera

Figure IV.23 Observation of the shear keys

IV.6. Loading protocols

A loading protocol was developed to investigate the mechanical behavior of an immersion joint in different directions. Three main loading protocols are considered, namely axial loading, compression-bending moment loading and compression-shear loading. It should be noted that the initial compression always exists in the joint due to the specific construction method of immersed tunnels. Hence, the compression always needs to be considered when studying the flexural and shear performance of the joint.

In the following, some more detailed information with regard to the difference between each loading case is provided.

IV.6.1. Axial and bending moment loading application

As immersed tunnel elements will be located at different water depths, the pressure acting on an immersion joint will vary with its location. During seismic movement of the stratum, the horizontal bending might change with the location along the tunnel length. Then a maximum bending moment can be obtained as the input maximum moment in the test. Hence, the loading is set at 5 stages with different axial forces but the same bending moment. The axial loading levels applied to the joint, listed in Table IV.6, account for the typical water pressure such as minimum water pressure and maximum water pressure. It should be noted that the values of the force are scaled down from the prototype based on the geometric scale. The bending moment, with a maximum value of 350 kN·m is applied to the joint when the axial force reaches a given level. This value results from the seismic

analysis (Xu and Yuan, 2013) on the response of an immersed tunnel by imposing the maximum design earthquake (the exceedance probability in 120 years is 10%). The process for applying the bending moment is as follows (Figure IV.24). After the initial unloaded situation, the axial force is increased to each of the predefined levels given in Table 2 (Figure IV.24 (b)). Then by adjusting the force of the jacks, a bending moment is applied to the joint (Figure IV.24 (c)).

Compression loading is applied through 4 hydraulic jacks. Their forces are increased synchronously until the total axial force reaches a target load level, as specified in Table IV.6. After the cyclic bending in the final stage, the jacks are gradually unloaded till the axial force becomes zero. The compression of the joint is measured at each loading/unloading stage, to get the relation between axial force and the compression of the joint.

Table IV.6 Axial and bending moment loading cases

Stages	Total axial force [kN]	Bending moment [kN·m]	Remark
1	500	350	Minimum water pressure (440kN)
2	1000		Final immersion joint (850kN)
3	1500		-
4	2000		Maximum water pressure (1760kN)
5	2500		-

Cyclic bending can be produced by differentiating the forces of the hydraulic jacks. As mentioned, at each loading stage, one couple of jacks (i.e. L1/L4) continue to load while the other couple of jacks (correspondingly L2/L3) starts to unload. A bending moment will result in the joint. When the maximum value (350kN·m) in the joint is reached, the two couples of jacks start to work inversely to produce a ‘negative’ moment in the joint until that all the jacks are operated to their original equal forces, which makes the bending moment to return to zero. In this way a bending moment loading cycle is completed and in total there are five bending moment cycles with five levels of axial forces. The compression of the joint is measured continuously during a loading/unloading cycle, in order to obtain the rotation of the joint as a function of the bending

moment. Figure IV.24 (d) shows the scheme of axial forces and bending moment from each hydraulic jack.

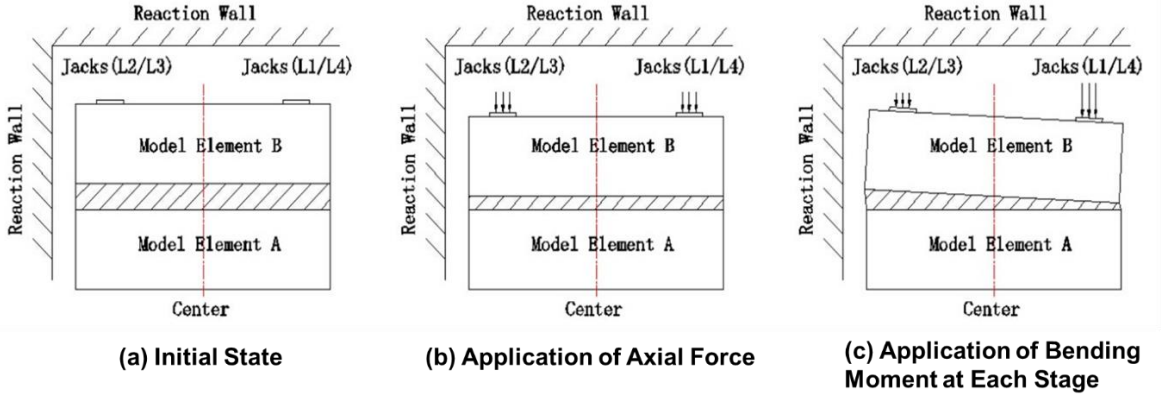

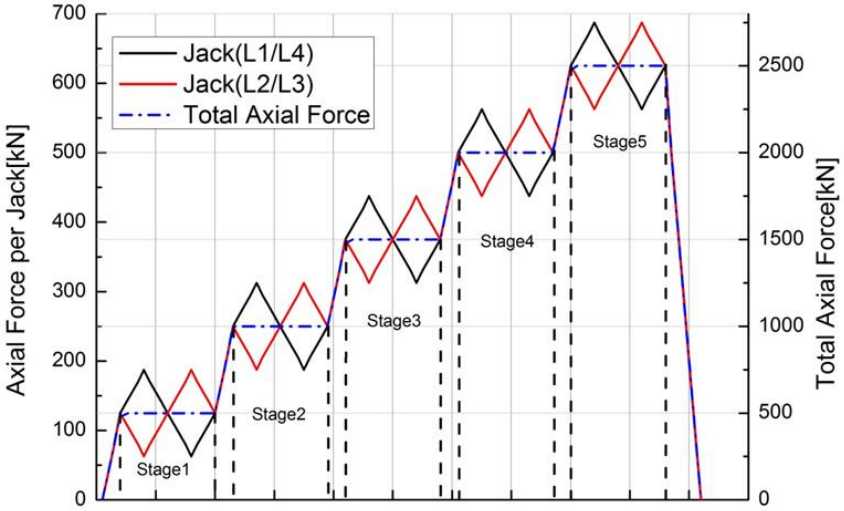

(d) Compression-bending moment loading patterns

Figure IV.24 Loading process of axial force and bending moment

IV.6.2. Shear loading application

As aforementioned, the combination of a shear force and an axial force is considered. The possible deformation of the joint subjected to compression and shear is shown schematically in Figure IV.26. When both axial and shear forces are applied to element B, a compression occurs as well as a lateral deformation. The shear load was applied by means of one actuator, providing a push or pull on the

element B as illustrated in Figure IV.19 (a) (yellow) and Figure IV.25. In order to have a comprehensive understanding of the shear behavior of an immersion joint, three sub-loading cases are applied.

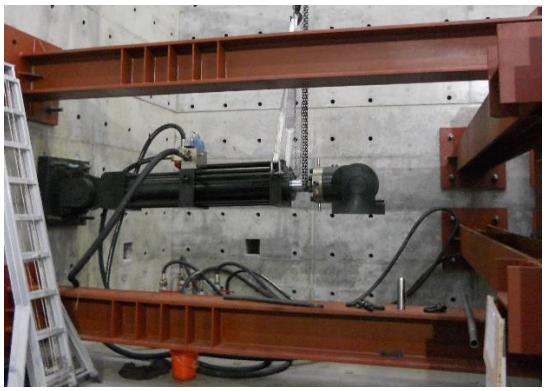

Figure IV.25 The used actuator in the test

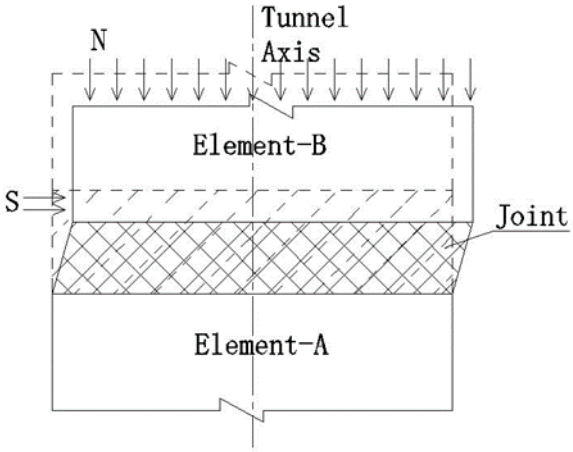

Figure IV.26 Compression-shear loading in the joint

(1) Static shear loading

In this loading case, different levels of the axial force, corresponding to the water pressure, are considered. The scaled-down axial forces corresponding to the minimum and the maximum water depths are 440kN and 1760kN. The detailed loading cases are listed in Table IV.7. During each loading case, the axial force is applied to the joint at a specific value. Then the a reciprocal shear force is applied with a maximum amplitude of 40kN in the loading and reversed loading direction.

As calculated in Section IV.3.3, the cracking strength of a single concrete shear keys is 42kN. In order to avoid unexpected damage in the shear key, a shear amplitude of 40kN is selected. With this shear amplitude, the shear keys are assumed to behave only in the elastic stage.

Table IV.7 Static shear loading cases

No.	Axial force [kN]	Shear amplitude [kN]
CSS-0-40	0	±40
CSS-440-40	440	
CSS-850-40	850	
CSS-1760-40	1760	

(2) Dynamic shear loading

Except for the static shear loading, the dynamic shear loading is also taken into account in this experiment. The influencing factor of the shear behavior of the joint, such as the shear amplitude, the input frequency and the axial force, are investigated. Based on the data from the design institute, the dynamic frequency of the full scale final immersion joint is 1.34Hz. The similarity coefficient of a dynamic test is listed in Table IV.8. Based on that, the input frequency in this experiment is 4.2Hz. In order to study the influence of the input frequency, different values of the frequency are applied as well, namely 1Hz, 2Hz and 3Hz. It should be noted that the maximum input loading frequency applied by the actuator is 4.5 Hz and therefore no frequency more than 4.2 Hz is applied in this part. Based on that, with different combinations of axial force, shear amplitude and frequency, there are 48 dynamic loading cases with a time duration of 8 seconds.

(3) Shear loading until failure

In this shear loading, only one axial force level is considered, referring to the water depth of the final joint in the actual project. Based on calculations, the axial force selected is 850kN. First, the constant axial force is applied at the design value to simulate the initial water pressure in an actual joint at a specific water depth. After that, a reciprocal shear force, instead of a monotonic shear force, is applied horizontally to account for seismic actions, while the axial force remains constant.

A reciprocal load means that first a load in the 'positive' direction is applied, followed by unloading. Then the loading and unloading in the 'negative' direction are applied. Such reciprocal load is applied repeatedly with increasing amplitude after each cycle to simulate the gradually increasing seismic excitation.

Table IV.8 Similarity coefficient of dynamic test

Physical parameter	Dimension	Similarity coefficient
Length *l*	L	S_l
Displacement *S*	L	S_l
Elastic modulus *E*	FL^{-2}	1
Stress σ/Strain ε	FL^{-2}/-	1/1
Acceleration *a*	LT^{-2}	1
Time *t*	T	$\sqrt{S_l}$
Force *P*	F	S_l^2
Bending moment *M*	FL	S_l^3
Frequency *f*	T^{-1}	$1/\sqrt{S_l}$

As the horizontal shear action is mainly due to a seismic loading, a quasi-static loading mode for the shear force is applied (Figure IV.27). In order to obtain the complete force-displacement behavior of the joint, the actuator is servo-controlled as a combination of force control and displacement control. Force control is used in the first part of the test because the joint is displacement-sensitive as the stiffness is high. However, in the second part of the test, the joint is force-sensitive due to the possible occurrence of plastic behavior or sudden brittle failure of the shear keys. Therefore, during the test, a force-control is adopted, followed by a displacement-control. First, reciprocal loading is applied in force-control until the shear force reaches a value of 400 kN, which is about 50% of the design shear capacity as recommended by the Chinese code (JGJ/T 101-2015). Then, the loading mode is switched and the actuator applies a reciprocal shear displacement at increasing amplitude until the joint fails. As shown in Figure IV.27, the test does

not stop as the loading mode is switched and the first point of input shear displacement corresponds to the last point of the input shear force. It should be noted that the loading and displacement rates are 1 kN/s and 0.1 mm/s respectively.

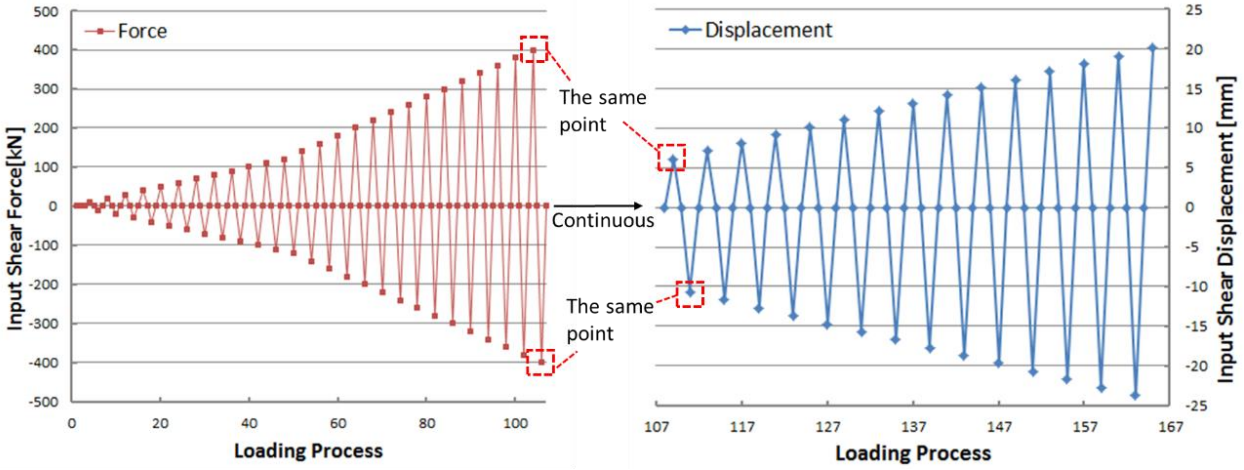

Figure IV.27 Loading patterns for shear loading until failure

IV.7. Summary

A comprehensive experimental investigation on mechanical behavior of the immersion joint subjected to various loading conditions is conducted for the first time as presented in this chapter. The detailed information regarding justification of the experiment, the specimens, the test set-up, the loading protocols as well as the measurements are provided.

According to some limitations, the geometric scale of 1:10 was selected. Based on that, two sets of specimens with steel shear keys and concrete shear keys respectively were designed. Each set of specimens contained two tunnel elements and one GINA rubber seal. The detailed design of the specimens were provided according to Chinese code. Then a unique experimental set-up was developed. The test set-up includes three major steel frames, allowing that one element is fixed and the other element is movable, resulting in a deformation in the joint. A special joint was designed to consider the proper force transfer from the frame and the hydraulic jack to the element. In order to obtain reliable data, transducers are installed symmetrically along the cross section of the tunnel

element to eliminate possible errors. Moreover, a four-camera recording system was applied to observe the real time situation inside the element.

In consideration of different loading applications, three different loading protocols were justified, namely the axial loading case, the compression-bending moment case and the shear loading case. For the shear loading case, the static and dynamic shear loading were both considered. Finally, the failure of an immersion joint subjected to compression-shear load was investigated.

IV.8. References

JGJ/T 101-2015 Specification of Testing Methods for Earthquake Resistant Building. China Academy of Building Research, Beijing. (in Chinese)

GB 50010-2010 Chinese Code for design of concrete structures. Ministry of Housing and Urban-Rural Development of the People's Republic of China, Beijing. (in Chinese)

GB 50017-2003 Chinese Code for design of Steel structures. Ministry of Housing and Urban-Rural Development of the People's Republic of China, Beijing. (in Chinese)

Xu, G., Yuan, Y., 2013. Seismic control technology of immersed tunnels. Report of the National Key Technology R&D Program. No.2011BAG07B01.

Yuan, Y., Xiao, W., Yu, H., et al., 2014. A type of large-scale reaction frame system. China: Patent. No. ZL 2014 2 0008829.1. (in Chinese)

CHAPTER V

AXIAL AND FLEXURAL PERFORMANCE OF THE JOINT

JF Kennedy immersed tunnel, Belgium

(source unknown)

V. Axial and Flexural Performance of the Joint

V.1. General introduction

The axial and flexural performance of the joint are combined and presented in this chapter. The design of the immersion joint has to consider various actions during its service life, such as water pressure, earthquakes, settlement of foundation, shock from shipwrecks, and other actions. Meanwhile, an immersion joint should include the water-proof part as an indispensable system. Therefore, knowledge of the deformation of a joint under loading is important for a safe, reliable, and water-proof design. Further, due to the water pressure in the construction phase, the immersion joint is submitted to an initial compression. It is vital to know the behavior of the immersion joint after immersion. Therefore, the axial stiffness for this situation is required for calculation and design. It should be noted that deformation of the immersion joint may be caused by compression and tension due to different types of actions in the tunnel elements. The differential extension of the immersion joint may be introduced as ‘‘snake” movement of an immersed tunnel along its longitudinal profile, whether from settlement of foundation or from stratum movement during earthquake.

The compression on the scaled model is applied axially to simulate the water pressure on the immersion joint at typical buried depths. Bending moments are applied cyclically at equal amplitude in the horizontal plane, by varying the load in the axial hydraulic jacks on each sidewall of the element. Through observed load–deformation curves, both the axial stiffness and the flexural stiffness of the joint will be derived for use in practice.

V.2. Axial performance of the joint

V.2.1. Compression-release curve

The recorded data for the major loading steps from nine transducers (Figure IV.22) are listed in Table V.1, including loading and unloading. The results of P-6 to P-9 are shown in Figure V.1**Error! Reference source not found.** as an example. The same trend of the compression of the joint as a function of the axial force can be found in these four measurement points, though there is a certain difference between them. It can be seen that the curve becomes more stiff as the axial force increases, showing the same non-linear behavior of the rubber as shown in Figure IV.6. It should be noted that the rubber in Figure IV.6 was tested without any clamping system. Moreover, the compression on top of the tunnel element (from P-1 to P-5) are a bit larger than the compressions measured inside the element, indicating that there is a small vertical rotation occurring in the joint. This may be caused by the friction force between the support columns and the element, which will be analyzed later on.

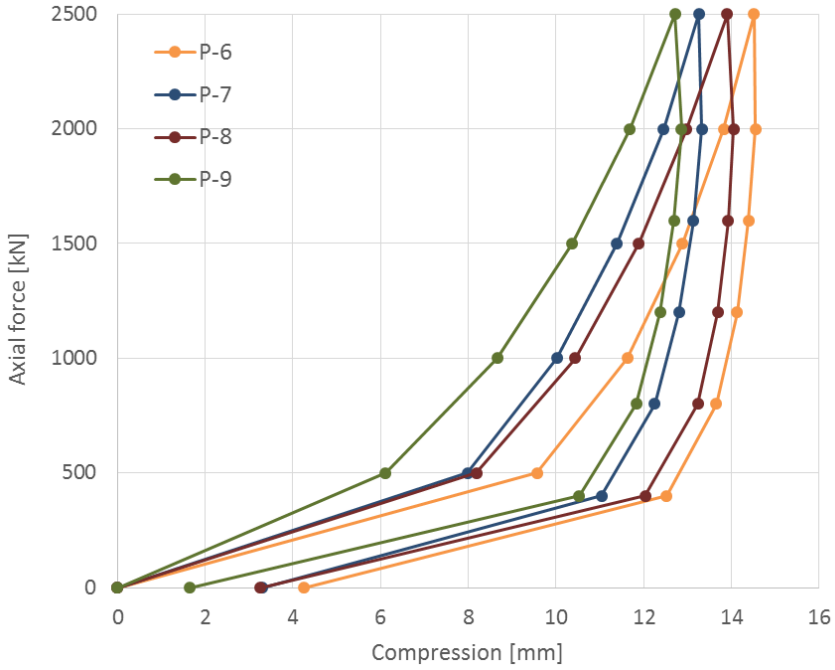

Figure V.1 Recorded data of P-6 to P-9

Table V.1 Recorded data from nine transducers [mm]

Axial force [kN]	P-1	P-2	P-3	P-4	P-5	P-6	P-7	P-8	P-9
500	10.12	9.92	9.91	10.09	10.43	9.57	7.98	8.19	6.11
1000	12.78	12.03	11.60	11.83	12.43	11.63	10.02	10.44	8.66
1500	14.59	13.19	12.29	12.60	13.53	12.89	11.39	11.89	10.37
2000	15.96	13.94	12.64	13.09	14.27	13.83	12.46	12.97	11.68
2500	17.00	14.64	12.90	13.47	14.84	14.52	13.26	13.90	12.72
2000	17.14	14.59	12.98	13.54	14.89	14.56	13.33	14.06	12.86
1600	16.94	14.51	12.97	13.51	14.77	14.39	13.14	13.93	12.69
1200	16.61	14.40	12.95	13.43	14.59	14.13	12.81	13.69	12.38
800	16.06	14.11	12.86	13.25	14.23	13.65	12.25	13.24	11.83
400	14.78	13.37	12.47	12.68	13.30	12.53	11.04	12.04	10.54
0	5.84	5.17	4.63	4.59	4.73	4.24	3.30	3.25	1.64

The average data from P6-P9 are plotted in Figure V.2. It shows the compression (closing) of the joint reaches a maximum value of 13.6 mm when it is subjected to an axial force of 2500kN. Then, compression recovers (extension of the joint) with decrease of the axial force. Finally, when the axial load is 0, a residual compression of 3.1mm remains, which is about 22.7% of the maximum compression. The occurrence of residual compression and a hysteretic loop between loading and unloading implies that the material of the GINA-type seal is viscoelastic, rather than hyper-elastic. Obviously, the compression–release curve can be divided into four portions. At initial loading, the slope of the curve of portion $\overline{OA}$ is about constant up to an axial force of 320 kN. At portion $\overline{AB}$ of the curve, the slope is no longer constant. The rapid change of it shows the same trend as presented in Figure IV.6. This means that the axial stiffness of the immersion joint is increasing with the axial force, and the amount of compression of the joint reaches almost its limit at the final load level of 2500kN. The slope of the curve at initial unloading, portion $\overline{BC}$, drops steeply. Release of the compression mainly happens in portion

$\overline{CD}$ when the axial force is less than 500 kN. The slope of this portion is nearly the same as that of the initial loading portion $\overline{OA}$. The values of δ_A to δ_D are 6.29 mm, 13.60 mm, 11.54 mm and 3.11 mm respectively. It has to be stated in this part that the choice of point C is limited by the fact that there is no extra point between the point C and point D.

In addition, two horizontal dotted lines are indicated, corresponding to the maximum water depth (MaWD) and minimum water depth (MiWD), with values equal to 1760 kN and 440 kN respectively. Obviously, both portions $\overline{OA}$ and $\overline{CD}$ are beneath the line of the MiWD. About the upper third of portion AB and portion BC are above the line of the MaWD, the rest of which is in the range between MaWD and MiWD. Hence, the immersion joints close to the MiWD behave less stiff, resulting in larger deformations. On the contrary, smaller deformations occur in the immersion joints which are situated in deeper sea. Moreover, below the line of the MiWD, the compression is much more sensitive to the axial force. A slight drop of the axial force will cause large deformations in the joint, resulting in extension of the joint. Hence, the softer GINA-type seal can be used here to ensure that the compression will be kept larger than the minimum compression. With respect to the joints close to the line of MaWD, stiffer GINA-type seal can be used to avoid excessive compression.

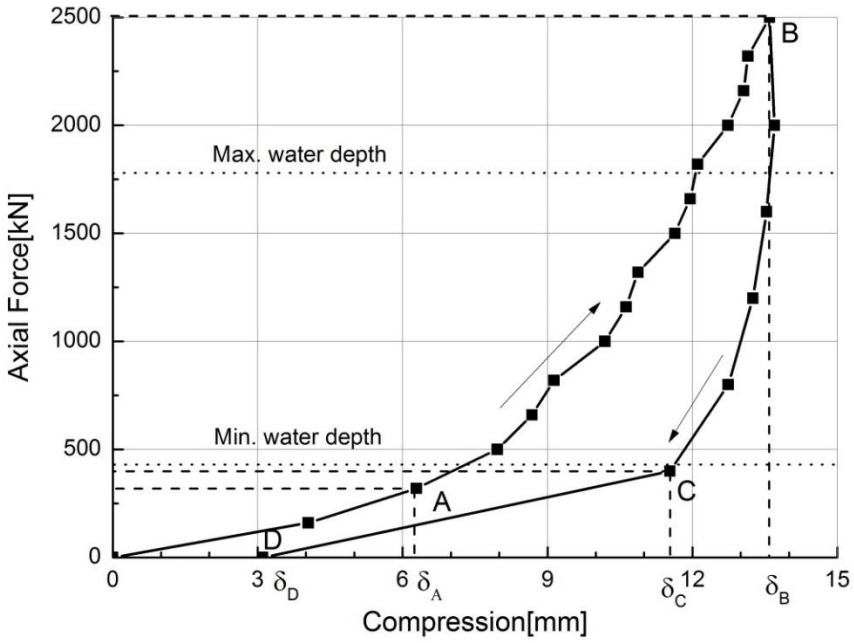

Figure V.2 Compression curve of the model immersion joint

V.2.2. Axial stiffness of the joint

In order to quantify the relationship between the axial force and the compression of the immersion joint, fitting curves F_1 to F_4 for each portion were determined to describe the compression–axial force relation of the model joint, which are presented in Figure V.3. The coefficients of the fitting curves are listed in Table V.2. The coefficients of determination in Table V.2 are used to measure the goodness of fit.

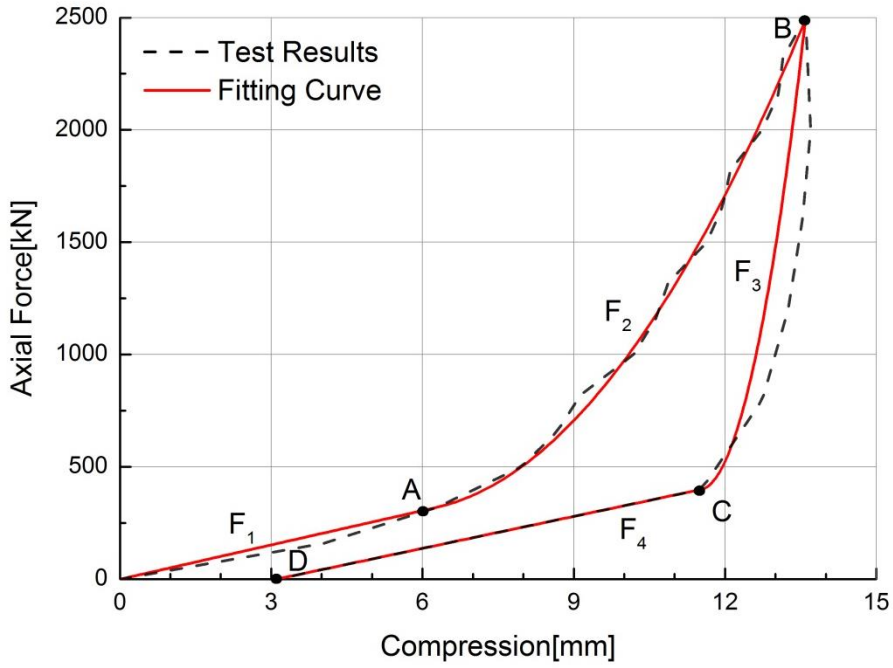

Figure V.3 Test results and the corresponding fitting curves

It can be seen that at the level of low axial force, F_1 and F_4 nearly share the same slope, the difference being only about 7%. A difference is found between the peaks of the fitted loading and unloading curve. The application conditions of the fitted curves vary from the loading situation. It is also noted that, with respect to the loading portion, the fitting curve is continuously differentiable at point A, so as to point C in the unloading part. Hence, once the axial force is determined, the corresponding static axial stiffness can be calculated.

Table V.2 Coefficients of fitting function

Quadratic fitting function: $F = a\delta^2 + b\delta + c$				Coefficient of determination
Portion	a	b	c	R-square
$\overline{OA}$	0	50.895	0	-
$\overline{AB}$	33.685	-372.699	1331.656	0.9954
$\overline{BC}$	470.424	-10805.235	62445.527	0.6718
$\overline{CD}$	0	47.450	-147.331	-
Units: F [kN]; δ [mm]				

For different construction water depths and loading situations, the initial water pressure is different and so is the axial spring stiffness k_0. The equation for the stiffness k_0 is obtained as the first derivative of F, which is also the slope of the tangent line at the point.

$$k_0\ \left(\frac{\text{kN}}{\text{mm}}\right) = \frac{dF}{d\delta} = \begin{cases} k_1 = 50.895 & 0 < \delta \le \delta_A \\ k_2 = 67.370\delta - 372.699 & \delta_A < \delta \le \delta_B \\ k_3 = 940.848\delta - 10805.235 & \delta_B < \delta \le \delta_C \\ k_4 = 47.450 & \delta_C < \delta \le \delta_D \end{cases} \tag{V.1}$$

where F and δ are the axial force and compression respectively; k_1 to k_4 correspond to the portions $\overline{OA}$ to $\overline{CD}$; δ_A to δ_D are the compression at point A to D.

The axial stiffness for both loading and unloading is described by a bi-linear model. The calculated axial stiffness for some particular axial forces is listed in Table V.3. Obviously, in the portion $\overline{AB}$ and $\overline{BC}$, the unloading axial stiffness is about two to three times the loading axial stiffness, showing the hysteresis behavior of the GINA-type seal subjected to axial loading. When the axial force remains at a sufficiently low level, the values of both loading and unloading stiffness are almost equal. By using Eq. (V.1), the loading and unloading axial stiffness of the immersion joint in different water depths can be predicted.

Table V.3 Axial spring stiffness for different water pressures (Scale:1:10)

Axial force [kN]	Corresponding water depth [m]	Compression [mm]		Initial loading axial stiffness [kN/mm]	Unloading axial stiffness [kN/mm]
		Loading	Unloading		
200	-	4.84	7.32	50.90	47.45
440	9.7	7.16	11.78	109.67	278.55
850	18.7	9.44	12.46	263.27	921.46
1000	22.0	10.03	12.62	303.02	1063.64
1500	33.1	11.55	13.01	405.42	1439.51
1760	38.8	12.17	13.19	447.19	1600.45
2000	-	12.66	13.32	480.21	1736.81
2500	-	13.59	13.59	542.86	1988.44

V.2.3. Possible influencing factors of the experimental results

In order to analyze the experimental results, a material test of a model GINA rubber seal was also conducted. A model GINA, having the same cross-sectional dimension as the experimental one but with a length of 20cm, was loaded in axial compression. Table V.4 shows the comparison of the experimental results and the results from the material test. It can be seen that an average 35% difference exists between these two results. The GINA rubber seal from the material tests appears to be softer, showing more compression under the same loading. When the axial force returns to zero, the difference reaches its maximum, up to 66%.

There are a lot of possible factors, such as the friction force, the length of the GINA rubber, the clamping system of the rubber and the shape of the GINA rubber, influencing the experimental results and such factors are analyzed as follows.

Table V.4 Comparison between the experimental and material results

Axial force [kN]	Material test [mm]	Experimental results [mm]	Difference	
			Absolute value [mm]	Relative value [%]
500	12.04	7.96	4.08	33.9
1000	16.17	10.19	5.98	37.0
1500	18.17	11.64	6.54	36.0
2500	20.4	13.60	6.80	33.3
2000	20.5	13.70	6.80	33.2
1600	20.4	13.54	6.87	33.7
1200	20.21	13.25	6.96	34.4
800	19.77	12.74	7.03	35.5
400	18.99	11.54	7.46	39.3
0	9.13	3.11	6.03	66.0

(1) Friction force

As mentioned, Element B in this experiment is movable and the friction force between the element and the support (shown in Figure V.4) is not negligible. The self-weight of one tunnel element is 5 tons and the friction coefficient between the steel is 0.1. According to the static friction law, the friction is calculated as about 5kN. Compared to the imposed axial force, such small friction force can be ignored.

Figure V.4 The contact between the element and the support

(2) The length of the GINA rubber

The results from the material test were obtained by testing a GINA specimen with a length of only 20cm. With respect to the boundary condition, there is no restraint along transversal direction of the rubber and the contact between the bottom of the rubber and the steel plate is defined as the friction contact. By scaling up the results to the same length as the structural experiment, the force-compression data from material test are obtained as shown in Table V.4. In order to deal with this issue, a three dimensional numerical analysis was conducted. The numerical model includes two specimens as shown in Figure V.5. The model 1 has a length of 20cm and there is no restraint at two ends while the length of the model 2 is 1m and the two ends are restrained.

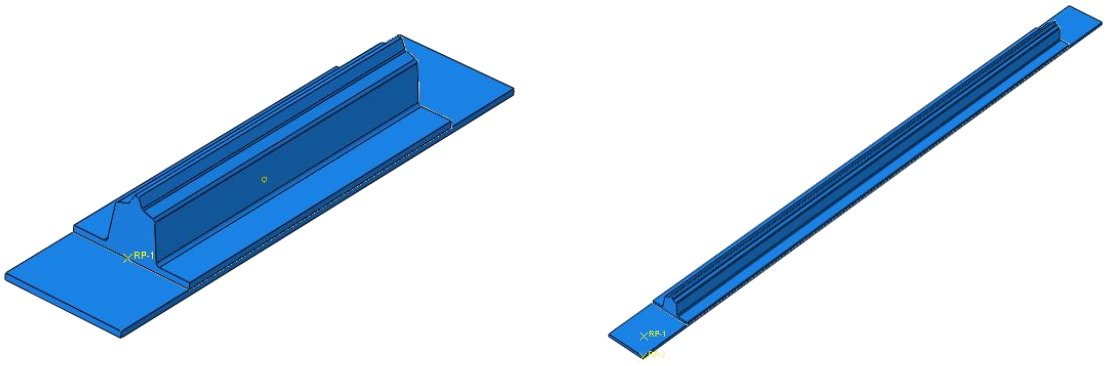

(a) Model 1 (b) Model 2

Figure V.5 Two different models in numerical analysis

The Mooney-Rivlin model, which is popular for modelling the large strain non-linear behavior of an incompressible material, is used as the constitute model for the GINA rubber seal. The model can be expressed by the following strain energy density function (Boyce and Arruda, 2000).

$$W = C_1(I_1 - 3) + C_2(I_2 - 3) \tag{V.2}$$

where $\boldsymbol{W}$ is the strain energy; C_1 and C_2 are empirically determined material constants, and I_1 and I_2 are the first and the second invariant of the unimodular component of the left Cauchy-Green deformation tensor.

Based on the literature by Zheng (2003) and Zuo (2008), material constants C_1 and C_2 can be calculated by the hardness of the material.

$$\begin{cases} 6C_1\left(1 + \frac{C_2}{C_1}\right) = 10^{0.0198H_r - 0.5432} \\ C_2/C_1 = 0.1 \end{cases} \tag{V.3}$$

where H_r is the hardness of the rubber (provided by the producer).

Figure V.6 illustrates the numerical results of these two models. In general, the same trend of these two model is observed. and even it can be seen that two models behave almost the same when the axial force amounts to 25kN. As the axial force increases, the two curves split and the difference gradually increases. This difference reaches a maximum at the end of the curves, which is about 6%. It should be noted that the loading rates of the material test and the experiment are different, which may also influence the results.

(3) Lateral restrain by the bolts

As mentioned in Chapter IV, the GINA rubber seal in the structural experiment was clamped to the embedded plate by bolts going through the flange. When the GINA rubber was highly compressed, it can be observed (Figure V.7) from the experiment that the transversal deformation of the rubber was restrained by the bolt head, making the rubber, to some extent,

stiffer in axial direction. However, in the material test, the clamping system was not taken into account and the GINA rubber was allowed to deform freely in the transversal direction.

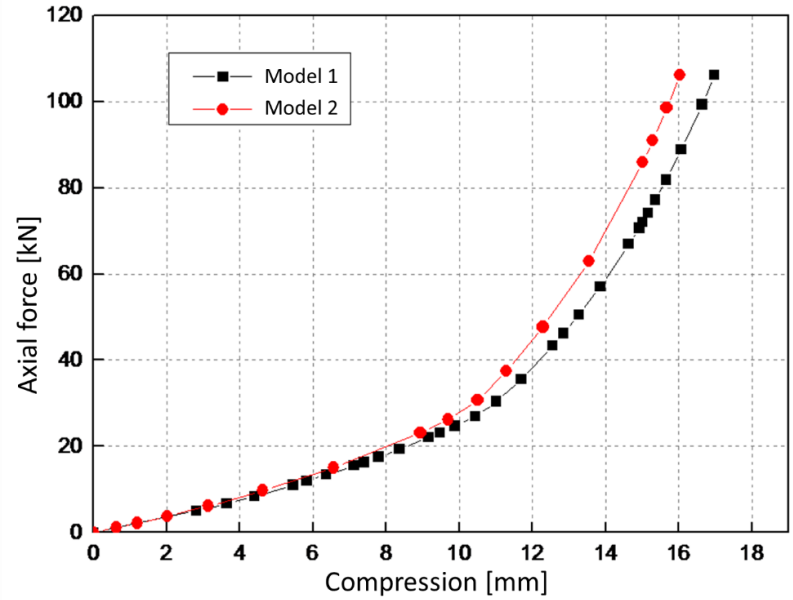

Figure V.6 Results of these two models

Figure V.7 The GINA rubber in the experiment

A two dimensional model was used to investigate this issue, as shown in Figure V.8. The same material model of the rubber and the same loading protocol as presented in the previous section were adopted. The transversal behavior of the GINA rubber seal on the left was confined by the strip but without contact between the bolt and the rubber. The obtained compression from these two models are both shown in Figure V.9. Under this loading, there is only a very slight difference, about 2%, between these two models, showing that the axial performance of the GINA rubber is only slightly influenced by the bolts.

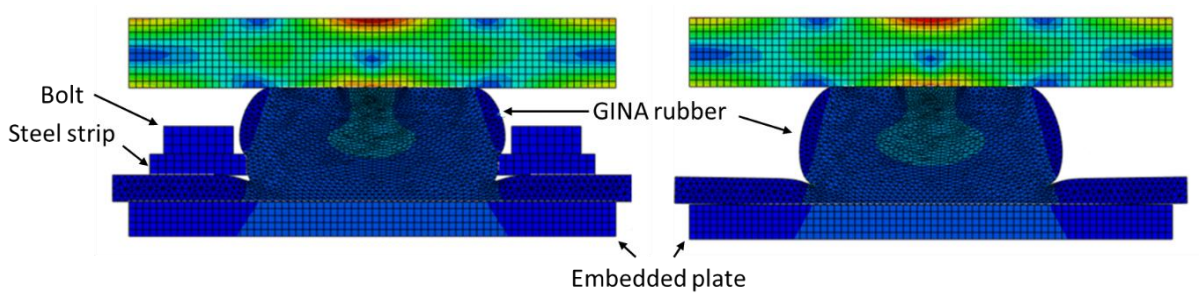

Figure V.8 Numerical model with and without clamping system

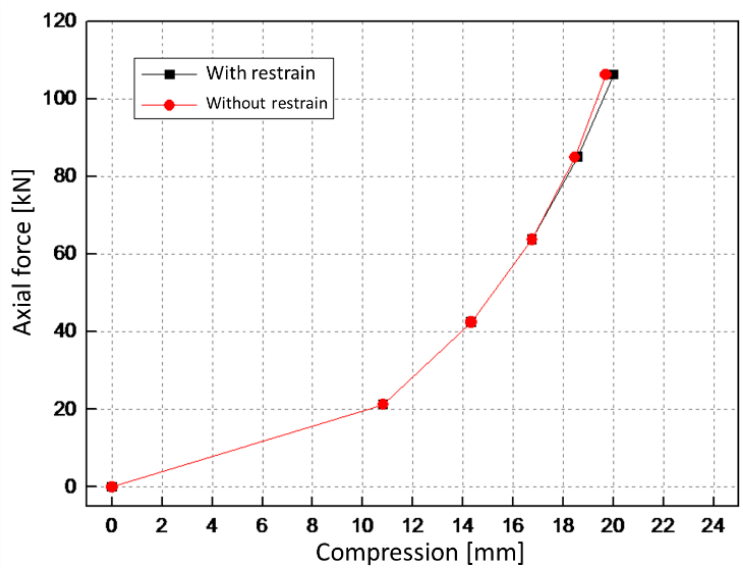

Figure V.9 Compression curve of the model with and without transversal restraint

(4) The shape of the rubber

The GINA rubber seal in the material test was a straight specimen with a total length of 20cm. However, in the experiment, the alignment of the GINA rubber seal was not always straight. As illustrated in Figure V.10 (a), the GINA rubber in the experiment turns 90 degrees at the corner part of the element, indicating that there is an initial compression on the inside part and an extension on the outside part, generating initial stresses inside the rubber. To figure out such influence on the compression of the rubber, a three dimensional numerical model, Model 3, was elaborated and compressed. The loading and the boundary condition of Model 3 are the same as those in Model 2. Both of the results of Model 2 and Model 3 are shown in Figure

V.11. It can be found that the two curves are almost in accordance with each other and under the maximum axial force, the difference between them is only 0.28mm (1.7%). It should be noted that due to a technical problem, there is no initial stress inside Model 3, which is a bit different from the actual situation. Such difference may also affect the results.

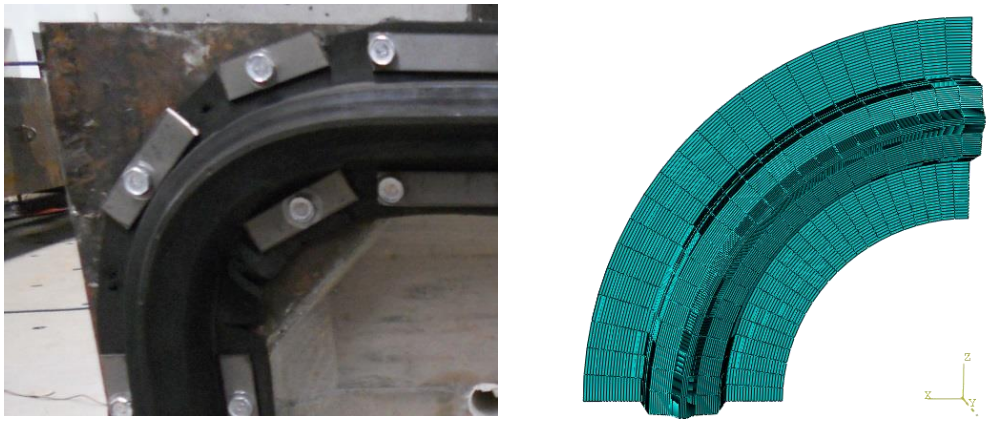

(a) The corner part of the GINA rubber (b) The numerical model: Model 3

Figure V.10 The GINA rubber seal at the corner

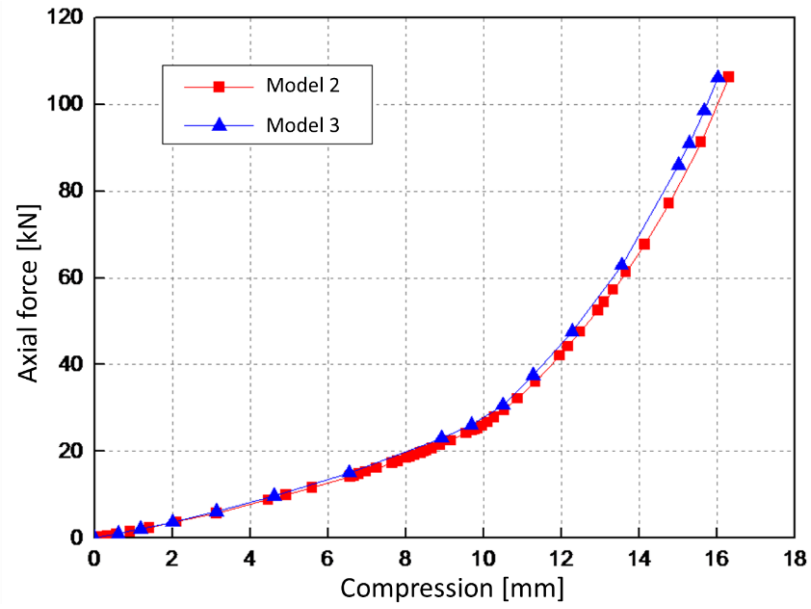

Figure V.11 Comparison between Model 2 and Model 3

(5) Summary

As known the axial behavior of the joint depends on the behavior of the GINA rubber. The behavior of the GINA rubber is affected by several factors, such as the friction force, the length, the lateral restraint and the shape of the rubber seal. Based on the aforementioned discussion, the influencing factors on the behavior of the rubber were studied and quantified. Except for the friction force, the behavior of the rubber is influenced by the properties of the rubber at different levels. It is assumed that such influencing factors can be linearly superimposed although it is not the case in reality. There would be an approximately 10% difference in total in consideration of all the aforementioned factors. However, such value is still far smaller than the obtained difference between the structural experiment and the material test. The modelling techniques and the used constitutive model for the rubber require further improvement to obtain more accurate results. The different loading rate may also have an impact on the results as the rubber is not a pure hyper-elastic material.

V.3. Flexural performance of the joint

V.3.1. Moment-rotation curve

To characterize the flexural performance of the immersion joint, the moment–rotation curve for an axial force of 500kN is presented in Figure V.12. In the beginning of the test, the rotation increases nearly linearly with the moment. Then the slope of the curve experiences a slight downward trend. The peak rotation of the immersion joint is 8.27×10^{-4}rad. Along the unloading part, there is a continuous decrease of the slope of the curve. Like in Figure V.2, also a residual rotation occurs in this case. When the moment increases reversely, the same increasing trend of the rotation can be observed as well. After a complete loading cycle, the final residual rotation of the joint reaches -3.45×10^{-3}rad.

The curve in Figure V.12 can be divided into six portions. At the beginning of the curve, the slope of portion $\overline{O'A'}$ is constant up to a rotation of 2.88×10^{-4}rad. At the transition point A', the

slope of the next portion $\overline{A'B'}$ changes slightly but it is still constant with a rotation up to 8.27x10^{-4}rad. After reaching the peak B' , the curve enters the unloading part. During this part, portion $\overline{B'C'}$, the slope first drops remarkably then gradually tends to be almost constant and close to that of portion $\overline{O'A'}$, resulting in a residual rotation C' . The reverse loading portion $\overline{C'D'}$ follows portion $\overline{B'C'}$. At the initial reverse loading part, the rotation still remains positive and the slope of this part is constant till the rotation of -3.66x10^{-4}rad at point D'. Like the slope of portion $\overline{A'B'}$, that of portion $\overline{D'E'}$ is also a constant, which is slightly smaller than that of portion $\overline{C'D'}$. Then the reverse loading curve peaks at point E'. Subsequently, the reverse unloading starts and the same trend can be found in portion $\overline{E'F'}$, compared to portion $\overline{B'C'}$. After applying a cyclic bending moment, a residual rotation occurs, resulting in an asymmetric deformation of the immersion joint.

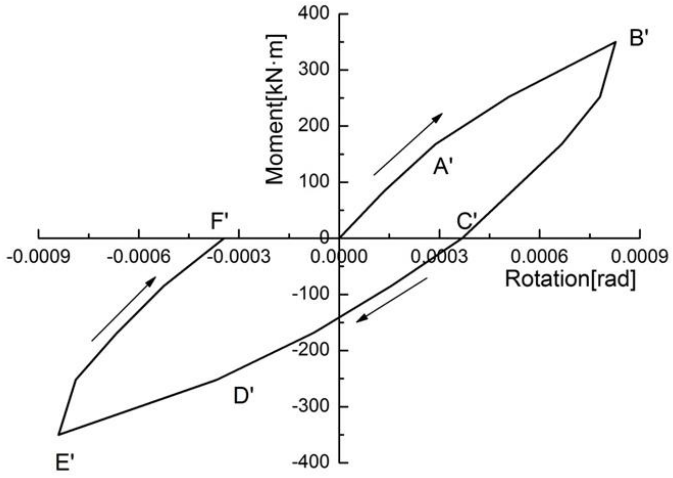

Figure V.12 Experimental moment-rotation curve of immersion joint for an axial force of 500kN

Table V.5 lists the rotation of the joint under different levels of compressive bending. During the test, 5 levels of axial force and 4 levels of bending moment are considered. It is clear that for the same magnitude of bending moment, the rotations of the joint decrease as the axial force increases. The rotation corresponding to the axial force of 500kN is about 10 times larger than that at 2500kN. From another point of view, with respect to the same magnitude of axial force, the rotations increase along with the bending moments. Also, rotations change non-linearly along with both axial force and bending moment.

Figure V.13 provides the moment–rotation curves of the immersion joint at different axial forces. The same trend as that in Figure V.12 can be observed. It is obvious that all the curves present a hysteretic behavior. Comparing the different curves in this figure, the envelop area decreases along with increasing axial force. That is, when the axial force grows gradually, the compressive stiffness of the GINA-type rubber increases rapidly. Also, the slope of the curves changes continuously during the test and a residual deformation occurs after each loading case.

Table V.5 Rotation of the joint under compressive bending [rad]

Axial force [kN]	Bending moment [kN·m]			
	84	168	252	350
500	13.4×10^{-5}	28.8×10^{-5}	50.7×10^{-5}	82.7×10^{-5}
1000	4.89×10^{-5}	8.91×10^{-5}	15.8×10^{-5}	24.7×10^{-5}
1500	3.07×10^{-5}	6.28×10^{-5}	10.9×10^{-5}	15.5×10^{-5}
2000	1.82×10^{-5}	4.38×10^{-5}	6.64×10^{-5}	9.56×10^{-5}
2500	1.17×10^{-5}	2.99×10^{-5}	5.04×10^{-5}	6.64×10^{-5}

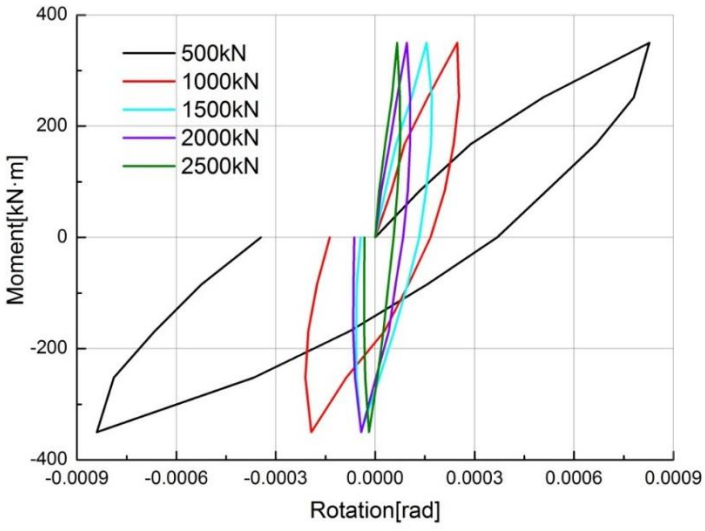

Figure V.13 Moment-rotation curve of immersion joint with different axial forces

V.3.2. Relative displacement of the joint

A relative displacement of the joint would result from its unbalanced loading/unloading, when subjected to a bending moment. It can be calculated from the measured displacements at each measuring point, with respect to its initial compressive state. Figure V.14 illustrates the relative displacement of the joint under the axial force of 500kN when subjected to a bending moment of 350kN·m. The initial state refers to the compression of the joint when no bending moment has been applied. That is, no relative displacement occurs in the initial state.

In this situation, it is obvious that the relative displacement increases with the moment. In portion $\overline{O'A'B'}$, the displacement of the joint behaves symmetrically, as shown in Figure V.14 (a), and the symmetry axis of the joint nearly remains in its geometric center during the cyclic bending. After unloading, the deformation of the joint cannot return to the initial state, which is shown in Figure V.14 (b). Regarding to reverse loading part $\overline{C'D'B'}$, though the initial state is different from portion $\overline{O'A'B'}$, the joint nearly behaves symmetrically and the maximum relative displacements are almost the same as the loading ones. During the loading and reverse loading process, it can be observed that the joint remains plane during compressive bending.

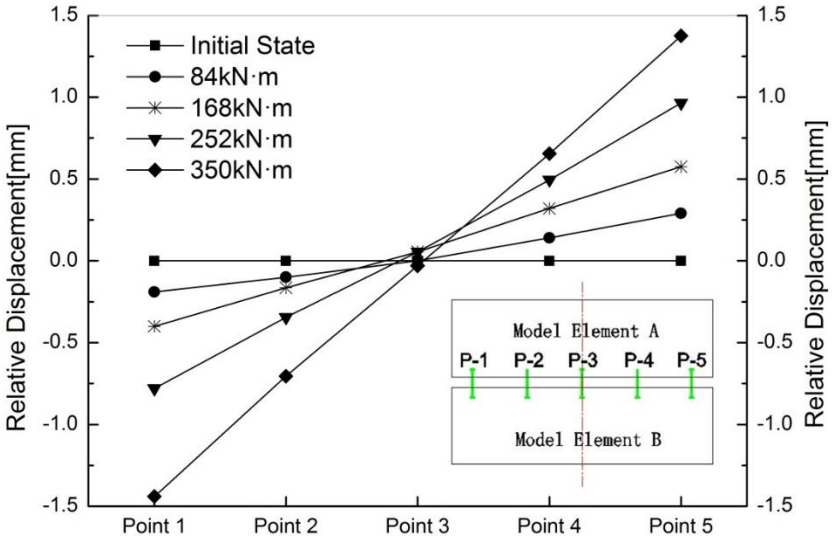

(a) Loading portion of moment-rotation curve

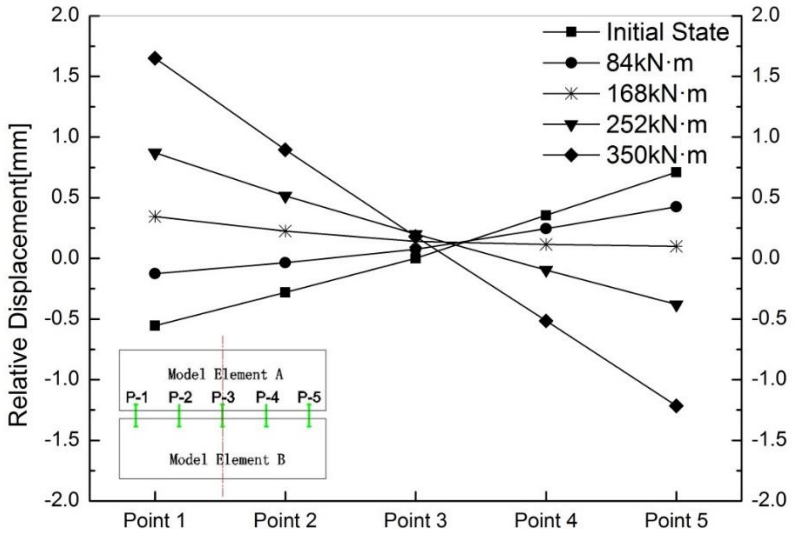

(b) Unloading portion of moment-rotation curve

Figure V.14 Rotation of immersion joint under an axial force of 500kN

When the axial force increases up to 1000kN (see Figure V.15(a)), the maximum relative displacement of the joint decreases remarkably. The joint behaves anti-symmetrically and the center of rotation starts to move away from the geometric center of the joint to somewhere between P-2 and P-3. As the axial force continues increasing to 1500kN, the center of rotation moves further on at around P2 and the maximum rotation becomes smaller. When the axial force reaches 2000kN, the same behavior can be observed as well. Under the maximum axial force, the rotation center is already at P1 and the maximum relative displacement, measured at P-5, is 0.20mm, which is almost 7 times that measured at P-1.

It should be noted that when the joint is subjected to compression and bending, the jacks at P-5 unload and the jacks at P-1 load for the same amount, generating a bending moment in the joint. As can be seen in Figure V.15 (a) to (d), the displacements at two sides of the joint are different from each other, which means the displacements of loading and unloading vary from each other, proving that the GINA rubber is a visco-elastic material. This phenomenon is in accordance with the obtained results shown in Figure V.2.

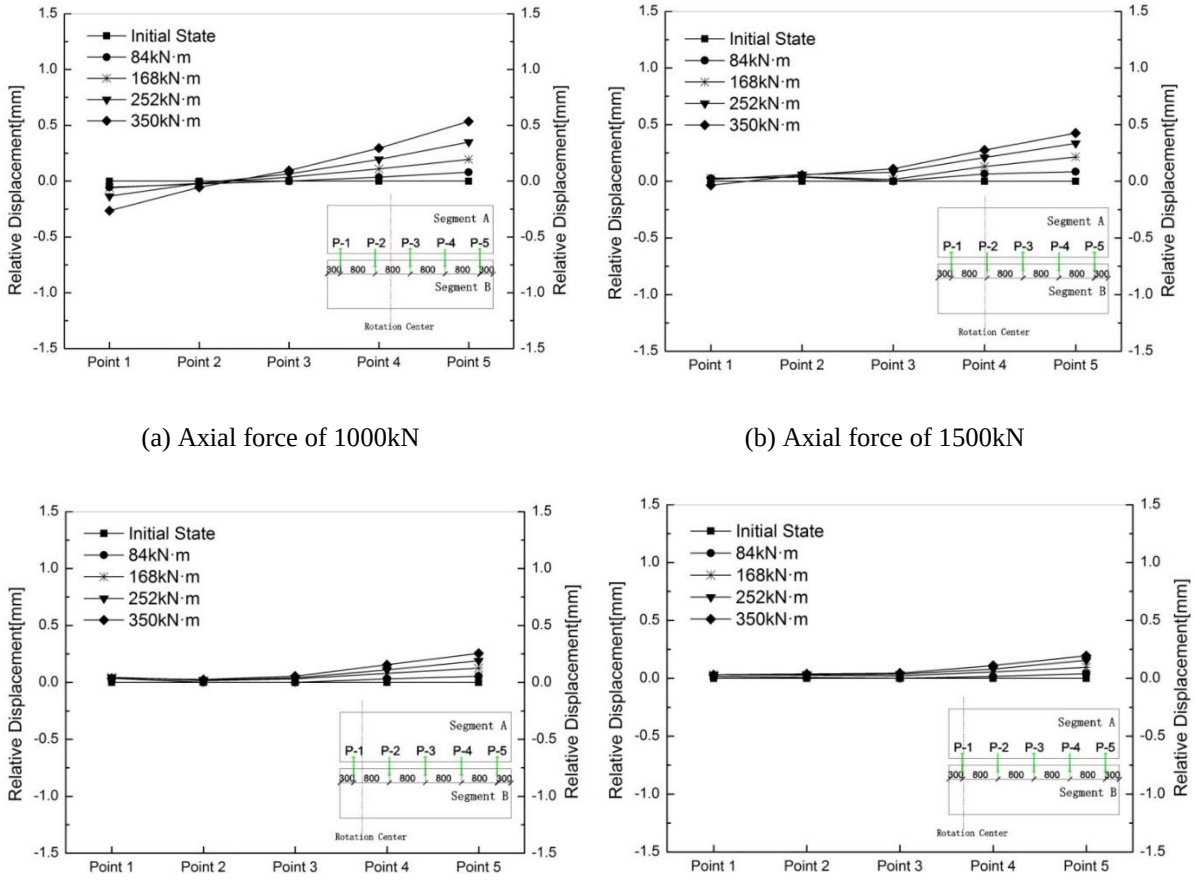

(a) Axial force of 1000kN

(b) Axial force of 1500kN

(c) Axial force of 2000kN

(d) Axial force of 2500kN

Figure V.15 Rotation of immersion joint under different axial forces

V.3.3. Flexural stiffness of the joint

Two types of stiffness of the tested immersion joint are defined in Figure V.16, which are the secant loading stiffness k_s and the secant unloading stiffness k_s^u respectively. For the loading branch, the secant flexural stiffnesses of the immersion joint are presented in Figure V.17, showing an increasing trend with the applied axial force. Polynomial fitting curves were developed. The flexural stiffness increases significantly, i.e. by one order of magnitude and hence, the variation of flexural stiffness needs to be considered in design. It follows that the behavior of the immersion joint varies according to the real loading situation, making it difficult

to evaluate the performance of the immersion joint during an earthquake. For the unloading branch, the unloading secant stiffness is also shown in Figure V.17. Obviously, the flexural unloading stiffnesses increase with the axial force. From the slope of the curve, it can be found that, at the beginning of the curve, the flexural stiffness remains at high level, much larger than that of k_s. Then with the decrease of the axial force, the flexural unloading stiffness experiences a downwards trend and soon drops by 2 orders of magnitude. At the level of axial force of 500kN, the unloading flexural stiffness is close to the loading flexural stiffness.

It is clear that the changing trend of flexural stiffness follows that of the axial force. At each level of axial force, the situation of the GINA-type seal is different. Once the GINA-type seal is highly compressed, the corresponding rotation of the joint subjected to moment changes little, which results in the occurrence of a larger loading flexural stiffness as well as an unloading one. On the contrary, when the axial force is 500kN, the loading flexural stiffness has the same magnitude as that of the unloading one, which means that the GINA-type seal in the joint behaves elastically and the residual deformation is small. Also, a non-linear performance of the stiffness of the joint along with the axial force is obtained.

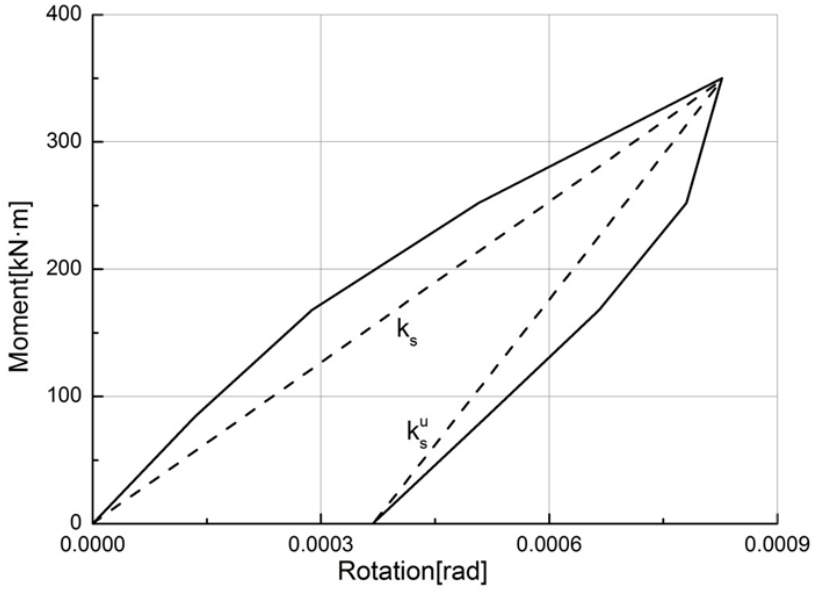

Figure V.16 Definition of stiffness of immersion joint

The polynomial fitting curves and corresponding equations for flexural stiffness are also given in Figure V.17. The values of flexural stiffness are listed in Table 6. The loading and unloading flexural stiffness of the joint subjected to a certain axial force can be predicted by using the presented equations.

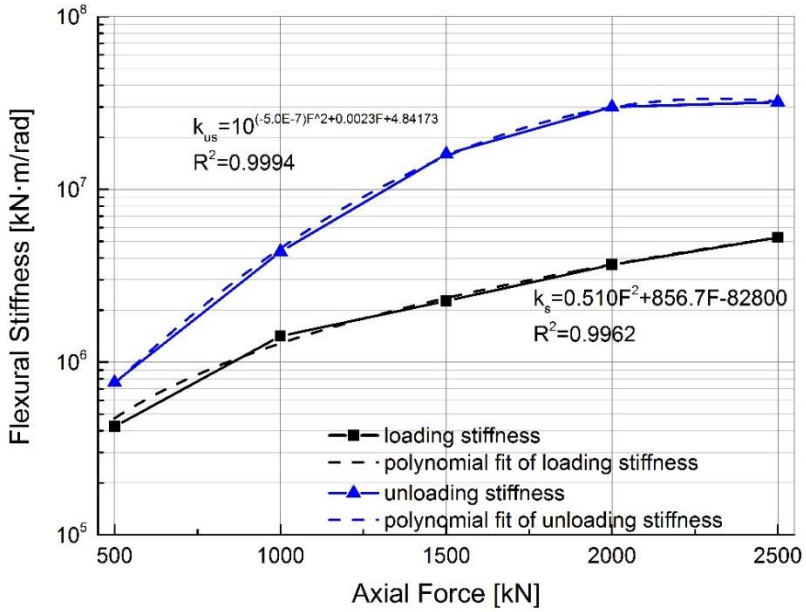

Figure V.17 Flexural stiffness of immersion joint

Table V.6 Flexural stiffness of immersion joint subjected to axial force [MN·m/rad]

Axial force [kN]	500	1000	1500	2000	2500
k_s	423	1414	2262	3660	5269
k_s^u	762	4359	15983	29969	31967

V.4. Stiffness ratio of the joint

Another concern for immersed tunnel design is the ratio of the stiffness of the joint to that of the tunnel structure. An index for the ratio of stiffness is defined:

$$r_{axial} = \frac{k^j_{axial}}{k^s_{axial}} \tag{V.4}$$

$$r_{bend} = \frac{k^j_{bend}}{k^s_{bend}} \tag{V.5}$$

where k^j_{axial} and k^s_{axial} are the axial stiffness of the immersion joint and the tunnel structure (per unit length) respectively; k^j_{bend} and k^s_{bend} are the flexural stiffness of the immersion joint and the tunnel structure (per unit length) respectively. k^j_{axial} and k^j_{bend} are obtained by the method described in Eq. V.I and Figure V.16 from the large scale model test while k^s_{axial} and k^s_{bend} are constants, which are determined by the Young's modulus of concrete and the properties of the cross section of the runnel (per unit length). Based on these, r_{axial} and r_{bend} are calculated and displayed in Figure V.18.

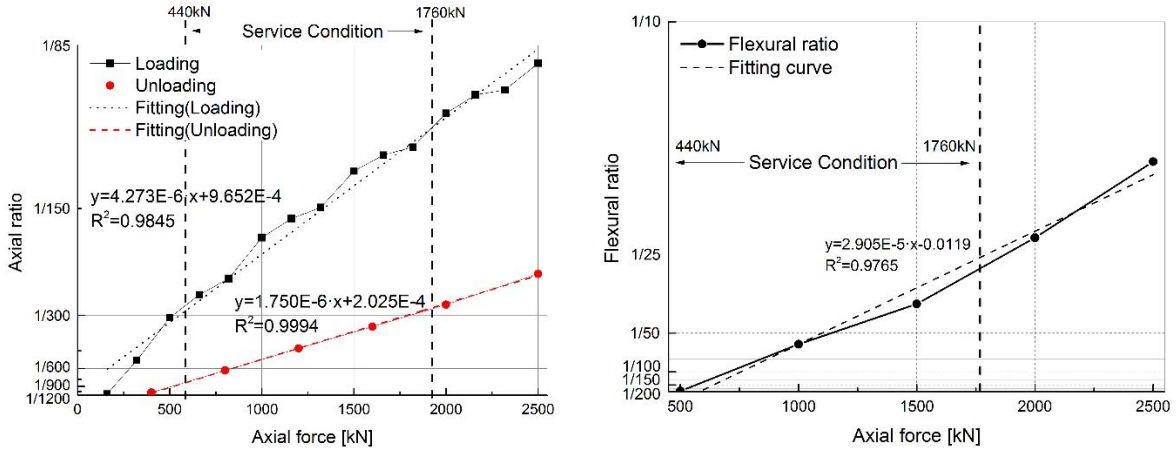

(a) Axial ratio of the model joint

(b) Flexural ratio of the model joint

Figure V.18 Stiffness ratio of immersion joint

Figure V.18 (a) shows the axial ratio r_{axial} of the tested immersion joint under the loading and unloading situations. During the loading part, the GINA-type seal in the joint is compressed continuously and becomes stiffer as the axial force increases. At the beginning of the test, the axial loading stiffness of the tunnel structure is about 1/1200 of that of the immersion joint. Then the ratio soon increases up to around 1/200 for an axial force of 1000kN. At this stage, large displacements occur in the immersion joint, as shown in Figure V.2 and the deformation

of the concrete can be ignored. Then a stage with continuous growth follows as the axial force increases from 1000kN to 2000kN. After that, the ratio remains around 1/100. The compression during this stage changes little, which can be seen in Figure V.2. The axial unloading stiffness experiences the same trend as the loading one but with a less stiff slope and smaller values. The fitting curves are used to describe the behavior of both stiffness ratios, showing the linear-like relation between the axial force and the stiffness ratio with a R-square value of 0.9845 and 0.9994 respectively as shown in the figure. The axial loading and unloading stiffness ratio in service condition are ranging between 1/362 to 1/120 and 1/1028 to 1/305 respectively, depending on the water depth of the joint.

The secant loading flexural stiffness ratios r_{bend} are presented in Figure V.18 (b) as well as the fitting curve. The flexural stiffness ratio experiences the same increasing trend as that in Figure V.18 (a). At the beginning of the test, the flexural stiffness of the tunnel structure is about 1/196 of that of the immersion joint. Then the ratio increases up to around 1/58 for an axial force of 1000kN. A stage with continuous increase follows as the axial force increases from 1000kN to 2000kN. After that, the ratio remains around 1/22. The peak ratios at different levels of axial force all appear in the situation of maximum axial force, among which the maximum value is 1/15.6. A linear-like relation between the axial force and the flexural ratio is also observed by the fitting curve with a R-square value of 0.9765. This flexural ratio behaves similarly as the axial force increase because in this situation the GINA-type seal is highly compressed and its stiffness varies little. Based on the interpolation method, the flexural loading stiffness ratio in service condition ranges from 1/29 to 1/212.

For the practical calculations, the axial and flexural stiffness ratios of the immersion joint can be predicted for different water depths, which are useful for simulations.

V.5. Summary and general conclusions

Although the behavior of the immersion joint subjected to axial force and bending moment was already investigated by other researchers (Kiyomiya et al., 1992), most published investigations

focused on the force-compression behavior under a single level of axial force or bending moment-rotation curves under a single level of bending moment. The relation between axial force and compression, the axial force and the bending moment, especially the issue regarding the stiffness, has much less been the subject of research. However, in the case of mechanical behavior of the immersion joint, these are of vital importance.

In order to study the behavior of the joint subjected to axial and bending moment in a comprehensive way, a model immersion joint composed by two model tunnel elements, was tested where the GINA-type rubber seal in the joint was the main concern.

The model immersion joint was loaded by an axial force and bending moment at the same time to simulate the initial water pressure at the joint in reality due to its specific construction method. The axial force was applied in five levels and at each level a cycle of the bending moment was applied to the joint without changing the axial force. After the application of each bending moment cycle, the axial force increased to the next level and the loading protocol was repeated until the fifth level of loading was finished. Then the unloading of the axial force followed until the axial force acting on the joint returned to zero.

From the experimental investigations, the following results were obtained:

(1) The hysteretic loop of the compression–force curve indicates that recovery of compression during unloading does follow the same path as for loading. The residual compression of the joint indicates that removal of the axial force is problematic for the water tightness of the joint. The axial stiffness of the immersion joint varies with the level of the axial force, whether loading or unloading. A fitting curve based on the compression curve of the joint was given and the loading and unloading axial stiffness of the immersion joint in different water depths can be predicted.

(2) Possible influencing factors of the results were performed to investigate the influencing factors on the axial behavior of the joint, namely the friction force, the length of the GINA rubber, the clamping system of the rubber and the shape of the GINA rubber. Except for the friction force, the behavior of the rubber was influenced by the properties of the rubber at different levels, resulting in an approximately 10% total difference. However, it is still far

smaller than 35% (the obtained difference). The modelling techniques and the used constitutive model for the rubber require further improvement to obtain more accurate results.

(3) The moment–rotation curve shows a hysteretic loop. This indicates that there is energy–dissipation during bending. However, the area of the loop reduces with increasing axial force. The deformation of the joint appears to be asymmetric as a residual rotation is observed at each bending cycle. The flexural stiffness of the joint was obtained and it was found that it increases with axial force during bending.

(4) The joint remains plane during bending. Rotation of the joint increases with bending moment but it decreases with axial force. When the axial force is at a low level, the joint behaved symmetrically and the rotation center remained in the geometric middle. As the axial force increased, an asymmetric bending behavior was observed and the rotation center moved from the middle to one side of the joint. The joint under compression and bending moment behaves in a non-linear way at service condition.

(5) The axial and flexural stiffness ratio of the joint to the tunnel element were obtained. The axial loading and unloading stiffness ratios both behave linearly along with the axial force based on the fitting curve. A similar trend can be found for the flexural stiffness ratio. In service condition, the axial loading and unloading stiffness of the joint fall in a relative linear state with values ranging from 1/360 to 1/120 and 1/1028 to 1/305 that of element respectively. For the flexural stiffness ratio, it varies between 1/212 and 1/29 of that of the tunnel element.

V.6. References

Boyce, M., Arruda, E., 1992. Constitutive Models of Rubber Elasticity: A Review. Rubber Chemistry and Technology. 73(3), 504-523.

Kiyomiya, O., Fujisawa, T., Yamada, M., et al., 1992. Mechanical Properties of Flexible Joint between Submerged Tunnel Elements. Report of the Port and Harbour Research Institute. No.728. (in Japanese)

Zheng, M., Wang, W., Chen, Z., et al., 2003. Determination for mechanical constants of rubber Mooney-Rilvin model. China Rubber Industry. 50(8), 462-465. (in Chinese)

Zuo, L., Xiao, F., 2008. A determination method for the coefficient in Mooney-Rivlin rubber constitute model. Machinery. 46(7), 38-40. (in Chinese)

CHAPTER VI

SHEAR PERFORMANCE OF THE JOINT

Istanbul Marmaray immersed tunnel, Turkey

(source unknown)

VI. Shear Performance of the Joint

VI.1. General introduction

When the joint is subjected to different loadings, besides the axial and flexural behavior, the shear behavior of the joint is also one of the main concerns for a safe and reliable water-proof design. Excessive shear deformation in the joint may result in a higher risk of leakage than the axial deformation due to the fact that the shear deformation is confined by the shear keys and the shear keys have a large shear capacity. In this respect, the shear performance of the joint was less focused on in research.

Unlike the axial or flexural behavior, the shear behavior of the joint involves both axial and shear loadings. Such combined loading submits the GINA rubber to a more complicated situation and the cooperation between the shear keys and the GINA rubber remains unclear. Previous research regarding the shear performance of the joint is rare and only the separate shear behavior of the rubber seal and the shear keys was found. It is assumed that the shear stiffness of the joint tends to be infinite as a simplification and the contribution of the rubber is not considered (Anastasopoulos et al., 2007; Lyngs, 2008). Such assumption seems to improve the calculation efficiency but to sacrifice the accuracy of the results. Furthermore, in current numerical research, the obtained results depend on the values of the input parameters, such as the shear stiffness of the joint subjected to axial and shear force and the lack of the experimental support makes the numerical results less convincing (Yu et al., 2012). Therefore, it is of crucial importance to investigate the shear performance of the joint by a large scale experiment.

In this chapter, first of all, the shear performance of the joint subjected to a cyclic static shear force with different levels of axial forces is presented in Section VI.2. The shear force-displacement curves are obtained as well as the shear stiffness of the joint. Then section VI.3 is dedicated to the dynamic performance of the joint subjected to a cyclic dynamic shear force with different levels of axial force. The influencing factors of the dynamic shear performance of the joint, namely the input shear frequency, the input shear amplitude and the axial force, are

discussed. A special attention was paid to the static and dynamic stiffness, which are discussed in Section VI.4 . Finally a brief summary of this chapter is given in Section VI.5.

VI.2. Static shear performance

VI.2.1. Brief introduction of the loading protocol

The loading protocol in this section is listed in Table VI.1. There are four loading cases in total, CSS-0-40, CSS-440-40, CSS-850-40 and CSS-1760-40 respectively. The first number represents the value of the axial force while the second one means the shear amplitude of ±40kN which is the same in all cases. The selected value of the axial force and the shear amplitude were justified in Chapter IV.

Figure VI.1(a) shows the loading process of this experiment. At the beginning, the expected axial force was applied to the joint, followed by a reciprocating shear force with an increasing amplitude of 10kN until reaching the maximum shear force of 40kN. This loading process was repeated with different levels of axial force. Figure VI.1 (b) demonstrated the expected deformations in the joint, which are compression and the relative shear displacement between the elements, and they were measured by four displacement transducers indicated in Figure IV.22 (a).

Table VI.1 Loading protocol for static shear test

Case No.	Axial force [kN]	Shear amplitude [kN]
CSS-0-40	0	±40
CSS-440-40	440	±40
CSS-850-40	850	±40
CSS-1760-40	1760	±40

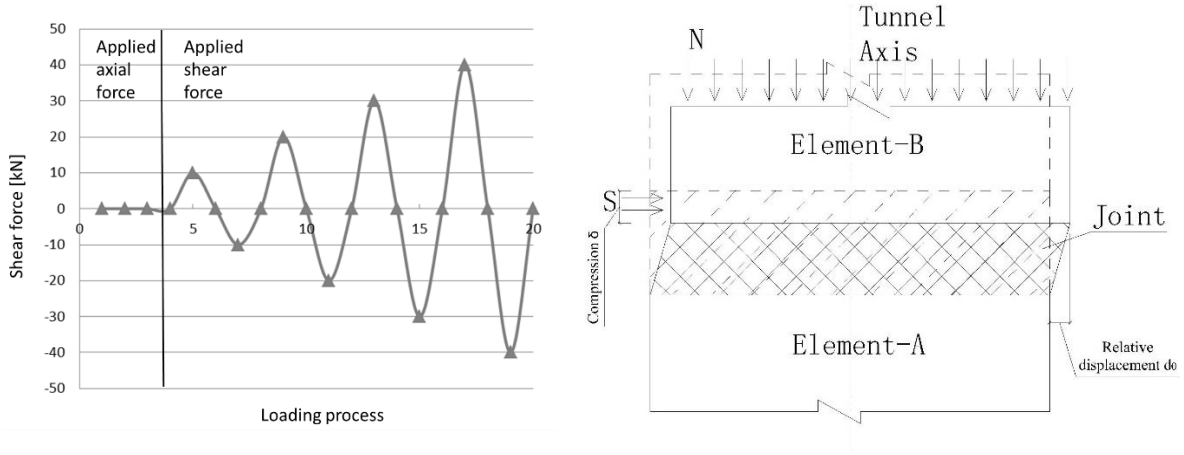

(a) Cyclic shear loading (b) Deformations of the joint

Figure VI.1 Loading protocol in this section and the expected deformation

VI.2.2. The recorded data and the displacement curve

The recorded shear displacement of the joint at each loading step (x-axis) are shown in Figure VI.2 for all cases. The number #1 to #4 indicate the number of transducers as mentioned before. It can be seen that the displacement basically follows the trend of the input shear force and the recorded data from the four transducers are in accordance with each other except #1. Therefore, the data from 1# were neglected. For the rest of the data, the displacement of the joint is taken as the average value from the three other transducers. The average displacement of the joint and the ratio of the force to the displacement in each case is listed in Table VI.2 and

Table VI.3 respectively.

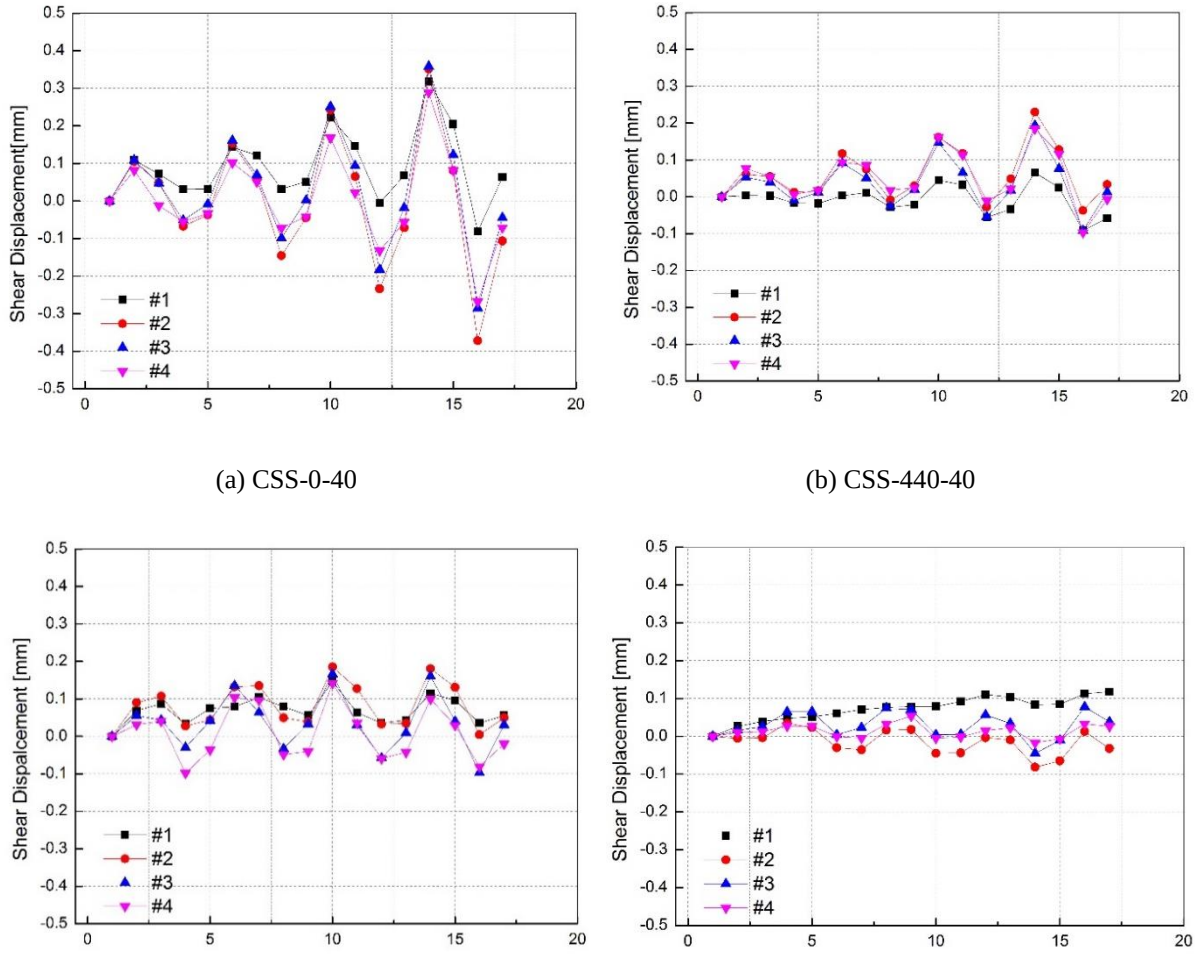

(a) CSS-0-40

(b) CSS-440-40

(c) CSS-850-40

(d) CSS-1760-40

Figure VI.2 Recorded data from the transducers

To obtain a more direct knowledge on the relation between the shear force and the shear displacement in Table VI.2, the force-displacement curves are drawn and shown in Figure VI.3. It can easily be observed that the shear displacement of the joint increases with the shear force under the same level of axial force. With the same shear force, the displacement decreases along with the axial force. The shear displacements in CSS-1760-40 are really small and are about 10 times smaller than those in CSS-0-40. That is because the higher the axial force, the stiffer the GINA rubber becomes, resulting in a higher shear stiffness. Moreover, the joint behaves almost elastically, showing little hysteresis and such hysteretic performance is less pronounced as the

axial force increases. Moreover, a residual dislocation occurs in all cases, indicating that the joint did not move back completely to its original position after unloading.

Table VI.2 Displacement of the joint [mm]

Shear force [kN]	CSS-0-40	CSS-440-40	CSS-850-40	CSS-1760-40
10	0.1009	0.0636	0.0615	-0.0067
-10	-0.0355	0.0032	-0.0167	-0.0421
20	0.1399	0.1011	0.1129	0.0087
-20	-0.0709	-0.0054	0.0121	-0.0414
30	0.2210	0.1571	0.1600	0.0152
-30	-0.1380	-0.0308	-0.0121	-0.0228
40	0.3290	0.20302	0.1389	0.0477
-40	-0.2514	-0.0751	-0.0342	-0.0414

Table VI.3 Ratio of shear force to shear displacement [kN/mm]

Shear force [kN]	CSS-0-40	CSS-440-40	CSS-850-40	CSS-1760-40
10	99.10	157.23	162.60	-1492.53
-10	281.69	-3125.00	598.80	237.52
20	142.95	197.82	177.14	2298.85
-20	282.08	3703.70	-1652.89	483.09
30	135.74	190.96	187.50	1973.68
-30	217.39	974.02	2479.33	1315.78
40	121.58	197.02	287.97	838.57
-40	159.10	532.62	1169.59	966.18

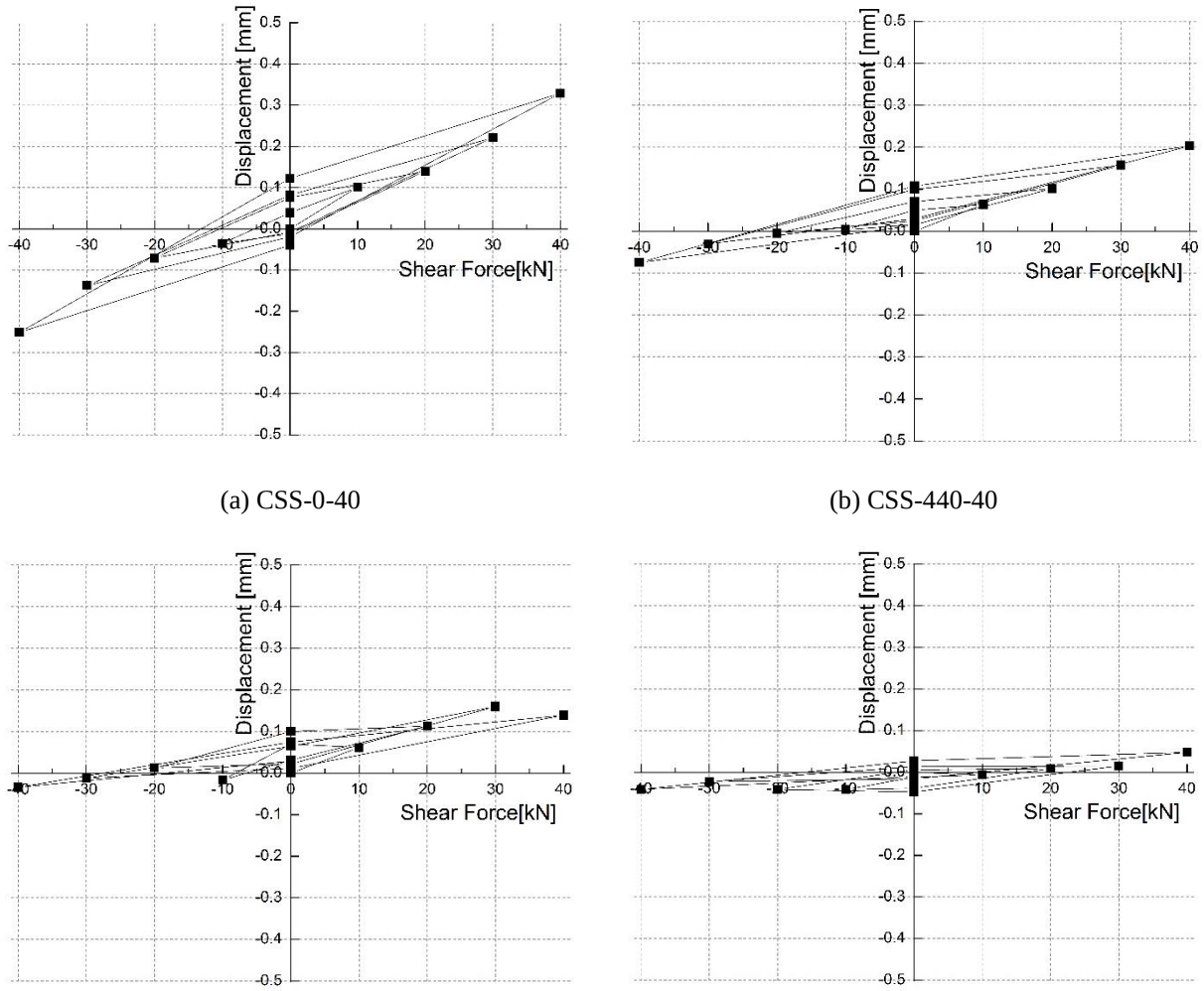

(a) CSS-0-40

(b) CSS-440-40

(c) CSS-850-40

(d) CSS-1760-40

Figure VI.3 Displacement-shear force curves of the joint

VI.2.3. Static shear stiffness and stiffness ratio

The static shear stiffness of the joint can be defined as follows:

$$k_j^s = \left|\frac{\Delta Q}{\Delta d_j}\right| \tag{VI.1}$$

where Q represents the difference between the maximum (40kN) and minimum (-40kN) shear force to minimize the error possibly caused by the too small shear force, which is 80kN in this case, and d_j is the difference between the corresponding shear displacements.

Based on this equation, the static shear stiffness of the joint can be calculated and is shown in Table VI.4 and the relation between the stiffness and the axial force is presented in Figure VI.4. The fitted curve, with a correlation coefficient of 0.99, is also shown. Obviously, the static shear stiffness increases linearly with the axial force despite the non-linear axial performance of the joint. The shear stiffness under the maximum axial force is about 6.5 times that without axial force. In the service condition, the stiffness under maximum water pressure (1760kN) is about 3 times that under minimum water pressure (440kN). It should be noted that there is no axial force in the case CSS-0-40, meaning that the GINA rubber was not compressed at all. Hence the shear stiffness in this case is only provided by the shear keys and the shear stiffness of the shear keys is 137.84kN/mm under the presented shear load.

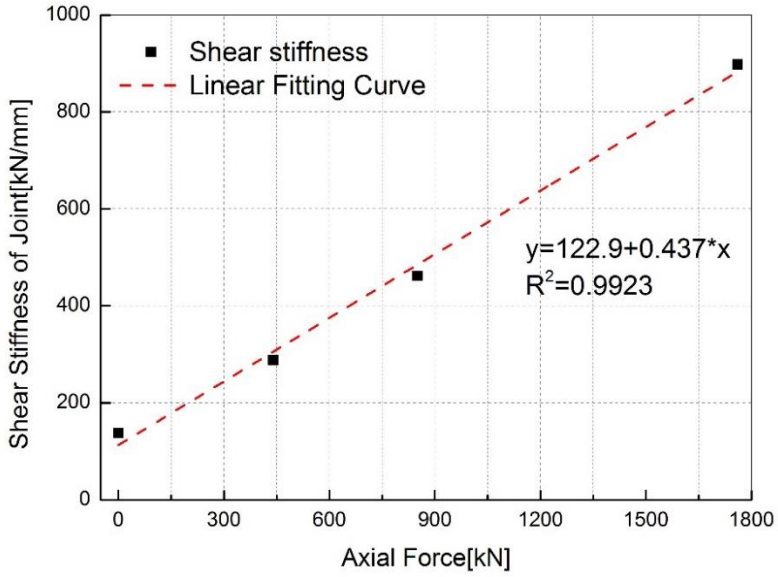

Figure VI.4 Relation between the shear stiffness and the axial force

Table VI.4 Static shear stiffness of the joint

Loading case	CSS-0-40	CSS-440-40	CSS-850-40	CSS-1760-40
Shear stiffness [kN/mm]	137.8	287.7	462.2	897.9

The shear stiffness ratio r_s of the joint to the tunnel element is defined as follows:

$$r_s = \frac{k_j^s}{k_s^s} \tag{VI.2}$$

where k_j^s is the static shear stiffness of the joint obtained from the experiment; k_s^s is the shear stiffness of the tunnel element (per unit length), which is determined by the properties of the concrete and the cross section of the tunnel.

In this experiment, C50 concrete was used and the Young's modulus is 3.45×10^4MPa. Then the shear modulus can be calculated as 1.45×10^4MPa based on the elastic mechanics. The area of the cross section of the tunnel element is 1.490m^2. Then the shear stiffness of the tunnel element per unit length is calculated by the product of shear modulus and the shear area, which is 2.16×10^4kN/mm.

Based on Eq. (VI.2), the stiffness ratio is calculated and shown in Figure VI.5. It can be seen that the shear stiffness of the tunnel element is one to two orders of magnitude larger than that of the joint, which varies from 24 to 156 times. In the beginning, when the axial force is 0kN, the stiffness ratio is calculated as 1/156.8. When the axial force increases up to 440kN, the ratio soon increases up to 1/76.1. Then the stiffness ratio gradually increases. It reaches 1/24.1 under the maximum axial force, which means the stiffness of the tunnel is still about 24 times that of the joint. In the service condition, the shear stiffness ratio ranges from 1/76.1 to 1/24.1. Compared to the axial and flexural stiffness of the joint in Chapter IV, the shear stiffness ratio is smaller, showing that the joint has a relatively stiffer behavior in shear. The obtained shear ratio can be used in numerical analysis.

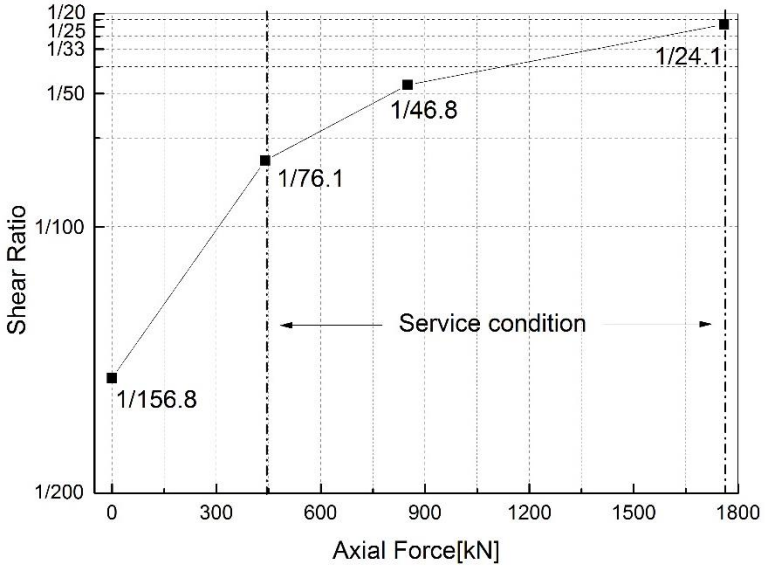

Figure VI.5 Static shear stiffness ratio

VI.3. Dynamic shear performance

VI.3.1. Brief introduction of the loading protocol

The influencing factors of the dynamic shear performance of the joint, such as the axial force, the input frequency, and the input shear amplitude, are all considered in this section. The loading cases in the dynamic experiment is designated as CSD-A-B-C. The letter A represents the axial force, which is 0kN, 440kN and 1760kN respectively. The letter B means the shear frequency, namely 1Hz, 2Hz, 3Hz and 4.2Hz. The last letter C is the input shear amplitudes and they are equal to 10kN, 20kN, 30kN and 40kN, which are the same as in the static shear test. By the combination of these influencing factor, there are in total 48 different loading cases. It should be noted the value of these factors has been justified in Chapter IV. Figure VI.6 shows the loading process of the dynamic test and the linear reciprocating loading was applied with a duration of 8 seconds. Q_{max} means the input shear amplitude as mentioned.

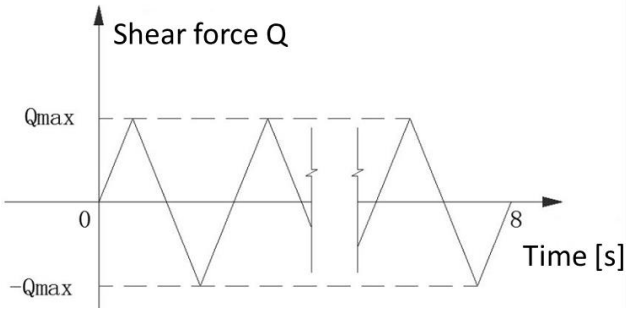

Figure VI.6 Loading process of the dynamic test

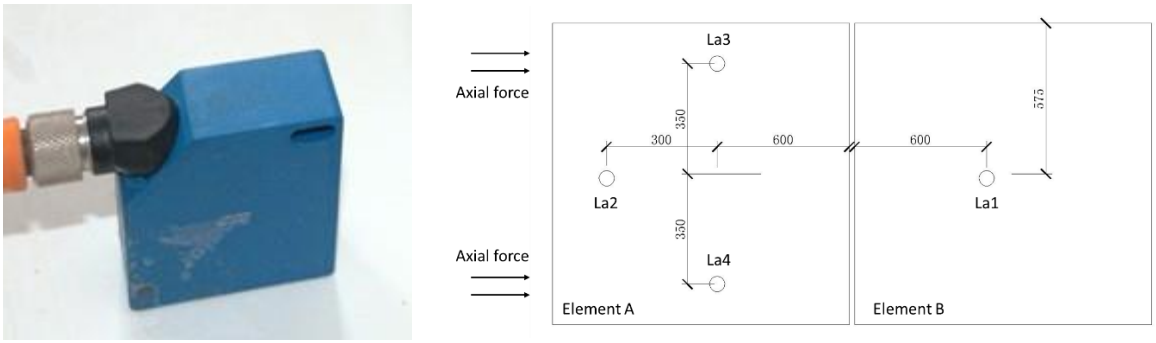

(a) Photo of the laser transducer (b) Position of the laser transducers

Figure VI.7 Laser transducers for the dynamic test

To obtain the shear deformation of the joint, special transducers, laser displacement transducers (Figure VI.7 (a)), were used to record the dynamic deformations. As there are in total only four laser transducers, a specific positioning was applied in this experiment. As mentioned, the element B was fixed while the element A was moveable. Hence, one laser transducer is placed on the side of element B along the shear direction and the other three are installed on the element A as shown in Figure VI.7 (b). It should be noted that the obtained deformations from the laser transducers are the absolute deformations against the ground. Therefore, the dislocation d_{dyn} of the joint can be calculated as follows:

$$d_{dyn} = \frac{d_{la2}+d_{la3}+d_{la4}}{3} - d_{la1} \tag{VI.3}$$

where d_{la1} to d_{la4} represent the recorded displacement from laser transducers La1 to La4.

VI.3.2. Recorded data

Only the recorded data from some cases are shown here as there are 48 loading cases in total. Two groups of data from CSD-0-2-X and CSD-0-X-20 (X here means all the values) are provided in Figure VI.8 and Figure VI.9 respectively. In general, from the selected data, the displacements basically follow the trend of the input shear force as shown in Figure VI.6. It can be observed that the shear displacements behave stable under the same loading protocol and there is no jumping in the curves though the displacement has a small fluctuation at each peak of the cycles.

For example, from Figure VI.8 (a) to (d), it is obvious that the shear displacement increases along with the shear amplitude when the joint is subjected to the same axial force and input frequency. Details are given in the following section.

To sum up, the obtained data appear to be reliable and the next step is to proceed with the analysis.

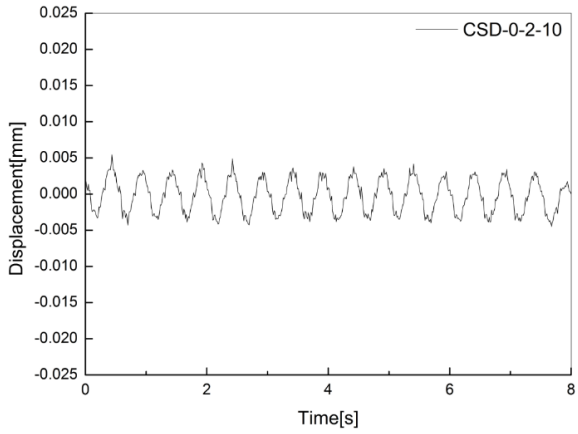

(a) CSD-0-2-10

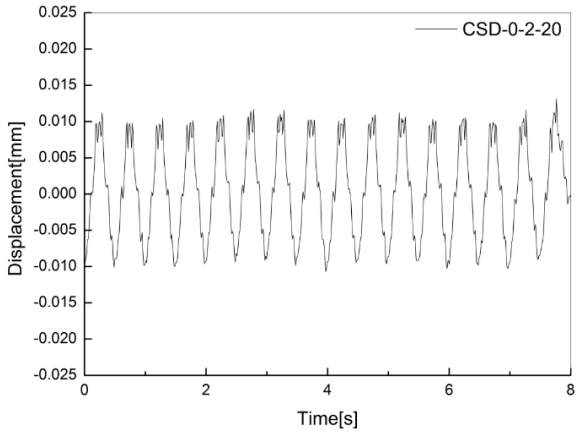

(b) CSD-0-2-20

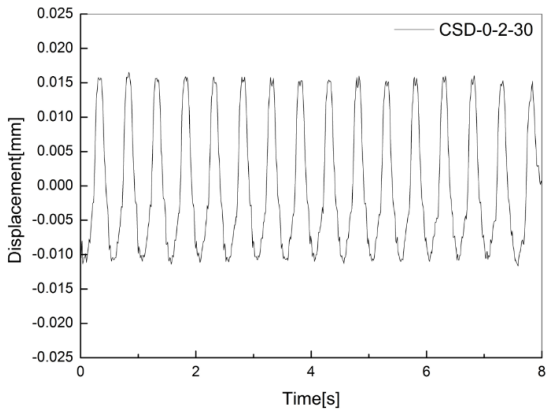

(c) CSD-0-2-30

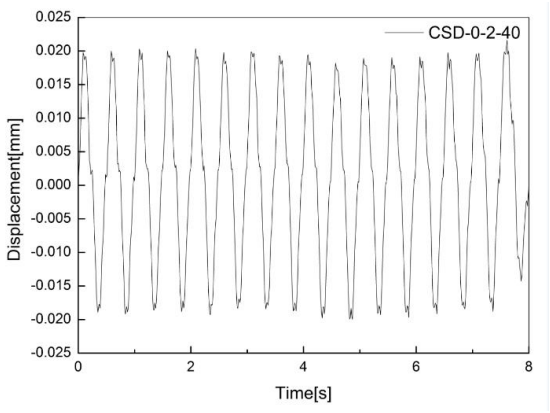

(d) CSD-0-2-40

Figure VI.8 Recorded data of CSD-0-2-X

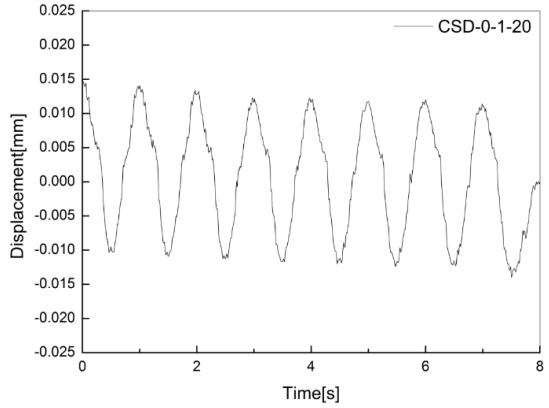

(a) CSD-0-1-20

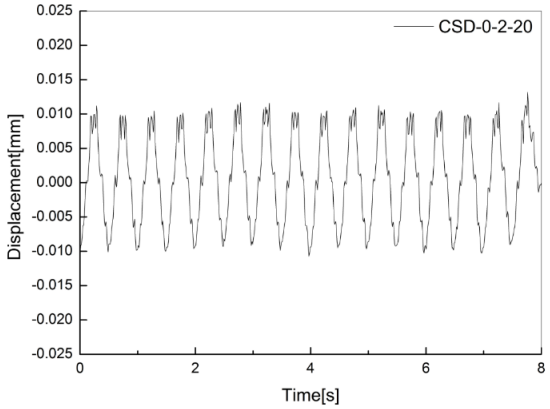

(b) CSD-0-2-20

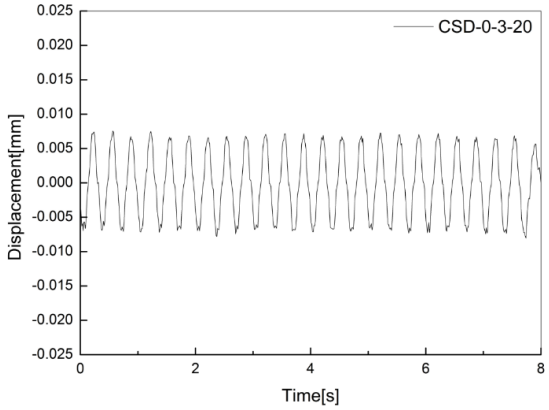

(c) CSD-0-3-20

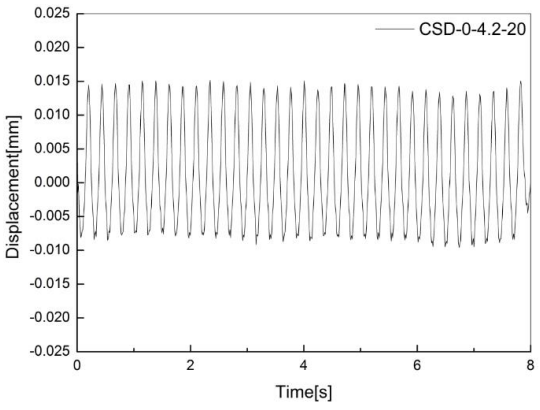

(d) CSD-0-4.2-20

Figure VI.9 Recorded data of CSD-0-X-20

VI.3.3. Dynamic stiffness

In order to obtain the dynamic stiffness of the joint, the following method is applied. Firstly the data of the first and the last two seconds are cut off to obtain a stable part of the recorded data. Secondly, the first order Fourier equation *f(t)* in the Curve Fitting Tool of Matlab (2011b) (shown in Figure VI.10) is applied to describe the curves.

$$f(t) = a_0 + a_1 \cos(\omega t) + b_1 \sin(\omega t) \tag{VI.4}$$

where a_0, a_1, b_1 and ω are the fitting coefficients.

The dynamic shear stiffness of the joint could be defined as follows:

$$k_j^d = \left| \frac{Q_{max} - Q_{min}}{d_{max} - d_{min}} \right| \tag{VI.5}$$

where Q_{max} and Q_{min} are the positive and negative amplitude of the shear displacement, which means $Q_{max} = -Q_{min}$ in this case; d_{max} and d_{min} are the corresponding maximum and minimum shear displacement respectively;

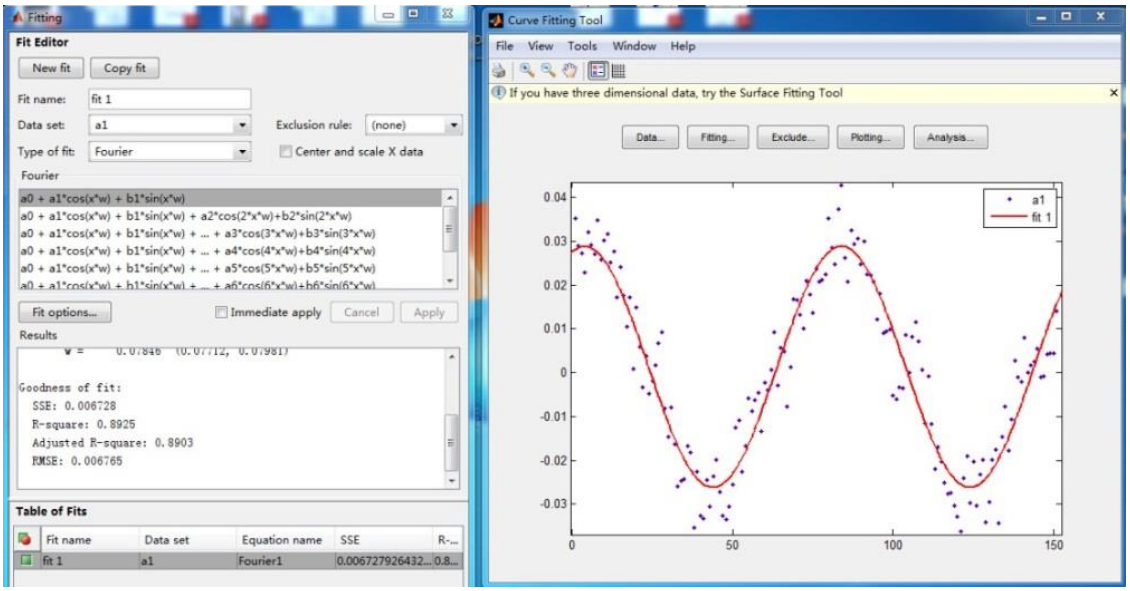

Figure VI.10 CFTool in Matlab (2011b)

It can be derived that:

$$\begin{cases} d_{max} = a_0 + \sqrt{a_1^2 + b_1^2} \\ d_{min} = a_0 - \sqrt{a_1^2 + b_1^2} \end{cases} \tag{VI.6}$$

Therefore, based on Eq. (VI.6), the dynamic stiffness of the joint can be calculated as follows:

$$k_j^d = \left|\frac{Q_{max} - Q_{min}}{d_{max} - d_{min}}\right| = \frac{Q_{max}}{\sqrt{a_1^2 + b_1^2}} \tag{VI.7}$$

Based on Eq. (VI.7), the dynamic stiffness of the joint can be approximately calculated and the influencing factors, such as the axial force, the input frequency and the shear amplitude, can be analyzed. In the following, the results are discussed in detail.

(1) Axial force

Figure VI.11 (a) to (d) show the relation between the dynamic shear stiffness and the axial force with different input frequencies. Obviously, from all the loading cases, the higher axial force introduces the higher dynamic stiffness due to the influence from the GINA rubber. However, under different input frequencies, the increase of the dynamic stiffness varies. For instance, when the input frequency is 1Hz, a larger increase of the dynamic stiffness can be found, compared to the results from the other input frequencies, and the smallest shear amplitude has the largest increase. In Figure VI.11 (a) to (c), the increase of the dynamic stiffness becomes less and is observed to be linear. In general, the maximum dynamic stiffness of the joint is 2.5 to 6 times the minimum one. Note that if there is no axial force in the joint, the dynamic shear stiffness of the joint is provided by the shear keys only.

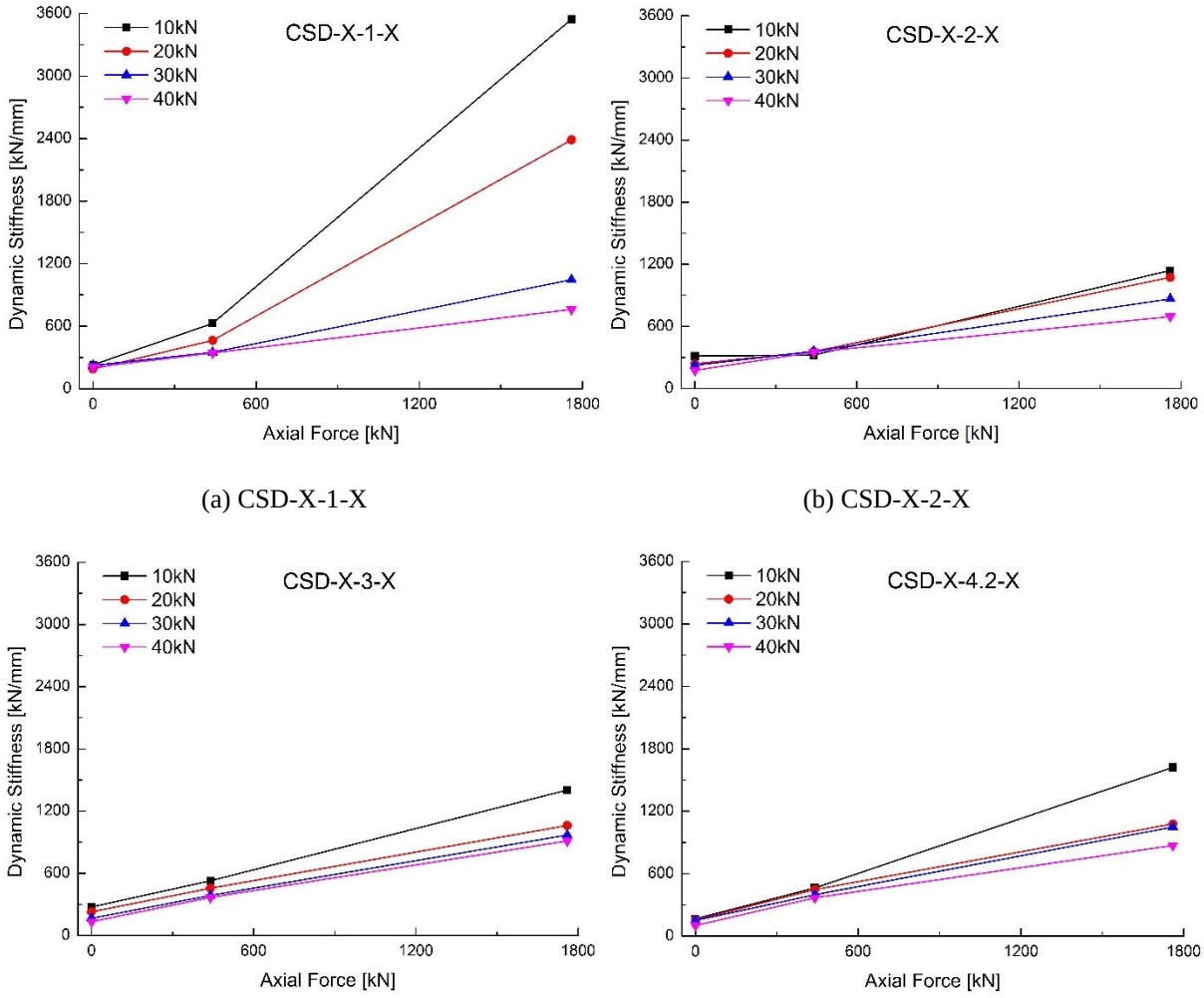

(a) CSD-X-1-X

(b) CSD-X-2-X

(c) CSD-X-3-X

(d) CSD-X-4.2-X

Figure VI.11 Dynamic shear stiffness as a function of the axial force

(2) Shear frequency

The relation between the dynamic stiffness and the shear frequency is given by Figure VI.12 (a) to (c). When the axial force is 0kN together with a shear amplitude of 10kN or 20kN, the dynamic shear stiffness of the joint has a short increase then followed by a gradual decrease as the dynamic frequency increases from 1Hz to 4.2Hz. As the shear amplitude increases up to 30kN and 40kN, only the decreasing trend is found. Considering the case with an axial force of

440kN, the reverse trend is observed. In other words, a short decrease of the dynamic stiffness is observed then it increases again under a shear amplitude of 10kN or 20kN while the dynamic stiffness experiences the increasing trend when the shear amplitude is 30kN and 40kN. As a result of an axial force of 1760kN, the dynamic stiffness seems to have different trends compared to the loading case with the axial force of 0kN and 440kN. In general, it is difficult to determine that how the shear frequency has an impact on the dynamic stiffness as various trends are found. However, when the shear amplitude is small, the dynamic stiffness seems to behave less stable, of which value changes a lot.

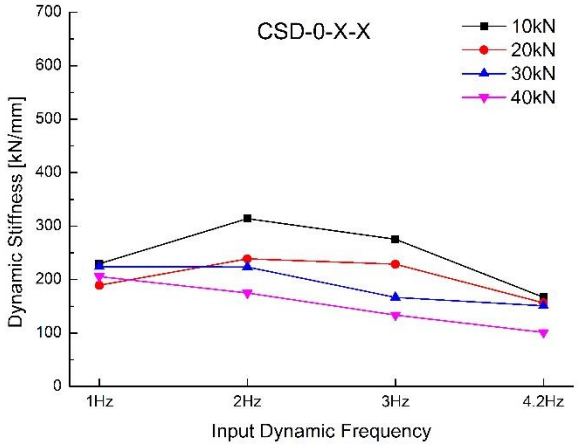

(a) CSD-0-X-X

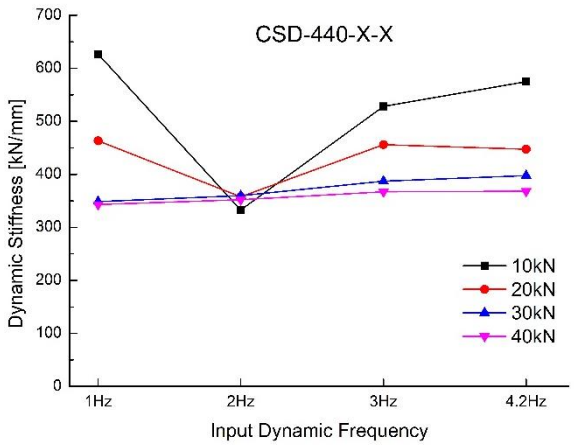

(b) CSD-440-X-X

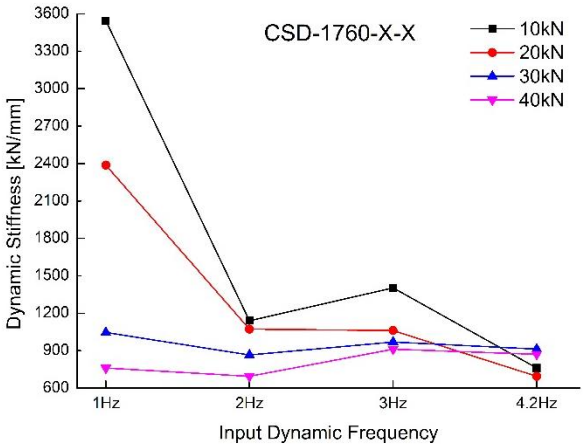

(c) CSD-1760-X-X

Figure VI.12 Dynamic shear stiffness as a function of the shear frequency

(3) Shear amplitude

Figure VI.13 (a) to (c) shows how the dynamic stiffness of the joint behaves under different shear amplitudes. When the axial force is 0kN as shown in Figure VI.13(a), the dynamic stiffness basically experiences a slight decreasing trend. The dynamic stiffness changes from 229kN/mm-169kN/mm to 205kN/mm-101kN/mm. When the axial force is 440kN, the same decreasing trend but with a steeper slope is observed, except the case with the shear frequency of 2Hz. The non-uniform results of 2Hz are possibly due to error in the test. In Figure VI.13 (b), the dynamic stiffness of the joint changes from 626kN/mm-332kN/mm to 368kN/mm-343kN/mm. Finally, a decreasing trend is also found for an axial force of 1760kN. The dynamic stiffness decreases remarkably, from 3545kN/mm to 761kN/mm at a shear frequency of 1Hz. At the other levels of shear frequency, a decreasing trend is observed but the decreasing in amplitude is smaller than that for a shear frequency of 1Hz, which may be caused by an error. In this case, the dynamic stiffness ranges from 1622kN/mm-1140kN/mm to 913kN/mm-694kN/mm.

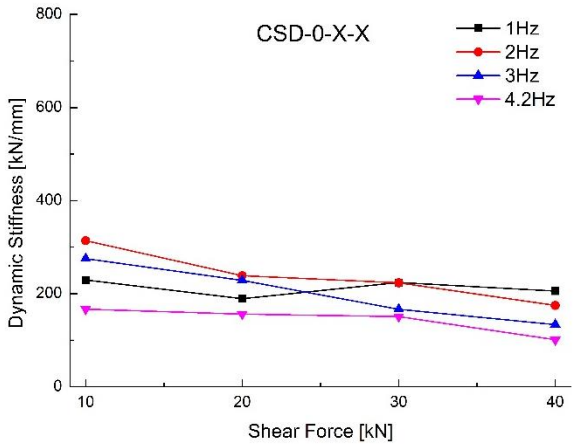

(a) CSD-0-X-X

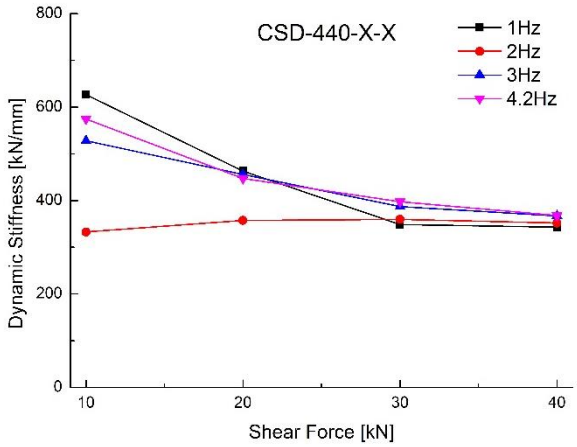

(b) CSD-440-X-X

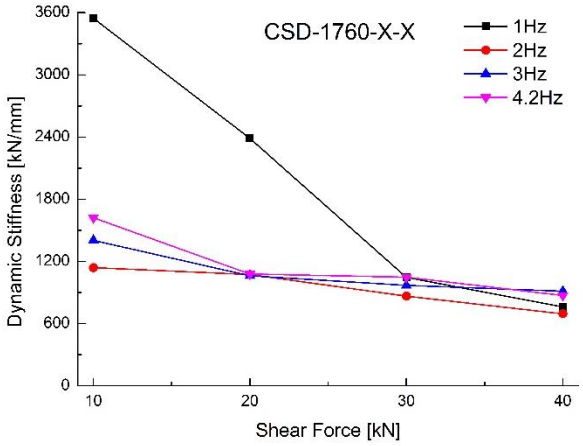

(c) CSD-1760-X-X

Figure VI.13 Dynamic shear stiffness as a function of the shear amplitude

(4) Summary of the influencing factors

As can be seen, under a larger axial force the dynamic stiffness of the joint increases as the GINA rubber becomes stiffer. As for the other factors, it seems that the dynamic stiffness decreases with the larger shear amplitude and the relation between the shear frequency and the dynamic stiffness is not obvious. Moreover, when the shear frequency and the shear amplitude are small, it seems the dynamic stiffness of the joint behaves in a rather strange way and differently from the other cases. Therefore, in order to calculate the dynamic stiffness, only the results from CSD-X-3-40 and CSD-X-4.2-40 are chosen and the dynamic stiffness of the joint is the average value from these two cases, which is listed in Table VI.5. The value for the axial force of 850kN is obtained through linear interpolation.

Table VI.5 Dynamic shear stiffness of the joint

Axial force [kN]	0	440	850	1760
Dynamic stiffness [kN/mm]	117.3	367.6	520.2	891.2

VI.4. Comparison between the static and dynamic stiffness

Both the static and dynamic stiffness of the joint are given in Figure VI.14. In general, these two stiffnesses both show an almost linear trend. At the beginning of the curve, when the joint is subjected to no axial force, the stiffnesses are almost the same. As the axial force increases up to 440kN, the dynamic stiffness experiences a faster increasing trend than the static one and at that point the dynamic stiffness is 1.28 times the static one as the rubber is loading rate-dependent material (Johnson et al., 1992). With further axial force application, the difference becomes less and the two stiffnesses are almost the same again when the axial force reaches the value of 1760kN. It should be noted that if the cases with zero axial force are not considered, the difference between the dynamic and static results experiences a decreasing trend with increasing axial force.

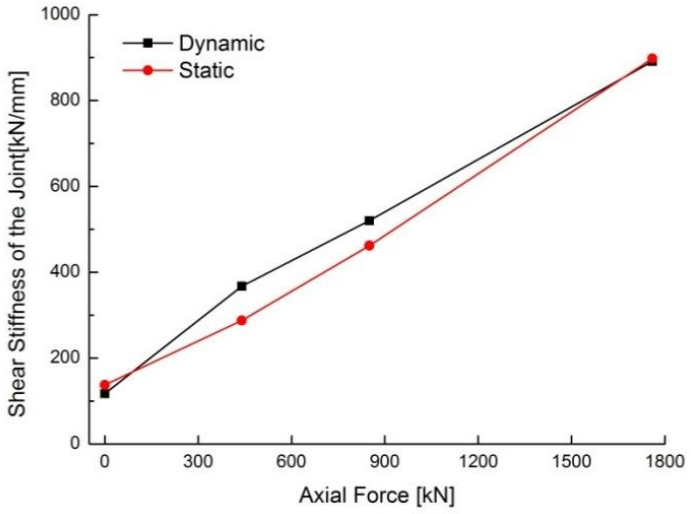

Figure VI.14 Comparison between the static and dynamic stiffness

Initially without axial force, it is confirmed that both the stiffnesses are approximately the same possibly due to the small shear amplitude and the input frequency that the shear keys remain in elastic stage. As a result of the application of axial force, the GINA rubber starts to get involved in shear resistance. Due to the non-elastic properties of the rubber, the dynamic response of the joint becomes smaller, leading to a relatively larger stiffness compared to the static stiffness. However, eventually these two stiffnesses comes to the same value at the axial force of 1760kN.

At this load, the GINA rubber is highly compressed, exhibiting a significant stiffening or hardening (Cornelius et al., 2002), and the influence of the non-elastic behavior of the rubber is, to some extent, eliminated. However, the contribution of the GINA rubber in shear direction is unneglectable. In the service condition, between the maximum and minimum water pressure, the dynamic stiffness has a maximum 1.3 times the static one.

VI.5. Summary

The shear stiffness of the immersion joint is of crucial importance regarding the investigation of the shear behavior of the joint. In order to investigate the shear stiffness of the joint subjected to static and dynamic loading respectively, a series of experiments was conducted. In each loading case, an axial force was imposed to the joint, followed by a cyclic static or dynamic shear force. The shear force-displacement curves under different loading cases were obtained. The parametric analysis of the shear stiffness was given by considering the influence of the axial force, the shear amplitude and the shear frequency (in the dynamic part).

Based on the experimental results, the following conclusions are obtained:

(1) The relation between the static shear force and the shear displacement is observed to be linear with increasing shear force, and the higher axial force, the smaller the shear displacement. The obtained static stiffness also experiences a linear increasing trend with the axial force. When there is no axial force in the joint, the stiffness of the joint is provided only by the shear keys with a calculated value of 137.8kN/mm, which is the smallest value in this case. Under service conditions, between the maximum and minimum water pressure, the static shear stiffness ranges from 287.7kN/mm to 897.9kN/mm.

(2) The shear stiffness ratio of the joint to that of the tunnel element was defined and calculated. In the service condition, the shear stiffness ratio ranges from 1/76.1 to 1/24.1. Compared to the axial and flexural stiffness of the joint, the shear stiffness ratio is smaller, showing that the joint has a relatively stiffer behavior in shear.

(3) The dynamic displacement responses of the joint were obtained by using the fitting curve from the first order Fourier equation. Accordingly, the equation for the dynamic stiffness of the joint was given. By a parametric study, the influences of the axial force, the shear amplitude and the shear frequency was provided. Experimental results show that a larger axial force can increase the dynamic stiffness of the joint and the two other factors seem to have less impact on the dynamic stiffness. As calculated, the dynamic stiffness of the joint under maximum and minimum water pressure is 367.6kN/mm and 891.2kN/mm respectively.

(4) By comparison between the static and dynamic stiffness, the differences between these are not that large. For the axial force equal to 0kN and 1760kN, the two stiffnesses are almost the same. In between, the dynamic stiffness is a bit larger than the static one and the difference reaches a peak at the axial force of 440kN. At this point, the dynamic stiffness is 1.28 times higher than the static one.

VI.6. References

Anastasopoulos, I., Gerolymos, N., Drosos, V., 2007. Nonlinear Response of Deep Immersed Tunnel to Strong Seismic Shaking. Journal of Geotechnical and Geoenvironmental Engineering. 133, 1067-1090.

Cornelius, O., Saccomandi, G., 2002. Constitutive Modelling of Rubber-like and Biological Materials with Limiting Chain Extensibility. Mathematics and Mechanics of Solids. 7(4), 353-371.

Johnson, A., Quigley, C., 1992. A viscohyperelastic Maxwell model for rubber viscoelasticity. Rubber Chemistry and Technology. 65(1), 137-153.

Lyngs, J., 2008. Model accuracy in aseismic design of immersed tunnel. Master thesis, Aalborg University, Aalborg, Denmark.

Mathworks Inc., 2011b. User's Guide: Curve Fitting Toolbox.

Yu, H., Yuan, Y., Liu, H., et al., 2012. Mechanical Model and Analytical Solution for Stiffness in the Joints of an Immersed-Tube Tunnel. Engineering Mechanics. 31(6), 145-150. (in Chinese)

CHAPTER VII

SHEAR CAPACITY OF A JOINT SUBJECTED TO COMBINED LOADINGS

Coatzacoalcos immersed tunnel, Mexico

(source unknown)

VII. Shear Capacity of a Joint Subjected to Combined Loadings

VII.1. General introduction

Besides the elastic shear stiffness of the joint, the shear capacity of the joint subjected to extreme loading is also one of the most important concerns for the design of the joint. However, research related to this issue seems to be rarely found although some experiments have been performed on the performance of shear keys. In some previous numerical analyses, the stiffness of the shear keys is assumed as infinity, which could be satisfactory for a simplification in an elastic analysis but it does not correspond to reality. This may be due to the fact the in actual design, the shear keys are designed to resist the shear force through their high shear strength. In this regard, the shear capacity of the joint was never considered and included in previous researches on immersed tunneling though such techniques have been used for many years. In order to investigate the shear capacity of a joint, a series experiments were conducted, involving two types of shear keys, i.e. steel shear keys and reinforced concrete shear keys respectively. The shear capacity of the joint was analyzed as well as the failure mode.

This chapter is divided into two parts, one for steel shear keys and the other one for concrete shear keys respectively. First of all, Part I for the steel shear keys is provided. Section VII.2 provides a brief introduction on this part of the test, followed by Section VII.3 which presents the results of the shear stiffness. Sections VII.4 and VII.5 give the detailed analysis and discussion on the failure mode and the shear capacity and of the joint respectively.

Part II presents the results of the joint with the reinforced concrete shear keys. A brief introduction of this part is given in Section VII.6. Then Sections VII.7 to VII.9 discuss the shear stiffness, failure mode and shear capacity of this type of joint respectively.

Finally, a comparison between the results of the joint with steel and concrete shear keys is made (Section VII.10), followed by a general summary of this chapter.

PART I Steel Shear Keys

VII.2. Brief introduction and recorded data

VII.2.1. Brief introduction

As mentioned in Chapter IV, the justification for the detailed design of the steel shear keys is provided mainly according to the geometric scale in this test. Two types of steel shear keys, namely HSK1 and HSK2 are considered, staggering with each other. The information on these two shear keys is listed in Table VII.1. Note that the HSK2 has a smaller shear capacity, meaning that the HSK2 is expected to fail first during the test.

Table VII.1 Information on steel shear keys

	Dimension [mm]	Configuration of bolts	Ultimate shear capacity [kN]
HSK1	240x75x55	$8\phi12$ and $2\phi8$	420
HSK2	240x75x55	$4\phi10$ and $4\phi6$	180

A combination of force control and displacement control is adopted in this test. At the beginning of the test, the shear displacement is very small and a force-control is more reasonable. However, as the test continues, especially when the joint enters Stage 4, the joint may suffer from a sudden brittle failure and a gradual failure will not occur if keeping the force increasing. That is why during the test, a force-control is replaced by a displacement-control. Therefore, the loading procedure in this case is (1) Apply the axial force of 850kN and keep it constant during the test to simulate the initial water pressure; (2) The reciprocating shear force with increasing amplitude is imposed by an actuator until the shear force reaches 400kN; (3) A reciprocating shear deformation is applied until the failure of the joint. The loading process was already explained in Chapter IV.

The shear deformation as well as the axial deformation are measured and recorded by a data acquisition system. As shown in Figure VII.1, transducers 1 to 4 are installed to measure relative shear deformations and the other transducers are for measuring the axial deformation.

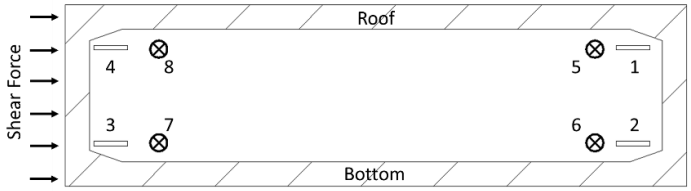

Figure VII.1 Layout of the transducers

VII.2.2. The recorded data and the displacement curves

The mean recorded average compression is measured as 9.31 mm at the axial force of 850kN with transducers 5 to 8 (see Figure VII.1). Data of the relative shear displacement from the transducers 1 to 4 via a data recording acquisition system are plotted in Figure VII.2 and the x-axis represents the data from each loading step. The numbers 1 till 4 in the legend represent the transducers 1 till 4 respectively. It shows that the data from the four transducers are nearly identical to each other during the whole loading process, except for the last part of the test. Hence, the shear displacement of the joint can be taken as the average of the values measured by the four transducers.

The shear force versus shear displacement is shown in Figure VII.3, in which "positive" and "negative" represent the loading directions. It can be seen that under quasi-static reciprocal loading, the joint behaves hysteretically. As long as the displacement of the joint ranges between 0 and 2.50mm, a linear elastic behavior and minor residual displacements are observed. The deformation of the joint is restored to its initial position. As the shear displacement increases up to around 7mm, the rate of increase of the peak shear force starts to slow down gradually. Then the test switches to displacement-control. The shear force no longer increases with the displacement and it starts to go up and down, the maximum basically remaining around

500kN. The hysteretic loop starts after the shear displacement exceeds 2.50mm and from then on the hysteresis effect keeps growing until the end of the test.

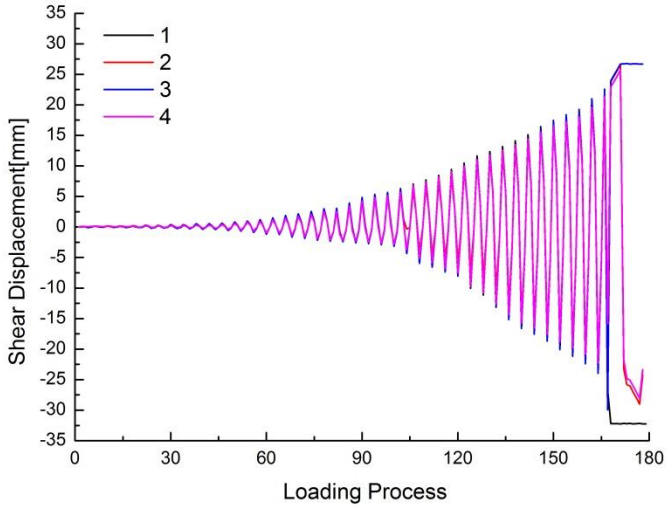

Figure VII.2 Data of shear displacement recorded by transducers #1-#4 (Steel shear keys)

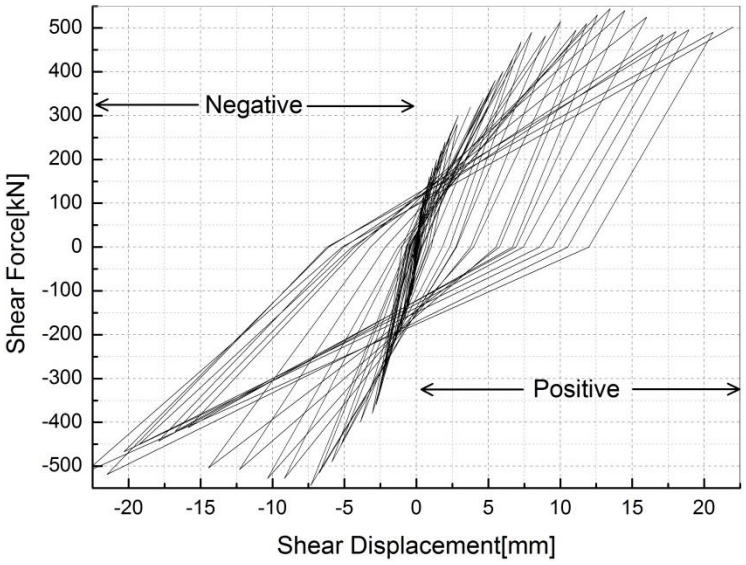

Figure VII.3 Shear force-displacement curves (Steel shear keys)

VII.3. Shear stiffness (Steel shear keys)

The envelop shear force-displacement curve of the joint is derived by selecting the peak point if each hysteretic loop from Figure VII.3. Consecutive points are connected by a line, resulting in Figure VII.4, in which both the Positive and Negative envelope curves are placed in the first quadrant for the ease of comparison. Based on the obtained shear performance of the joint, the complete behavior of the joint can be divided into 4 stages.

• Stage I: At the beginning of the test, from 0mm to 0.50mm, it is clear that the positive behavior of the joint is in accordance with the negative behavior, indicating that the same behavior occurs in both directions. The steepest part of the curves can be found in this stage, while the shear displacement is relatively small.

• Stage II: As the test continues, the slope of the envelope curves starts to reduce slightly with small differences between both directions. The two curves clearly split after the shear displacement increases up to around 2.50mm, indicating a difference between the behavior in the two directions.

• Stage III: In this stage the first damage within the joint occurs (details will be discussed in Section VII.4), resulting in the separation of both curves. From a displacement of about 3mm on, both curves remain almost parallel until the negative curve reaches its peak value at a shear displacement of about 7mm.

• Stage IV: The shear force fluctuates around 500kN as mentioned above. The curves go up and down and the joint entered into a state of increasing displacement without much increase of the shear force in the 'Positive' curve but decrease of the shear force in the 'Negative' curve. This corresponds to failure of the shear keys and the rubber seal (to be discussed in Section VII.4).

It can be seen that the positive and negative behavior of the joint are basically in accordance with each other, though there are some differences found in Stage IV. In other words, the joint almost behaved synchronously at the beginning of the test and then, when the joint entered the

last stage, an anti-synchronous behavior occurs, due to the failure of the shear keys, which influences the displacements in the 'positive' and 'negative' direction in a different way.

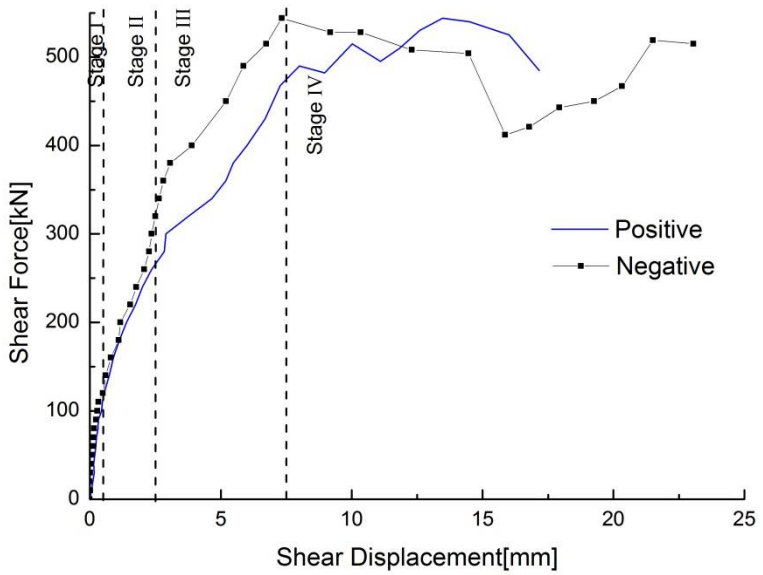

Figure VII.4 Envelope curve of the shear behavior of the joint (Steel shear keys)

Based on that, the shear stiffness, an important parameter in the evaluation of the shear performance of the joint, can be calculated. Under the axial force of 850kN, from equation (5) the shear stiffness k^{sf} at each loading step *i* is obtained, which is the slope of the secant line at that point:

$$k_i^{sf} = \frac{Q_i}{d_i} \tag{VII.1}$$

where Q_i and d_i are the shear force and the shear displacement of the joint respectively at the end of step *i* of the test. The calculated stiffnesses for both directions are shown in Figure VII.5. The curve is divided into the same four stages as mentioned before.

It can be seen that, as the shear displacement increases, the shear stiffnesses from the two curves are completely different at Stage I. For the positive direction, the curve fluctuates at around 250kN/mm while the stiffnesses in the 'negative' curve are relatively large (maximum:

2489kN/mm). At this stage, the shear displacements are very small (< 0.5mm). The installation inaccuracies of the reaction frame may be of the same order of magnitude as the shear displacement in this stage, which results in significant fluctuations and dissimilarities in the value of k_i^{sf}. Both curves of the stiffness start to drop in Stage II, in which the value ranges decreases from 200 to 100kN/mm, showing a degradation of the joint characteristics. In Stage III, the stiffness keeps decreasing but more slowly. The shear stiffness drops down to around 60kN/mm before the joint enters into the final failure Stage IV. In this situation, the stiffness of the joint decreases and eventually tends to be constant value at around 25kN/mm. It should be noted that the calculated shear stiffness of the model reinforcement concrete element is 21,610kN/mm. This means that the shear stiffness ratio between the model element and the model joint ranges from about 54 to 864 at the given compressive force. Since the shear stiffness ratio is a non-dimensional value, it is more applicable than the obtained shear stiffness of the joint in further numerical analyses due to its scale-independent character.

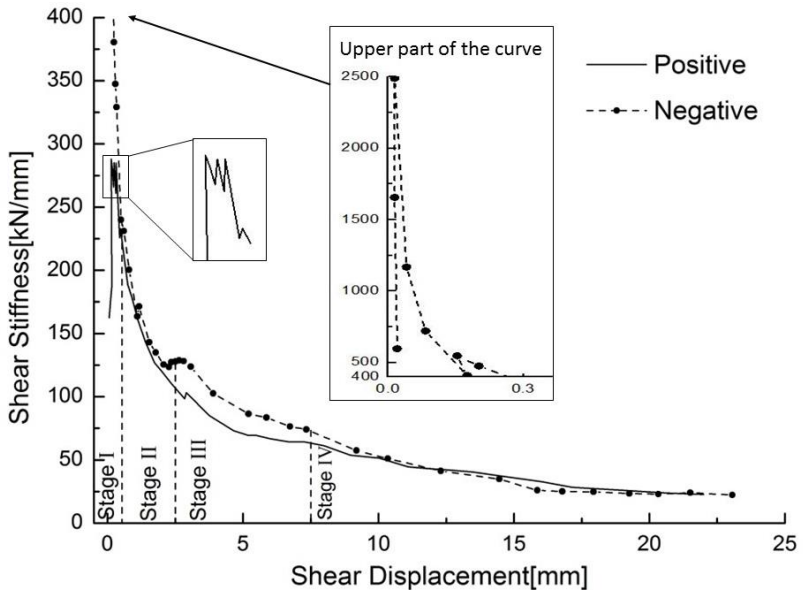

Figure VII.5 Relationship between shear stiffness and shear displacement (Steel shear keys)

Compared to the obtained static shear stiffness in Chapter VI, the shear stiffness here illustrates the stiffness of the joint after the elastic stage especially in the stage when the joint starts to fail. It can be noticed that a nonlinear decreasing behavior can be observed as the shear displacement

increases. However, an initial short linear-like uplift (the shear deformation smaller than 0.3mm) is observed in both directions, which is in accordance the results of the static shear stiffness (referred to Table VI.3). The decreasing stiffness indicates that the deformation capacity increases along with the increasing displacement, which has possibly to be attributed to the non-linear behavior of the rubber.

VII.4. Failure of the joint (Steel shear keys)

VII.4.1. General process

As aforementioned, the shear keys are the key component in the shear capacity of the immersion joint. Once complete failure of the shear keys occurs, there is no limitation for the shear displacement, resulting in complete destruction of the joint. So far, no literature on the failure of immersion joints and the shear keys is available. Before discussing the failure mode, the definition of "failure" needs to be addressed. In this paper failure of the shear keys means that the shear keys lose their shear capacity completely. In the test, if the shear keys in the top slab fall down or the shear keys at the bottom slab lose contact with the tunnel element, the shear keys are no longer fixed to the concrete element and the failure state is reached.

Figure VII.6 shows an example of the 'failure' of shear keys in the joint. Figure VII.6 (a) displays a HSK2 fallen from the roof during the test while Figure VII.6 (b) shows a damaged HSK2, which has lost contact with the element. In both cases, all the bolts in the HSK2s are broken and the keys have lost their shear capacity. Moreover, through the camera observations, it can be noticed that all the HSK2s and not the HKS1s, are damaged one after another. For the HSK1s, the main bodies are basically preserved, and they remain in their initial position. After the test, some damage is found in the rubber as well.

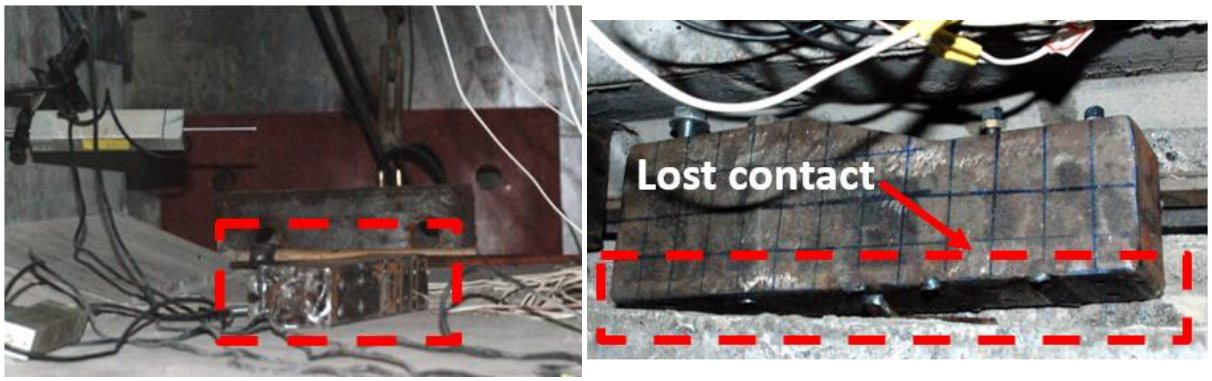

(a) A HKS2 fallen from the roof (b) A damaged HSK2 in the bottom slab

Figure VII.6 Observed failure of the shear keys

VII.4.2. Tearing of the rubber seal

Damage also occurred in the rubber seal. Different types and levels of damage can be found only when the two elements are separated after the test. It should be noted that the rubber is fixed on element A and the rubber has contact with element B. The rubber seal in the side walls suffers the most serious damage, which is shown in Figure VII.7 (a). It can also be observed that broken bolts have fallen from the embedded steel plate and that the steel strips were hardly fixed to the rubber seal any more. Local damage of the rubber is shown in Figure VII.7 (b). Such damage over a small distance may be caused by many factors, such as initial imperfections, fallen dust and so on. When the rubber is subjected to a shear force, such initial imperfections or other factors may cause force concentrations, resulting in local damage in the rubber. On the element B, the black mark of the rubber is left on the surface of the concrete because the rubber scraps adhere to the concrete (Figure VII.7 (c)). This is because the rubber seal was highly compressed and large shear displacements of the joint cause a frictional sliding between rubber and concrete. However, such sliding has not been measured in this test.

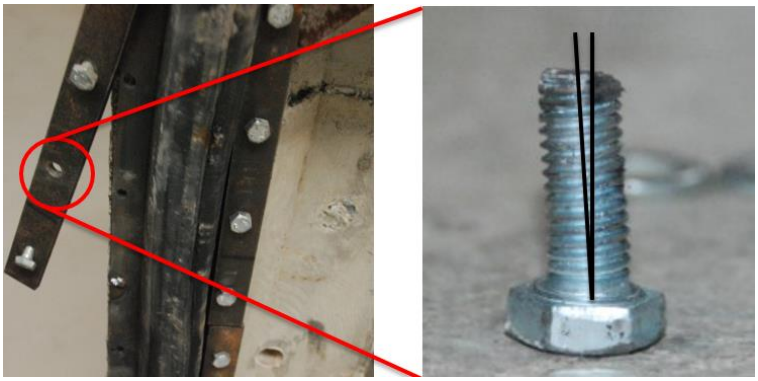

(a) Broken bolts and loose steel strips on side wal

(b) Local damage of the rubber sea on roof slab

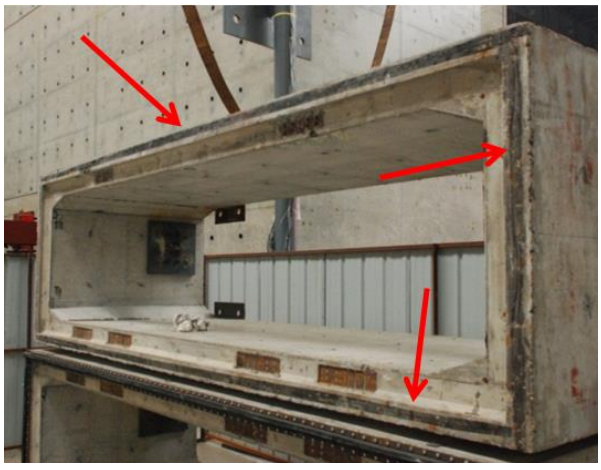

(c) Rubber scraps adhering to concrete element B

Figure VII.7 Damage observed in the rubber seal

VII.4.3. Damage of the steel shear keys

All the HSK2 steel shear keys are found to have failed one by one as aforementioned. Instead, the HSK1's are well preserved and no serious deformation nor cracks are observed. The final shear displacement amounted to 21 mm, being 0.5% of the width of the tunnel segment in the lateral direction.

One of the almost intact HSK1's is shown in Figure VII.8. The HSK1 is still connected firmly to the tunnel element. From the square grid marked on the surface before the start of the test, it can be seen that neither plastic deformations nor cracks occurred. On the contrary, the HSK2's suffered serious damage. After failure of the bolts, no plastic elongation of the bolts is observed and all the bolts were cut by the shear force. The fracture surfaces are even and smooth, as shown in Figure VII.9. Hence, it can be concluded that the bolts failed in a brittle way. No damage is found in the main bodies of the shear keys and they are preserved quite well. This also proves that in this test, the shear capacity of the shear keys relies on the shear capacity of the bolts.

Figure VII.8 Almost intact HSK1 at the bottom slab

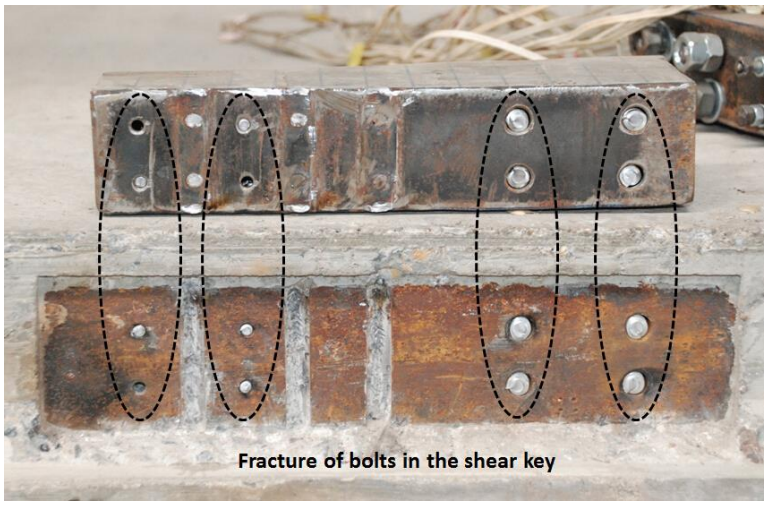

Figure VII.9 Sheared-off cross-section of a HSK2

VII.5. Shear capacity of the joint subjected to reciprocal loading (Steel shear keys)

VII.5.1. Damage and failure of the joint

In Figure VII.10 (a) eight typical damage points of the shear keys are indicated by red stars. The location of each damage point refers to the shear keys indicated in Figure VII.10 (b). In the figure, P and N represent the direction Positive and Negative respectively while the following number means the order of the damage. The first failure of the shear keys occurred at a shear displacement of 2.81mm in the positive direction. When the shear displacement reaches 8mm (9mm in the negative direction), the second and third damage point are found in both positive and negative direction, corresponding to shear forces of 490kN and 528kN respectively. As the test continues, the damage at the other shear keys occurs one after one. At a displacement of 23mm, the last shear key fails resulting in complete failure of the joint.

The detailed information of the damage points is listed in Table VII.2. The relative shear force in the table is the ratio of the shear force applied to the design value, which is 720kN as mentioned in the previous section. For example, when the P2 shear key fails, the shear force

corresponds to only 68.1% of the design value. It can be seen that besides the first damaged shear keys, the rest of the shear keys all fail in Stage IV and the corresponding shear force is around 500kN. The corresponding maximum and minimum shear forces when the rest of the shear keys fail are 528kN and 485kN respectively. The corresponding relative shear forces are 73.3% and 67.4%. It can be found that the shear force corresponding to failure of the shear key varies from each other, but the occurring differences of the shear capacities of the shear keys are deemed to be in an acceptable range.

As discussed, except for the first damage occurring at shear key P1, damage to the shear keys starts to occur when the joint reaches the peak shear in the Negative curve. It can be easily found from Figure VII.10 that the damage occurs at different times, which means that the shear keys in the joint fail one by one, instead of all together. During the test, the first damage (P1) appears in the positive direction when the shear force is 280kN (end of stage II) while no damage occurred in the negative direction up to then. However, the shear force keeps increasing as the test continues.

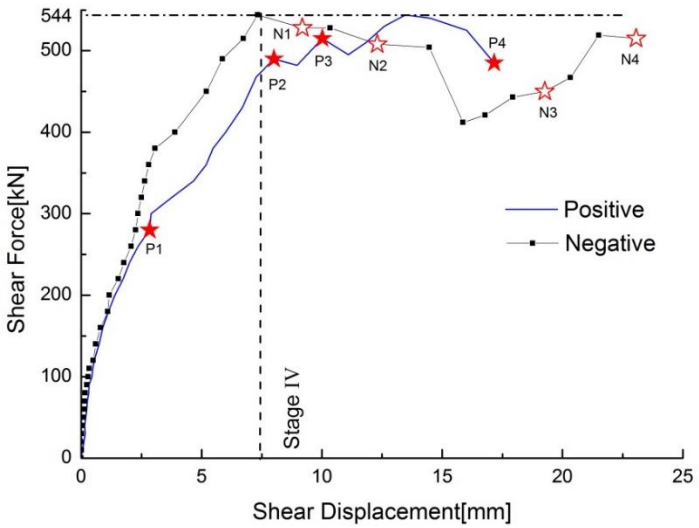

(a) Occurrence of damage points

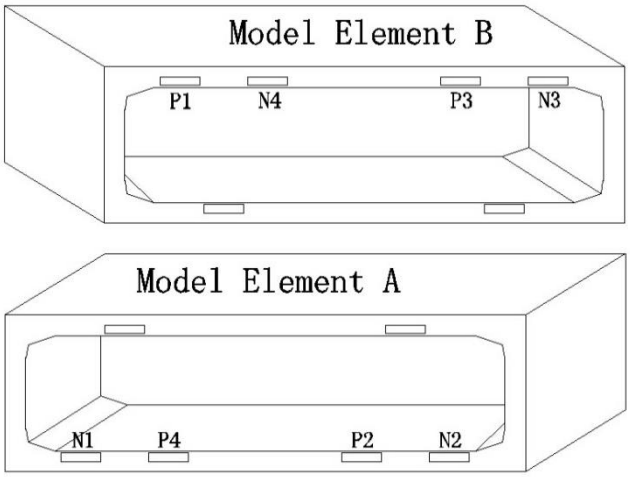

(b) Locations of damaged keys

Figure VII.10 Damage process of the shear keys

Table VII.2 Detailed information on the failure points

Failure point	Shear displacement [mm]	Relative shear force [%]
Positive		
P1	2.84	38.9
P2	8.00	68.1
P3	10.01	71.5
P4	17.16	67.4
Negative		
N1	9.19	73.3
N2	12.30	70.6
N3	19.26	67.4
N4	23.06	71.5

VII.5.2. Discussion about the shear bearing capacity of the shear keys

Given the peak value of both the positive and the negative envelope curves in Figure VII.4, it can be concluded that the shear capacity of the joint is 544kN. For a single steel shear key, the first failure, as shown in Figure VII.10 (a), appears when the joint is subjected to a shear force of 280kN. At a shear displacement of 2.81 mm, the rubber seal and the steel shear key provide the shear capacity together. In order to know the behavior of the rubber seal separately, it is assumed that before the first damage, the rubber seal behaves elastically and no sliding occurred. The deformation of the rubber seal is shown in Figure VII.11. A compression d_a and a shear displacement d_s occur as well as a shear strain γ when the joint is subjected to an axial force F_a and a shear force Q.

Based on the above assumptions, the shear stiffness of the rubber k_{rubber} up to a shear displacement of 2.81mm can be estimated by the following equation:

$$k_{rubber} = \frac{Q}{d_s} \approx \frac{\gamma G A_s}{d_s} = \frac{G A_s}{d - d_a} = \frac{E A_s}{2(1+\lambda)(d-d_a)} = \frac{F_a d}{2 d_a (1+\lambda)(d-d_a)}$$

$$= \frac{k_a d}{2(1+\lambda)(d-d_a)} \qquad \text{(VII.2)}$$

where Q and F_a are the shear force and axial force applied to the rubber seal; d, d_s and d_a are the original height of rubber seal and, the shear and axial displacement respectively; λ means the Poisson ratio, which is 0.5 in this case due to the incompressible properties of the rubber; A_s is the estimated cross-sectional area of the rubber; k_a represents the axial stiffness of the rubber as obtained in Chapter V. It should be noted that this equation only works up to this shear displacement and it cannot be applied to the later-on situation due to the assumption.

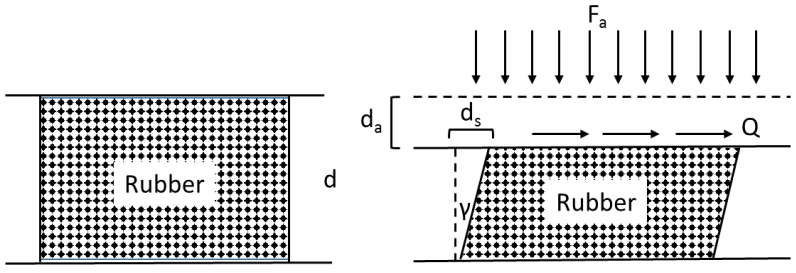

Figure VII.11 Deformation of the rubber seal

Then the shear stiffness of the rubber seal can be easily calculated as 31.8kN/mm. Hence the shear force, allocated to the rubber seal, is obtained by the product of the shear stiffness and the shear displacement, which results in a value of 89.4kN. As the rubber seal and the shear keys resist the shear force together, the shear force acting on the shear key is 190.6kN when the first failure occurs. At this moment, the rubber seal takes up about 32% of the total shear force of the joint.

Table VII.3 Design value of the shear capacities and test results [kN]

	Single shear key	Immersion joint
Design value	180	720
Test results	191	544

The comparison between the design value and the test results of the shear capacities is shown in Table VII.3. It can be seen that the designed and obtained shear capacities of a single shear key are 180kN and 190.6kN respectively while the designed and obtained ones of a joint are 720kN and 544kN respectively. It should be noted that the shear capacity of the joint was assumed to be the sum of the shear capacities of all the shear keys. In this case, the capacity of the joint is 4 times the capacity of the keys. Although the design capacity of a single shear key is only 6% more than the obtained capacity, the design capacity of the immersion joint is 33% larger than the obtained value. The shear capacity of the immersion joint (540kN) is not equal to the sum of that of all the shear keys (720kN), which was not expected.

In conclusion, not all the steel shear keys fail at the same time, resulting in a smaller shear capacity of the joint. There are installation inaccuracies in the test set-up, which means that some of the shear keys are not perfectly installed at the target location and an error of about ±3mm exists. In other words, the initial gaps between the shear keys vary between each other. This means that the different groups of shear keys get in touch with one another at different shear displacements. This situation may reduce the shear capacity of the joint because not all the shear keys are activated at the same time. In the real project, rubber bearings are used to fill the gap between the shear keys to make all the shear keys work together.

The shear capacity of the immersion joint is about 2.8 times that of a single steel shear key. In the last stage of the test, a large displacement in the joint is obtained as well as a large shear deformation of the rubber seal. Although the shear force of the rubber seal at a displacement of 2.81mm is obtained by Eq. (VII.2), afterwards its behavior remains unknown and cannot be measured and quantified.

But it is a fact that part of the total shear force is transferred by the rubber seal, which is about 32% (89.4kN of 280kN) of the total force when the first failure occurs. As the test continued, it is believed that the shear force taken by the rubber may also increase along with the input shear force due to the friction force. However, the shear capacity of the rubber remains unknown as the coefficient of friction is unclear and impossible to measure in this test. Also, the unpredictable failure behavior of the shear keys adds a complexity to this issue. From the view of the designer, it tends to be more conservative due to the contribution of the rubber as such contribution is never considered in actual design. Although the shear capacity of the rubber cannot be obtained, its contribution in shear direction should be taken into account in reality and further numerical analysis is required to elaborate the behavior of the rubber separately.

PART II Concrete Shear Keys

VII.6. Brief introduction and Test Observations

VII.6.1. Brief introduction

The same as for the steel shear keys, a justification based on the Chinese code and the geometric scale for the design of the reinforced concrete shear keys is presented in Chapter IV. Figure VII.12 illustrates the schematic of the concrete shear keys in the model immersed tunnel. The reinforced concrete shear keys also have two types: HSK1 with three tenons on element A and HSK2 with two tenons on element B, staggering with each other. In total, there are four shear keys in two groups and each group has a pair of different concrete shear keys as shown in Figure

VII.12. For one tenon, the cracking force and shear capacity are 42kN and 70kN respectively. It can be noticed that four tenons are theoretically activated at the same time when the joint is subjected to a shear force. Therefore, the cracking force and the shear capacity of the joint is assumed as the sum of a single tenon, which are 168kN and 280kN respectively.

It should be noted that the experimental set-up and the instrumentation as well as the reciprocating loading protocol are the same as for the steel shear keys. Moreover, video recording cameras (Figure VII.13 (a)) are used to observe the situation during the test due to the limited space inside the tunnel element. The cracking performance can be observed through the cameras and the photo captured from the camera is shown in Figure VII.13 (b).

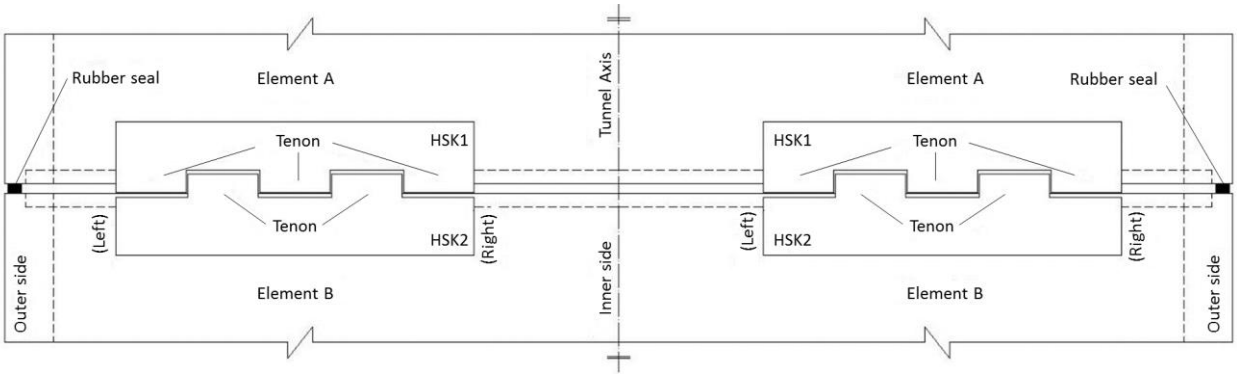

Figure VII.12 Concrete shear keys in the test

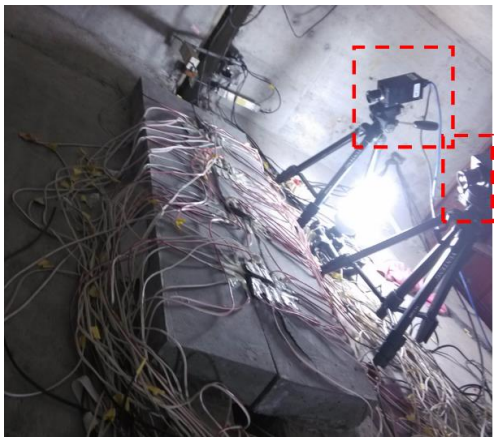

(a) Cameras inside the element

(b) Photo captured from the camera at the beginning of the test

Figure VII.13 Video recording system

VII.6.2. Recorded Data and Test Observations

The recorded shear displacements from transducers 1 to 4 in this case are provided by Figure VII.14. The numbers 1 till 4 in the legend represent the transducers 1 till 4 respectively. Similar to the results with the steel shear keys, it also shows that the data from the four transducers are nearly in accordance with each other during the whole loading process, except for the last part of the test. Hence, the shear displacement of the joint can also be taken as the average of the values measured by the four transducers. It should be noted that the reciprocating loading application shifted to monotonic loading application at the last stage of the test. For the last few steps of the test, the displacement is first applied to one direction until complete failure of the shear keys in this direction and then shifts to the other direction until complete failure of the shear keys in the other direction.

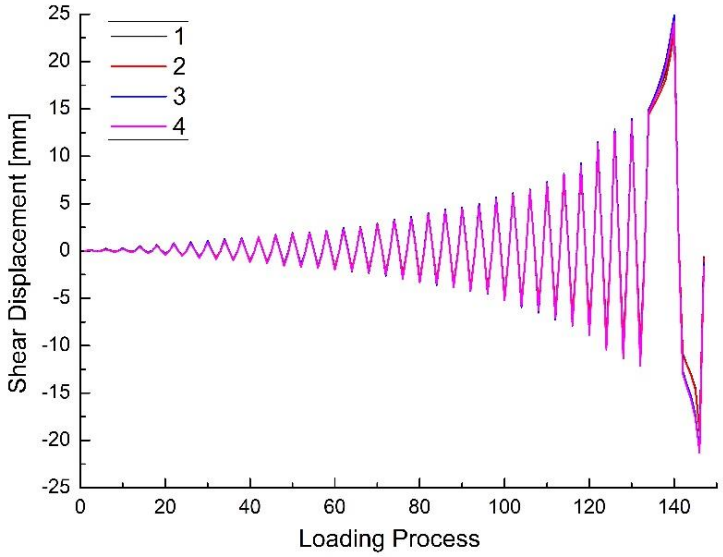

Figure VII.14 Data of shear displacement recorded by transducers #1-#4 (Concrete shear keys)

The shear force-displacement curves for the concrete shear keys is shown in Figure VII.15. The "positive" and "negative" parts refer to the loading direction. Hysteretic loops are also observed during the test and the loop is growing along with the increase of the shear displacement. In the initial stage, when the shear displacement is between ±2.5mm, there is also an elastic part with little residual shear deformation, which is in accordance with the test with steel shear keys. In particular, the peak of the curve is smaller than the one with the steel shear keys. It should be

noted that the "tail" at the end represents the change from reciprocating loading to monotonic loading as aforementioned.

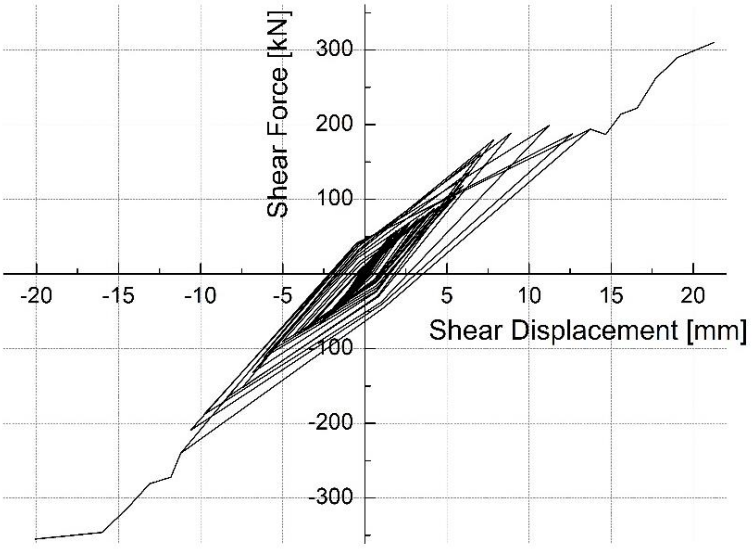

Figure VII.15 Shear force-displacement curves (Concrete shear keys)

Figure VII.16 shows the configuration of the cameras inside the tunnel and the numbering of the tenons. Figure VII.17 to Figure VII.20 display the photos captured from camera 1 to 4, directly showing the concrete shear keys before and after failure.

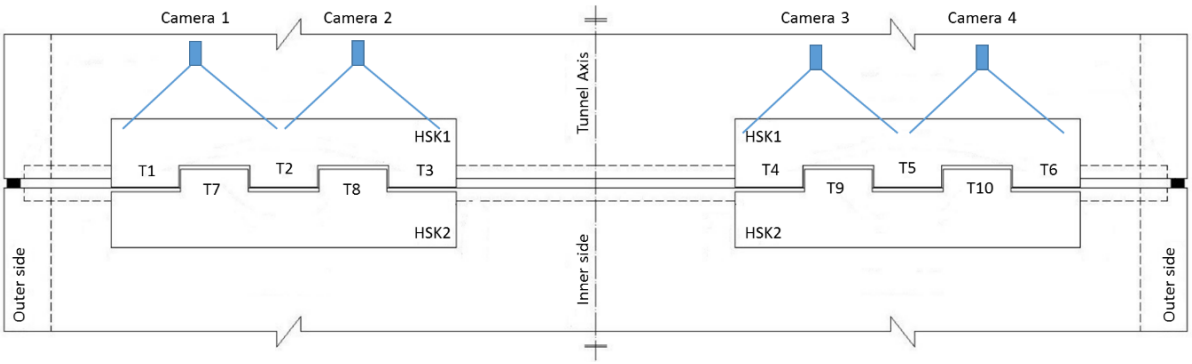

Figure VII.16 Configuration of the cameras inside the tunnel element

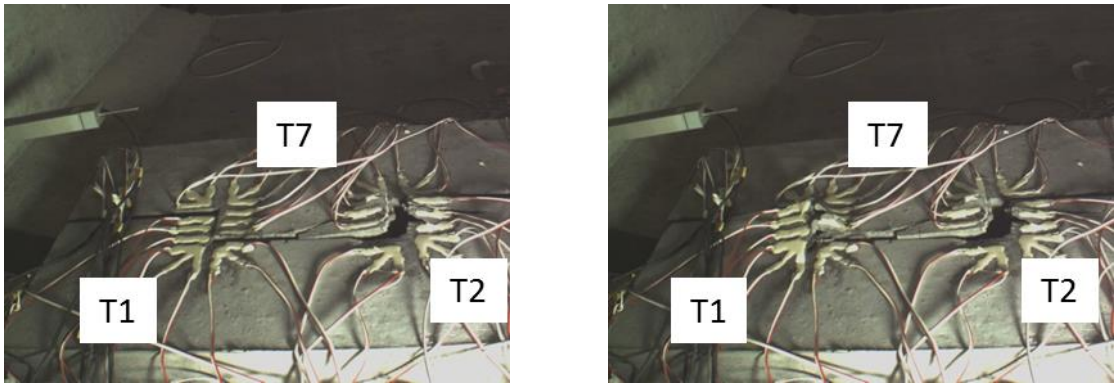

(a) Before failure (T1) (b) After failure (T1)

Figure VII.17 Photos from Camera 1

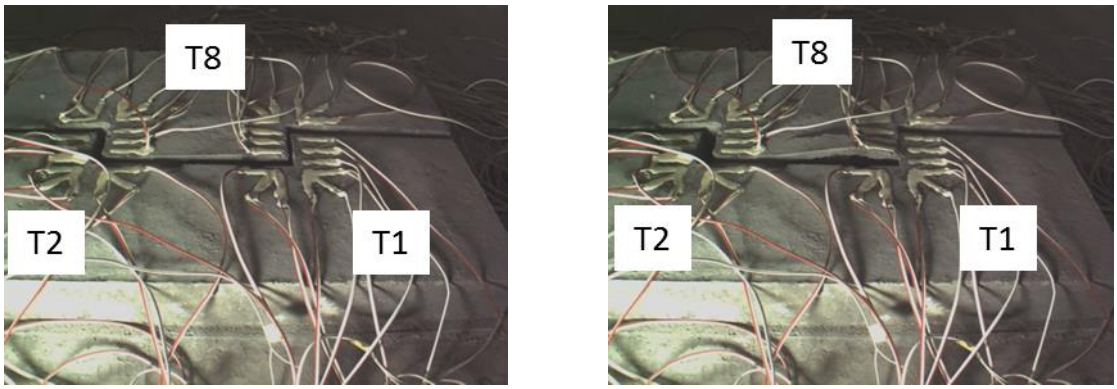

(a) Before failure (T8) (b) After failure (T8)

Figure VII.18 Photos from Camera 2

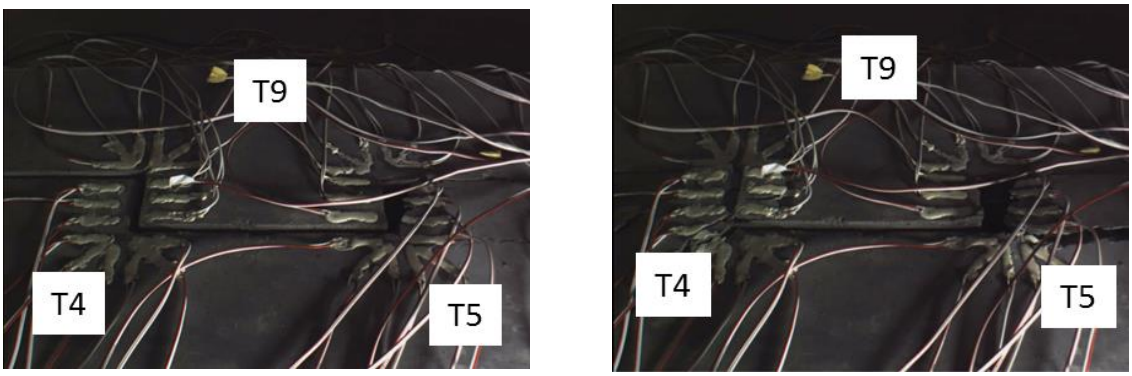

(a) Before failure (T5) (b) After failure (T5)

Figure VII.19 Photos from Camera 3

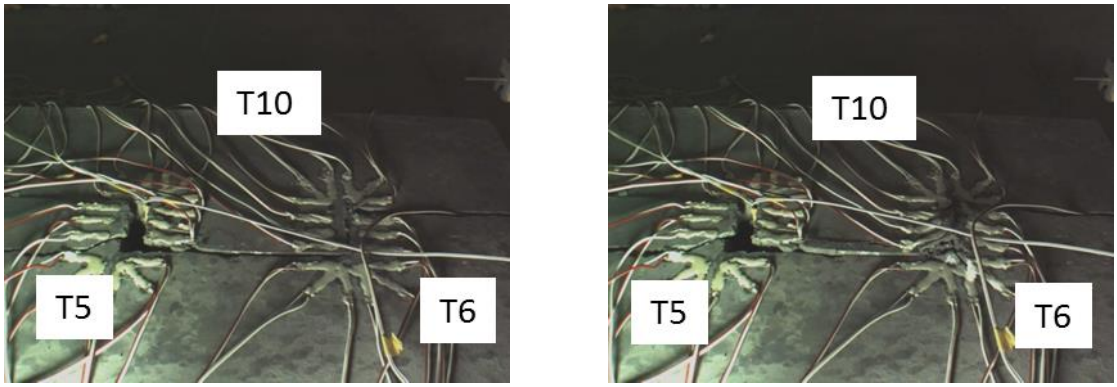

(a) Before failure (T10) (b) After failure (T10)

Figure VII.20 Photos from Camera 4

Besides the force-displacement curve and the observation of the concrete shear keys, another issue, the racking problem, requires attention, which is shown schematically in Figure VII.21. Such issue is due to the fact that the shear keys are installed at the bottom slab but the input shear force is distributed evenly along the height of the element, resulting in a relative deformation d_r and a racking angle θ_r as shown in Figure VII.21. The relative deformation can be obtained by the differences between the upper (transducers 1 and 4) and lower (transducers 2 and 3) transducers while the racking angle is approximately the ratio of the relative deformation to the height of the element. Based on the obtained data from Figure VII.14, an example of the calculated relative deformation and the racking angle in the negative direction are listed in Table VII.4.

Generally, during the test, the shear displacement at the level of the roof slab is approximately 13% to 36% larger than that of the bottom slab, indicating the existence of racking. When the shear displacement is small, the difference seems to be smaller because in this stage, the rubber seal dominates the shear behavior of the joint. As the shear displacement increases, a larger difference is observed and the relative deformation reaches its peak value (5.82mm) when the shear displacement is 16.0mm. The relative deformation amounts up to one third of the shear displacement. Such phenomenon indicates that in engineering practice attention should be paid to the roof deformation and accordingly measurement is required during operation if such type of the shear keys are applied.

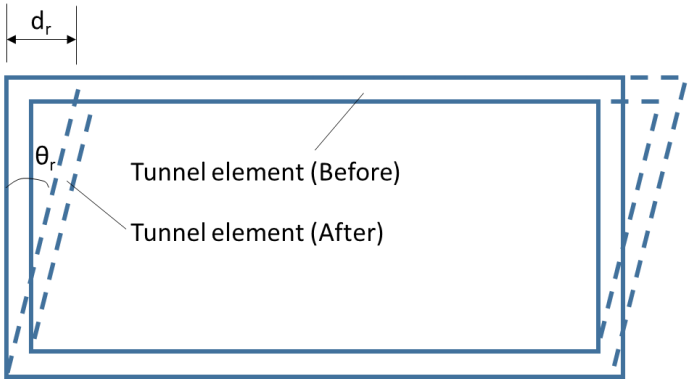

Figure VII.21 Racking of the element

Table VII.4 Detailed data on the racking issue

Shear displacement [mm]	Relative deformation [mm]	Ratio of relative deformation to shear displacement [%]	Racking angle [x10^{-3}rad]
0.00	0.00	-	0.00
1.43	0.34	23.8	0.35
3.42	0.54	15.8	0.54
4.36	0.58	13.4	0.57
6.16	1.00	16.2	1.00
7.47	1.60	21.4	1.61
8.40	1.82	21.6	1.83
9.83	2.38	24.2	2.39
11.22	3.34	29.8	3.34
13.11	4.38	33.4	4.38
14.31	4.94	34.4	4.94
15.99	5.82	36.4	5.82
20.07	4.44	22.2	4.43

VII.7. Shear stiffness (concrete shear keys)

Taking the peak point of each hysteretic loop in Figure VII.15, the envelope shear force-displacement curve of the joint with concrete shear keys is plotted and shown in Figure VII.22. P and N represent the positive and negative loading direction respectively. Various characteristics of the joint are observed as the shear displacement increases.

- When the relative displacement ranges from 0 to (±)2mm, the joint remains in the elastic stage and the displacement returns to 0 after unloading.
- When the displacement enters into the range of 2 to 5mm(±), the slope of the curve experiences a slightly decrease and a residual displacement occurs as well as a hysteretic loop.
- When the shear displacement is between 5 to 7mm, the hysteretic performance becomes more obvious.
- After a shear displacement exceeding 7mm, the concrete shear keys start to fail and the joint enters the failure stage.

Based on these results, the shear performance of the joint can be divided into three stages. It should be noted that after the shear displacements reaches14mm (-12mm), the cyclic loading is changed into one-directional loading until failure.

- Stage I (Between 0 and 2mm): A linear relationship is found between shear force and displacement which means the shear stiffness of the joint is constant. In this stage, only the rubber seal provides the shear capacity due to the gap between the shear keys.
- Stage II (Between 2 and 5.5mm): A slight decrease occurs in the curves but still a linear behavior is observed. The concrete shear keys are not in contact.
- Stage III (More than 5.5mm): The concrete shear keys start to touch each other resulting in the increase of the slope of the curves. With the increase of the shear displacement, the non-linear behavior of the joint becomes more obvious. At the same time, the damage occurs successively at this stage.

The two curves separate when the shear displacement increases up to 10 mm. In this stage, serious damages occur in the concrete shear keys. In the positive direction, between 8mm to 15mm, there is a plateau in the curve, indicating that the shear force remains almost constant as the shear displacement increases. This may be due to the damage of the tenons in this direction.

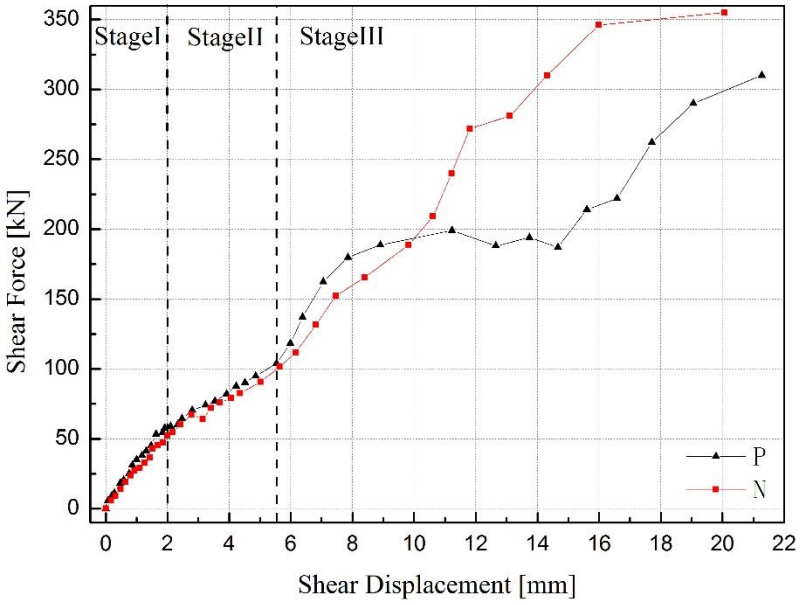

Figure VII.22 Envelope curve of the shear behavior of the joint (concrete shear keys)

The same equation as Eq. (VII.1) is applied to calculate the shear stiffness of the joint with the concrete shear keys, which is shown as follows:

$$k_i^{cf} = \frac{Q_i}{d_i} \tag{VII.3}$$

where Q_i and d_i are the shear force and the shear displacement of the joint respectively at the end of step *i* of the test. The evolution of the calculated stiffnesses for both directions is shown in Figure VII.23. The curve is divided into the same three stages as mentioned before.

The stiffness in this case also experiences a general decreasing trend initially then followed by a fluctuation around 20kN/mm. In the first stage, a significant decrease is observed together with a slight fluctuation at the end of this stage. Such decreasing trend slows down in stage II,

ranging from 30kN/mm to 20kN/mm. After entering stage III, the stiffness fluctuates at around 20kN/mm.

Compared to the results of the steel shear keys, a similar degradation of stiffness is observed for the concrete shear keys. However, the initial stiffness of the steel shear keys is much larger than that of the concrete shear keys, which makes sense as the elastic modulus of the steel is larger. Moreover, the final parts of both results appear to be approximately the same, namely 25kN/mm for the steel shear keys and 20kN/mm for the concrete shear keys, due to the fact that the rubber seal dominates the behavior of the joint as most of the shear keys already failed.

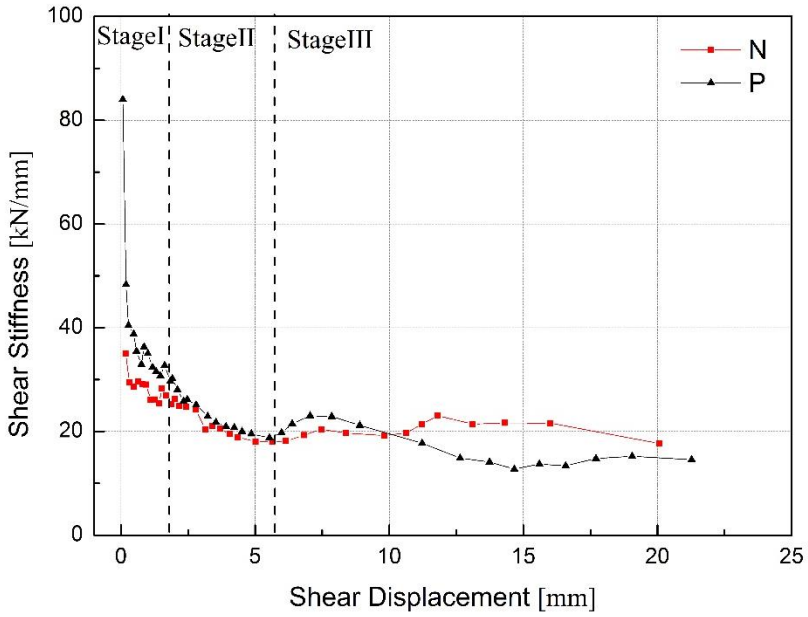

Figure VII.23 Relationship between shear stiffness and shear displacement (Concrete shear keys)

VII.8. Failure of the joint (concrete shear keys)

Figure VII.24 defines the numbering of the tenons in the shear keys where T1 to T10 refer to the tenons No. 1 to No.10. The crack patterns observed at the location of each tenon at different loading stages are shown in Figure VII.25. The numbers in the figure indicate the order of the crack occurrence. In some figures there are positive and negative shear forces for the same

crack number because such cracks occur in the same loading cycle but are induced by a positive and negative shear forces respectively. To avoid large numbers, the cracks appearing in the same loading cycle are grouped and numbered the same. Figure VII.25 (a) illustrates the first crack appearing at a shear force of 74.1kN and -60.2kN (at the end of stage I). The positive and negative values represent the loading direction as a reciprocating loading is applied. Further, the crack pattern developing through the bottom of a tenon is provided in Figure VII.25 (b). As can be seen, a crack starts at the corner bottom part of T5 and goes almost through the whole bottom of this tenon at a shear force of -71.9kN. As the shear force increases, the crack (No.3) completely goes through the tenon by the imposed reversed shear force as shown in Figure VII.25 (c) and a small crack occurs at the corner bottom part of T1 as well. A pair of cracks appear on T3 and T8 as shown in Figure VII.25 (d) as well as a small crack on top of T5. After the 'negative' shear force reaches 209kN, a similar crack pattern occurs in T4, starting at the corner bottom part and developing along a direction of approximately 45 degrees (crack No.6 in Figure VII.25 (e)). Further on, an analogous crack (No.8) occurs in T10 and the No. 5 crack develops further into two separate cracks (No.9) at a shear force of 310kN, leading to a complete damage in T3, which is shown in Figure VII.25 (f). Crack development for No.10 and No.11 is given by Figure VII.25 (h) under the final monotonic positive shear force. Finally, a negative monotonic shear force is applied, resulting in crack No.12 in both T8 and T10, indicating the final damages, as displayed in Figure VII.25 (i).

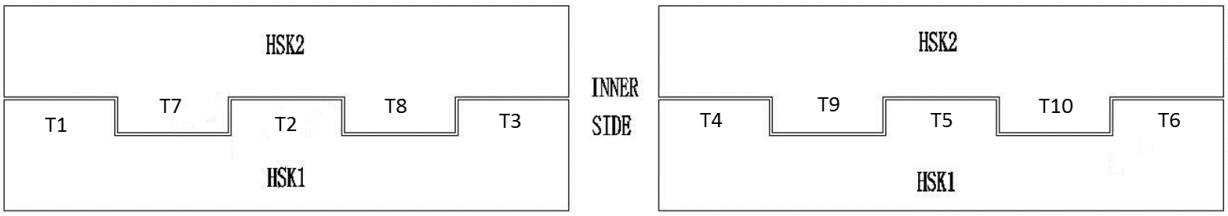

Figure VII.24 Numbering of the tenons

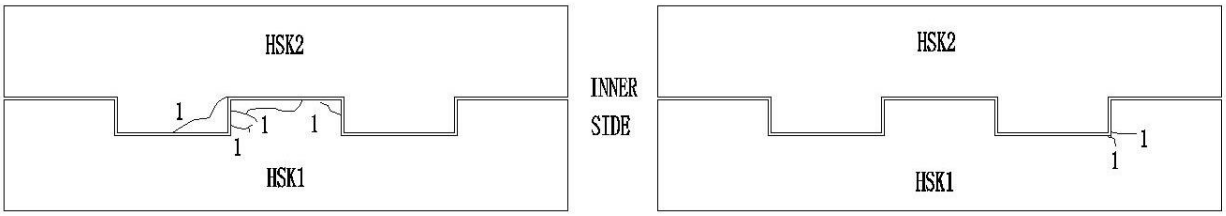

(a) Shear force 74.1kN (-60.2kN)

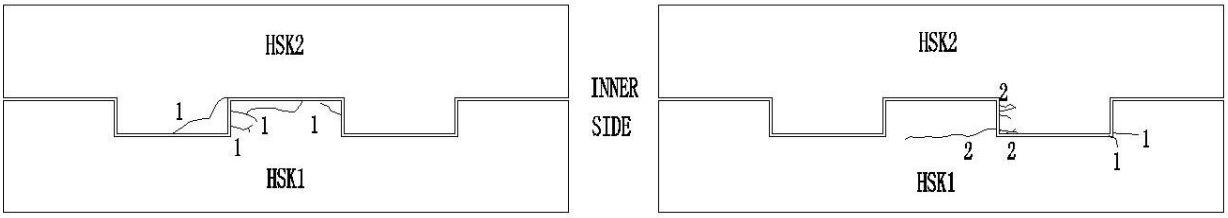

(b) Shear force -71.9kN for no.2

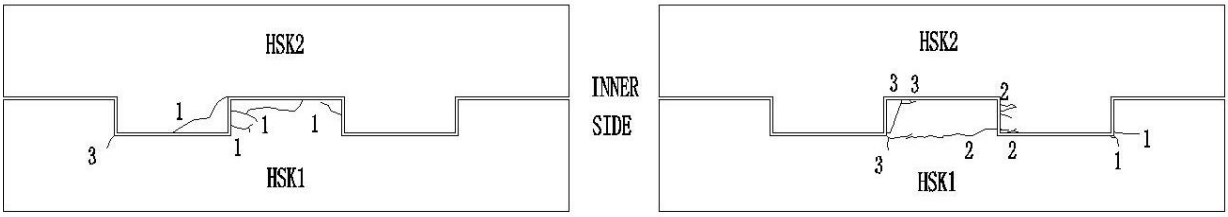

(c) Shear force -82.5kN (103.9kN) for no.3

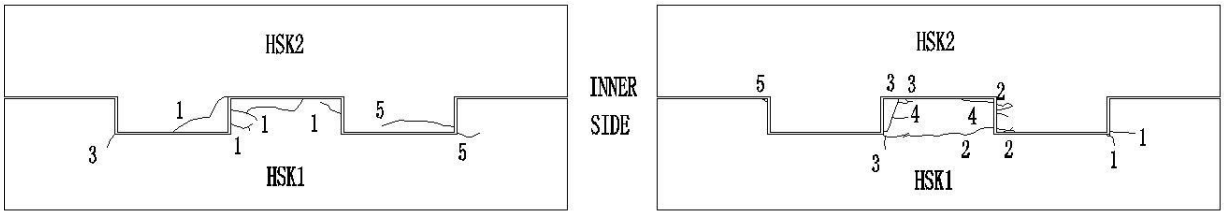

(d) Shear force -111.7kN for no. 4 (179kN for no.5)

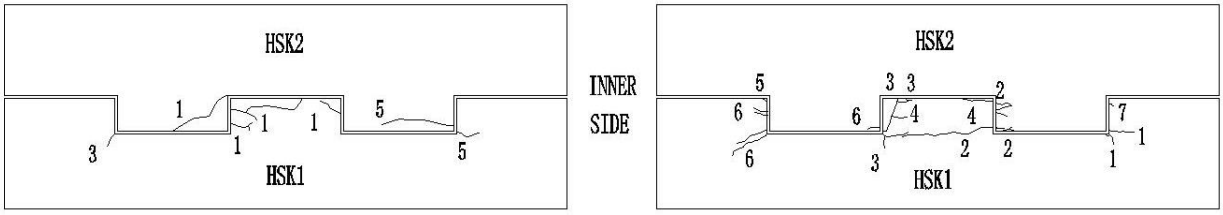

(e) Shear force -209kN for no. 6 (214kN for no.7)

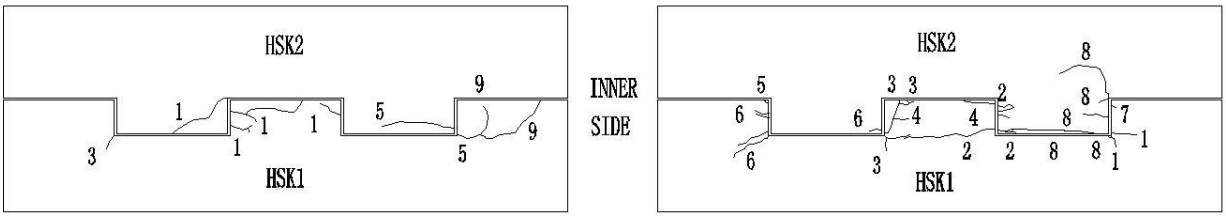

(f) Shear force 262.0kN for no. 8 (310.0kN for no.9)

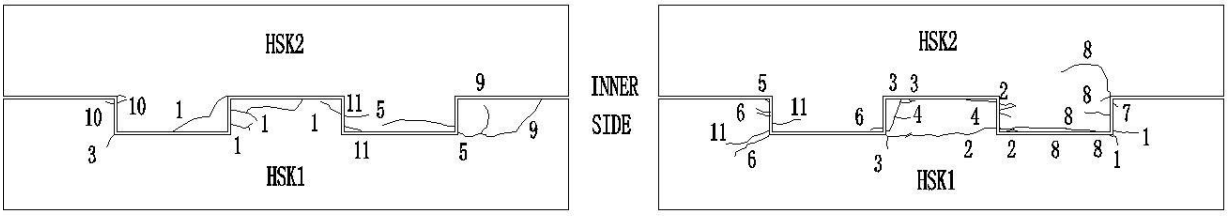

(h) Shear force -281.0kN for no. 10 (-310.0kN for no.11)

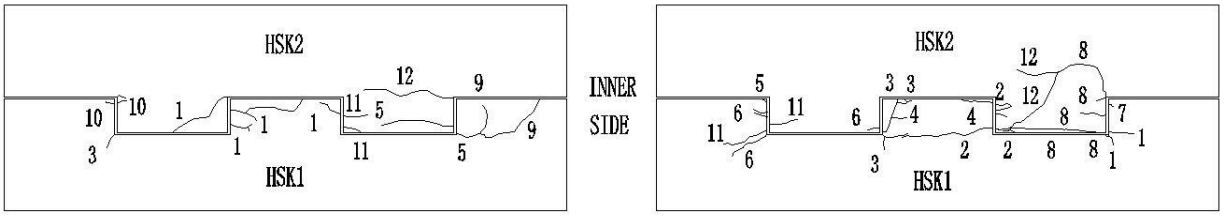

(i) Shear force -355.0kN for no. 12

Figure VII.25 Cracking development of the concrete shear keys

It can be concluded that the failure of the shear keys is determined by the cracks starting from the bottom part of the tenon to the inner part of the shear keys at a direction of approximately 45 degrees or less, such as cracks No.1. No.2, No.3, No.5, No.6, No.8 and No.12. Such cracks are basically caused by tensile failure of the concrete (Mertens, 2016) and cross the longitudinal reinforcement, which determines the shear strength of the shear keys as presented in Chapter IV. Moreover, there are also quite a lot of small cracks appearing near the contact face together with spalling on the tenon surface (Figure VII.26). This may be attributed to stress concentration caused by the uneven contact between two tenons. The development of the cracking pattern indicates that not all the tenons are activated at the same time, which means that one tenon remains intact while a crack already occurs in another tenon. It should be noted

that the observed cracks presented in Figure VII.25 are only obtained through the observation of the surface of the shear keys. How the crack develops beneath the surface and whether the crack first starts from the bottom remains unclear and impossible to observe during the test.

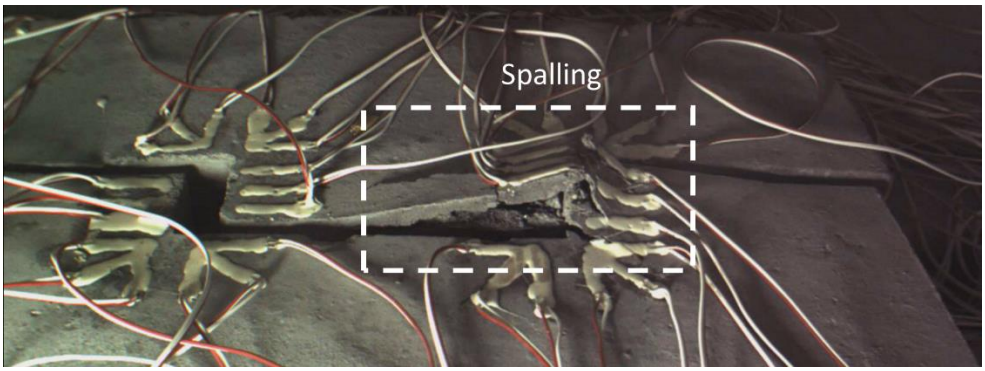

Figure VII.26 An example: spalling on T8

VII.9. Shear capacity of the joint subjected to reciprocal loading (concrete shear keys)

Figure VII.27 illustrates the occurrence of the major cracks observed on the concrete shear keys. P and N in the figure represent the positive and negative direction while the numbers 1 to 12 correspond to the order of the crack appearance, which corresponds to Figure VII.25. Before the joint enters the stage II, a linear behavior is found in both curves and afterwards there is a turning point, indicating the start of the cracking. The first observed crack of the shear keys occurs at a shear displacement of 2.43mm in negative direction in stage II. When the shear displacement reaches 3.23mm (3.42mm in the negative direction), the following cracks are found, corresponding to shear forces of 74.1kN and 60.2kN. Then other major cracks are observed in T5, cracks no.3 and no.4, resulting in a complete failure. As the test continues, and the joint enters in stage III, the slope of the curve increases as more shear keys are activated due to the differences of the gap. Later on, more cracks are observed in this stage and the tenon starts to fail. The maximum capacity of the tested joint amounted to 310kN in positive direction and 355kN in negative direction at a shear displacement of 20.1mm and 21.3mm respectively.

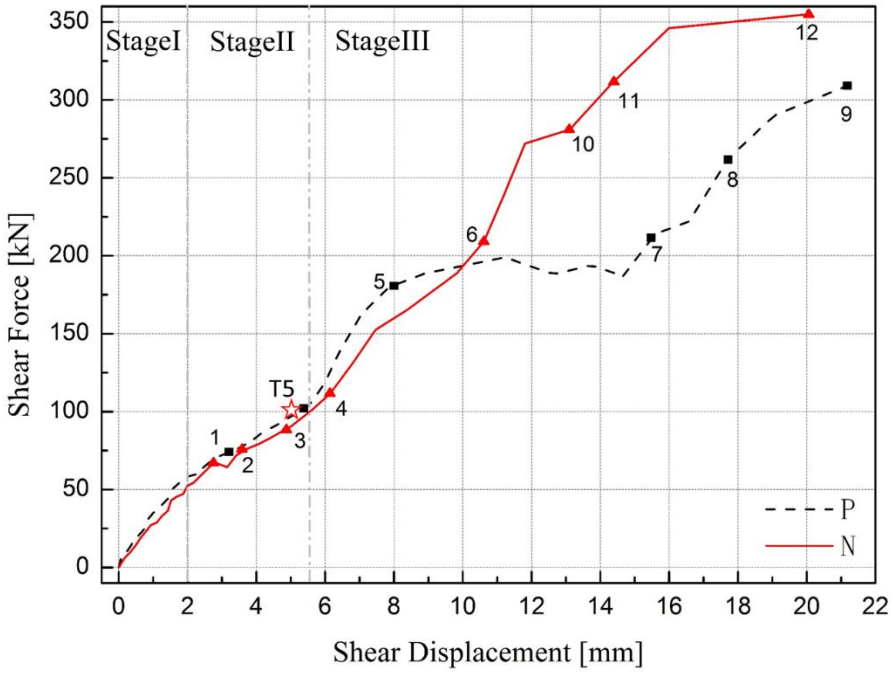

Figure VII.27 Occurrence of the major cracking in the concrete shear keys

The first failure of a tenon is observed on T5 at a shear force of around 100kN, indicated by a red star between crack no.3 and no.4 in Figure VII.27. Due to the mentioned racking problem, the proposed Eq. (VII.2) cannot be used due to the difference in behavior between the roof and bottom slab. As the behavior of the rubber seal cannot be determined, the actual shear capacity of one tenon remains unclear as well as the cracking resistance. However, the contribution of the rubber seal cannot be ignored. After cracks no.9 and no.12, the final failure of the tenon for both positive and negative direction is observed, indicating the shear capacity of the joint is 310kN (positive) and 355kN (negative).

The comparison between the design value and the test results on the cracking resistance and the shear capacity is presented in Table VII.5. It should be noted that the test result of a single tenon is unknown. The cracking strength and the shear capacity of the immersion joint with concrete shear keys are 74kN (60kN) and 310kN (355kN). The two different values correspond to the two loading directions. Obviously the obtained cracking resistance of the joint is smaller than the design value due to the fact that the shear keys are not activated at the same time which is similar to the results of the steel shear keys. Moreover, the obtained cracking resistance of the

joint is larger than that of a single tenon because of the contribution of the rubber seal. Regarding the shear capacity, the test results are a bit larger than the design value also due to the contribution of the rubber seal. However, the shear capacity of the joint is not equal to the sum of that of all single tenons as the situation in the joint subjected to combined loading is complicated and the influence of the rubber seal and the construction accuracy needs to be considered. Moreover, the reciprocating loading may induce progressive and cumulative damage of the concrete shear keys, resulting in smaller test values compared to the design value.

Table VII.5 Design value and test results of the cracking resistance and shear capacities [kN]

	Single tenon		Immersion joint	
	Cracking strength	Shear capacity	Cracking strength	Shear capacity
Design value	42	70	168	280
Test results	<60	<100	60/74	310/355

VII.10. Summary of the two parts

This chapter presents the experimental results of a study on a scaled immersion joint, with steel shear keys and concrete shear keys respectively, subjected to compression-shear loading. Based on an actual project, a constant compressive axial force of 850kN was applied as well as a reciprocating horizontal shear force with increasing amplitudes. For both steel and concrete shear keys, a hysteresis effect was observed during the test and the area of the hysteretic loop increases with the shear force. An envelope curve of the shear force-displacement of the joint was obtained and divided into different stages based on the observed shear behavior of the joint. The shear stiffness of the immersion joint was also calculated, showing a non-linear change with the shear displacement. The shear capacity of the model immersion joint and that of a single steel shear key were evaluated as well. Analysis of the experimental results leads to the following conclusions.

Part I Steel shear keys

(1) Under a reciprocal horizontal shear force, a clear hysteretic loop is found and the area of it increases with the shear force. According to the obtained behavior of the joint, the envelope curve of the shear force-displacement of the joint can be divided into four stages based on the performance of the immersion joint corresponding to a decreasing shear stiffness.

(2) It is observed that the failure mode of the immersion joint relies on the failure of the steel shear keys. Moreover, the HSK2's are found to be damaged and they fail one after another. Based on the fracture of the bolts, the failure mode of a single shear key turns out to be a brittle shear failure. Also, damage of the rubber seal is occurring. The failure of the joint shows a step-by-step character.

(3) The maximum shear capacity of the immersion joint and that of a single steel shear key are 544kN and 191kN respectively. The obtained capacity of the joint is lower than the designed one due to the fact that all the shear keys do not experience the same force at the same time. In an actual project, care has been taken for this aspect by installing bearing rubber between the shear keys, to assure that the shear forces are evenly distributed to all shear keys as practically as possible. It is also found that the rubber seal has a certain contribution to the shear capacity.

Part II Concrete shear keys

(4) Similar to the results obtained on the steel shear keys, a clear hysteretic loop is also found and the area of it increases with the shear force. Based on the observed behavior of the joint, the envelope curve of the shear force-displacement of the joint can be divided into three stages The corresponding stiffness is also calculated, indicating a degradation along with the increase of the shear displacement. However, the shear stiffness is smaller than the stiffness with the steel shear keys. Moreover, differing from the steel shear keys, the racking problem arises in the joint with concrete shear keys due to the asymmetric installation of the shear keys.

(5) The cracking behavior of the shear keys is observed through installed cameras. A detailed cracking pattern is obtained, indicating the development of the cracks. It can be noticed that the cracks start from the bottom part of the tenon to the inner part of the shear keys at a direction of approximately 45 degrees or less and then go through the bottom of the tenon due to the

tensile damage. Moreover, small cracks appearing near the contact face together with the spalling on the tenon surface are observed possibly due to the force concentration.

(6) The obtained cracking strength and the shear capacity of the joint with concrete shear keys are 74kN (60kN) and 310kN (355kN) respectively. The two different values correspond to the loading directions. For the cracking resistance, the obtained value is smaller than the design value due to the fact the shear keys are not activated at the same time. Regarding the shear capacity, the test results are a bit larger than the design value due to the contribution of the rubber seal. However, the results of a single tenon cannot be evaluated due to the unpredictable contribution of the rubber seal.

The limitations of this experiment should be realized. The presented results on the shear behavior of the immersion joint rely on the material properties of the rubber seal and the shear keys, construction quality and the loading protocol. The size effect needs to be taken into account as well. A larger axial force or a monotonic loading protocol may increase the shear capacity as a stiffer rubber seal is obtained or cumulative damage does not occur. Another type of the rubber seal may also influence the results. Such factors cannot be considered at the same time in this large-scale structural experiment. Moreover, the separate behavior of the rubber still remains unclear and it cannot be quantified due to the impossibility of measurements in the test and the complex configuration of the rubber. A separate numerical and experimental analysis is required to elaborate this issue. However, the global shear behavior and the failure mode of the model immersion joint have been obtained from this test as well as the fact that the rubber seal contributes a lot to the shear resistance.

VII.11. References

GB 50010-2010 Chinese Code for design of concrete structures. Ministry of Housing and Urban-Rural Development of the People's Republic of China, Beijing. (in Chinese)

GB 50017-2003 Chinese Code for design of Steel structures. Ministry of Housing and Urban-Rural Development of the People's Republic of China, Beijing. (in Chinese)

Mertens, T., 2016. Structural Behavior of Concrete Shear Keys in the Nanchang Red Valley Immersed Tunnel. Master thesis, Ghent University, Ghent, Belgium.

CHAPTER VIII

SEISMIC MITIGATION DESIGN PROCEDURE FOR IMMERSION JOINTS

Busan-Geojo immersed tunnel, South Korea

(source unknown)

VIII. Seismic Mitigation Design Procedure for Immersion Joints

VIII.1. General introduction

Many immersed tunnels were constructed in earthquake sensitive regions, such as the BART Tunnel in San Francisco, several immersed tunnels in Japan, the Bosphorus Tunnel in Turkey, the Busan Tunnel in South Korea (pictures on previous page) and recently the Hongkong-Zhuhai-Macao immersed tunnel in China. In fact, as one of the main deformable parts in an immersed tunnel, the joints may have a relatively large deformation capacity subjected to seismic loading, compared with that of the adjacent tunnel elements. The complex configuration of the immersion joint also contributes to its uncertainty regarding its mechanical behavior. Hence, with regard to immersed tunnels in regions with seismic activity, the behavior and reliability of the immersion joint, especially under seismic loading, deserves more attention. Previous research revealed that the seismic response of tunnels is affected considerably by the kinematic energy induced by the surrounding ground, while the inertial loads of the structure itself are of secondary importance (Wang, 1993; Hashash et al., 2001; Bobet, 2003; Huo et al., 2006; Yu et al., 2013a, 2013b; Pitilakis and Tsinidis, 2014; Yu et al., 2016). Therefore, large differences exist between the seismic mitigation design of underground structures and surface structures. Until now however, current or recent research on seismic mitigation or isolation of underground structures is very rare in literature. One of the possible measures discussed so far was to cover a tunnel with a soft layer in order to minimize the shear forces on the tunnel-soil interface. The seismic isolation effect of the soft layer material that spreads over the tunnel linings was investigated by using simple solutions to idealized problem statements. Another possible measure was proposed for mountain tunnels, i.e. a shock absorbing layer (isolation layer) or a grouting layer that was installed in the surrounding rock to absorb the energy induced by earthquakes.

However, in fact, these seismic mitigation measures are not suitable for immersed tunnels due to the special characteristics of the tunnel construction method, the structural feature and the surrounding environment. Keeping this in mind, a seismic mitigation device installed on the immersion joint and working together with the joint could be an additional way to dissipate the energy caused by an earthquake. Hence, a new concept of seismic mitigation for immersion joints is proposed and discussed.

In this chapter, first of all, the mechanism of application of the seismic mitigation device in the joint is introduced in Section VIII.2. Based on that, Section VIII.3 proposes a mechanical model of an immersion joint with the seismic mitigation device. Then Section VIII.4 is dedicated to provide the design procedure about the seismic mitigation device in the joint by means of a parametric optimization method. Finally a brief summary of this chapter is given in Section VIII.5.

VIII.2. Mechanics of the seismic mitigation for immersion joints

In order to ensure the safety of a building under earthquake, seismic mitigation methods consist in specific mitigation devices or adjusting the dynamic characteristics of the structure, which are well developed in seismic design and analysis of surface structures. As discussed in Chapter III, the dynamic response of a surface structure subjected to seismic loading could be remarkably reduced by adjusting the natural frequency ω or natural period T (by changing M and K), and/or by increasing the damping C or applying a proper external force $F(t)$. As a result, the acceleration, the velocity and the displacement can be limited to the allowable values to ensure the safety of the structure and the occupants and the equipment in it within the serviceability limit states. In fact, the seismic mitigation in buildings aims to increase the damping C in such a way that the seismic response can be reduced.

From the perspective of energy conversion during an earthquake, the concept of seismic mitigation can be explained by the following equations. For a conventional earthquake-resistant structure, it is presented as:

$$E_{in} = E_R + E_D + E_S \tag{VIII.1}$$

and for a structure provided with seismic mitigation devices as:

$$E_{in} = E_R + E_D + E_S + E_A \tag{VIII.2}$$

where E_{in} is the input earthquake energy; E_R represents the kinetic and potential energy of the structural vibration; E_D represents the energy consumed by damping; E_S is the consumed energy due to the non-elastic deformation or damage of the main structure; and E_A is the energy consumed by the seismic mitigation devices.

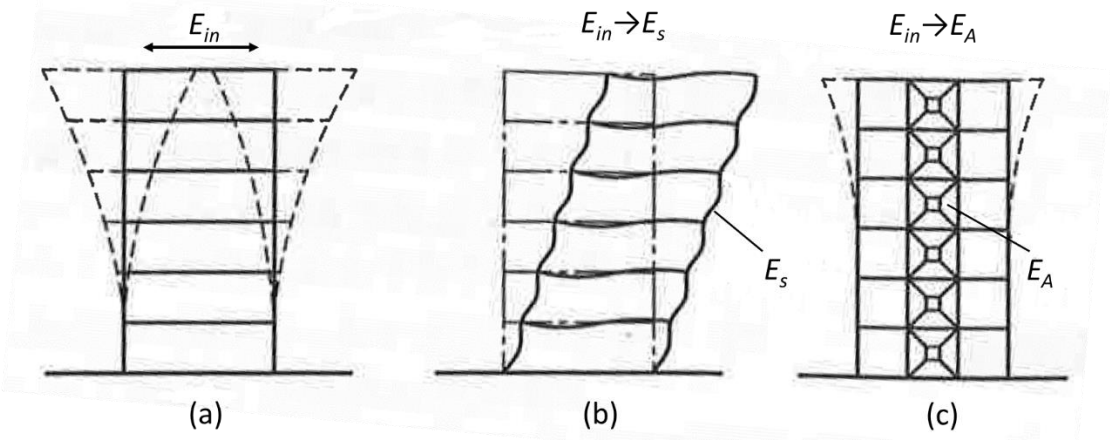

Figure VIII.1 Schematic of mechanism of seismic mitigation: (a) Input action; (b)Conventional structure; (c)Structure with seismic mitigation devices (Shang, 2002)

In conventional structures, E_D can be ignored as it only consumes maximum 5% of E_{in} (Shang, 2002). To absorb the energy from the earthquake, the main structure has to move to the non-elastic deformation stage or even to a damaged stage, which means that E_{in} is transferred to E_S as presented in Figure VIII.1 (b).

If seismic mitigation devices are introduced in the structure, the devices are designed to be activated before the occurrence of non-elastic deformations or damage. In this way, the

earthquake energy is mostly taken by the devices, decreasing the seismic response of the structure (Figure VIII.1 (c)) and thus protecting the main structure.

With respect to immersed tunnels, as mentioned before the current methods for reduction of the seismic response of underground structures seem to be inefficient due to the specific features and the construction method of immersed tunnels. Hence, a seismic mitigation device installed on the immersion joint and working together with the joint could be an additional way to dissipate the energy induced by an earthquake. Therefore, a buckling energy-dissipation device (BEDD) on the basis of the buckling restrained brace, also referred to as BRB, is introduced as an example to explain the application of seismic mitigation methods in immersion joints. It should be noted that the form of the seismic mitigation device is not limited to BEDD and other devices, such as a liquid damping or metal damping device, could be applied as well.

VIII.3. Mechanical model of the immersion joint with BEDD

VIII.3.1. General introduction of the BEDD

Currently, various types of seismic mitigation devices have been developed and widely applied in both structural engineering and bridge engineering. The Buckling Restrained Braces (BRB's), which are made from encasing a steel core into a steel tube, and confined with infill material, have been widely adopted as seismic mitigation device worldwide. In the past decade, many novel concepts and designs of BRB's have been proposed and verified via full-scale component and frame tests in different countries especially in Japan, the United States and China. More importantly, this technology has successfully been transferred to the industry, and implemented in a wide range of building applications. The excellent hysteretic performance of the BRB's has been widely reported in both experimental and numerical analysis, which was already noted by a number of researchers (Black et al., 2004; Xie, 2005; Iwata and Murai, 2006). In view of

the special characteristics of the immersion joint, as discussed in the previous section, the BRB-based device could be a feasible option for seismic mitigation of immersion joints.

In this section, a new-type of BEDD based on the TJ-II™ (Sun et al., 2011) is applied, as illustrated in Figure VIII.2. This type of device has the following components: (1) a steel plate core; (2) a surface layer of silicone; and (3) a concrete-filled steel tube to restrain buckling.

The steel core is made of two types of steels, i.e. a low yield strength steel or low carbon steel is adopted for the yielding segment (the yielding core steel plate) and a high strength steel is used for the elastic segment (the connecting region). The high strength steel is connected to the yielding segment by butt welding. The steel core is designed to carry the axial load (both tension and compression) without experiencing buckling failure. The surface layer on the steel plate is used to reduce the friction force and to avoid adhesion between the steel plate and the filling material. The buckling restraint (the steel tube) is intended to limit the buckling of the core steel plate. This type of BRB has been regarded as a stable energy mitigation device due to the inelastic axial deformation of the steel core and the effective load-resisting component without overall buckling when the structure is subjected to strong seismic excitations (Sun et al., 2011).

The steel type Q235 is used as the low yield strength steel core. According to the Chinese Code for design of steel structures (GB 50017-2003), the elastic modulus and the yield stress of Q235 are 206GPa and 268MPa respectively. An ideal bi-linear hysteretic model, shown in Figure VIII.3, is suggested in the literature (Lankesoft, 2016). The force-displacement relationship in bi-linear hysteretic systems is composed of piecewise linear and continuous relationships. The initial loading branch has a slope k_{b1}, followed by the post yielding behavior after the yielding point with a slope of $0.03k_{b1}$. There are so-called turning points, which correspond to the peak values of this model. The first one has co-ordinates $(\delta_1,\ F_1)$. Then the unloading branch follows a line with the same slope as the loading part and it intersects the x-axis at the point C with a residual displacement of δ_c until the force has decreased by two times the yielding force F_y. Thereafter, the BEDD yields again along the line with a slope of $0.03k_{b1}$ until reaching the minimum turning point, with co-ordinates $(\delta_2,\ F_2)$. Then a loading portion starts with the same slope k_{b1} until reaching the yielding point again. The hysteretic loop is completed as shown. It

can be noticed that the hysteretic loop performs symmetrically and the compression and extension of the BEDD are in accordance with each other.

Two BEDD members, one for each side, are installed on the side walls of each two adjacent tunnel element. Generally, BEDD members are connected to the main structure by welding, bolting or pin shafts. To be more cost-effective and have a more compact connection, a welded end connection is adopted between the ends of the BEDD and the embedded steel supports on the side walls, as shown in Figure VIII.4. Note that, the BEDD members can only be installed after the complete immersion and connection of the tunnel elements.

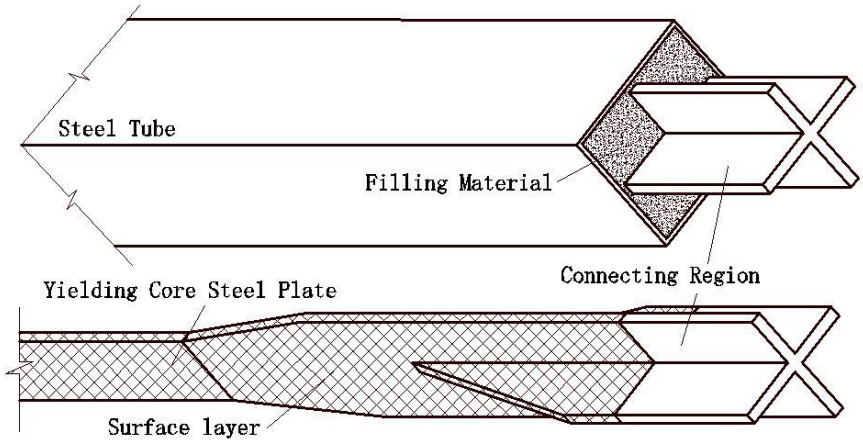

Figure VIII.2 Configuration of the BEDD in this experiment

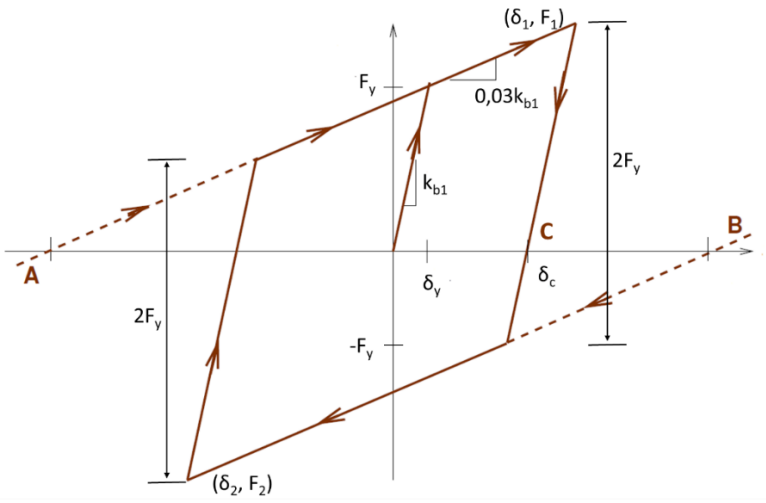

Figure VIII.3 Idealized bi-linear force-displacement model for Q235 steel

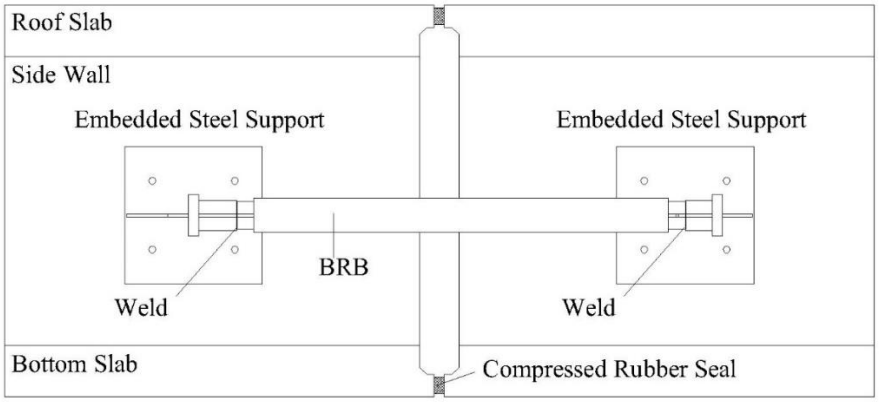

Figure VIII.4 Layout of the BEDD inside the tunnel

VIII.3.2. Mechanical model of the joint

It should be noted that in seismic mitigation design of immersion joints, only the GINA rubber seal is considered because of its great contribution to large deformations in the axial direction as aforementioned. The other components will not be considered in the following discussion.

After the immersion of the tunnel elements, an initial compression occurs at each of the immersion joints as exerted by the hydraulic pressure. Then, the BEDD's are installed inside the tunnel and they work together with the joint under seismic loading. As was mentioned in the previous chapter regarding the axial and shear behavior of the joint, the axial compression or decompression of the immersion joint can reach the centimeter level at the geometric scale of 1/10, in contrast to the shear one. Furthermore, shear deformations due to lateral and vertical oscillations are not as serious a problem, since large "shear keys" will take part of the induced loads. This is due to the fact that the shear stiffness of an immersion joint is much larger than the axial one (compression or decompression), resulting in a relatively small shear deformation during earthquake. Thus, it is unnecessary to consider seismic mitigation design along the transversal (shear) direction and moreover, this would be impossible to realize in practice. Therefore, seismic mitigation design for immersion joints is required and especially more attention should be paid to the axial compression and decompression responses. Hence, the

combined loadings of compressive force N and bending moment M should be considered and taken as one of the most severe loading situations for seismic design of the immersion joint.

The mechanical behavior of the immersion joint with the BEDD under the compression-bending moment loading is shown in Figure VIII.5. It can be clearly observed that when the joint rotates under the applied bending moment *M*, the BEDD on one side is extended and the one on the other side is compressed. The former deformation is critical for seismic performance of the immersed tunnel since it may lead to decompression of the joint gaskets, jeopardizing the water-tightness. Therefore, the bending moment induced by seismic action should be considered in the seismic mitigation design of the joint with the BEDD. Since a parallel connection is presented between the immersion joint and the BEDD along the longitudinal tunnel axis (shown in Figure VIII.5), the mechanical behavior of the joint and the BEDD are linearly combined when the tunnel element is subjected to combined loadings. The input axial force and the bending moment are taken by the rubber and the BEDD together. Therefore, the proposed mechanical model for the immersion joint with the BEDD is expressed as

$$\begin{cases} d_j = d_{BEDD} = d_{ru} \\ N_j = N_{BEDD} + N_{ru} \\ M_j = M_{BEDD} + M_{ru} \end{cases} \tag{VIII.3}$$

where d_j, d_{BEDD} and d_{ru} are the deformation of the joint, the BEDD and the rubber seal respectively, and $N_j(M_j)$, $N_{BEDD}(M_{BEDD})$ and $N_{ru}(M_{ru})$ are the force (bending moment) of the joint, the BEDD and the rubber seal respectively.

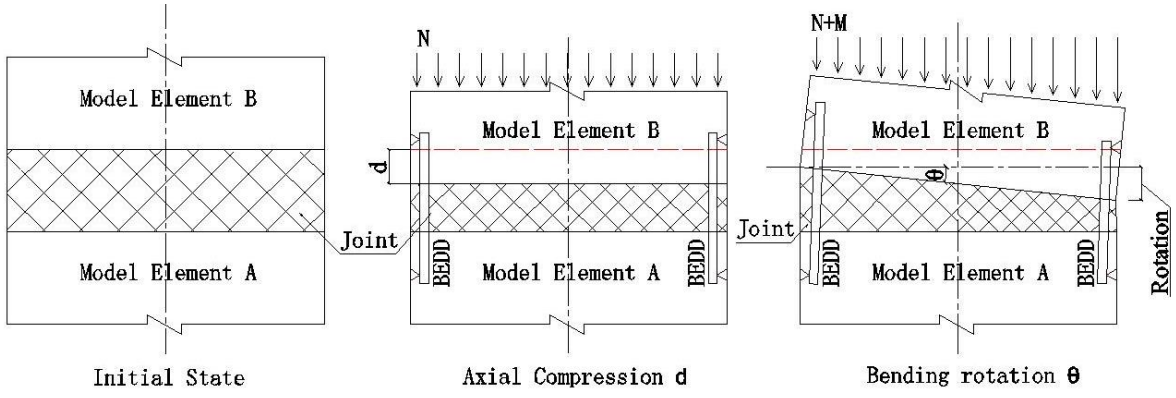

Figure VIII.5 Compression and bending of the joint with the BEDD

VIII.4. Parametric optimization

In order to obtain the expected behavior of the joint with the BEDD, the critical mechanical parameters of the BEDD, i.e. the total length *l* (see Figure VIII.4), the yielding deformation δ_y and the elastic stiffness k_{BEDD} (referred to k_{b1} in Figure VIII.3), should be determined for the optimized design of seismic mitigation. Herein, a scaled model of the immersion joint with a 1/10 geometric scale, which is the same as presented in Chapter IV, will be taken as an example to illustrate the design and validation of seismic mitigation for immersion joints.

The total length of the BEDD and the length of the yielding core steel plate, as shown in Figure VIII.2, are confined by the configuration of the model element. The total length cannot be too long due to the actual length of the model element or too short, which would result in a short yielding core plate. Based on these considerations, the total length *l* of the BEDD is selected as 1.3 m. According to the previously presented results, the relative displacement of the joint subjected to compression-bending loading remains at the centimeter level. The BEDD should be designed to yield soon in order to consume more energy, but meanwhile the manufacturing possibilities of the BEDD should also be considered. Thus, the yielding deformation δ_y of the BEDD is determined as 0.5 mm, which is the minimum manufactured yielding deformation according to the factory.

The elastic stiffness k_{BEDD} of the BEDD is defined as the tension/compression stiffness of the BEDD before yielding, which also affects the area of the hysteretic loop of the BEDD. A parametric optimization method is applied to obtain the optimized value of the elastic stiffness k_{BEDD}. Given that the maximum energy dissipation is reached when the hysteretic loop of the joint, together with the BEDD, reaches its maximum area under compression-bending loading. The optimization objective function *F* of the joint with the BEDD can be defined as

$$F = \max\{S\} \tag{VIII.4}$$

where S is the area of the hysteretic loop of the joint with the BEDD.

The detailed design procedure for the joint with the BEDD under compression-bending loading is presented as follows.

Step.1 Representation of mechanical model of the joint

The bending moment-rotation curve of the joint without BEDD was firstly obtained from the model test with the same specimens, and a bilinear simplified model is used to describe this curve, as shown in Figure VIII.6 (a). From the figure, the loading portion is divided into two parts, with slope k_1 (kN m/rad) and k_2 (kN m/rad) respectively. The rotation of the joint at the intersection of the two parts is defined as θ_1 (rad) while the maximum rotation of the joint is θ_2 (rad). The unloading portion is described by a linear model with slope k_1. The bending moment-rotation curve of the joint without BEDD can be expressed as

$$M_L = \begin{cases} k_1\theta & (0 < \theta \le \theta_1) \\ k_1\theta_1 + k_2(\theta - \theta_1) & (\theta_1 < \theta) \end{cases} \qquad \text{(VIII.5)}$$
$$M_{LU} = (k_1 - k_2)(\theta_1 - \theta_2) + k_1\theta$$

where M_L and M_{LU} represent the loading and unloading branches respectively.

A compression-bending test under a bending moment of 1000kN·m together with an axial force of 850kN was conducted and the results are shown in Figure VIII.7. A bi-linear fitting curve is applied to describe the behavior of joint only with the rubber obtained from the test, which is plotted in Figure VIII.7, in which the parameters k_1, k_2, and θ_1 are 6.57×10^5kN·m/rad, 3.73×10^5kN·m/rad and 7.6×10^{-4}rad respectively. The figure shows that the proposed simplified model fits well with the test results.

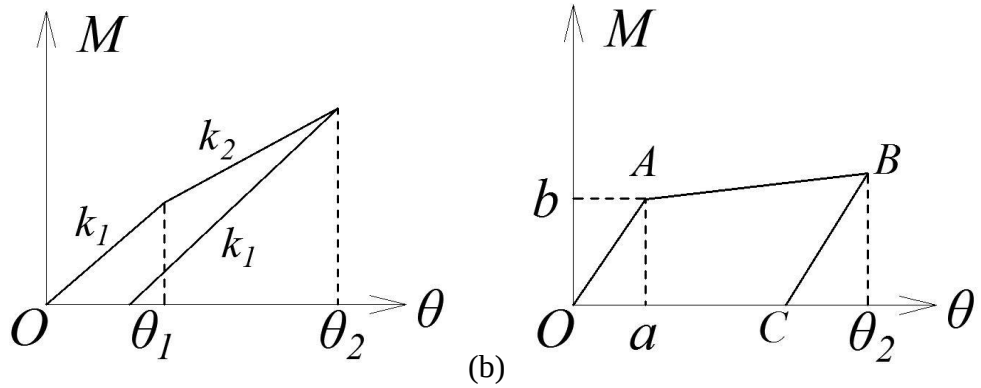

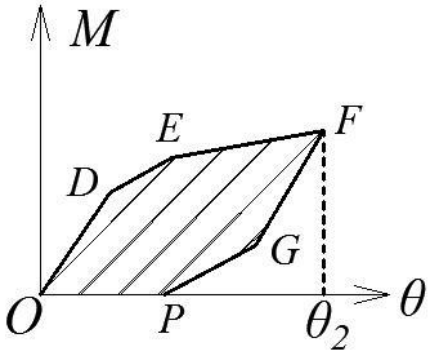

(c)

Figure VIII.6 Mechanical models of (a) the rubber seal, (b) the BEDD and (c) the joint with the BEDD

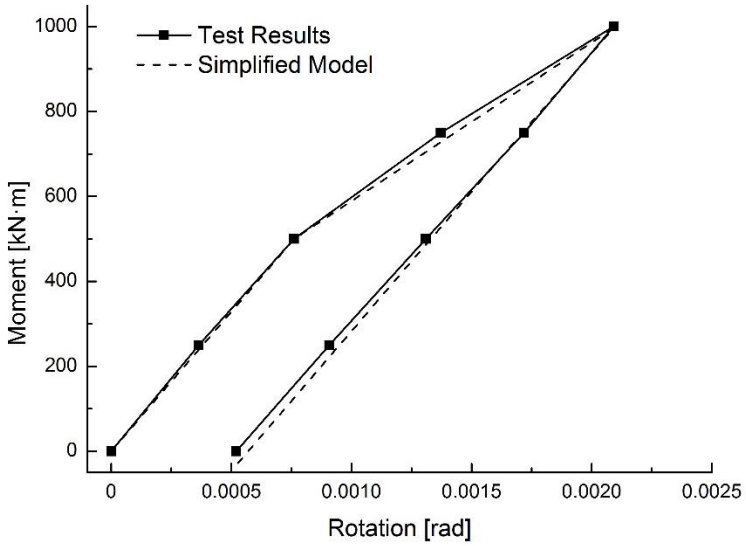

Figure VIII.7 Comparison between the test results and the simplified model

Step.2 Representation of the mechanical model of the BEDD

For the mechanical behavior of the BEDD, the assumptions include: (1) during the compression-bending loading (see Figure VIII.5), the joint behaves symmetrically, which means that the value of the compression of the BEDD on one side is equal to the extension of the BEDD on the other side; and (2) the axial deformation of the rubber seal is the same as that of the BEDD due to their parallel working system, as illustrated in Eq. (VIII.3). Hence, the bi-linear hysteretic model is used to simplify the behavior of the BEDD in the joint, as shown in

Figure VIII.6 (b). It should be noted that, in order to apply a superposition of the curves of the BEDD and the joint, the same maximum rotation angle θ_2 is applied in the model of the BEDD. Then the bending moment-rotation curve of the BEDD is expressed as

$$M_L = \begin{cases} \frac{b}{a}\theta & (0 < \theta \leq a) \\ b + 0.03\frac{b}{a}(\theta - a) & (a < \theta \leq \theta_2) \end{cases} \qquad \text{(VIII.6)}$$

$$M_{LU} = 0.97\frac{b}{a}(a - \theta_2) + \frac{b}{a}\theta \quad (\theta < \theta_2)$$

where a (rad) and b (kN·m) represent the rotation angle and the bending moment at the first yielding point A (see Figure VIII.6 (b)) of the BEDD, respectively, and a can be obtained by

$$a = \frac{2\delta_y}{L} \qquad \text{(VIII.7)}$$

where δ_y is the yielding deformation of the BEDD, i.e. 0.5mm as aforementioned, and L is the distance between the two BEDD installed on each side of the model element, i.e. 3400 mm in this test. Thus, the rotation angle a is obtained as $2.9\text{x}10^{-4}$ rad.

Step.3 Representation of the mechanical model of the joint with the BEDD

Based on the parallel working condition of the joint and the BEDD, the behavior of the joint with the BEDD is obtained as shown in Figure VIII.6 (c). The calculated coordinates of each point in the figure are given in Table VIII.1, in which k_1, k_2 and θ_1 are known parameters while a, b and θ_2 remain unknown.

Table VIII.1 Co-ordinates of the points in Figure VIII.6 (c)

Point	Rotation θ	Bending moment M
D	a	$b + ak_1$
E	θ_1	$\theta_1 k_1 + b + 0.03\frac{b}{a}(\theta_1 - a)$
F	θ_2	$\theta_1 k_1 + (\theta_2 - \theta_1)k_2 + b + 0.03\frac{b}{a}(\theta_2 - a)$

G	$\theta_2 - 2a$	$\theta_1 k_1 + (\theta_2 - \theta_1)k_2 + b + 0.03\frac{b}{a}(\theta_2 - a) - 2ak_1 - 2b$
P	$\theta_2 - 2a$ $-\frac{\theta_1 k_1 + (\theta_2 - \theta_1)k_2 + b + 0.03\frac{b}{a}(\theta_2 - a) - 2ak_1 - 2b}{k_1 + 0.03\frac{b}{a}}$	

Step.4 Representation of the optimization objective function *F*

In the model test, the maximum bending moment is set at 1000kN·m, that is the value of the bending moment at point F (Figure VIII.6 (c)). Based on the coordinate expression at point F in Table VIII.1 and the known parameters above, the parameter *b* can be obtained as

$$b = \frac{100a[1000-\theta_1(k_1-k_2)-\theta_2 k_2]}{97a+3\theta_2} \quad \text{(VIII.8)}$$

Then, according to the coordinate expressions at each point in Figure VIII.6 (c) and in Table 1, the total area of the hysteretic loop of the joint with the BEDD can be calculated by using their coordinates, based on the geometric relationship in the Cartesian coordinate system in Figure VIII.6 (c). Hence the equation for ***S*** can be obtained as

$$S = \frac{-20}{100ak_1+3b}(5a\theta_1^2k_1^2 - 7.5a\theta_1^2k_1k_2 + 2.5a\theta_1^2k_1^2 - 5a\theta_1\theta_2k_1^2 + 10a\theta_1\theta_2k_1k_2 - 5a\theta_1\theta_2k_2^2 - 2.5a\theta_2^2k_1k_2 + 2.5a\theta_2^2k_2^2 + 12.13a^2bk_1 - 4.85ab\theta_1k_1 + 4.85ab\theta_1k_2 - 4.85ab\theta_2k_1 - ab\theta_2k_2 + 0.075b\theta_1^2k_1 - 0.075b\theta_1^2k_2 - 0.075b\theta_2^2k_1 + 0.075b\theta_2^2k_2 + 2.72ab^2 - 0.29b\theta_2)$$

(VIII.9)

Since a, k_1, k_2 and θ_1 are known parameters and the relation between *b* and θ_2 is given by Eq. (VIII.8), the function *S* can be further simplified as

$$S(\theta_2) = -\frac{9.72\times10^5\theta_2^3+10.97\times10^4\theta_2^2-368.46\theta_2+0.17}{8.52\times10^2\theta_2^2+28.8\theta_2+0.195} \quad (7.6\times10^{-4} < \theta_2 < 21\times10^{-4})$$

(VIII.10)

and then the objective function $F = \max\{S\}$ can be obtained. Note that in Eq. (VIII.10), the lower bound of θ_2 is determined by the fact that the maximum rotation of the joint should be larger than θ_1 while the upper bound of θ_2 is calculated by the condition $b > 0$ in Eq. (VIII.8).

Step.5 Determination of the optimal mechanical parameters of the BEDD

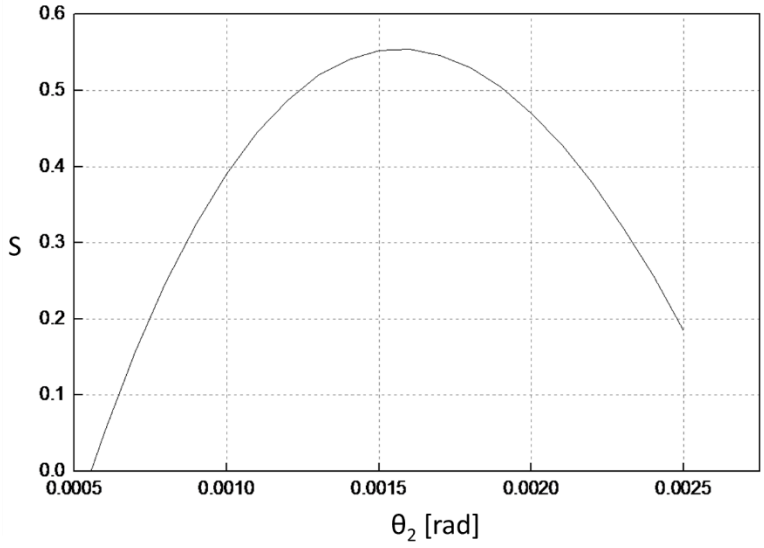

Figure VIII.8 Diagram of $S(\theta_2)$

The diagram of the function $S(\theta_2)$ is shown in Figure VIII.8. Within the domain of the function, the area of the hysteretic loop in the first quadrant can reach a maximum value. It can be quickly computed by MATLAB (2011b) that the objective function $F = \max\{S\}$ will reach the peak when θ_2 equals to 0.00157rad, and then b=175kN·m is obtained by Eq. (VIII.8). The optimized mechanical parameters of the BEDD are listed in Table VIII.2, in which the elastic stiffness k_{BRB} and the yielding force N_q (denoted as F_y in Figure VIII.3) of the BEDD are obtained respectively by

$$k_{BEDD} = \frac{F_A}{d_A} = \frac{2b}{aL^2} \tag{VIII.11}$$

$$N_q = k_{BEDD}\delta_y \tag{VIII.12}$$

where F_A and d_A are the force and deformation of the BEDD at point A in Figure VIII.6 (b), respectively.

Table VIII.2 Mechanical parameters of the BEDD

Total length *l*	1.3m
Elastic stiffness k_{BEDD}	104.4x10^3 kN/m
Yielding deformation δ_y	0.5mm
Yielding force N_q	52.2kN

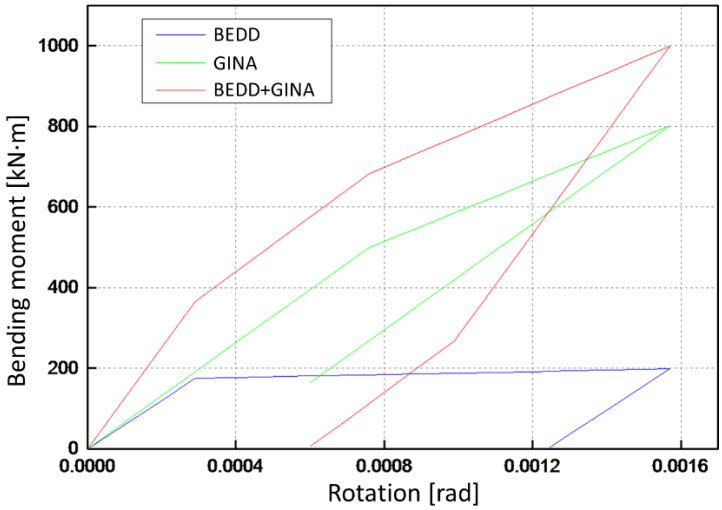

Figure VIII.9 Expected bending moment-rotation curve of the joint in this experiment

Based on the mentioned design procedure, the expected bending moment-rotation curve of the joint as well as the contribution of the rubber and the BEDD respectively are shown in Figure VIII.9. Initially, when the bending moment remains at a small level, the BEDD and the GINA rubber share almost the same amount of the bending moment. After the yielding point of the BEDD, the stiffness of the BEDD reduces, resulting in the fact that the rubber seal starts to dominate the experiment. It can be noticed that before unloading most of the bending moment is expected to be taken by the rubber possibly due to the fact that such high bending moment results in a relatively high stiffness of the rubber and the behavior of the rubber contributes a lot to the stiffness of the joint with the BEDD. In the unloading portion, the bending moment of the BEDD precedes that of the GINA rubber to return to zero as the bending moment

decreases. In other words, during the unloading of the bending moment, the BEDD will behave from a compression(extension) component to an extension (compression) component.

VIII.5. Summary

The seismic analysis of immersed tunnels was subject of research since 1995 and the increasing number of projects also promoted the development of the seismic analysis. However, previous research regarding the seismic performance of immersed tunnels remained limited to numerical modeling and the soil-structure interaction rather than the structure itself. During the same period, some suggestions were formulated to improve the seismic performance of other forms of underground structures, such as the isolation layer for shield tunnels or ground treatment for metro stations etc. However, such improvements may work but they are not suitable for immersed tunnels due to the special configuration of the surrounding soil and the unique construction method. Hence, a new concept was proposed based on the seismic mitigation theory. The efficiency of the seismic mitigation method in seismic response reduction was proved by both research and actual practice in the building area but it was never introduced to underground structures before. As such, a seismic mitigation device installed on the immersion joint and working together with the joint could be an additional way to dissipate the energy induced by the earthquake.

To achieve the application of seismic mitigation in immersion joints, the mechanisms of seismic mitigation method for buildings were studied and discussed through the energy conversion equations. A buckling energy-dissipation device (BEDD) was introduced on the basis of the BRB. Based on the principle of maximum hysteretic performance of the joint, the optimization design procedure of the seismic mitigation device is illustrated in detail through a parametric analysis, including the critical parameters, such as the elastic stiffness and the yielding deformation of the BEDD. The design procedure was provided through five steps: (1) representation of the mechanical model of the joint; (2) representation of the mechanical model of the BEDD; (3) representation of the mechanical model of the joint with the BEDD; (4)

representation of the optimization objective function ***F***; and (5) determination of the optimal mechanical parameters of the BEDD. Finally, the optimized parameters for the BEDD, such as yielding deformation, elastic stiffness and the total length of the device are designed to ensure that the device works in coordination with the immersion joint in such a way that the maximum energy dissipation is reached.

VIII.6. References

Black, C., Makris, N., Aiken, I., 2004. Component testing, seismic evaluation and characterization of buckling-restrained braces. Journal of Structural Engineering-ASCE. 130 (6), 880–894.

Bobet, A., 2003. Effect of pore water pressure on tunnel support during static and seismic loading. Tunnelling and Underground Space Technology. 18, 377–393.

Hashash, Y., Hook, J., Schmidt, B., et al., 2001. Seismic design and analysis of underground structures. Tunnelling and Underground Space Technology. 16, 247–293.

Huo, H., Bobet, A., Fernández, G., Ramírez, J., 2006. Analytical solution for deep rectangular structures subject to far-field shear stresses. Tunnelling and Underground Space Technology. 21, 613–625.

Iwata, M., Murai, M., 2006. Buckling-restrained brace using steel mortar planks; performance evaluation as a hysteretic damper. Earthquake Engineering and Structural Dynamics. 35, 1807-1826.

Lankesoft Inc., 2016. Design guide book for metal seismic mitigation techniques (Sixth edition). <www.lankesoft.com>. (in Chinese)

Ministry of Housing and Urban-Rural Development of the People's Republic of China, 2003. Code for Design of Steel Structures (GB 50017-2003). China Architecture & Building Press, Beijing. (in Chinese)

Pitilakis, K., Tsinidis, G., 2014. Performance and seismic design of underground structures. In: Maugeri, M., Soccodato, C. (Eds.), Earthquake Geotechnical Engineering Design, Geotechnical Geological and Earthquake Engineering, vol. 28. Springer International Publishing, Switzerland, pp. 279–340.

Shang, S., Zhou, F., 2003. Structural seismic design. Higher Education Press, Beijing. (in Chinese)

Sun, F., Li, G., Guo, X., Hu, D., Hu, B., 2011. Development of a new-type buckling restrained braces and their application in aseismic steel frameworks. Advanced Structural Engineering. 14(4), 717–730.

Wang, J., 1993. Seismic Design of Tunnels: A Simple State of the Art Design Approach. Parsons Brinckerhoff Inc., New York.

Xie, Q., 2005. State of the art of buckling-restrained braces in Asia. Journal of Construction Steel Research. 61, 727–748.

Yu, H., Yuan, Y., Bobet, A., 2013a. Multiscale method for long tunnels subjected to seismic loading. International Journal for Numerical and Analytical Method in Geomechanics. 37 (4), 374–398.

Yu, H., Yuan, Y., Qiao, Z., et al., 2013b. Seismic analysis of a long tunnel based on multi-scale method. Engineering Structures. 49, 572–587.

Yu, H., Cai, C., Guan, X., et al., 2016. Analytical solution for long lined tunnels subjected to travelling loads. Tunnelling and Underground Space Technology. 58, 209–215.

CHAPTER IX

Seismic Mitigation for Immersion Joints: Validation

Oresund immersed tunnel, Denmark and Sweden

(COWI)

IX. Seismic Mitigation for Immersion Joints: Validation

IX.1. General introduction

Seismic mitigation devices for immersion joints is a new concept for disaster reduction of underground structures which were never applied in practice. In order to introduce this method in immersed tunnels, the mechanism of seismic mitigation, the mechanical model for this method and the design procedure are provided in the previous chapter. Based on that, the mechanical parameters of the selected seismic mitigation device, namely the buckling energy-dissipation device (BEDD), were determined, which are the total length, the yielding deformation and the elastic stiffness. In this chapter, a test series involving compression-bending loading on a large-scale immersion joint was realized. The basic aim was to validate the proposed design and have a complete understanding of the application of seismic mitigation in immersion joints.

First of all, the information about the scaled immersion joint and the BEDD are given in Section IX.2, explaining in detail their design and configuration in the experiment. Accordingly, the test set-up as such is explained in Section IX.3, giving the information about the detailed design and the measurement arrangement. Furthermore, an overview of the loading protocol is provided.

Section IX.4 is dedicated to the observations during the executed loading test and the obtained results are explained and discussed. A comparison is made between the specimen with and without BEDD. Ample attention is paid to the compression behavior and the compression-bending behavior of the joint with the BEDD as well as the performance of the BEDD itself.

Finally, a discussion about the seismic mitigation issue in the joint is given in Section IX.5 followed by a brief summary (Section IX.6) of this chapter.

IX.2. Test specimens

IX.2.1. Scaled immersion joint

The scaled immersion joint in this chapter consists of two model tunnel elements and one joint in between as shown in Figure IX.1, which is actually the same as the specimen displayed in Chapter IV. A single tunnel element with a width of 3800 mm, a height of 1150 mm, and a length of 1250 mm, as well as a 150 mm-thick concrete slabs and walls is shown. Referring to the Chinese Code for design of concrete structures (GB50010-2010), the types of concrete and reinforcement are C50 and HRB400 respectively. The model immersion joint follows the design of the HZM immersed tunnel and the geometric lay-out is simplified for the purpose of the experiment (see Chapter IV). The steel shell and omega profile are not provided in this model joint due to the lack of contribution to the flexural behavior of the immersion joint. A certain type of GINA seal is designed and manufactured independently for this experiment. A detailed overview of the scaled model of the immersion joint and its physical parameters can be found in previous chapters.

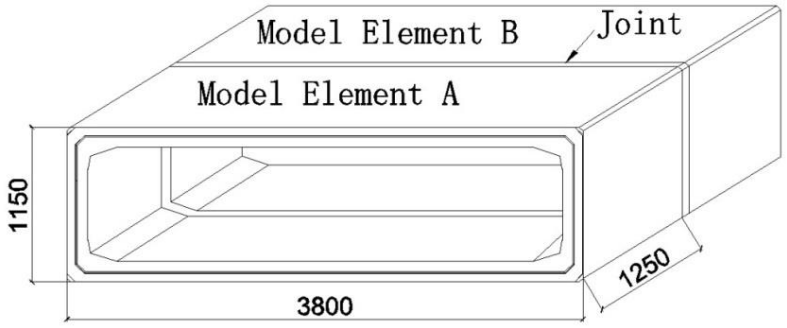

Figure IX.1 Scaled immersion joint [mm]

IX.2.2. Buckling energy-dissipation device

As mentioned in the previous chapter, the applied BEDD in this experiment is based on the TJ-II^{TM} (Sun et al., 2011). As shown in Figure IX.2 (a), the total length of the BEDD is 1.3m with a total cross-section of 90mm x 100mm and an expected yielding deformation of 0.5mm. The

Q235 steel was used as the core steel plate with a tested yielding strength of 268MPa. The core steel plate is I-shaped and is placed vertically. Due to the trade secret, the detailed information of the core plate is confidential and not provided in this section. The cross section of the connecting region is cross-shaped with a cross sectional area of 1216 mm^2 (Figure IX.2 (c)). The BEDD is welded on the steel plate with a thickness of 20 mm, which is embedded in the wall of the tunnel element. Generally, a hinge connection between the BEDD and the support should be used in order to eliminate the bending moment possibly generated during the test. However, due to the small yielding deformation, a hinge connection, for example using a pin connection, may affect the yielding performance because of the manufacturing accuracy. The detailed position of the steel plates and the BEDD is shown in Figure IX.2 (a) and (b). The horizontal axis distance between the two BEDD's is 3400mm.

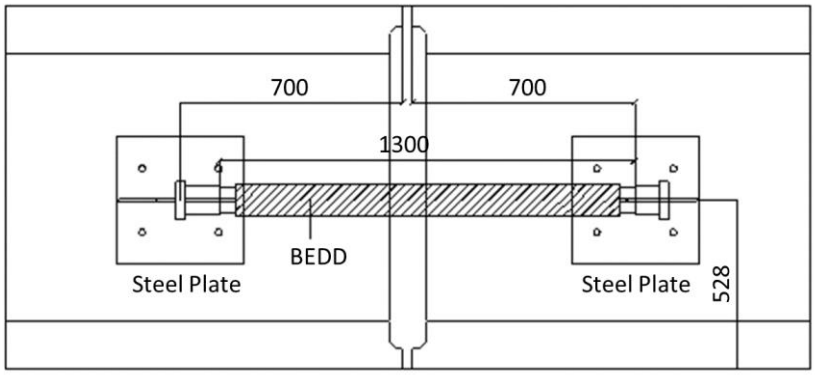

(a) The position of the BEDD (side view)

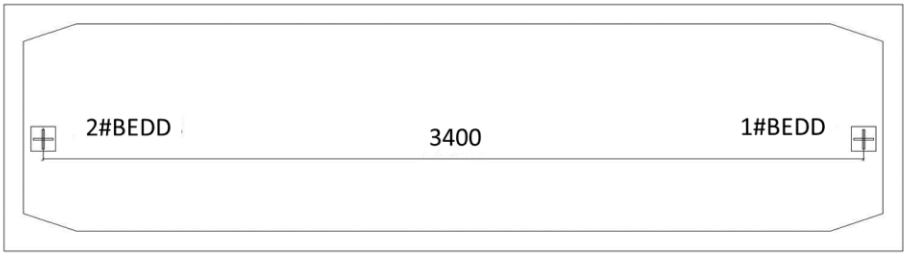

(b) The position of the BEDD (front view)

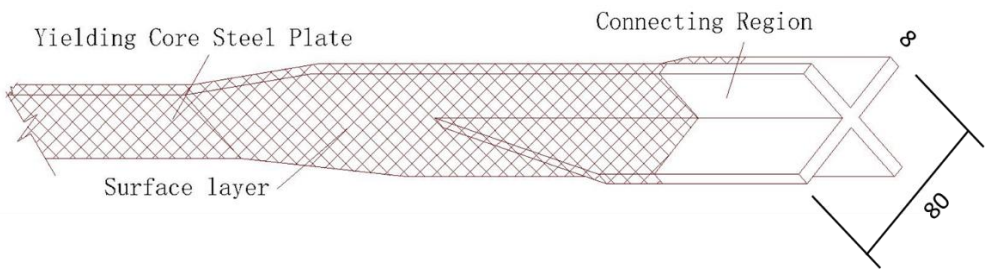

(c) Layout of the steel plate of the BEDD (symmetrical)

Figure IX.2 Position and dimensions of the BEDD [mm]

IX.3. Experimental set-up and loading protocol

IX.3.1. Experimental set-up

As mentioned in Figure VIII.5, one element (Element A) is fixed and the axial force is applied on the other element (Element B), resulting in compression and bending deformations in the immersion joint. In view of this, a test set-up was designed where the tunnel model was placed in a steel loading frame, as shown in Figure IX.3. During a typical experiment, one tunnel element (Model Element A) is fixed horizontally while the other one (Model Element B) is movable, controlled by the jacks and the actuator. Figure IX.3 (b) shows the four loading points of the test, applying the axial force to Model Element B. Thus, four hydraulic jacks are situated between this element and the reaction wall, as displayed in Figure IX.3 (a). These jacks can only provide compression to the element but no tension. By controlling the jacks, different levels of axial force and bending moment can be applied in the element. In order to figure out the flexural behavior of the immersion joint, this experiment employs a moment reversed quasi-static loading pattern.

This reaction frame includes an axial reaction part and a supporting system. To increase the axial stiffness of the reaction frame, two horizontal gantry frames are used. The model elements are placed inside the frames with a certain type of hinge in between them to ensure that no moment would occur during the test. Moreover, to avoid friction between the element and the

reaction floor, several columns with spherical hinge bearing on their top are installed before the elements are placed, as shown in Figure IX.3 (b). It should be noted that this experimental set-up is the same as the one presented in Chapter IV but the vertical frame is not displayed in this figure.

Figure IX.4 shows a view of the test model after installation. Note that the BEDD members are installed after the complete connection of the tunnel elements. A welded end connection is adopted between the ends of the BEDD and the steel supports embedded in the side walls. After welding, strain gauges were applied on the connecting region after the steel was cooled down because the high temperatures might damage the strain gauges.

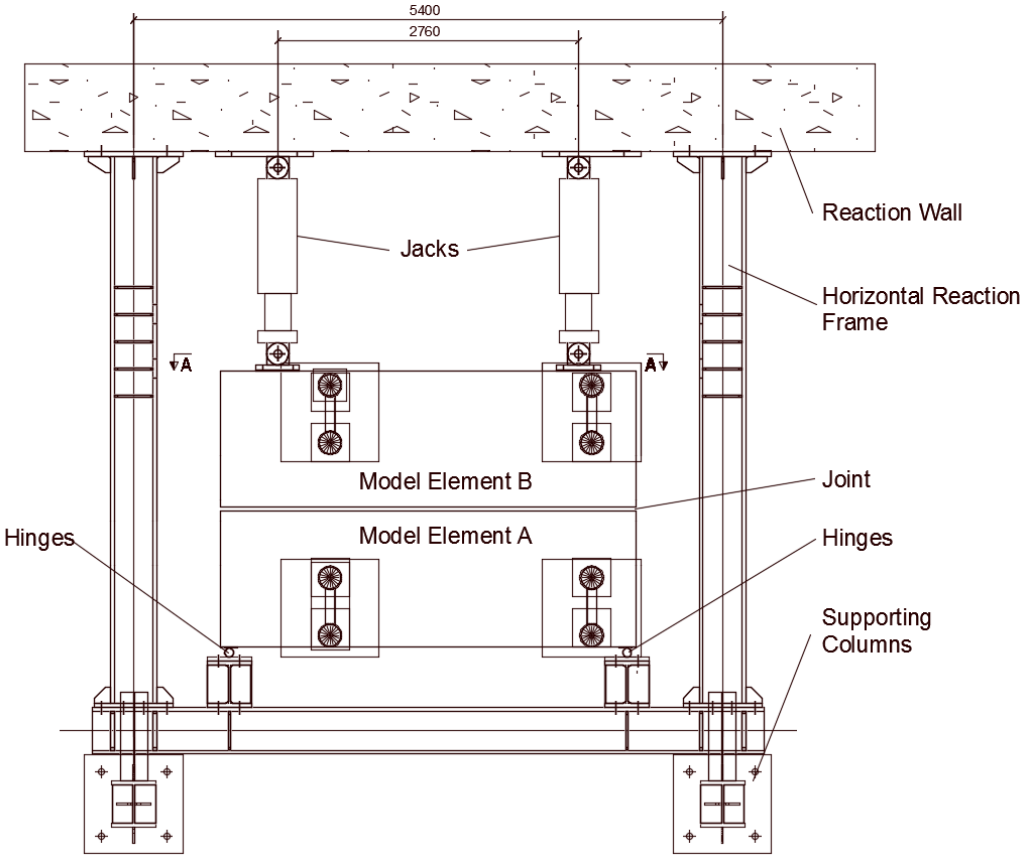

(a)

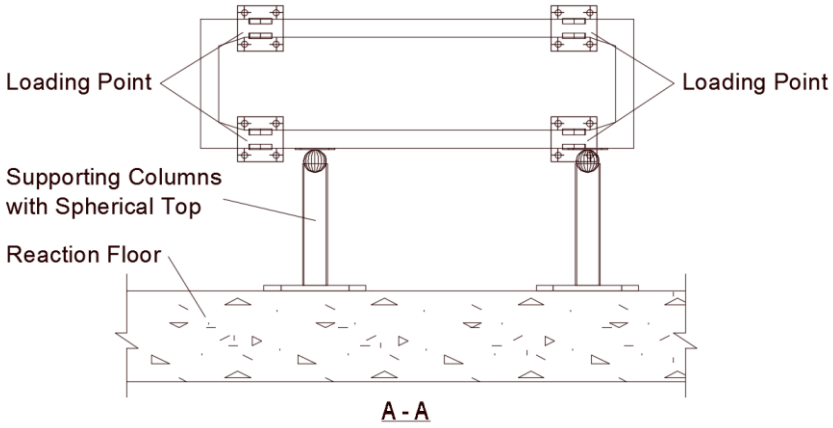

(b)

Figure IX.3 Layout of the test set-up in (a) plan view and (b) detailed view A-A

Figure IX.4 Detailed view of the BEDD installed on each side of the tunnel element

IX.3.2. Instrumentation

In order to figure out the flexural behavior of the immersion joint during the test, the deformation of the joint is monitored. Hence, four displacement transducers (#1–#4) are placed respectively at each of the corners inside the tunnel element, as shown in Figure IX.5 (a). Two strain sensors are also placed on the connecting region of each of the BEDD to obtain the internal force of the BEDD, as shown in Figure IX.5 (b). The sequence number of the strain sensors is #5 and #6 for one of the BEDD while #7 and #8 for the other. All the data are collected by a digital data acquisition system.

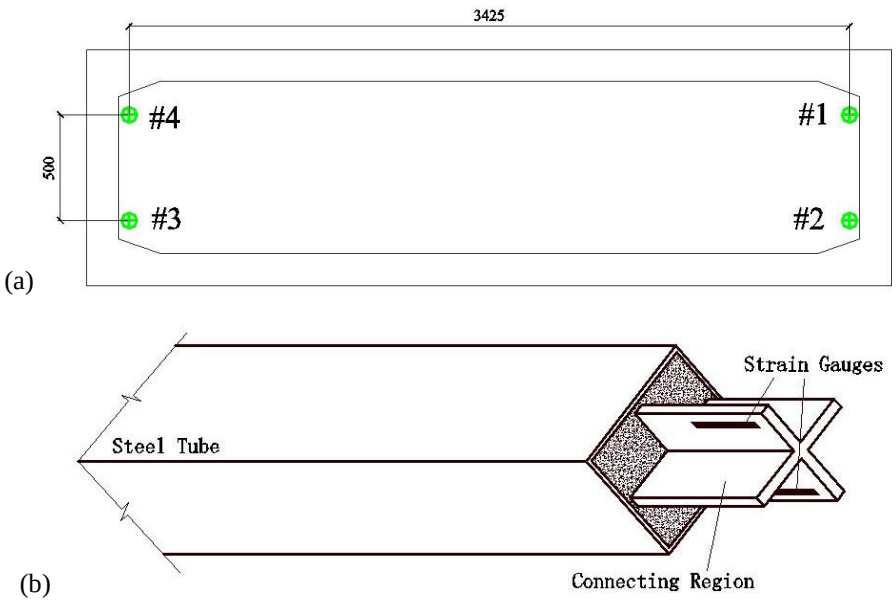

Figure IX.5 Layout of the measurements: (a) axial displacement transducers (Unit: mm); and (b) strain gauges on the BEDD

IX.3.3. Loading protocols

A similar compression-bending moment protocol, which has been mentioned in Chapter IV, was applied. In this loading case, only one water depth is considered, referring to the water depth of the final joint, which is one of the most important joints in the immersed tunnel. Hence, this level of the axial force is selected at 850kN (scaled down). During seismic movement of the stratum, the horizontal bending might change with the location along the tunnel length. A maximum bending moment of 1000kN·m (scaled down) is reasonable from design considerations. It should be noted that the process for applying the axial load and bending moment is the same as the aforementioned compression-bending moment test (see Chapter IV). The compression of the joint is measured continuously during a loading/unloading cycle, in order to obtain the rotation of the joint as a function of the bending moment. It should be note that the loading rate in the test equals 1kN/s.

Two comparison tests of the immersion joint, with and without the optimized BEDD device, are employed to validate the proposed seismic mitigation method for the immersion joint, as

illustrated in Table IX.1. Note that the hysteretic performance of the joint (i.e. the objective function in Eq. (VIII.4)) is taken as an evaluation criterion of energy dissipation.

Table IX.1 Loading protocol of this section

Case No.	Axial force [kN]	Max. bending moment [kN·m]	Max. rotation [rad]	Remarks
1	850	1000	-	with BEDD
2	850	-	the same as Case 1	without BEDD

IX.4. Experimental results

IX.4.1. Results of the tests without BEDD

Before the compression-bending test, a compression test of the model immersion joint with the primary rubber seal was conducted as shown in Figure IX.6. The axial force was applied to the joint until reaching 850kN, followed by an unloading stage. A nonlinear compression behavior and a hysteretic loop are observed. The unloading path does not follow the loading one, which means the joint behaved non-elastically when it is subjected to the compression or extension loadings. The compression of the joint is 16.10 mm, corresponding to the axial force of 850kN.

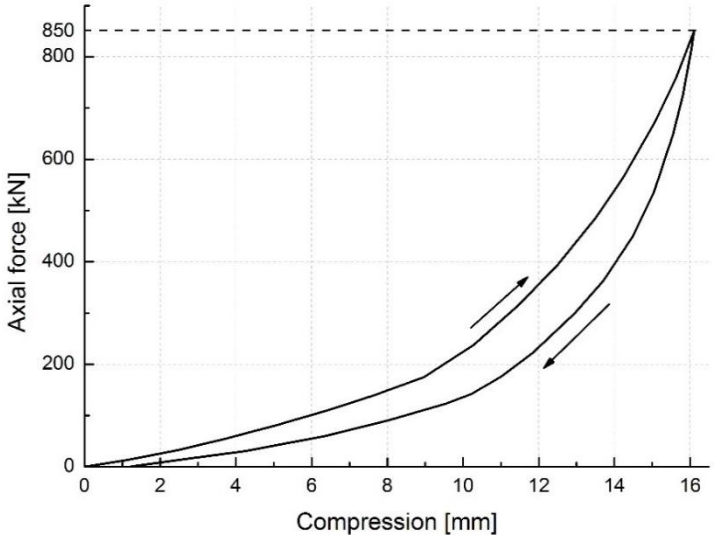

Figure IX.6 The compression behavior of the joint without the BEDD

After application of the axial force, the bending moment cycle is applied. The recorded displacements are shown in Figure IX.7 (a). A positive displacement represents compression of the joint while a negative one means extension. It is obvious that the compression and extension behavior of the joint are different and the joint behaved unsymmetrically due to the difference between the loading and unloading axial behaviors of the joint as mentioned before (Figure IX.6). Also, a residual displacement is found. Most importantly, the recorded displacements of the transducers at the same side behave nearly identically. Hence, the rotation of the joint subjected to the bending moment can be approximated as:

$$\theta = \frac{d_{a1} - d_{a2}}{L_T} \tag{IX.1}$$

where L_T is the distance between the transducers on the two sides of the model element, which is 3425mm in this test; $d_{a1} = (d_1 + d_2)/2$ and $d_{a2} = (d_3 + d_4)/2$ is the average displacement of the transducers at the same side; d_1 to d_4 represent the recorded displacement of #1 to #4 transducers in Figure IX.5 (a) respectively.

The calculated rotation of the joint without the BEDD is shown in Figure IX.7 (b), which is a typical compression-bending behavior of the joint as shown in Chapter V. Obviously the hysteretic loop is also found in this curve as well as a residual rotation, which is also due to the different behavior between the loading and unloading parts.

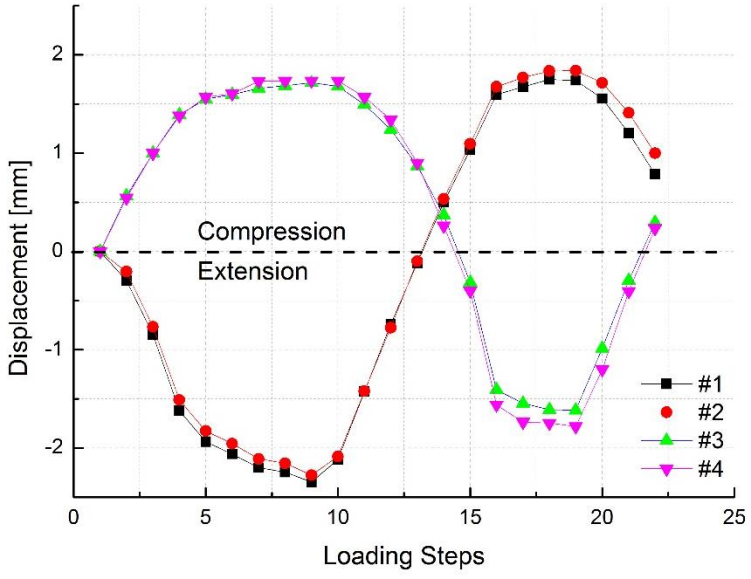

(a)

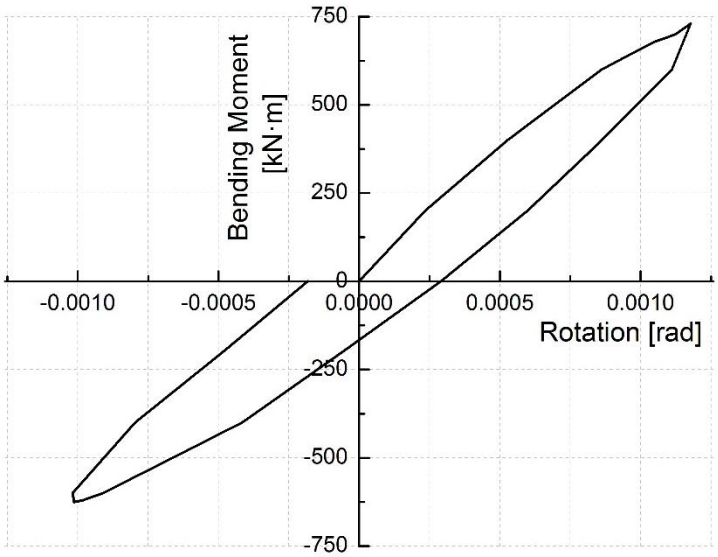

(b)

Figure IX.7 The compression-bending behavior of the joint without the BEDD: (a) recorded displacement of the joint and (b) moment-rotation curve of the joint

IX.4.2. Results of the tests with BEDD

The recorded displacements of the joint with the BEDD (Case 1) are shown in Figure IX.8 (a). When the joint was subjected to the compression-bending loading, the same trend as the one without the BEDD is found. The joint also behaved unsymmetrically due to the mentioned compression behavior of the joint. Moreover, the maximum displacements at both sides are in agreement with each other. Then, the rotation of the joint in this case can also be calculated by Eq. (IX.1). Figure IX.8 (b) shows the recorded stains of the BEDD in Case 1. The positive strain represents an extension of the BEDD while a negative one represents compression. It can be seen from the figure that the strains experience the same trend as the displacements in Figure IX.8 (a). In both curves, turning points can be observed when the BEDD's are extended, which is not the case in Figure IX.7 (a). Inversely, such points are less obvious when the BEDD's are compressed. What is more interesting is that, residual negative strains are derived in the figure, which indicates that the joint was still under compression after one load cycle.

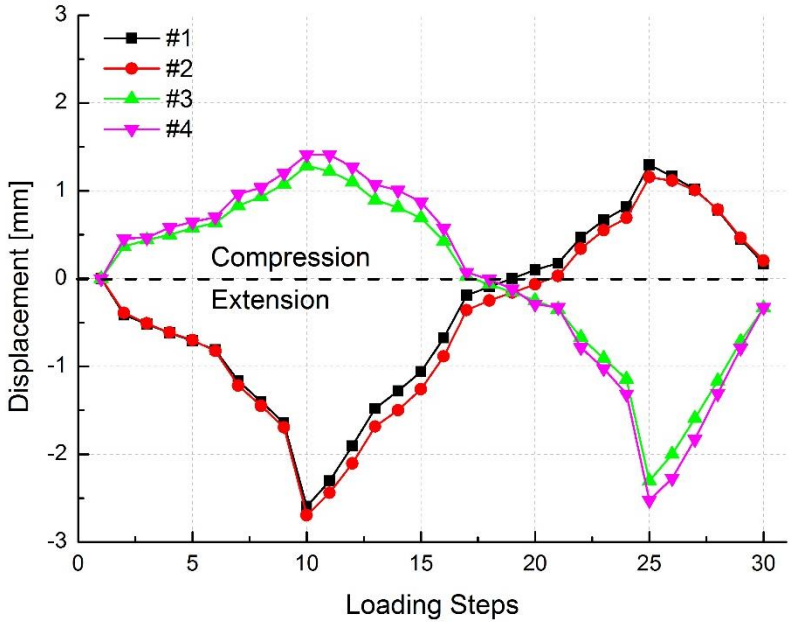

(a)

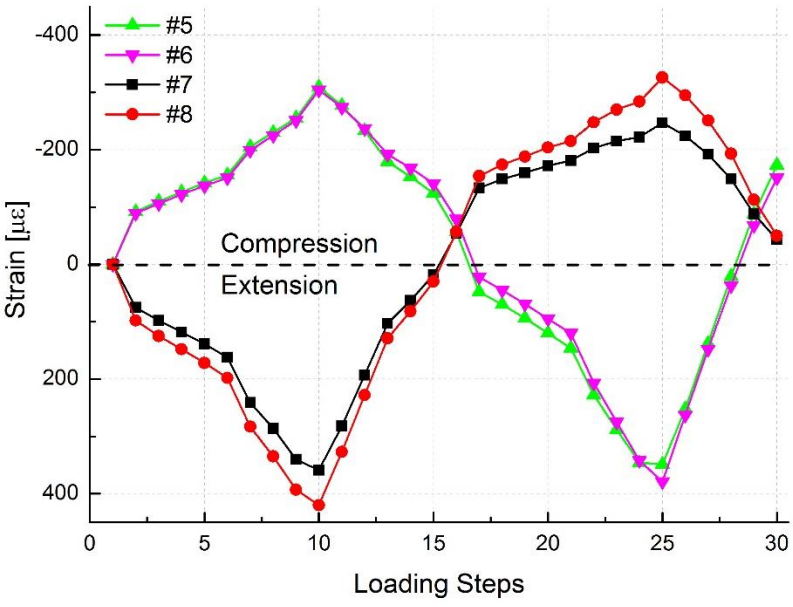

(b)

Figure IX.8 Test results: (a) recorded displacements of the joint with BEDD; (b) recorded strains of the two BEDD's;

IX.4.3. Comparison between the results without and with the BEDD

The moment-rotation curves of both joints with and without the BEDD subjected to combined loading can be seen in Figure IX.9. The figure shows that the two curves show a similar hysteretic performance of the joint. However, both the slope and the hysteretic loop of the joint with the BEDD are larger than those without the BEDD. Under the same rotation, the joint with the BEDD can resist over 37% bending moment, from 730kN·m up to 1000kN·m. The yielding performance of the joint with the BEDD is less noticeable from the figure and only a slight change in the slope of the curve is observed when the bending moment increases up to ±800kN·m. Moreover, the same residual rotations occur in both curves.

As mentioned in Section VIII.4, the area of the hysteretic loop of the moment-rotation curve of the joint is utilized to evaluate the seismic mitigation effect of the joint. Some characteristics of the hysteretic performance of the joint are given in Table IX.2, as obtained from Figure IX.9. The area of the hysteretic loop of the joint with the BEDD increases by about 69%, compared to that of the joint without the BEDD. Therefore, the hysteretic performance of the joint with the BEDD enhances remarkably by 69%, which indicates that the proposed seismic mitigation device for immersion joints can absorb significantly more energy under the same maximum rotation.

The diagonal flexural stiffness of the joint is defined as:

$$k_f = \frac{M_{max} - M_{min}}{\theta_{max} - \theta_{min}} \quad \text{(IX.2)}$$

where M_{max} and M_{min} are the applied maximum and minimum bending moments respectively; θ_{max} and θ_{min} are the corresponding rotations of the joint respectively.

After the installation of the BEDD, the joint behaves stiffer in the bending direction. The bending resistance increases by 37% and the flexural stiffness of the joint increases by 45%.

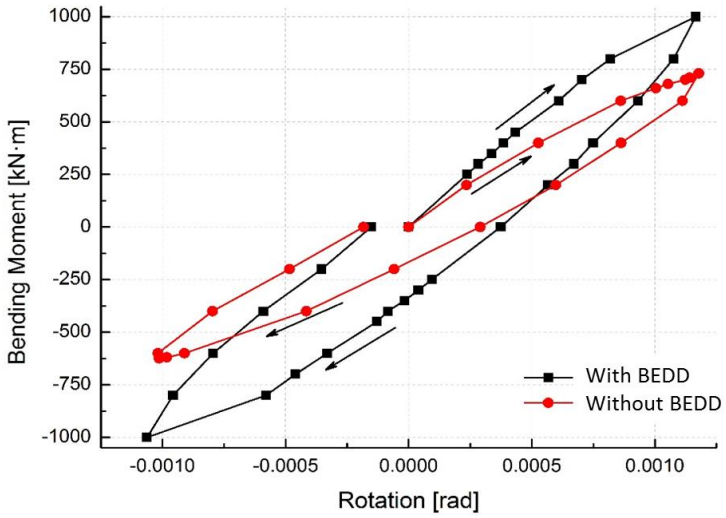

Figure IX.9 Moment-rotation curves of the joint for two cases

Table IX.2 Effects of the hysteretic performance of the joint provided by the BEDD

	Max. moment [kN·m]	Flexural stiffness [kN·m/rad]	Hysteretic loop
Case 1	1000	8.97×10^5	169%
Case 2	730	6.19×10^5	100%
Effect of the BEDD	+37%	+45%	+69%

IX.5. Detailed discussion

In view of the fact that the connecting region of the BEDD will not yield, the internal force F_B of the BEDD can be obtained by:

$$F_B = \varepsilon EA \tag{IX.3}$$

where ε is the obtained strain of the BEDD, i.e. the average strains from #5/#6 or #7/#8 from Figure IX.8 (b). E is the Young's Modulus of the steel, i.e. 206 GPa in this test, and A is the cross-sectional area of the connecting region, i.e. 1216 mm^2 in this test.

The calculated internal force from Eq. (IX.3) and the recorded displacements of two BEDD's are presented in Figure IX.10. Obviously, one BEDD yields in both tension and compression during the test while the other one only yields in tension. When the BEDD's are extended, a plateau can be clearly observed in the figure, which represents the plastic performance of the BEDD. This can be considered as an explanation for the turning points in the extension direction in Figure IX.8 (b). However, such plastic plateau segment is relatively small, compared to the elastic part. With respect to compression behavior of the BEDD's, the yielding performance is less obvious in one curve (from #7/8 in Figure IX.10) and even no plastic segment is found in the other curve (from #5/#6 in Figure IX.10). It means that both the BEDD yield in extension but not yield or just start to yield in compression. In other words, the extension behavior of the BEDD's shows a better plastic performance than the compression one in this experiment.

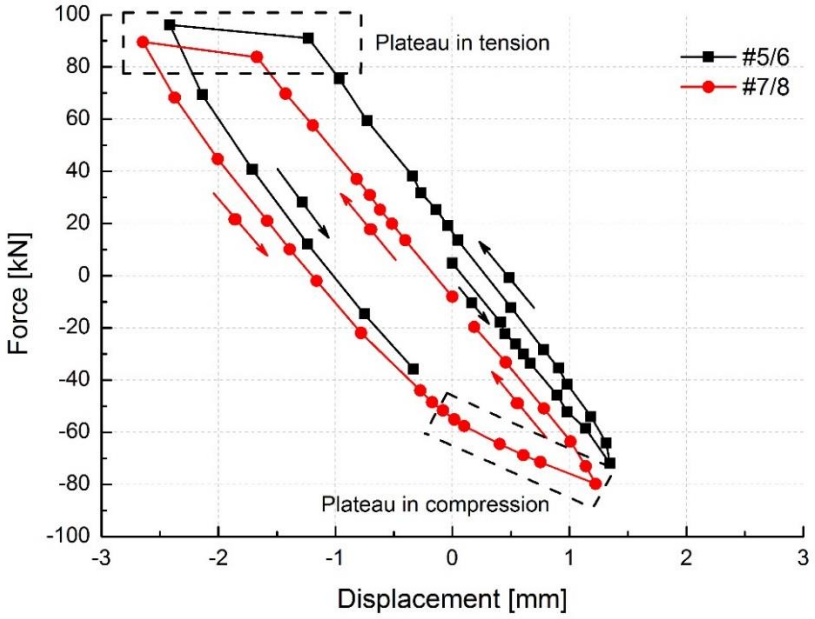

Figure IX.10 Force-displacement curves of the BEDD

Figure IX.11 illustrates the flexural behavior of the profile of the joint with and without the BEDD as well as the displacement of the BEDD in both sides. The long-and-short dashed line in the figure represents the original state of the profile while the dashed line and the continuous line represent the profiles of the joint with and without the BEDD respectively during the test.

When the bending moment was applied to the joint, the joint rotated clockwise, resulting in the different displacements of the BEDD at both sides. As shown in the figure, the compression of the BEDD on the right side is only 1.348mm while the extension of the other side is 2.645mm. However, the compressed BEDD did not yield though the compression is larger than the yielding deformation of the BEDD. It can also be observed from Figure IX.11 that a smaller compression on one side of the joint and a larger extension on the other side are obtained from the test with the BEDD, compared to those in the joint without the BEDD. This is due to the fact that, the bending stiffnesses of the joints with and without the BEDD are different. The reverse bending moment is applied in the same way. The accumulated compression and extension for the BEDD are 2.005mm and 2.915mm respectively. A larger extension of the joint under reverse bending moment is also obtained from the test.

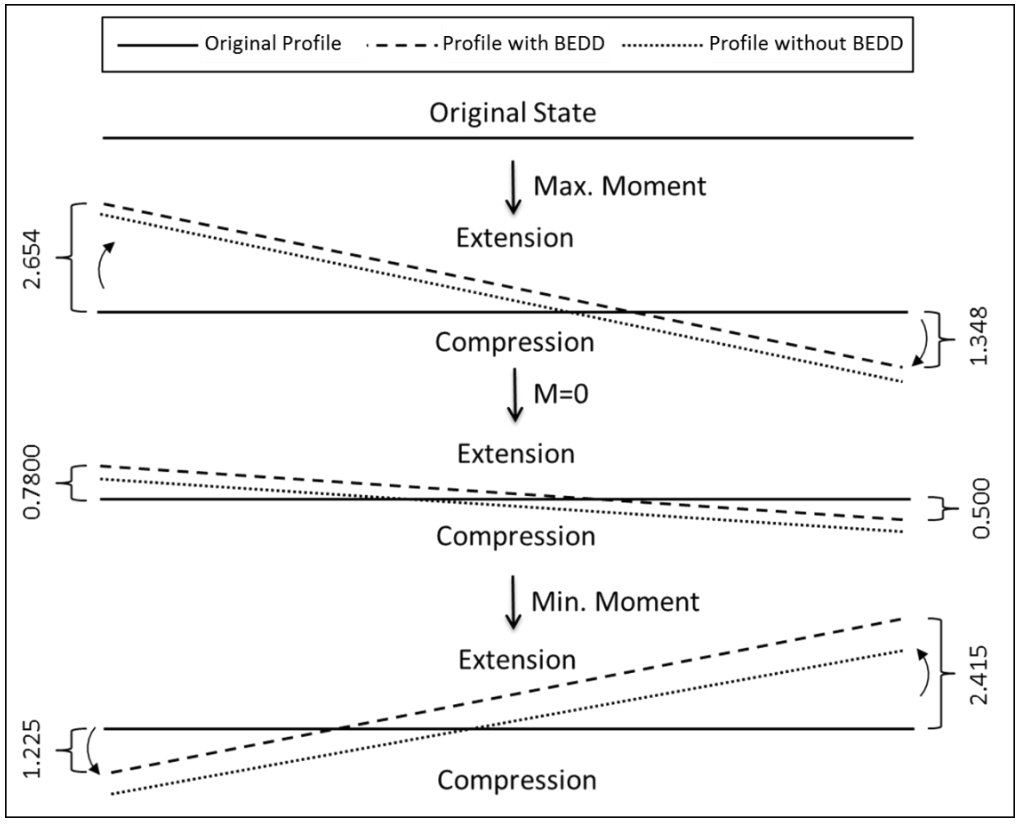

Figure IX.11 Mechanical behavior of the joints with and without the BEDD subjected to different bending moments [displacements in mm]

Based on the obtained internal forces of the BEDD's, the bending moment M_{BEDD} shared by the BEDD can be calculated by:

$$M_{BEDD} = \frac{F_{B1} - F_{B2}}{L_T} \quad \text{(IX.4)}$$

where F_{B1} and F_{B2} are the internal forces of the two BEDD's respectively.

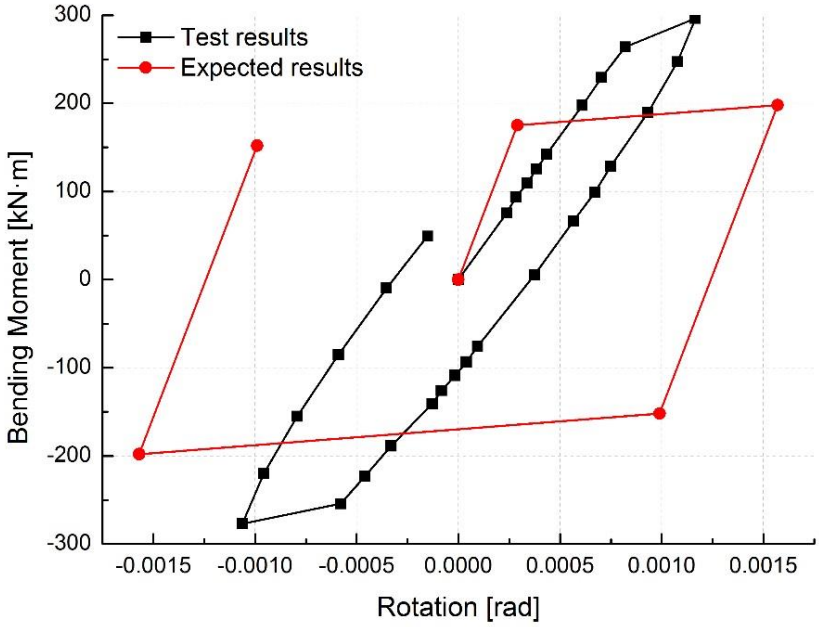

Figure IX.12 Moment-rotation curves of the BEDD's

Table IX.3 Comparison of the designed and obtained parameters of the BEDD

	Design	Test results (Average value from two BEDD)
Elastic stiffness [kN/mm]	104.4	57.0
Yielding deformation [mm]	0.5	1.7
Yielding force [kN]	52.2	96.9

The bending moment-rotation curve of the BEDD's obtained from the test is plotted in Figure IX.12. Significant differences can be observed from the figure between the response of the joint predicted by the proposed design procedure and the one derived from the tests. Note that the

proposed design approach may only show a very general idea of the expected response. Generally, the BEDD's show a good hysteretic performance and the yielding points are clearly observed from the curve except that the yielding stage does not last long. The expected moment-rotation curve of the BEDD from the model given in the previous chapter, is also illustrated in this figure. Compared to the expected results, the hysteretic loop of the BEDD in the test has a smaller area and a lower slope as well as a higher yielding deformation. The parameters of the BEDD obtained from the design and the test results are listed in Table IX.3. It can be seen from the table that the obtained elastic stiffness of the BEDD is only half of the design value while the obtained yielding deformation is more than three times the design value. This may be due to the additional effect of the fixed end of the BEDD, resulting in extra moment in the BEDD and less energy dissipation in the axial direction. Furthermore, the asymmetric bending behavior of the joint (see Figure IX.11) may also contribute to this issue. Since the installed BEDD's increase the stiffness of the joint, the compressive displacements of the joint become smaller compared to the extension side, as shown in Figure IX.11, this may lead to a retardation in compressive yielding of the BEDD.

In addition, the maximum bending moment resisted by the BEDD is 296kN·m (Figure IX.11), which is only 29.6% of the maximum input bending moment. In other words, the bending moment of the joint is mainly resisted by the rubber seal. Under the axial force of 850kN, the rubber seal has been already highly compressed and thus becomes much stiffer as plotted in Figure IX.6, which indicates that most of the bending moment of the joint will be shared by the rubber seal. To increase the seismic mitigation effect of the BEDD's, the following improvement measures are proposed: (1) a softer rubber seal is suggested to increase the bending rotation of the joint and thus to elongate the yielding stage of the BEDD's; and (2) a hinge-end connection should be applied to reduce the extra bending moment in the BEDD.

Although the BEDD's do not reach the expectation, the enhancement of the hysteretic performance of the joint with the BEDD has been proved as well as the feasibility of the application of the seismic mitigation device in immersion joints. If the installation of the BEDD or the design of the rubber seal could be improved as suggested in the previous statements, the hysteretic performance of the joint could be further enhanced. Further research will focus on

the enhancement of the mechanical performance of the BEDD's and also the improvement of their contribution to the seismic mitigation effect for immersion joints.

IX.6. Summary

Based on the presented design of the seismic mitigation device in immersion joints, a validation experiment, involving two cases with and without the optimized BEDD subjected to both compression and bending loadings, are presented with a large geometric scale of 1/10. The displacement of the joint was measured as well as the strain of the connecting region of the BEDD's. Based on the measured data, the bending-rotation curves of the joint with and without BEDD's and the force-displacement curve of the BEDD's were obtained. The performance of the BEDD's was discussed and compared to the design values.

The obtained experimental results indicate that the particular seismic mitigation device, the optimized BEDD in this test, can enhance the hysteretic performance of the immersion joint by 69%, compared to that without such device. Furthermore, the resistance of the bending moment of the joint is increased by 37% while the flexural stiffness of the joint with the BEDD increases by 45%.

Although a significant enhancement of the hysteretic performance of the joint with the BEDD has been proved by the validation test, the performance of the BEDD itself does not reach the expectation as designed, due to the influences of the stiff rubber seal in the joint and the fixed-end support of the BEDD. The properties of the rubber seal should be taken into consideration in the seismic mitigation design of the joint because of its significant contribution to the bending moment resistance of the joint. Furthermore, the installation of the BEDD's should also be improved, by using a hinged-end connection instead of a fixed end connection.

IX.7. References

Ministry of Housing and Urban-Rural Development of the People's Republic of China, 2010. Code for Design of Concrete Structures (GB 50010-2010). China Architecture & Building Press, Beijing. (in Chinese)

Sun, F., Li, G., Guo, X., Hu, D., Hu, B., 2011. Development of a new-type buckling restrained braces and their application in aseismic steel frameworks. Advanced Structural Engineering. 14(4), 717–730.

CHAPTER X

CONCLUSIONS AND PERSPECTIVES

Fehmarnbelt immersed tunnel (planned), Germany and Denmark

(femern.com)

X. Conclusions and Perspectives

X.1. General conclusions

In this final chapter, the conclusions drawn from each chapter are summarized and some major points of intention are highlighted. Finally, perspectives for further research are made.

X.1.1. Developed experimental method

In the framework of Part B: Mechanical behavior of an immersion joint of the present PhD thesis, an experimental investigation method was proposed. As mentioned, the current experiments mainly focused on the flexural behavior of the joint or the single shear keys, while the global behavior of the joint subjected to combined loadings, especially the shear force, was unknown. Moreover, the input parameters in the numerical method required experimental support. Hence, the experimental investigation on the mechanical behavior of a joint subjected to combined loadings is of crucial importance. As such, the necessity of the elaboration of an experimental investigation method, incorporating combined imposed loading is a necessity in the context of the modelling of the mechanical behavior of an immersion joint.

Therefore, a comprehensive experimental investigation on the mechanical behavior of an immersion joint subjected to various loading condition as presented in Chapter IV was conducted for the first time. The detailed information regarding the justification of the experiment, the specimens, the test set-up, the loading protocols as well as the measurements are provided.

According to some testing limitations, a geometric scale of 1:10 was selected. Based on that, two sets of specimens with steel shear keys and concrete shear keys respectively were designed in consideration of an actual tunnel project. Each set of specimens contained two tunnel elements and one GINA rubber seal. The detailed design of the specimens was provided according to the relevant Chinese codes. Then a unique experimental set-up is given as well the measurements. The test set-up includes three major steel frames, allowing that one element is fixed and the other element is movable, resulting in a deformation in the joint. A special joint

was designed to consider the proper force transfer from the frame and the hydraulic jack to the element. In order to obtain reliable test data, transducers were installed symmetrically along the cross section of the tunnel element to eliminate possible errors. Moreover, a four-camera recording system was applied to observe the real time situation inside the element.

In consideration of different loading applications, three different loading protocols were justified, namely the axial loading case, compression-bending moment case and the shear loading case. For the shear loading case, static and dynamic shear loading were both considered. Moreover, the failure of an immersion joint subjected to compression-shear load was investigated.

The proposed experimental set-up has been patented by the State Intellectual Property Office of The People's Republic of China.

X.1.2. Axial and flexural performance

Although the behavior of the immersion joint subjected to axial force and bending moment was already investigated by other researchers, most published investigations focused on the force-compression behavior or bending moment-rotation curve under a single level of axial force. The relation between axial force and compression, the axial force and the bending moment, especially the issue regarding the stiffness, has been much less the subject of research. However, the modelling of the mechanical behavior of the immersion joint, these aspects are of vital importance.

In order to study the behavior of the joint subjected to axial force and bending moment in a comprehensive way, a model immersion joint, composed by two model tunnel elements, were performed and the GINA-type rubber seal in the joint was the main concern.

The model immersion joint was loaded by the axial force and bending moment at the same time, to simulate the initial water pressure at the joint in reality due to its specific construction method. The axial force was divided into five levels and at each level a cycle of the bending moment was applied to the joint without changing the axial force. After the application of one bending moment, the axial force increased to the next level and the loading protocol was repeated until

the fifth level of loading was finished. Then unloading of the axial force followed until the axial force acting on the joint returned to zero.

Based on the experimental investigations, the following results regarding the axial and flexural performance are obtained:

(1) The hysteretic loop of the compression force curve indicates that recovery of compression during unloading does follow the same path as for loading. A residual compression of the joint warns that removal of the axial force is unsafe with respect to the water tightness of the joint. The axial stiffness of the immersion joint varies with the level of the axial force, whether loading or unloading. A fitting curve based on the experimental compression curve of the joint was derived and the loading and unloading axial stiffness of the immersion joint under different water depths can be predicted.

(2) Possible influencing factors of the results were performed to investigate the influencing factors on the axial behavior of the joint, namely the friction force, the length of the GINA rubber, the clamping system of the rubber and the shape of the GINA rubber. Except for the friction force, the behavior of the rubber was influenced by the properties of the rubber at different compression levels, resulting in approximately 10% total differences. The modelling techniques and the used constitutive model for the rubber require further improvement to obtain more accurate results.

(3) The moment–rotation curve shows a hysteretic loop. It indicates that there is energy–dissipation during bending. However, the area of the loop reduces with increasing axial force. The deformation of the joint might be asymmetric as a residual rotation of it is observed at each bending cycle. The values of the flexural stiffness of the joint were obtained and it was found that it increases with axial forces during bending.

(4) The joint remains plane during bending. Rotation of the joint increases with bending moment but it decreases with axial force. When the axial force was at a low level, the joint behaved symmetrically and the rotation center remained in the middle. As the axial force increased, an asymmetric bending behavior was observed and the rotation center moved from

the middle to one side of the joint. The joint under compression and bending moment works in non-linear state at service conditions.

(5) From the tests, the axial and flexural stiffness ratio of the joint to the tunnel element were obtained. The axial loading and unloading stiffness ratios both behaved linearly along with the axial force based on the fitting curve. A similar trend can be found for the flexural stiffness ratio. In service conditions, the axial loading and unloading stiffness of the joint decrease in a relative linear way with values ranging from 1/360 to 1/120 and 1/1028 to 1/305 that of the tunnel element respectively. For the flexural stiffness ratio, it varies from a low bound of 1/212 to an upper of 1/29 of that of the element.

X.1.3. Shear performance

The shear stiffness of the immersion joint is of crucial importance regarding the investigation of the shear behavior of the joint. In previous research, it was assumed that the shear stiffness of the joint tends to be infinite as a simplification and the contribution of the rubber was not considered. Such assumption seems to improve the calculation efficiency but sacrificing the accuracy of the results. Moreover, such assumption lacked experimental support. Hence, a series of experiments was conducted on the investigation of the shear stiffness of the joint subjected to static and dynamic loadings respectively. In each loading case, an axial force was imposed to the joint, followed by a cyclic static or dynamic shear force. Shear force-displacement curves under different loading cases were obtained. The parametric study on the shear stiffness was given by considering the influence of the axial force, the shear amplitude and the shear frequency (in the dynamic part).

Based on the experimental results, the following conclusion are obtained:

(1) The relation between the static shear force and the shear displacement is observed to be linear under increasing shear force, and the higher the axial force, the smaller the measured shear displacement. The obtained static stiffness also experiences a linear increasing trend along with the axial force. When there is no axial force in the joint, the stiffness of the joint is provided only by the shear keys with a calculated value of 137.84kN/mm, which is the smallest value in

this case. In service conditions, between the maximum and minimum water pressure, the static shear stiffness ranges between 287.7kN/mm and 897.9kN/mm.

(2) The shear stiffness ratio of the joint to the tunnel element was defined and calculated. In service conditions, the shear stiffness ratio ranges from 1/76.1 to 1/24.1. Compared to the axial and flexural stiffness of the joint, the shear stiffness ratio is smaller, showing that the joint has a relatively stiffer behavior in shear direction.

(3) The dynamic displacement responses of the joint were obtained by using the first order Fourier equation. Accordingly, the equation for the dynamic stiffness of the joint was given. By a parametric study, the influences of the axial force, the shear amplitude and the shear frequency was provided. Experimental results show that a larger axial force can increase the dynamic stiffness of the joint and the other two factors seem to have a smaller or unpredictable impact on the dynamic stiffness. As calculated, the dynamic stiffness of the joint with maximum and minimum water pressure is 367.6kN/mm and 891.2kN/mm respectively.

(4) By comparison of the static and dynamic stiffness, the difference between these are not that large. As the axial force is 0kN and 1760kN, the corresponding stiffnesses are almost the same. In between, the dynamic stiffness is a bit larger than the static one and the difference reaches a peak at the axial force of 440kN. At this point, the dynamic stiffness is 1.28 times the static one.

X.1.4. Shear failure

Besides the aforementioned shear performance of a joint, the experimental results of a study on a scaled immersion joint, with steel shear keys and concrete shear keys respectively, subjected to compression-shear loadings were also provided. Based on an actual project, a constant compressive axial force of 850kN was applied as well as a reciprocating horizontal shear force with increasing amplitudes. For both the steel and concrete shear keys, a hysteresis effect was observed during the test and the area of the hysteretic loop increases with the shear force. An envelope curve of the shear force-displacement of the joint was obtained and divided into stages based on the observed shear behavior of the joint. The shear stiffness of the immersion joint was also calculated, showing a non-linear variation with the shear displacement. The shear

capacity of the model immersion joint and that of a single steel shear key were evaluated as well. Analysis of the experimental results leads to the following conclusions.

Part I Steel shear keys

(1) Under a reciprocal horizontal shear force, a clear hysteretic loop is found and the area of it increases with the shear force. According to the obtained behavior of the joint, the envelope curve of the shear force-displacement of the joint can be divided into four stages based on the performance of the immersion joint corresponding to a decreasing shear stiffness.

(2) It is observed that the failure mode of the immersion joint relies on the failure of the steel shear keys. Moreover, the HSK2's are found to be damaged and they fail one after another. Based on the fracture of the bolts, the failure mode of a single shear key turns out to be a brittle shear failure. Also, damage of the rubber seal is occurring. The failure of the joint shows a step-by-step character.

(3) The maximum shear capacity of the immersion joint and that of a single steel shear key are 544kN and 191kN respectively. The obtained capacity of the joint is lower than the designed one due to the fact that all the shear keys do not work at the same time. In an actual project, care should be seriously taken, i.e. installing bearing rubber between the shear keys, to assure that the shear forces are evenly distributed to all shear keys as practically possible. It is also found that the rubber seal has a certain contribution to the shear capacity.

Part II Concrete shear keys

(4) Similar to the results of the steel shear keys, a clear hysteretic loop is also found and the area of it increases with the shear force. Based on the observed behavior of the joint, the envelope curve of the shear force-displacement of the joint can be divided into three stages The corresponding stiffness is also calculated, indicating a degradation along with the increase of the shear displacement. However, the shear stiffness is smaller than the stiffness with the steel shear keys. Moreover, differing from the steel shear keys, the racking problem arises in the joint with concrete shear keys due to the asymmetrical installation of the shear keys.

(5) The cracking behavior of the shear keys is observed through the installed cameras. A detailed cracking pattern is obtained, indicating the development of successive cracks. It can be

noticed that the cracks start from the bottom part of the tenon to the inner part of the shear keys at a direction of approximately 45 degree or less and then go through the bottom of the tenon due to the tensile damage. Moreover, small cracks appearing near the contact face together with spalling on the tenon surface are observed possibly due to force concentrations.

(6) The obtained cracking strength and the shear capacity of the joint with concrete shear keys are 74kN (60kN) and 310kN (355kN) respectively. The two different values correspond to the loading directions. For the cracking strength, the obtained value is smaller than the design value due to the fact that all the shear keys are not activated at the same time. Regarding the shear capacity, the test results are a bit larger than the design value also due to the contribution of the rubber seal. However, the results of a single tenon cannot be evaluated precisely due to the unpredictable contribution of the rubber seal.

X.1.5. Seismic mitigation method

The seismic analysis of immersed tunnels was the subject of research since 1995 and the increasing number of projects also promoted the development of the seismic analysis. However, previous research regarding the seismic performance of immersed tunnels remained limited to numerical modeling and to the soil-structure interaction rather than the structure itself. During the same period, some suggestions were formulated to improve the seismic performance of other types of underground structures, such as the isolation layer for shield tunnels or soil treatment for metro stations etc. However, such improvements may work but are not suitable for immersed tunnels due to their special surrounding soil condition and the specific construction method. Hence, a new concept was proposed based on the seismic mitigation theory. The efficiency of the seismic mitigation method in seismic response reduction was proved by both research and actual practice in the building sector but it was never introduced to underground structures before. As such, a seismic mitigation device installed on the immersion joint and working together with the joint, could be an additional way to dissipate the energy induced by earthquakes.

To achieve the application of seismic mitigation in immersion joints, the mechanisms of seismic mitigation method for buildings were studied and discussed through the energy conversion

equations. A buckling energy-dissipation device (BEDD) was introduced on the basis of the BRB. Based on the principle of maximum hysteretic performance of the joint, the optimization design procedure of the seismic mitigation device is illustrated in detail through a parametric analysis, including the critical parameters, such as the elastic stiffness and the yielding deformation of the BEDD's. The design procedure was provided through five steps: (1) representation of the mechanical model of the joint; (2) representation of the mechanical model of the BEDD; (3) representation of the mechanical model of the joint with the BEDD's; (4) representation of the optimization objective function $\boldsymbol{F}$; and (5) optimization of the mechanical parameters of the BEDD's. Finally, the optimized parameters for the BEDD, such as yielding deformation, elastic stiffness and the total length of the device are designed to ensure that the device works in coordination with the immersion joint in such a way that the maximum energy dissipation is reached.

Based on the presented design method of the seismic mitigation device in immersion joints, a validation experiment, involving two cases, one with and one without the optimized BEDD subjected to both compression and bending loadings, are presented with a large geometric scale of 1/10. The displacement of the joint was measured as well as the strain of the connecting region of the BEDD's. Based on the measured data, the bending-rotation curves of the joint with and without BEDD's and the force-displacement curve of the BEDD were obtained. The performance of the BEDD was discussed and compared to the design value.

The obtained experimental results indicate that the seismic mitigation device, the optimized BEDD's in this test, can enhance the hysteretic performance of the immersion joint by 69%, compared to that without such device. Furthermore, the resistance of the bending moment of the joint is increased by 37% while the flexural stiffness of the joint with the BEDD increases up to 45%.

Although a significant enhancement of the hysteretic performance of the joint with the BEDD's was obtained in the validation test, the performance of the BEDD itself did not reach the expectation as designed, due to the influences of the stiff rubber seal in the joint and the fixed-end support of the BEDD's. The properties of the rubber seal should be taken into consideration in the seismic mitigation design of the joint because of its significant contribution to the bending

moment resistance of the joint. Furthermore, the installation of the BEDD's should also be improved, such as using a hinged-end connection instead of the fixed one.

X.2. Perspectives and recommendations for further research

X.2.1. Investigation method

The newly developed test set-up has shown to be very efficient in terms of laboratory experiments on large-scale immersed tunnel elements subjected to axial force, bending moment and shear force. As such, it is recommended to make use of the already existing test set-up as well as the measurement system and procedure in order to investigate further influencing aspects. However, the experimental set-up is only suitable for horizontal loadings, the vertical loading, normally induced by differential settlements, is another issue, which may also raise a very large interest in both the scientific community and the industry.

In the course of the experimental investigation, only the reciprocating shear loading is taken into account as there is a seismic background to this thesis. The cyclic test may induce progressive and cumulative damage in the specimens, especially in the concrete shear keys and the rubber seal. This aspect is suggested for the future experimental work.

For the concrete shear keys, more advanced measuring techniques need to be adopted to obtain the cracking development in a more accurate way. Moreover, a three-dimensional finite element model including detailed material models for concrete, concrete cracking behavior and the bond-slip relationship for the reinforcement bars could be established in order to enhance the accuracy of the analysis or to illustrate specific failure mechanisms. The same applies to the steel shear keys.

Along with experimental investigations to support and consolidate the influencing aspects, numerical investigations could be undertaken. Due to a time limitations, the numerical investigation is not included in this thesis. However, it is necessary to finalize the complete

research on the mechanical behavior of the joint. A 3D numerical model is recommended as the combination of the axial force and the shear loading is required to be considered. It has to be said that the presented results on the shear behavior of the immersion joint rely on the material properties of the rubber seal and the shear keys, construction quality and the loading protocol. The size effect needs to be taken into account as well. Hence, a numerical investigation can solve such issues easily by changing input parameters without any substantial additional cost, but the challenges in both calculation time as well as numerical stability need to be solved.

X.2.2. Immersion joint

In this thesis, the main focus is the global mechanical behavior of the joint and therefore, the performance of a single specimen is paid less attention. However, in the large-scale experiments, the separate behavior of the rubber still remains unclear and it cannot be quantified due to the impossibility of accurate measurements in the test and the complex configuration of the rubber. In this regard, it is necessary to conduct separate tests on the rubber seal supplementary in order to quantify the contribution of the rubber seal. The global behavior and the visco-hyperelastic properties of the rubber need to be taken into account.

A large-scale experimental method is a common approach to investigate the mechanical behavior of a structure. However, the geometric scale may induce a size effect, as is the case, e.g. for the bolts in the steel shear keys. A study to quantify such influence on the performance of the steel shear keys in a numerical or experimental way would have been of particular interest as well.

X.2.3. Seismic mitigation issue

The concept of seismic mitigation is not new in buildings but in this thesis it is the first time ever to be introduced in underground structures, specifically in immersed tunnels. Although significant enhancement of the hysteretic performance of the joint with the BEDD has been proved by the validation test, the performance of the BEDD itself does not reach the expectation as designed. How to maximize the performance of the BEDD in the joint requires a further investigation. The influencing aspects, such as the performance of the rubber seal, the end

support of the BEDD (e.g. a hinged end connection) and even the properties of the BEDD itself, need more studies both in a numerical and an experimental way. In this regard, a more advanced analysis of the BEDD in the joint might also enable an effective application of the BEDD in order to enhance seismic performance. An elaborate theory needs to be established and a proposal for guidelines for the design of the seismic mitigation in immersed tunnels is necessary in the future.

It is also proposed to study the seismic mitigation in immersion joints by adopting other seismic mitigation devices, i.e. lead-rubber damper or viscoelastic and viscous dampers, which have been proven to be effective in seismic-response reduction in buildings. Such topics appear to be innovative from the perspective of design due to the fact that the seismic mitigation method is not limited to one device.

Moreover, the design procedure for the seismic mitigation method was conceived in order to investigate the seismic performance in the flexural direction. Expanding this one-directional approach towards the shear direction or a two-directional configuration, is of particular interest since the seismic excitation could also be active in the shear direction.

PROFILE

Personal Information

Name	Wenhao Xiao
Date of birth	November 05, 1989
Place of birth	Guangdong, China
Nationality	Chinese
Email	Wenhao.Xiao@Ugent.be

Education

2008-2012	Bachelor of Engineering Major: Civil Engineering Faculty of Civil Engineering, Hunan University, Changsha, China
2012-2014	Master of Engineering Major: Tunnelling and Underground Structural Engineering Faculty of Civil Engineering, Tongji University, Shanghai, China
2015-2018	Doctorate of Civil Engineering Faculty of Engineering and Architecture, Ghent University, Ghent, Belgium

A1 publication

Xiao, W., Yu, H., Yuan, Y., Taerwe, L., Chai, R. (2015). Compression-bending behavior of a scaled immersion joint. Tunnelling and Underground Space Technology. 49, 426-437.

Yu, H., **Xiao, W.,** Yuan, Y., Taerwe, L. (2017). Seismic mitigation for immersion joints: Design and validation. Tunnelling and Underground Space Technology. 67, 39-51.

Xiao, W., Yu, H., Yuan, Y., Taerwe, L., Xu, G. (2015). Compression-shear behavior of a scaled immersion joint with steel shear keys. Tunnelling and Underground Space Technology. 70, 76-88.

A2 publication

Yu, H., **Xiao, W.,** Yuan, Y., Taerwe, L. (2017). Compression Performance of Flexible Joints in Immersed Tunnel. China Journal of Highway and Transport. (Submitted)

C1 publication

Xiao, W., Yu, H., Yuan, Y., Taerwe, L., Chai, R. (2015). Experimental investigation on the flexural mechanical behavior of an immersion joint. Proceedings of the ITA WTC 2016 Congress and 41st General Assembly, Dubrovnik, Croatia, 22-28 May 2015.

Xiao, W., Yuan, Y., Taerwe, L. (2016). Experimental investigation on static shear stiffness of an immersion joint. Proceedings of the ITA WTC 2016 Congress and 42nd General Assembly, San Francisco, USA, 22-28 April 2016.

Xiao, W., Yuan, Y., Taerwe, L., Yu, H. (2016). Static and Dynamic Experimental Analysis of an Immersion Joint. Proceedings of the IABSE Conference 2016, Guangzhou, China, 8-11 May 2016.

Xiao, W., Taerwe, L., Yuan, Y. (2016). Shear Performance of Immersion Joint with Concrete Shear Keys. Proceedings of the 11th *fib* International PhD Symposium in Civil Engineering, Tokyo, Japan, 29-31 August 2016.

Xiao, W., Taerwe, L., Yuan, Y. (2017). Numerical Analysis of the Concrete Shear Keys in Immersion Joints. Proceedings of the ECCOMAS Thematic Conference EURO: TUN 2017, Innsbruck, Austria, 18-20 April 2017.

Xiao, W., Yu, H., Taerwe, L., Yuan, Y. (2017). A New Concept for Seismic Mitigation Method for Immersion Joints. Proceedings of the ITA WTC 2016 Congress and 43rd General Assembly, Bergen, Norway, 6-15 June 2017.